
Spin-wave generation and transport in magnetic microstructures

DISSERTATION

zur Erlangung des akademischen Grades

**Doctor rerum naturalium
(Dr. rer. nat.)**

vorgelegt

**der Fakultät Mathematik und Naturwissenschaften
der Technischen Universität Dresden**

von

M.Sc. Kai Wagner

geboren am 09.10.1986 in Hilden

Eingereicht am 26. Januar 2018

Die Dissertation wurde in der Zeit von Februar 2014 bis Januar 2018 am **Institut
für Ionenstrahlphysik und Materialforschung am Helmholtz-Zentrum
Dresden - Rossendorf** angefertigt.

Betreuer: Dr. rer. nat. H. Schultheiss
Prof. Dr. rer. nat. J. Fassbender

1. Gutachter: Prof. Dr. rer. nat. J. Fassbender

2. Gutachter: Dr. rer. nat. H. Schultheiss

3. Gutachter: Prof. Dr. rer. nat. B. Hillebrands

Abstract

Spin-wave generation and transport in magnetic microstructures

Kai Wagner, Dissertation, Technische Universität Dresden

Generating, miniaturizing and controlling spin waves on the nanometer scale is of great interest for magnonics. For instance, this holds the prospect of exploring wave-based logic concepts and reduced Joule heating, by avoiding charge transport, in spin-wave circuitry. In this work, a novel approach is for the first time confirmed experimentally, which allows confining spin-wave transport to nanometre-wide channels defined by magnetic domain walls. This is investigated for different domain wall types (90° and 180° Néel walls) in two material systems of polycrystalline $\text{Ni}_{81}\text{Fe}_{19}$ and epitaxial Fe. The study covers the thermal, linear and non-linear regime utilizing micro-focused Brillouin light scattering microscopy complemented by micromagnetic simulations. An initially linear dispersion dominated by dipolar interactions is found for the guided spin waves. These are transversally confined to sub-wavelength wide beams with a well-defined wave vector along the domain wall channel. In the non-linear regime, higher harmonic generation of additional spin-wave beams at the sides of the domain wall channel is observed. Furthermore, the possibility to shift the position of the domain wall over several microns by small magnetic fields is demonstrated, while maintaining its spin-wave channeling functionality. Additionally, spin-wave transmittance along domain walls, which change direction at the edges of the structure as well as between interconnected walls of identical and different type is studied. Characterization of spin-wave transmission through interconnected domain walls is an important step towards the development of magnonic circuitry based on domain wall(-networks).

With respect to developing flexible and scalable spin-wave sources, the second part of this thesis addresses auto-oscillations in spin Hall oscillators (based on a Pt / $\text{Ni}_{81}\text{Fe}_{19}$ bilayer) of tapered nanowire geometry. In these systems, a simultaneous formation of two separate spin-wave bullets of distinct localization and frequency has been indicated. This spin-wave bullet formation is confirmed experimentally and investigated for different driving currents. Subsequently, control over these bullets by injecting external microwave signals of varying frequency and power is demonstrated, switching the oscillator into single-mode operation. Three synchronized auto-oscillatory states are observed, which can be selected by the frequency of the externally imprinted signal. This synchronization results in linewidth reduction and frequency-locking of the individual bullet modes. Simultaneously the bullet-amplitude is amplified and is found to scale as $P^{2/3}$ with the injected microwave power P . This amplification and control over position and frequency of the spin-wave bullets is promising for the development of microwave amplifiers/detectors and spin-wave sources on the nanoscale based on spin Hall oscillators.

But I shall certainly admit a system as empirical or scientific only if it is capable of being tested by experience. These considerations suggest that not the verifiability but the falsifiability of a system is to be taken as a criterion of demarcation. In other words: I shall not require of a scientific system that it shall be capable of being singled out, once and for all, in a positive sense; but I shall require that its logical form shall be such that it can be singled out, by means of empirical tests, in a negative sense: it must be possible for an empirical scientific system to be refuted by experience.

Karl Raimund Popper

Contents

List of Figures	vi
List of Tables	vii
List of Abbreviations and Acronyms	viii
List of Symbols	ix
1 Introduction	1
2 Theoretical background	4
2.1 Energy density of thin film ferromagnets and domain(wall) formation	5
2.2 Magnetization dynamics in thin film ferromagnets	11
2.2.1 Spin-wave dispersion in the linear regime	13
2.2.2 Magnetization dynamics in the non-linear regime	17
2.3 Spin Hall Oscillators	21
2.3.1 Spin Hall effect and spin transfer torque in a ferromagnet/heavy-metal bi-layer system	21
2.3.2 Characteristics of magnetization auto-oscillations	25
2.3.3 Improvement of monochromaticity, coherence and output power by injection locking	28
3 Materials and Methods	31
3.1 Electron Beam Lithography, EBL	31
3.2 $\text{Ni}_{81}\text{Fe}_{19}$ microstructures	32

3.3	Fe microstructures	34
3.4	Tapered spin Hall oscillators	35
3.5	Micro-focused Brillouin Light Scattering Spectroscopy, μ BLS	36
3.5.1	μ BLS spatial resolution	40
4	Experimental results	43
4.1	Spin-wave dynamics in multi-domain magnetic configurations	43
4.1.1	Spin-wave dynamics of 180° Néel walls in rectangular elements	44
4.1.2	Spin-wave dynamics of 90° Néel walls in square elements	63
4.1.3	Spin-wave dynamics of interconnected Néel walls in Fe wires	76
4.2	Auto-oscillation in tapered wire geometries	88
4.2.1	Initial static magnetic configuration and effective field	89
4.2.2	Thermally excited dynamics and spectral properties	91
4.2.3	Direct microwave excitation of spin-wave dynamics	93
4.2.4	Auto-oscillatory response	96
4.2.5	Microwave amplification and injection locking	104
5	Summary and outlook	114
	Own publications	118
	Bibliography	120
	Acknowledgement	141
A	Appendix	143
A.1	Splitting process in magnetic domains confined by domain walls	143
A.2	reconfigurable remanent states in square structures stabilized by local ion irradiation	144
A.3	Domain wall displacements induced by a scanning laser beam	145
A.4	Magnetic Force Microscopy investigation of the domain wall type and width	147
A.5	Micromagnetic simulations: problem definition and analysis	149
A.6	Current dependence of auto-oscillations in the tapered SHO	152
A.7	Fabrication of $\text{Ni}_{81}\text{Fe}_{19}$ microstructures for spin waves in domain walls	153

List of Figures

2.1	Schematic of domain patterns and domain walls	7
2.2	Dependence of the domain wall type on the film thickness and energy contributions	9
2.3	Schematic of cross-tie patterns. Magnetization profile and effective field well of a 180° Néel wall	10
2.4	Precessional damped motion of the magnetization in an external magnetic field . .	12
2.5	Schematic of a spin wave together with its phase and wavelength.	14
2.6	Spin-wave dispersion relation for an infinite thin film and field sensitivity of spin waves.	15
2.7	Illustration of the spin Hall effect in a heavy metal and working principle of spin Hall oscillators.	23
2.8	Dependence of the non-linear frequency shift of spin waves on the magnetization angle in infinite thin films.	26
2.9	Illustration of the spin-wave bullet formation in tapered spin Hall oscillators for different driving currents	27
2.10	Phase-noise creation by amplitude- and phase-fluctuations in spin Hall oscillators .	29
3.1	SEM micrographs of the investigated spin-wave waveguide structures based on Ni ₈₁ Fe ₁₉	33
3.2	Microscope image of the spin-wave waveguide structure based on Fe.	34
3.3	SEM micrograph of the investigated tapered spin Hall oscillator.	36
3.4	Schematic of inelastic Brillouin-scattering of photons and spin waves.	38
3.5	Experimental determination of the spatial resolution of the μ BLS set-up	41
4.1	SEM micrograph and magnetic configuration of a “bottle-shaped” spin-wave waveguide. Schematic and simulation of the effective field well in the center of the waveguide.	45
4.2	Experimentally recorded thermal spin-wave spectra of a 180° Néel wall and neighbouring domain	47

4.3	Experimentally recorded spin-wave excitation efficiency of a 180° Néel wall and neighbouring domain as a function of excitation frequency.	48
4.4	Experimentally studied parametric excitation and spin-wave confinement in domains separated by a 180° Néel wall.	51
4.5	Experimentally recorded spin-wave intensity-profiles for a 180° Néel wall and surrounding domains in dependence on the spin-wave frequency.	53
4.6	Simulated spin-wave intensity profiles and dispersion relation for a 180° Néel wall	55
4.7	Details on the derivation and analysis of the spin-wave dispersion along 180° Néel walls	56
4.8	Comparison between the experimentally determined and simulated spin-wave intensity-profile and channel width for a 180° Néel wall.	57
4.9	Experimental study on the possibility to steer spin-wave propagation by moving a domain wall channel using magnetic fields.	58
4.10	Experimentally observed influence of pinning sites on domain wall positioning . .	59
4.11	Experimental study on enhanced spin-wave transport along domain wall channels using small magnetic fields applied perpendicular to the wall: magnetic contrast. .	60
4.12	Experimental study on enhanced spin-wave transport along domain wall channels using small magnetic fields applied perpendicular to the wall: spin-wave intensities.	61
4.13	SEM micrograph and magnetic configuration of a square waveguide. 90° Néel wall and simulated effective field well.	64
4.14	Experimentally recorded thermal spin-wave spectra of a 180° Néel wall and neighbouring domain	65
4.15	Experimentally recorded spin-wave excitation efficiency of a 90° Néel wall and neighbouring domain as a function of excitation frequency.	66
4.16	Simulated spin-wave intensity profiles and dispersion relation for a 90° Néel wall .	67
4.17	Experimentally determined and simulated spin-wave intensity-profile for a 90° Néel wall.	68
4.18	Non-linear excitation and higher harmonic generation in 90° Néel walls: spectra and line-profile	71
4.19	Frequency dependence of linear and non-linear excitation in 90° Néel walls	72
4.20	Simulated higher order spin-wave intensity profiles across 90° Néel walls.	73

4.21	Spatial resolved measurements of the higher harmonic generation in 90° Néel walls.	74
4.22	Microscope image and magnetic configuration of the spin-wave waveguide based on Fe.	76
4.23	Experimentally recorded thermal spin-wave spectra of a 180° Néel wall in Fe and neighbouring domain.	77
4.24	Experimentally recorded spin-wave excitation efficiency for two differently oriented 90° Néel walls. Spin-wave transport in two 90° Néel walls interconnected to a 180° Néel wall.	79
4.25	Experimentally recorded spin-wave transport in 90° Néel walls around a diamond domain, which suddenly change in direction.	81
4.26	Selective spin-wave transport in two 90° Néel walls depending on the spin-wave frequency (multiplexing).	82
4.27	Non-linear spin-wave excitation and transport in a diamond domain and surrounding Néel walls.	84
4.28	Effective field well and recorded channel width in Fe based systems.	85
4.29	Experimentally recorded spin-wave transport across four interconnected 90° Néel walls.	87
4.30	SEM micrograph, magnetic configuration and effective field distribution in the tapered SHO.	90
4.31	Experimentally recorded thermal spin-wave spectra of the tapered SHO.	91
4.32	Induced Oersted field in the SHO, when injecting currents.	94
4.33	Experimentally recorded direct excitation of spin waves in the SHO by the induced Oersted field.	95
4.34	Experimentally recorded auto-oscillations in the SHO for a current of 2 mA.	97
4.35	Experimentally recorded auto-oscillations for a current of 2.5 mA.	99
4.36	Spectral and spatial analysis of the auto-oscillations in comparison with a model system.	100
4.37	Experimentally recorded dependence of the auto-oscillation intensity on the injected current in comparison with an analytical model.	103
4.38	Experimentally recorded auto-oscillation spectra of a spin-wave bullet during injection-locking for exemplary injected frequencies.	105

4.39	Injection locking regime, linewidth reduction and amplitude enhancement for injected microwave frequencies covering the auto-oscillation spectra.	106
4.40	Experimentally determined microwave amplification by the SHO in dependence of the injected microwave power.	108
4.41	Spatially resolved measurements of the synchronized single bullet states.	109
4.42	Spatially resolved measurements of the synchronized double bullet state.	111
A.1	Experimentally measured 3-magnon splitting in domains separated by a domain wall.	143
A.2	Reconfigurability of remanent magnetic configurations in square structures using ion implantation.	145
A.3	Domain wall manipulation by a scanning laser spot.	146
A.4	Magnetic Force Microscopy of the “bottle-shaped” spin-wave waveguide in comparison with simulations of the expected strayfields.	147
A.5	Schematic magnetic configuration of the “bottle-shaped” spin-wave waveguide. . .	148
A.6	Simulated spin-wave mode profiles across the spin Hall oscillator	151
A.7	Dependence of the auto-oscillation intensity and frequency on the injected current for different positions of the SHO.	152

List of Tables

3.1	Magnetic parameters of the $\text{Ni}_{81}\text{Fe}_{19}$ microstructures for the study of channeled spin-wave transport	34
3.2	Magnetic parameters of the Fe microstructures	35
A.1	Parameters of the micromagnetic finite difference simulations	150
A.2	Recipe for the fabrication of $\text{Ni}_{81}\text{Fe}_{19}$ microstructures in the NanoFaro facility of the Helmholtz-Zentrum Dresden - Rossendorf	153

List of Abbreviations and Acronyms

(TR)MOKE	(time resolved) magneto-optical Kerr-effect (set-up)
μ BLS	micro-focused Brillouin light scattering microscopy
DBS	SHO in double bullet state DBS
EBL	electron beam lithography
FM	ferromagnet
FWHM	full width half maximum value
GMR	giant magneto-resistance
HM	heavy metal
LASER	light amplification by stimulated emission of radiation
MFM	magnetic force microscopy
MRAM	magnetic random access memory
NA	numerical aperture
NLFS	non-linear frequency-shift
RMS	root mean square
SB A/B	SHO in single bullet state A/B
SEM	secondary electron microscope
SHG	second harmonic generation
STT	spin transfer torque
THG	third harmonic generation
Ti:Sa fs-LASER	titanium sapphire femtosecond LASER
TMR	tunneling magneto-resistance

List of Symbols

A	exchange constant
α_G	Gilbert damping parameter
$a(r)$	creation and annihilation operators of spin waves (magnons)
\mathbf{j}^c	charge current density
Δ_f	spectral resolution
Δ_x	spatial resolution
M_S	saturation magnetization
e	electron charge
ϵ_{cub}	cubic crystalline anisotropy energy density
ϵ_{dip}	dipolar energy density
ϵ_{ex}	exchange energy density
ϵ_{zee}	Zeeman energy density
ϵ	energy density of a ferromagnet
η	noise background for the SHO
γ	gyromagnetic ratio
g	g-factor
\mathcal{H}_n	Hamiltonian of n-th order in $a(r)$
\hbar	planck constant
$\mathbf{H}_{\text{dipolar}}$	dipolar magnetic field
\mathbf{H}_{eff}	effective field acting on the magnetization
\mathbf{T}_{eff}	torque of the effective field on the magnetization
\mathbf{H}_{ext}	external magnetic field
λ_L	Landau-Lifshitz damping parameter
\mathbf{M}	magnetization vector
ρ_M	magnetic pseudo-charge
∇M	divergence of magnetization
f_{exc}	microwave (spin-wave excitation) frequency
P	microwave (spin-wave excitation) power
\mathbf{h}_P	microwave (spin-wave excitation) field
D	spin-wave stiffness
N	non-linear frequency-shift constant
Q	non-linear damping parameter
\mathbf{R}	damping torque acting on the magnetization
\mathbf{j}^s	spin current density
\mathbf{P}	spin-polarization of spin-current

θ_{SH}	spin Hall angle
c_k	spin-wave amplitude
ω_k	spin-wave angular frequency
φ_k	spin-wave propagation angle with respect to \mathbf{M}
\mathbf{m}	magnetization deflection vector
v_G	spin-wave group velocity
λ	spin-wave wavelength
\mathbf{k}	spin-wave wave vector
d	ferromagnetic film thickness
ζ	critical current density for auto-oscillation

CHAPTER 1

Introduction

The field of Spintronics, which aims to utilize the spin of electrons in conventional electronic circuitries to provide novel functionalities for data storage and its transport, has gained enormous interest in the last decades [1, 2]. Its development is inspired by the exploration of effects allowing to control and sense the electron spin by electrical means. Magnetic systems take a unique role in this field since the spin-degree of freedom manifests itself macroscopically as the magnetization and can not only be probed, manipulated and stabilized, but is also intrinsically connected to the spin-polarization and the electrical resistance of the electron transport.

In this context, the discovery of the giant magnetoresistance (GMR) [3, 4], tunneling magnetoresistance (TMR) [5] and the spin transfer torque effects (STT) [6, 7] were of particular importance connecting electron transport with the electron spin. This established a direct link between the magnetization and charge currents, resulting in diverse applications of magnetic nanostructures. For example, already nine years after its discovery, the resistive GMR effect was the new technological standard for the read-out-operation in magnetic hard drives. And the recent development of the commercially available STT-MRAM design combines the TMR with the STT effect both for reading and writing operations of information in magnetic bits for non-volatile energy efficient storage [8, 9].

Using the change of the electrical resistance by the magnetization to store and transport data holds the prospect of non-volatility, reconfigurability and radiation hardness. The connected desired high operating speeds above several GHz for switching the magnetic bits and their miniaturization couples these technologies with the magnetization dynamics and its damping. Therefore, to understand and design magnetic spectra and their resonance frequencies, the wave-like eigenmodes referred to as spin waves, are intensively studied in micro- and nanostructured systems of various geometries [10–14] and novel materials of optimized damping tailored to the application [15, 16] are researched.

Besides optimized and low-loss switching of magnetic bits (enhanced) by thermal [17, 18], optical [19], electrical [20] or magnetic means, the field magnonics (or magnon spintronics) [21, 22] branches out to explore the possibility to directly involve spin waves (where the quanta are referred to as magnons) in logic circuitry to transport and process information. The related approaches are based on the utilization of amplitude, phase or frequency of the spin waves combined with effects of interference, diffraction/refraction and non-linearities. This holds the prospect of wave-based logic circuitry, paving the road for non-boolean computer architectures, such as neuronal networks and may furthermore allow to reduce the waste heat generated by Joule heating by avoiding charge transport. Importantly, the spin-pumping and (inverse) spin Hall effect facilitate interconversion and mutual engagement between charge currents and spin waves, easing the combination with existing technologies. Of particular importance in the field of magnonic circuitry is the development of efficient means to control and miniaturize the propagation path of spin waves. Current schemes are mainly based on a geometrical definition of waveguides lacking high flexibility or requiring additional energy for their operation. Another concept is based on utilizing effective field wells at the structure edges [23]. However, these are often delicate and sensitive to fabrication processes.

In view of this background, the **first part** of this thesis addresses the control of spin-wave propagation in magnetic micro- or nanostructures. A concept, based on utilizing magnetic domain walls as spin-wave channels on the nanometer-scale is explored both experimentally and by micromagnetic simulations. For Bloch walls this channeled propagation has been predicted analytically first in 1961 by Winter [24], later in 1979 by Lévy [25] and recently during the time of this thesis by micromagnetic simulations [26]. However, experimental evidence of this channeled propagation has been missing and different type of domain walls and their networks have only been simulated in very specific cases regarding spin-wave transport along them so far. Within this thesis the successful realization of channeled spin waves guided within domain walls is for the first time confirmed experimentally in $\text{Ni}_{81}\text{Fe}_{19}$ as well as Fe based thin film microstructures at the example of 180° and 90° Néel walls. This is studied for the thermal, linear and non-linear regime of spin-wave dynamics by micro-focused Brillouin Light Spectroscopy (μBLS). Moreover, spin-wave transmittance through interconnected domain walls of different and identical type, which suddenly change in direction is observed for the first time. Additionally, the possibility to directly control the spin-wave flow in these microstructures via manipulation of the domain wall channel by small external fields is demonstrated experimentally. These results are a promising first step towards utilization of reconfigurable and non-volatile domain wall networks in spin-wave circuitry. Besides guiding spin waves, such networks of topological solitons may also be used to store information, which can be probed by spin waves.

The **second part** is devoted to excitation of spin waves. In this context, the STT is a promising candidate for the development of highly flexible spin wave sources, since it allows to excite or amplify arbitrary spin waves of different nature such as propagating spin waves [27–30], spin-wave bul-

lets [31], droplets [32] or vortex gyration [33]. This can be readily achieved by applying constant currents in magnetic nanostructures of suitable geometry, such as the spin transfer torque oscillators (STO) and the closely related spin Hall oscillators (SHO) [34, 35]. The excitation mechanism is based on compensation of the intrinsic damping of the magnetization dynamics by electrical means. The basis of this is the injection of a spin current into a magnetic layer, which then acts on the magnetization by the STT effect.

In the anti-damped regime self-induced magnetic oscillations emerge at points of sufficiently high current density, also referred to as auto-oscillations. As a clear advantage over conventional methods, the excitation of spin waves by STT facilitates miniaturization and universal amplification of the dynamics. This grants coverage of the entire spin-wave spectrum including large wave vectors and operating frequencies, without the need for phase- or frequency matching schemes. Additionally, the possibility to convert the magnetic oscillations back into electrical signals by magnetoresistive effects has motivated research of such devices as the next generation of controllable oscillators, e.g., in telecommunication [36]. However, the monochromaticity, coherence and output power of STO and SHO still remain to be improved to render them fully competitive sources of magnetization dynamics or electrical signals. Hence, a deep understanding of their characteristics, dependence on device geometry and excited magnetic spectra by STT is needed. In this thesis, auto-oscillations in SHO of micron-sized tapered nanowire geometry are studied using μ BLS. For the investigated devices, a predicted multi-mode operation is confirmed experimentally, where distinct self-localized spin-wave bullets of different frequency form simultaneously within the SHO. Subsequently, the control of the auto-oscillatory state by small externally imprinted microwave signals is demonstrated, switching the SHO from multi- into single-mode operation resulting in amplitude enhancements, linewidth reduction and microwave signal amplification.

The thesis starts with **chapter two** presenting the theoretical background required for understanding the presented experimental work. In particular, the domain wall formation, as well as the spin-wave dispersion relation, in thin film ferromagnets is presented. The second part of the chapter is devoted to the theoretical foundation of magnetization auto-oscillations.

In the **third chapter** the main experimental method of micro-focused Brillouin light scattering spectroscopy (μ BLS) as a sophisticated tool to investigate the spin-wave dynamics is presented as well as sample fabrication and their parameters.

The **fourth chapter** presents the experimental results including micromagnetic simulations and comparison with the theoretical expectations both of the channeled spin-wave propagation within domain walls and for the auto-oscillatory state in the tapered SHO.

The thesis closes with **chapter five** giving a summary of the major results, conclusions and an outlook regarding opportunities and suggested orientation of future studies. In this context, also the synergy of STT sources and domain wall channels is mentioned.

CHAPTER 2

Theoretical background

This chapter presents the theoretical background as a basis for understanding and classification of the presented experimental results on magnetization dynamics in microstructures. It is devoted mainly to the two investigated topics of spin-wave transport confined to nanometre-wide effective field wells created by magnetic domain walls, as well as on the control over spin-wave generation in spin Hall oscillators (SHO). Since a detailed discussion of all the underlying physical principles would exceed the framework of this thesis by far and, moreover, cloud a clear view on the main essentials and synergies for the observed phenomena, here, a rather concise and selected representation is chosen, while providing references for the interested reader. Comprehensive descriptions on (confined) spin-wave dynamics (in microstructures) can, for example, be found in several textbooks such as the ones by Stancil [37], Gurevich [38] or Demokritov [39]. A detailed and extensive discussion on the theoretical and experimental investigations of domain(-wall) formation is given in the book of Hubert and Schaefer [40]. A good overview covering spin transfer torque and spin Hall oscillators is provided in the book chapter from Joo-Von Kim with numerous references [41], as well as in a review from Chen [36], while non-linear magnetization dynamics are for example discussed in [42–44]. Further references are given in the respected sections.

The following **section 1** starts by introducing a formalism to describe the energy density of a thin film ferromagnet depending on the orientation of the magnetization. In particular the dipolar energy and its characteristics are presented as the main reason for domain pattern formation in magnetic thin film elements. Subsequently, the spatial transition between differently oriented domains is discussed for symmetric/asymmetric Bloch and Néel walls, as well as cross-tie structures for different film thicknesses. The section closes by presenting the expected domain wall type and width for systems studied within this thesis.

In **section 2** magnetization dynamics is discussed following the concept of an effective field, which connects the energy density with occurring dynamics. Also the phenomenological damping terms,

as proposed by Gilbert [45] and Landau-Lifshitz [46] are introduced. The spin-wave dispersion relation for a magnetic thin film (in the linear regime) based on the analytical model of Kalinikos and Slavin [47] or Arias and Mills [48] is presented to illustrate the anisotropy and effective field dependence of the spin-wave dispersion.

Section 3 introduces non-linearities occurring for high spin-wave densities. In this regime of large precession amplitudes, the damping, as well as effective field torques are influenced non-linearly by the dynamic itself. This results in additional spin-wave excitation mechanisms, such as parametric amplification and higher harmonic generation. In addition, the non-linear reduction of the spin-wave frequency with increasing spin-wave amplitude is described.

Section 4 covers SHO in the non-linear auto-oscillation regime. The working principle on driving magnetic auto-oscillations in the studied device geometry is presented and the underlying phenomena of spin Hall effect and spin transfer torque are discussed. Characteristics of the auto-oscillations, including spin-wave bullet formation, is presented. The soliton-like bullets are self-contracting and decrease in size, with increasing spin-wave amplitude. Subsequently, the prediction, that due to the size-reduction of the spin-wave bullets for higher oscillation amplitudes, the studied spin Hall oscillators spatial extend is sufficient to simultaneously host several localized spin-wave bullets of distinct frequencies is discussed. The chapter closes on the concept of “injection-locking” SHO to externally imprinted microwave signals to improve their spectral quality and output power.

2.1 Energy density of thin film ferromagnets and domain(wall) formation

The energy density ϵ of a thin film ferromagnet governs not only the static magnetization pattern formation in terms of relaxation towards local energy minima, but also magnetization dynamics such as reversal processes or magnetic oscillations around these configurations of minimized energy. In general it consists of a variety of contributions, as, for example, the long-range dipolar interactions [49], interlayer coupling phenomena [50–52], magnetocrystalline anisotropy [53], magnetoelastic effects [54] or spin-dependent potentials. However, it is often sufficient to consider simplified phenomenological descriptions restricted to symmetrically less complex contributions, e.g., the short-ranged exchange interactions in the Heisenberg Hamiltonian formulation [55–57] and Zeeman-energies of a magnetic body in an external field (see e.g. [58]) for approximation.

Taking into account the exchange energy ϵ_{ex} , zeeman-energy ϵ_{zee} , dipolar energies ϵ_{dip} and cubic crystalline anisotropies ϵ_{cub} , one can describe the total resulting energy density ϵ ¹ [37, 38]:

¹For the sake of simplicity the magnetocrystalline anisotropy was assumed to be cubic, matching the symmetry

$$\mathcal{E} = \mathcal{E}_{\text{ex}} + \mathcal{E}_{\text{dip}} + \mathcal{E}_{\text{zee}} + \mathcal{E}_{\text{cub}} \quad (2.1)$$

$$\mathcal{E}_{\text{ex}} = \frac{2\mu_0}{V_K} \int_{V_K} \mathbf{H}_{\text{ex}} \cdot \mathbf{M} dV_K \quad (2.2)$$

with exchange field $\mathbf{H}_{\text{ex}} = \frac{D}{2\mu_0 M_s} \Delta \mathbf{M}$ and spin-wave stiffness $D = 2A/M_s$

$$\mathcal{E}_{\text{dip}} = \frac{\mu_0}{2V_K} \int_{V_K} \mathbf{H}_{\text{dip}} \cdot \mathbf{M} dV_K \quad (2.3)$$

$$\mathcal{E}_{\text{zee}} = -\frac{\mu_0}{V_K} \int_{V_K} \mathbf{H}_{\text{zee}} \cdot \mathbf{M} dV_K \quad (2.4)$$

$$\mathcal{E}_{\text{cub}} = K_0 + K_1 (\alpha_1^2 \alpha_2^2 + \alpha_2^2 \alpha_3^2 + \alpha_3^2 \alpha_1^2) + K_2 \alpha_1^2 \alpha_2^2 \alpha_3^2 \quad \text{with} \quad \alpha_i = \frac{M_i}{M} \quad (2.5)$$

Where the magnetization vector \mathbf{M} is defined by a local orientation within the ferromagnetic material and assumed to be of constant magnitude. Importantly, the minimization of the total energy does not necessarily result in a homogeneous magnetic texture and energy description, but, due to the dipolar-interactions, often an inhomogeneous magnetic ground states is favored [40]. So that in general, the magnetic texture of a ferromagnet consists of sub-volumes of homogenous magnetic orientation (domains) and a rather interfacial rotation transition at their boundaries to each other, called domain walls. For illustration, an exemplary magnetic configuration of a thin film element is schematically shown in Fig. 2.1 **a** indicating domains and domain walls.

The dipolar energy takes a key role for spatial dependent magnetic configurations and for the influence of the geometrical boundaries in microstructures on the magnetization dynamics. Even though in the notation of equation 2.3 its energy term looks mathematically similar to the zeeman-energy, the dipolar-field $\mathbf{H}_{\text{dipolar}}$ connects the local magnetization to the entire magnetic pattern and its boundaries, turning the description of magnetization into a non-local equation with non-negligible boundary conditions at the interfaces. In the magnetostatic limit calculation of this dipolar field reduces to [49, 59]:

$$\mathbf{H}(\mathbf{r}')_{\text{dip}} = \nabla' \left(\int_{V_S} dV \frac{\nabla \mathbf{M}}{|\mathbf{r}' - \mathbf{r}|} + \int_{\partial V_S} dA \frac{\mathbf{n} \mathbf{M}}{|\mathbf{r}' - \mathbf{r}|} \right) \quad (2.6)$$

investigated throughout this thesis (bcc-Fe).

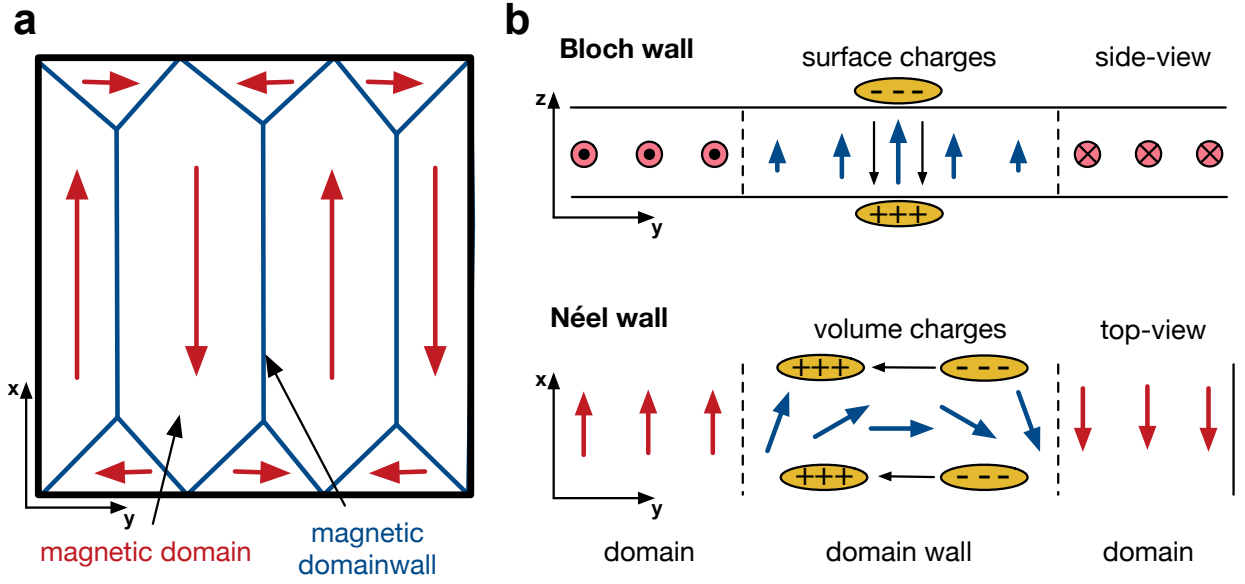


Figure 2.1: **a**, Schematic of a domain pattern in a ferromagnetic thin film element. At the interfaces of differently oriented magnetic domains (red arrows giving the direction of the magnetization) the magnetization rotates on much smaller length scales (blue dashed lines, typically tens of nanometer) than the domain size. **b**, Schematic of a Bloch- (top) and Néel wall (bottom) configuration, differing in the orientation of the magnetization-rotation axis. Depending on the wall type either opposite surface pseudo-charges at the top and bottom surface (Bloch-wall) or volume pseudo-charges with corresponding dipolar fields (black arrows) are created.

The integration is split into a volume contribution (integral over V_S) and a surface term (integral over ∂V_S) stemming from the spatial boundaries of the ferromagnetic body with normal vector \mathbf{n} . Since this poisson equation is mathematically identical to the one in electrostatics, when replacing the divergence of the magnetization by electric charges $\rho_{\text{charge}} = -\nabla M$, the divergences of \mathbf{M} are often referred to as magnetic "pseudo-charges" $\rho_M = -\nabla M$ [49]. Meaning, that the magnetic dipolar fields are identical to the electric fields, when substituting the magnetic pseudo-charge distribution by an electrical one.

However, in contrast to electronic charges, the more complex origin of these pseudo-charges complicates the development of simple equations of their general transport, creation or annihilation, attractive or repulsive forces etc. So only few phenomenological models describing pseudo-charge interaction, such as attraction or repulsion of domain walls [60–63] or pseudo-charge-currents in spin-ice systems [64], for selected cases have been explored. This complexity and non-local nature manifests itself also in micromagnetics, where the dipolar interaction and its minimization demands in almost every case the majority of the computational time.

Despite the aforementioned implications, helpful general characteristics of this dipolar energy and effective fields can be given:

First of all, the so called “pole-avoidance-principle” states, that every pseudo-charge resulting from the magnetic pattern (either at the boundaries or in the volume) will cost/increase energy, due to the creation of additional inner and outer stray fields and is, therefore, generally avoided [58]. At the surface of a magnetic body this is achieved by orienting the magnetization perpendicular to the surface normal, favouring the magnetization in thin film elements to be parallel to the structure sides as well as top and bottom surface.

Secondly, the emerging dipolar fields are in the vast majority of cases aligned antiparallel with the local orientation of the magnetization inside the body and, hence, also referred to as “demagnetization fields”.

Thirdly, the strayfield of a magnetic dipole [49], energetically favors the anti-parallel alignment of magnetic moments neighboring perpendicular to the moments direction, promoting a short-scale magnetic reorientation. The dipolar field generally favors so called flux-closure states, which avoid outer strayfields by formation of domains. If only the dipolar fields are considered, this energy would be minimized by an instantaneous “flip” of the magnetization at the interfaces of the differently magnetized domains. However, since the exchange energy would dramatically increase for an instantaneous flip-configuration the transition is smoothened to a continuous rotation on a length scale balancing the exchange-, dipolar- and magnetocrystalline energy in the form:

$$\lambda_{\text{wall}} \propto \lambda_{\text{ex}} = \sqrt{\frac{A}{(K_{\text{dip}} + K_{\text{mc}})}} \quad (2.7)$$

where K_{mc} is the magnetocrystalline energy density and K_{dip} represents the dipolar energy density, which takes the approximate form $1/2 \cdot \mu_0 M_s^2$ for thin film elements [58, 65]. For the case of $\text{Ni}_{81}\text{Fe}_{19}$ (Py) and Fe samples investigated (magnetic parameters in section 3), this exchange length is around $\lambda_{\text{ex}}^{\text{Py}} \approx 5.3 \text{ nm}$ and $\lambda_{\text{ex}}^{\text{Fe}} \approx 3.17 \text{ nm}$ and a characteristic length scale, on which the magnetization can only smoothly vary. For this reason, spatial dimensions, e.g. the film thicknesses, are often referred to in units of the exchange length.

The magnetization of the domain walls at the interfacial boundaries of domains will rotate around an axis minimizing the creation of pseudo-charges. For illustration, one can consider the transition between two domains of opposite orientation \mathbf{x} to $-\mathbf{x}$, at a “side-to-side” boundary. This configuration is sketched in Fig. 2.1 **b** and called a 180° wall, according to the 180° rotation of the magnetization from one domain to the other. In the chosen cartesian system, the domain wall is formed along the \mathbf{x} -direction and the connection line of the two domains is given by a perpendicular axis \mathbf{y} . In the case of a Bloch wall the magnetization rotates continuously around the \mathbf{y} -axis and lies in the xz -plane, avoiding any magnetization volume-charges by creating surface charges at the top and bottom of the magnetic film. Louis Néel concluded in 1955 [66] that in thin films, this rotation would lead to immense surface charge related energies. He discovered a different magnetic texture of minimal energy with decreasing film thickness, allowing for volume charges but

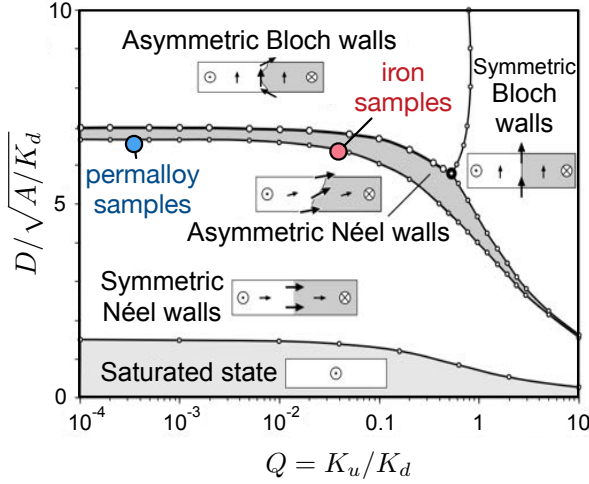


Figure 2.2: Domain wall type as a function of film-thickness D normalized by the exchange length for different ratios $Q = K_u/K_{\text{dip}}$. The nominal parameters of the studied materials are represented by colored dots (Permalloy ($\text{Ni}_{81}\text{Fe}_{19}$, blue): $D = 35$ nm, exchange length 5.3 nm, $Q = 2.5 \cdot 10^{-4}$, Iron (Fe, red): $D = 20$ nm, exchange length 3.17 nm, $Q = 2.7 \cdot 10^{-2}$) (adapted from [65]).

avoiding surface charges by in-plane rotation of the magnetization, called Néel walls. This domain wall configuration is shown in the bottom part of Fig. 2.1 b. Néel studied the thickness dependent transition from Bloch to Néel walls together with their energies, wall angles and deformation by in-plane fields. For films clearly below ≈ 7 times the exchange length (e.g. in $\text{Ni}_{81}\text{Fe}_{19} \approx 35$ nm) so called symmetric Néel walls occur, where a one-dimensional description of the wall magnetization is a good approximation. R. Kirchner succeeded first to numerically compute this type of wall using variable cell sizes in his simulations [67]. Even intermediate forms between pure Bloch- and Néel walls are reported (termed "asymmetric"), where the magnetic texture results from the complex interplay between surface- and volume-charges and their spatial interaction by the dipolar stray fields. This thickness-transition is shown in Fig. 2.2 for different ratios Q of anisotropy-energies and dipolar energies, where the nominal parameters of the samples investigated in this thesis have been marked by colored dots. The samples have a thickness of about 7 times the exchange length (35 nm for $\text{Ni}_{81}\text{Fe}_{19}$ and 20 nm for the case of Fe).

According to the micromagnetic one-dimensional calculations [65] a transition between symmetric Néel and asymmetric Néel wall configurations takes place for this parameter range. However, more complex structures are observed in this regime referred to as "cross-tie" patterns not covered in the one-dimensional calculation. This is in connection with the findings, that in this regime, the total pseudo-charge induced by a 180° Néel wall is more than 3 times larger, than for a 90° Néel wall and that as a consequence the energy of a 90° Néel wall is only about 12% of that of a 180° Néel wall in this model [68].

This energy difference is believed to be the reason, why a 180° Néel wall can be substituted by a more complex two-dimensional cross-tie pattern [69] consisting mainly of 90° Néel walls, even though a rigorous consistent theory of the cross-tie formation is still lacking [40]. The corresponding magnetic textures are shown schematically in Fig. 2.3 a for both configurations. Experimentally the case of 180° Néel walls as well as the cross-tie structure are observed in rectangular $\text{Ni}_{81}\text{Fe}_{19}$ -samples of elongated geometry.

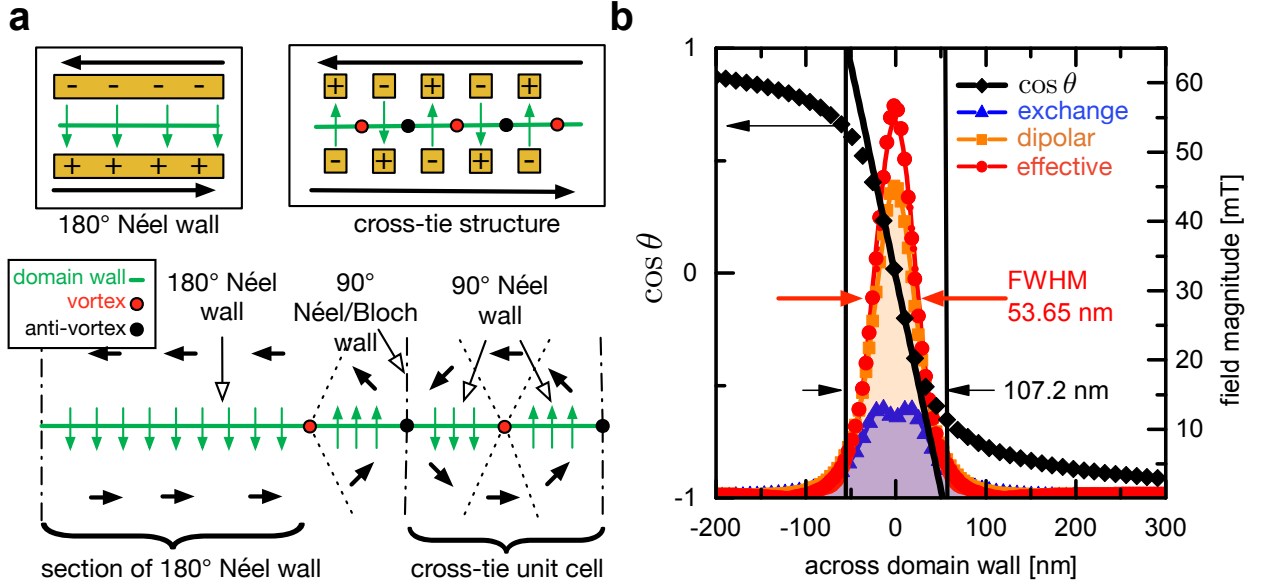


Figure 2.3: **a**, Schematic of the magnetic configuration (arrows), vortices (red dots), anti-vortices (black dots) and domain walls (green line) for the cross-tie structure. For this domain pattern 180° Néel walls (or sections of it) are replaced by a more complex structure of 90° Néel walls and (anti-)vortices. Black dashed-dotted lines are 90° asymmetric walls (along the lines), while dotted lines are rather smooth transitions. **b**, Magnetization-angle profile $\cos \theta$ of a 180° Néel wall (black diamonds) together with the effective field well (red dots). The effective field well is mainly determined by the dipolar fields (orange squares), with smaller contribution of the exchange field (blue triangles). The tangent construction on the wall-profile [70] yields a domain wall width of 107.2 nm and a Full Width Half Max of the field $\text{FWHM} = 53.65$ nm. Simulations for a rectangular geometry with material parameters of $\text{Ni}_{81}\text{Fe}_{19}$.

Next to its type, a domain wall can further be characterized by the width of the magnetization transition. For Néel walls the magnetization direction changes most rapidly at the domain wall center (core), followed by a smoother reorientation at the domain wall tails. The core width of the wall $\lambda_{\text{NW-core}}$ can, for example, be defined by a tangent on the magnetization-angle profile (e.g. Lilley [70] or Trunk [71]) and in general varies for Bloch as well as for Néel walls over an order of magnitude [71–73] depending on the film thickness and material parameters. Within this thesis, micromagnetic simulations are used to determine the arising wall profile and fields. This is illustrated in Fig. 2.3 **b** at the example of a simulated magnetization-angle profile for a 180° Néel wall based on $\text{Ni}_{81}\text{Fe}_{19}$, yielding a width of around 107 nm, together with the field well localized at the domain wall dominated by the dipolar field with an additional smaller exchange field contribution.

The field wells are characterized by their Full Width Half Maximum (FWHM), which is about half of the width-definition of the wall proposed by Lilley. For the $\text{Ni}_{81}\text{Fe}_{19}$ -systems this FWHM is

typically about 10 times the exchange length depending on the exact definition:

$$\lambda_{\text{wall}}^{\text{FWHM}} \approx 10\lambda_{\text{ex}} \approx 53 \text{ nm} \quad \text{for Ni}_{81}\text{Fe}_{19} \quad (2.8)$$

For the Fe systems a smaller width is found:

$$\lambda_{\text{wall}}^{\text{FWHM}} \approx 4\lambda_{\text{ex}} \approx 12 \text{ nm} \quad \text{for Fe} \quad (2.9)$$

A detailed analysis of thin film elements of arbitrary shape is given in [74] and a very good and broad overview can be found in [40,58] for deeper understanding of this interesting and challenging topic.

2.2 Magnetization dynamics in thin film ferromagnets

Analogous to a harmonic oscillator, the curvature of the energy landscape ε (previous section 2.1) defines the restoring torques, when deflecting the magnetization away from its ground state. Hence, this energy landscape also determines the eigenfrequencies of the magnetization dynamics. Therefore, a commonly used approach describes the torques acting on the magnetization by an effective field resulting from the gradient of the energy density with reorientation of the magnetization (e.g., see [75]):

$$H_{\text{eff}} \cdot \mathbf{e}_i = -\frac{\partial \varepsilon}{\partial \mathbf{M}_i} + \frac{\partial}{\partial r_\beta} \left[\frac{\partial \varepsilon}{\partial \left(\frac{\partial M_i}{\partial r_\beta} \right)} \right] \quad \text{with constraint} \quad |\mathbf{M}| = \text{const} \quad (2.10)$$

Where the magnetization vector \mathbf{M} is assumed to be of constant length, i, β are coordinate axis indices and \mathbf{e}_i denotes the unit basis-vector along the i -axis. This effective field may be decomposed into its single additive contributions such as \mathbf{H}_{ex} , \mathbf{H}_{dip} , $\mathbf{H}_{\text{cubic}}$ (previous section, equations 2.1 to 2.4), depending on the interactions taken into account. The torque on the magnetization is then given by [76]:

$$\dot{\mathbf{M}} = -\gamma (\mathbf{M} \times \mathbf{H}_{\text{eff}}) + \mathbf{R} = \mathbf{T}_{\text{eff}} + \mathbf{R} \quad (2.11)$$

Here γ denotes the gyromagnetic ratio and different terms \mathbf{R} to model damping processes have been proposed throughout the literature. One possible choice for such a damping torque, which ensures constant length of the magnetization and assumes a viscous damping accounting for dissipation, was proposed by Gilbert [45], in the following denoted as $\mathbf{R}_{\text{Gilbert}}$. The resulting equation for

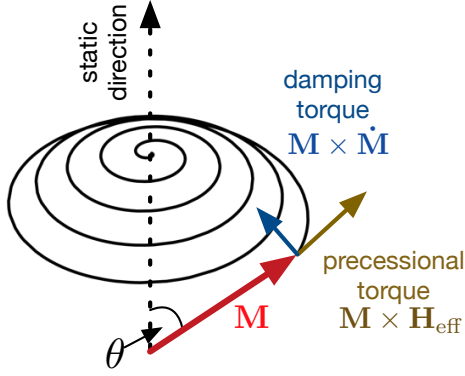


Figure 2.4: Precessional motion of the magnetization around the equilibrium direction according to the LLG equation 2.11 taking only the Zeeman-interaction into account. The field torque $\propto \mathbf{M} \times \mathbf{H}_{\text{eff}}$ drives the magnetization on a circular trajectory around the equilibrium direction with constant deflection angle θ . The additional damping torque $\propto \mathbf{M} \times \dot{\mathbf{M}}$ decreases this deflection angle during precession. A spiraling motion about the equilibrium results, where the frequency is determined by the field strength $|\mathbf{H}_{\text{eff}}|$.

the magnetization dynamic is equivalent to the one proposed by the damping choice of Landau-Lifshitz \mathbf{R}_{LL} [46] for material systems where the Gilbert-damping-parameter satisfies $\alpha_G^2 \ll 1$. This is the case for many commonly studied transition metal magnetic systems, with typical values around $\alpha_G^2 \approx 10^{-6}$:

$$\mathbf{R}_{\text{Gilbert}} = \frac{\alpha_G}{M} (\mathbf{M} \times \dot{\mathbf{M}}) \approx \mathbf{R}_{\text{LL}} = -\frac{\lambda_{\text{LL}}}{M^2} (\mathbf{M} \times (\mathbf{M} \times \mathbf{H}_{\text{eff}})) \quad \text{for } (1 + \alpha_G^2) \rightarrow 1 \quad (2.12)$$

Where the damping constants are connected via the relation $\lambda_{\text{LL}} = \gamma M \alpha_G$ [38]. The magnetization dynamic, after initial deflection of the magnetization away from equilibrium, according to this description is schematically shown in Fig. 2.4. For simplification only the Zeeman-interaction with an external field is taken into account in the presentation. In this case, the field torque $\mathbf{T}_{\text{eff}} \propto \mathbf{M} \times \mathbf{H}_{\text{eff}}$ drives the magnetization on a circular trajectory around the equilibrium direction without changing the deflection angle θ of the magnetization during a precessional motion. The damping torque $\propto \mathbf{M} \times \dot{\mathbf{M}}$ simultaneously reduces this deflection angle (or amplitude) over time and is directed towards the equilibrium. This phenomenological model of magnetic damping processes, results in a spiraling trajectory, ensuring a constant value of the magnetization. Thereby, the damping torque $\mathbf{R}_{\text{Gilbert}}$ proposed by Gilbert makes a linear scaling of the dissipation with the angular velocity of the magnetization and, hence, frequency (since it is proportional to $\dot{\mathbf{M}}$) obvious. On the other hand the term by Landau-Lifshitz is particularly useful in its mathematical similarity to additional “spin transfer torques” acting when spin(-polarized) currents are injected into the magnetic material, which are discussed later in section 2.3.1.

These damping parameters are often considered to be a constant material property. However, the wave vector dependent damping hypothesis (e.g. [77]), high frequency data (e.g. [78]), non-local [79] and inertia [80–82] damping contributions as well as temperature studies (e.g. in [83]) seem to insist on more elaborate models to describe a broader frequency-, field-, wave vector- and temperature-range, indicating that viewing the damping parameter as a material constant is a rather

strong simplification. Which could hold opportunities for future research on systems of reduced damping.

Nevertheless, for the experiments presented in this thesis, such a constant approximation of the damping parameters α_G or λ_{LL} with non-linear modifications for large angle deflections, as is, e.g., the case for the studied auto-oscillations of the magnetization (see also later section 2.3.2), seems to describe the dynamics well.

More detailed discussions about the dissipative processes within ferromagnets and their models can, for example, be found in [84–88].

2.2.1 Spin-wave dispersion in the linear regime

In the following the resonance conditions for wave-like deviations from the ground state called spin waves or magnons and their dispersion relation for thin film ferromagnets are discussed. Throughout the literature a variety of different formalisms have been developed to calculate the spin-wave transport for different scenarios and assumptions (e.g., [37, 38, 89–92]). For example, a quantum mechanical approach is often utilized for developing spin-wave theories to higher orders (to represent magnon-magnon-scattering processes), but can become particularly cumbersome and extensive for more complex forms of the Hamiltonian, e.g. with broken symmetries. Such an approach will be presented in the later section 2.2.2 in the discussion of non-linear dynamics and higher order effects. Here, another way to derive the linear dispersion relation by treating the LLG equation (equation 2.11) in the limiting case of small amplitude dynamic responses is sketched.

First the LLG equation 2.11 is linearized in terms of a deviation vector \mathbf{m} connecting the static equilibrium magnetization \mathbf{M}_{stat} with the actual orientation of the magnetization so that:

$$\mathbf{M} = \mathbf{M}_{\text{stat}} + \mathbf{m} \quad (2.13)$$

is fulfilled and projects \mathbf{m} on the plane perpendicular to the static magnetization \mathbf{M}_{stat} . Then one can decompose $\mathbf{m}(r)$ into its spatial Fourier-components \mathbf{m}_k or use diagonalization to find the eigenfrequencies and eigenmodes. Either way, one finds that in thin film ferromagnets the intrinsic polarization of these wave-like eigenmodes or spin waves is elliptical and all magnetic moments precess with the same frequency on an elliptical orbit around the equilibrium orientation. The wave-character of such an excitation is represented by the phase of this precession, denoted as ϕ , and increases linearly in a given direction of its wave vector $k = 2\pi/\lambda$. the wavelength λ is the distance between consecutive wave fronts of identical phase. This is illustrated in Fig. 2.5. As a peculiarity, since the precession-sense of the magnetic moments in time is fixed (small black arrow on the circular orbit), spin waves propagating in opposite directions can directly be distinguished,

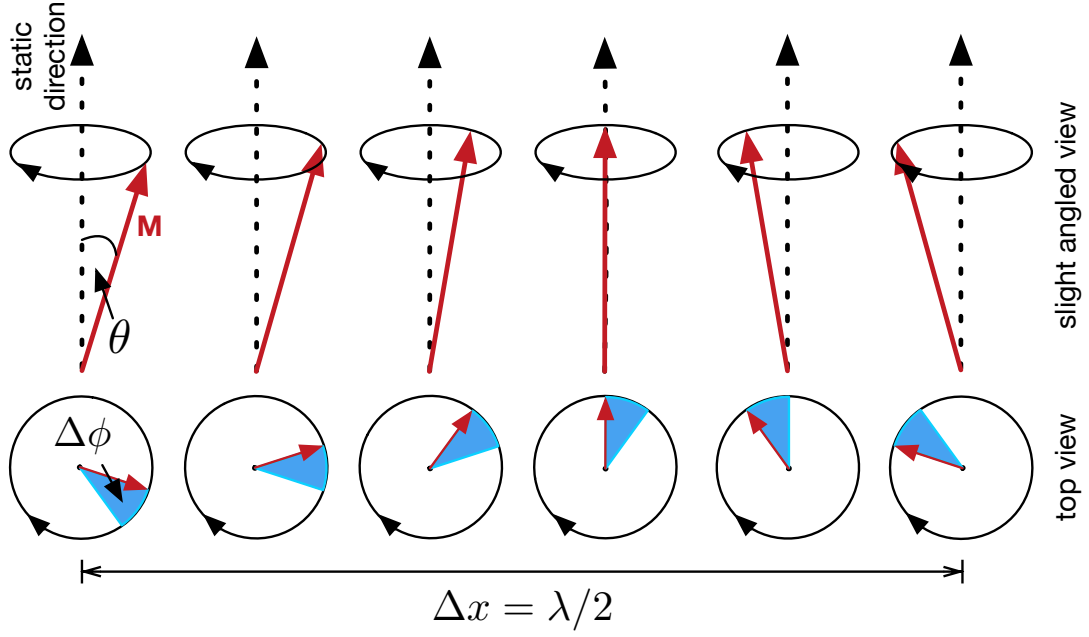


Figure 2.5: Schematic of a spin wave with its phase and wavelength traveling from left to right. All moments precess at the same frequency and constant deflection angle θ . The phase ϕ of the precession is a linear function of space (here represented by x) so that adjacent moments are dephased by an angle $\Delta\phi$. After half the wavelength λ the accumulated phase-shift is 180° and 360° for the full wavelength.

even from a “snapshot” for a single moment in time. In the illustrated case the spin wave travels unambiguously from left to right. This symmetry can be of importance for asymmetric mode profiles [37,93], non-reciprocities [94,95] as well as asymmetric excitation properties [96] even in otherwise translation invariant systems.

In the thin film limit, under the assumption of a uniform spin-wave profile along the thickness (as first used by Harte 1968 [97]) one finds for the corresponding dispersion relation (see for example the calculation of Kalinikos and Slavin [47] or Arias and Mills [48]):

$$\omega(k) = \gamma \sqrt{H_{x'} H_{y'}} \quad (2.14)$$

where $H_{x'}$ and $H_{y'}$ are:

$$H_{x'} = H + 4\pi M_s \left(1 - \frac{1 - \text{Exp}(-|k|d)}{|k|d} \right) \sin^2(\varphi_k) + Dk^2$$

$$H_{y'} = H + 4\pi M_s + H_s - 4\pi M_s \left(1 - \frac{1 - \text{Exp}(-|k|d)}{|k|d} \right) + Dk^2$$

Where H is the external magnetic field, M_s the saturation magnetization, k the spin-wave wave vector, d the thin-film thickness, D the spin-wave stiffness and φ_k the angle enclosed by k and

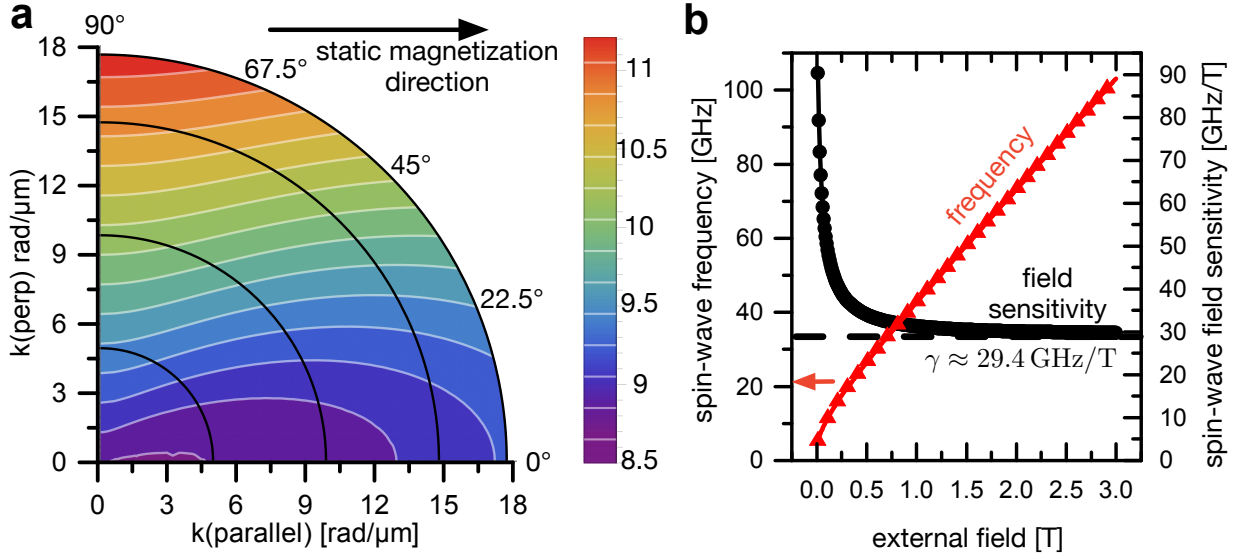


Figure 2.6: **a**, Linear spin-wave dispersion relation for an extended thin film, connecting spin-wave wave vector and frequency. The dipolar interaction leads to anisotropic spin-wave transport characteristics. **b**, Spin-wave frequency and its change with the effective field ("effective field sensitivity"), illustrated for a wave vector of $7 \text{ rad}/\mu\text{m}$ in Damon-Eshbach geometry ($\phi = 90^\circ$). This allows to confine spin waves to effective field wells, such as the ones created by domain walls. Calculated for material parameters: $M_S = 860 \text{ kA/m}$, $A = 13 \text{ pJ/m}$, $\gamma/2\pi = 29.8 \text{ GHz/T}$, $\mu_0 H_{\text{ext}} = 70 \text{ mT}$, **b**: $k = 7 \text{ rad}/\mu\text{m}$.

M_S . For simplicity additional crystalline anisotropies have been neglected here, but are included in the given references. To illustrate its characteristics, this dispersion relation is shown for a wave-vector quadrant in the μBLS detection regime (limited by wave vectors about $17.7 \text{ rad}/\mu\text{m}$, see later section 3.5) in Fig. 2.6 **a** for a 5-nm-thin $\text{Ni}_{81}\text{Fe}_{19}$ film and an external field of 70 mT (material parameters of the investigated spin Hall oscillator within this thesis).

As an additional characteristic spin waves have a lower limit of their frequency (here $\approx 8.47 \text{ GHz}$) referred to as magnetic band gap, so that spin-wave solutions exist only for frequencies higher than this onset. Above this onset, the anisotropic nature of the spin-wave dynamics becomes apparent by the non-circular iso-frequency curves (white lines). This can also be seen, when following the value of the dispersion relation for a constant wave vector length with varying propagation angle ϕ_k along the black circle-sections. Depending on the spin-wave propagation direction, important differences in their characteristics can be observed, where the two principal directions of 0° and 90° are referred to as Backward-Volume and Damon-Eshbach geometry, respectively. While spin waves in Backward-Volume geometry (0°) have initially negative and lower group velocities v_G (in this example $v_G \approx -0.06 \mu\text{m/s}$, for $k = 0.1 \text{ rad}/\mu\text{m}$), spin waves in the Damon-Eshbach geometry (90°) exhibit much higher ones ($v_G \approx 0.96 \mu\text{m/s}$, for $k = 0.1 \text{ rad}/\mu\text{m}$) and typically larger wave vec-

tor or smaller wavelength for a given frequency. It should be noted that the increased group velocity results in proportionally larger decay length [98]. These two reasons make the Damon-Eshbach geometry of modes propagating perpendicular to the equilibrium direction of the magnetization, the typically preferred candidate for spin-wave transport. Moreover, the iso-frequency curves are concave in the vicinity of this geometry leading to self-focussing effects of spin waves [99–101] depending on exact geometry and excitation frequency.

Even though this dispersion relation is derived only for thin films of infinite extend, this formula predicts the spin-wave dispersion often well even for the case of confined geometries, if the spin-wave wave vector is discretized to match the geometrical boundary conditions [102–105]. Note however, that determining the exact constraints and additional torques arising from a geometrical or interfacial boundary for the magnetization dynamics is a rather difficult task (e.g. [106, 107]). This is particularly the case for direct experimental determination, so that in many treatments either completely pinned, unpinned moments at the boundaries or mixed conditions represented by an effective geometry are considered [108–111].

Additionally, spin waves are sensitive to changes in the effective field as seen from equation 2.14. For example, in the limiting case of dominant Zeeman-energy, one can discard all terms other than the field H , directly giving a change in spin-wave frequency equal to $\gamma/2\pi = 29.4\text{GHz/T}$ in the high field regime. This is the asymptotic field sensitivity of the spin-wave frequency, but it is even more pronounced for smaller fields. For the calculated exemplary dispersion-relation and a spin wave of $7\text{rad}/\mu\text{m}$ wave vector in the Damon-Eshbach geometry this field sensitivity is found to be 90GHz/T , as presented in Fig. 2.6 b. Generally speaking, the spin-wave frequencies increase with increasing field in an initially steep dependence with values of several 10 GHz per Tesla. This effect can be exploited by utilizing areas, grooves, or wells of lowered effective field, confining spin waves of lower frequency to them, since the spin-wave spectra outside are of higher frequency [110, 112–116]. Such effective field wells commonly arise near the magnetic pseudo-charges due to the dipolar interactions, e.g., when the magnetization is forced to point outside geometrical boundaries (such as for a transversally magnetized waveguide). But effective field wells are also created near the magnetic charges at domain walls due to the sharp rotational transition (see section 2.1, for the field contributions and shape of the domain walls). These effective field wells of domain walls are additionally combined with a variation in propagation angle, since the magnetization is also rotating, to confine spin-wave transport by locally lowering their frequency.

Despite the reasonable advances in modeling spin-wave propagation in geometrically induced effective field wells with the concept of adequate boundary conditions, this approach did not yield satisfactory results for spin-wave propagation in the effective field wells of the domain walls. In the wall, the unique situation of a negative static effective field occurs, which would imply unphysical torques acting on the magnetization (e.g., the damping torque is oriented towards larger deflection angles and the precession sense of the moments would be reverted). When considering

a spin wave confined to the wall width, the dynamic exchange field Dk^2 can compensate this negative effective field and indeed recover some main characteristics, such as general low frequency and linear dispersion. However, the quantitative choice of the effective width and average effective field, acting on the spin waves, is not well supported, so that it is doubtful if physical meaning can be deduced from such an approach. This will be discussed in close relation to the micromagnetic results and numerical models in the later section 4.1.1 of the experimental results.

2.2.2 Magnetization dynamics in the non-linear regime

For large angles between the magnetization and the static equilibrium direction, the Landau-Lifshitz-Gilbert equation (equation 2.11) is not well approximated by linearization in terms of a deflection vector anymore. In this regime, the dynamics influence the frequency- and damping-governing torques considerably, giving rise to a variety of interactions between spin-waves. This includes self-interactions and self-localization [28], higher harmonic generation [117], parametric pumping [118] and multiple magnon scattering [119–121]. Also formation of spin-wave caustics, dark and bright solitons [122] as well as fold-over of spin-wave resonances [123, 124] has been reported. This is both the boon and bane of spin-wave dynamics, rendering analytical treatment of this regime complex, but serving at the same time as a rich test-bed for general non-linear phenomena.

Mainly two different approaches are used to develop non-linear magnetization dynamic approximations, which are shortly presented here. More elaborate introductions can be found in [37,38,42] as well as in-depth books as [125].

The first approach uses an expansion of the magnetization to increasing orders (up to n) $\mathbf{M} = \mathbf{M}_0 + \mathbf{M}_1 + \mathbf{M}_2 + \dots + \mathbf{M}_n$, similar to developing the scalar or vector products in the LLG-equation 2.11 (see e.g. [38]). Higher orders are then approximated iteratively based on the lower order results and their additional dynamic fields. Even though in principle an arbitrarily high order approximation can be reached this way, the terms become quickly extensive and increasingly complicated to solve and present analytically. This often aggravates a clear view on the principles and physical meaning behind the terms.

A more lucid presentation is developed in an approach, which formulates a Hamiltonian, utilizing bosonic annihilation and creation operators, a_k and a_k^* , to represent spin waves or magnons as quasi-particles of a ferromagnet. This formalism is sketched in the following to present the description of magnon-magnon-scattering and parametric amplification (as reported for spin-wave dynamics in domain structures within this thesis) and the non-linear frequency shift, which is the basis of spin-wave bullet formation in spin Hall oscillators.

A good starting representation of the operators a_k and a_k^* is chosen close to the spin-wave representation derived in section 2.2.1 for the linear regime. Following the most commonly used

Holstein-Primakoff transformation (developed 1940 [126], and first used by Schloemann [127]) the annihilation and creation operators are defined close to diagonalization as:

$$a(r) = \sum_k a_k \cdot e^{ikr} \quad \mathbf{m}_\perp(r) = a(r) \sqrt{2 - a(r)a^*(r)} \approx \sqrt{2}a(r) \left[1 - \frac{a(r)a^*(r)}{4} + \dots \right] \quad (2.15)$$

with $\mathbf{m}_\perp = im_x + m_y$ while ensuring $m_z = 1 - aa^*$

The first equation describes the transformation to wave-vector space. These operators ensure correct commutator relations as well as restriction to a finite-dimensional space. This representation already distinguishes the connection of the magnetization along the static direction m_z and the transversal ones m_\perp , designed to represent the spin waves as plane waves of elliptical polarization. However an intrinsic problem of this approach is the need to approximate the square root in $a(r)$ for the spatial Fourier transformation, neglecting the discrete limited amount of spin-states at a lattice site.

The Hamiltonian is then separated into terms of increasing order of annihilation and creation operators $\mathcal{H}_0 + \mathcal{H}_1 + \mathcal{H}_2 + \dots + \mathcal{H}_n$ and grouped into three parts of differing order in $a_k(r)$: constant, quadratic and higher order. The constant part corresponds to the static energy density and can be neglected when studying the dynamics, while the quadratic one gives the linear approximated dynamics arising from external transversal fields, such as microwave excitation of spin-wave dynamics.

Quadratic part of the Hamiltonian \mathcal{H}_2 and parallel parametric amplification

The quadratic term \mathcal{H}_2 includes effects such as parallel parametric pumping (first discovered by Schloemann, Green and Milano [128, 129]). In this process, spin waves of frequency $f/2$ interact with a dynamic effective field h_{eff} along the static direction at twice the frequency f [42]:

$$\mathcal{H}_2 = \dots + \sum_k (V' h_{eff} a_k^* a_k + c.c.) \dots \quad \text{sum over opposite and identical } k \quad (2.16)$$

Where “c.c.” is the complex conjugate of the previous term. These terms describe the parametric amplification of spin-wave pairs of opposite wave vector for half the frequency $f/2$ of h_{eff} . This amplification scales proportionally to the density of magnons already present in the system, different to a direct excitation. When a microwave field oriented along the static direction takes the role of h_{eff} , the process can be viewed as destruction of a single microwave photon to create 2 magnons at half the frequency and opposite k [42, 129]. This process contains 1 annihilation and 1 creation operator, like a simple 2-magnon-process, but can also be seen as a 3-wave process, since the microwave field appears similar to the creation and annihilation operator. This allows the interpretation of the photon as a scattering partner. A similarly expressed process but of different

wave vectors k is a 2-magnon scattering, where the effective field is time independent but exhibits periodic spatial variation, e.g., observed in magnonic crystals or a grating coupler [130, 131].

Higher order parts of the Hamiltonian \mathcal{H}_n and non-linear frequency shifts

The higher order parts $\mathcal{H}_{3,4,5,\dots}$ represent additional interactions between spin waves, such as self-interaction and self-induced frequency shifts. For this thesis in particular the frequency shift is important for the discussion of the studied spin Hall oscillator devices. These higher order parts can be treated in perturbation theory (such as S-theory [125] and Greenfunction formalism [132]) expressed in terms of the following structure:

$$\begin{aligned}\mathcal{H}_3 &= \dots + V_{k_1,k_2,k_3} \cdot (a_{k_1}^* a_{k_2}^* a_{k_3} + \text{c. c.}) + \dots \\ \mathcal{H}_4 &= \dots + V_{k_1,k_2,k_3,k_4} \cdot (a_{k_1}^{(*)} a_{k_2}^{(*)} a_{k_3} a_{k_4} + \text{c. c.}) + \dots\end{aligned}\tag{2.17}$$

The phase and magnitude of the vortices V define the interaction-cross section and contain the material parameters and field geometries. \mathcal{H}_3 , e.g., describes confluence processes (2 magnons destroyed - 1 created) or splitting processes (1 magnon destroyed - 2 created) in a similar fashion to the previously stated parametric excitation. As before, V can also take forms dependent on dynamic effective fields (either temporal or spatially), describing then four-wave processes between 3 magnons and a photon, e.g the saturation of the main resonance [133].

The four-wave processes, connecting 4 magnons are described in \mathcal{H}_4 such as a four-magnon process (2 destroyed - 2 created). The main challenge of higher harmonic generation and frequency shifts of spin-wave modes is, that they are expressed in many-fold nonlinear interactions inside the spin-wave system contained in various terms. To allow efficient treatment, the representation of the Hamiltonian is reshaped to group terms of importance together. These become increasingly complex and are just sketched out here, following the description given in [42]. Initially a second Holstein-Primakoff transformation (HPT) [126] or Bogoliubov-transformation [134] gives a description in the normal mode spin-wave amplitudes $b(k)$, diagonalizing $\mathcal{H}_2 = \sum_k \omega_k b_k^* b_k$ [126].

For simpler treatment the V_{k_1,k_2,k_3,k_4} describing the fourth-order processes get expressed for the new operators $b(k)$ and $b^*(k)$ terms as:

$$\begin{aligned}\mathcal{H}_4 &= \sum_k \delta(k_1 + k_2 - (k_3 + k_4)) W_{k_1,k_2,k_3,k_4} \cdot (b_{k_1}^* b_{k_2}^* b_{k_3} b_{k_4}) \\ &+ \delta(k_1 + k_2 + k_3 - k_4) G_{k_1,k_2,k_3,k_4} \cdot (b_{k_1} b_{k_2} b_{k_3} b_{k_4}^{(*)}) + \text{c. c. terms} \\ &+ \delta(k_1 + k_2 + k_3 + k_4) P_{k_1,k_2,k_3,k_4} \cdot (b_{k_1} b_{k_2} b_{k_3} b_{k_4}) + \text{c. c. terms}\end{aligned}\tag{2.18}$$

Now only the W class of interaction will be of importance describing processes where 2 magnons are destroyed and 2 other ones created.

If the so described processes are allowed (by sample geometry, parameters, external fields) they are called “resonant” (e.g. first-order instability described by Suhl [44]) otherwise “non-resonant”. Next to the above terms, 3-wave processes, do influence dynamics considerably even when “non-resonant”, as first described by Zakharov [135] and have to be accounted for. For this reason, another transformation (developed by Kasitskii 1990 [136]) is performed to cast the non-resonant 3-wave processes into a 4-wave process form, so that only \mathcal{H}_4 has to be treated, with new operators representing spin-wave amplitudes c_k and the transformed vortices $W \rightarrow W'$.

With this recast form, higher order non-linear effects can be treated appearing for large oscillation amplitudes. One of these effects, is a non-linear frequency shift (NLFS), which is of particular importance for the formation of solitons and spin-wave bullets in spin Hall oscillators, as will be discussed in the later section 2.3.2. This NLFS can be described to lowest order for chosen spin-wave amplitude c_k by a non-linear frequency shift coefficient N :

$$\omega_{\text{high amp}} = \omega_{\text{low amp}} + W'_{k,k,k,k} |c_k|^2 = \omega_{\text{low amp}} + N |c_k|^2 \quad (2.19)$$

with $\omega_{\text{low amp}}$ linear (unperturbed) spin-wave frequency

Implying that spin-waves of identical wave vector k interact with each other, rendering this a self-induced effect. The frequency red-shift for $N < 0$ results then in bullet-mode formation. The approximated expression for N will be discussed in the later section 2.3.2 connected with the characteristics of auto-oscillations. Here it was intended to sketch the main analytical formalism and how to derive and define expressions for non-linear effects providing references.

2.3 Spin Hall Oscillators

The following sections cover spin Hall oscillator devices (SHO) and the main characteristics of the emerging auto-oscillations, which are self-induced precessions in the non-linear regime.

In the first subsection 2.3.1 the underlying physical mechanisms, the spin Hall effect and spin transfer torque, are introduced. Subsequently, the spin Hall oscillator working principle to drive self-induced magnetization dynamics is explained.

Characteristics of auto-oscillations are then covered in the following subsection 2.3.2, such as spin-wave bullet formation based on the non-linear frequency shift. These bullets are soliton-like and compensate dispersion-broadening by non-linear contraction. As a result of this self-contraction they decrease in size, with increasing spin-wave amplitude. This bullet-formation is illustrated for the tapered micron-sized SHO, which is predicted to be large enough to host several bullets simultaneously separated in frequency and position.

The section closes by a discussion on “injection-locking” of SHOs to externally imprinted microwave signals in subsection 2.3.3. This phenomena can be used to select the operating frequency within the locking regime and improve the coherency, monochromaticity and output power of the SHO, e.g., as a basis for their use in telecommunication systems.

2.3.1 Spin Hall effect and spin transfer torque in a ferromagnet/heavy-metal bilayer system

In 1879, Edwin H. Hall discovered a measurable voltage at the sides of a current carrying conductor when subjected to transverse magnetic fields [137]. This effect is referred to as “Hall effect” and attributed to the Lorentz force acting on the conducting electrons resulting in a voltage difference perpendicular to the current flow and magnetic field direction. It was not much later, that a similar observation was made even in the absence of magnetic fields, when the conductor was made of a ferromagnetic material (FM) [138]. This effect is called anomalous Hall effect (AHE) and the transverse voltage could not be explained by the simple additive contribution of magnetic field and magnetization in the material equation to the magnetic induction. Instead it showed to be of much greater extend, e.g., about ten times higher in ferromagnetic iron than in non-magnetic conductors [139]. This phenomenon is based on a different (relativistic) mechanism and is linked to the intrinsic spin-polarization of currents inside ferromagnetic conductors [140]. The spin-polarization of currents traversed through a FM is a consequence of the spin-dependent electron bands resulting in differences in density of states for the mediating electrons at the fermi-surface. This suggests

classification of the conduction electrons into majority and minority carriers dependent on their spin.

The majority electrons and lesser number of minority electrons comprising the current, are then subjected to transverse acting spin-dependent forces, when moving through the magnet, leading to a detectable transverse charge imbalance. The occurring ex- and intrinsic, spin-dependent forces (such as asymmetric scattering, spin-skew scattering or side jump mechanisms [141, 142]) attracted great attention and their utilization is expected to advance our current technologies towards Spintronics, extending charge based electronics by spin-dependent phenomena, such as the giant magnetoresistance effect [143].

Ferromagnets are quite suited for observing these effects. This is due to the fact, that studying spin-dependent forces requires a sufficient (preferably controllable) coupling between the spin “world” and charges, such as the strong spin-orbit coupling in magnetic materials [140], and manipulable spin-polarization by magnetic fields connected with this intrinsic spin-polarization manifested by the magnetization.

However, spin-orbit coupling is present even in non-magnetic materials such as Platinum. Because of it’s relativistic origin greater conversion of charge into spin currents by the intrinsic Spin Hall Effects is expected, the higher the atomic numbers Z become, since the electric potentials and relativistic magnetic fields increase for heavy metals. In contrast to the AHE in magnetic materials, charge currents in a HM are not intrinsically spin-polarized, so that no net charge imbalance can be detected in such a case. However, similar to the charge imbalance from the AHE, a spin-polarization imbalance of the conduction electrons occurs transversally. This effect is referred to as “spin Hall effect” (SHE) and describes the emerging transverse spin current when a charge current is flowing through a non-magnetic conductor with spin-orbit coupling (HM). This was first described and predicted in 1971 by Dyakonov [144] and 33 years later in 2004 observed for the first time in a semiconductor by Kato [145]. Since oppositely polarized electrons feel opposite transverse forces, while traveling through the conductor, the spin accumulation is a pure interface effect and all contributions inside the material average out, as is schematically shown in Fig. 2.7 a.

The conversion efficiency is given by the Spin Hall angle θ_{SH} as the ratio between the charge current j^c and resulting transversal spin currents j^s [146]:

$$\theta_{SH} = \frac{e}{\hbar} \frac{j_{\perp}^s}{j_{\parallel}^c} \quad (2.20)$$

Experimentally, both signs of Spin Hall angle are observed. In materials with positive Spin Hall angles, such as Platinum, the spin-polarization at the sides follow the right-hand rule with the charge current direction [147]. This mechanism can not only be used to generate spin currents but also for their detection. Meaning that, when spin(-polarized) currents are injected into a material

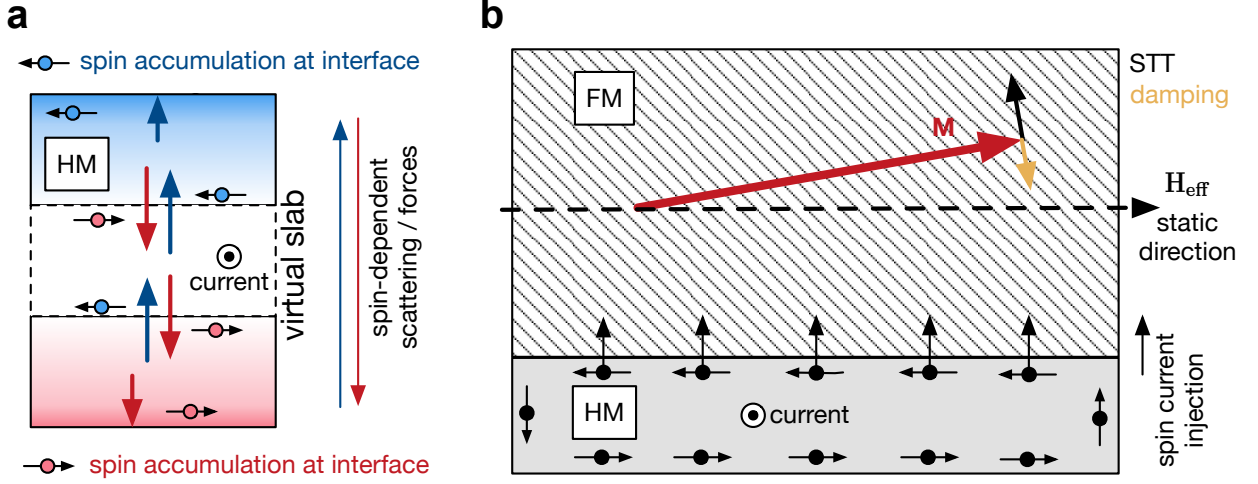


Figure 2.7: **a**, Schematic of the SHE in a HM. An unpolarized charge current flows perpendicularly to the viewing plane. The spin-dependent scattering mechanisms and forces lead to transversal spin currents (red/blue arrows). For every virtual slab inside the material, the incoming and outgoing transverse spin currents cancel out, except at the interface resulting in spin-accumulation. The simultaneously occurring up- and down-polarized spin-accumulations at the left and right side-interfaces are not shown for simplicity. **b**, Working principle of a SHO. The SHE in a HM is used to inject a spin current into an adjacent ferromagnetic layer. When the effective field is chosen collinear to the polarization of the spin current the spin transfer torque acting on the magnetization results in a controllable (anti-)damping-like torque.

of non-zero θ_{SH} (e.g. through a polarizing magnet), the spin-dependent forces do not cancel out and result in detectable charge accumulation. This effect is referred to as the “inverse spin Hall effect” [148] as counter-part of the SHE.

Spin transfer torque

As mentioned above, magnetic layers can be used to spin-polarize currents according to the orientation of the magnetization. In a ferromagnet carrying a spin(-polarized) current, the magnetization exerts a torque on the spin of the moving electrons towards the intrinsic spin-polarization set by the magnetization. Importantly, also the opposite process happens simultaneously. The arising mutual torques of a spin(-polarized) current traversing through a magnet on the magnetization are referred to as “spin transfer torque” (STT) and described in 1996 by Berger and Slonczewski [6, 7]. This is the equivalent of an angular momentum transfer between spin(-polarized) currents and magnetization and can be described by an additional torque term τ_s in the Landau-Lifshitz-Equation [7]:

$$\tau_s = \frac{I \cdot g}{M^2 e} (\mathbf{M} \times (\mathbf{M} \times \mathbf{P})) \quad \text{where} \quad g = \left[-4 + (1 + \mathcal{P})^3 (3 + \mathbf{m} \cdot \mathbf{P}) / 4\mathcal{P}^{3/2} \right]^{-1} \quad (2.21)$$

With a spin(-polarized) current of magnitude I , degree of polarization \mathcal{P} and spin-direction \mathbf{P} . The

sign of I is positive if the current is “injected into” or negative if “extracted from” the magnetic material. If one approximates the pre-factor g as a constant (best valid for small angle deflections between \mathbf{m} and \mathbf{P}), an identical term occurs to the previously mentioned damping-torque (see 2.12) towards the direction of spin-polarization, which forms the basis of the working principle behind spin Hall oscillators (SHO).

Device structure and working principle

SHOs harness the combined effects of generating a spin current via the SHE and using its STT to drive oscillations of the magnetization. They consist of a bi-layer structure of a non-magnetic heavy metal conductor, HM, as a spin current injector and a FM-layer subjected to the STT from the injected spin current. A side-view of this geometry is sketched in Fig. 2.7 **b**. In the first step, a charge current flowing within the HM (such as Platinum) is converted into transverse spin currents leading to a spin-potential difference at its sides. The conductors side is then interfaced with the FM resulting in spin current diffusion/injection into the adjacent ferromagnet and corresponding spin transfer torques (STT) acting on the magnetization dynamics (eq. 2.21).

The magnetization is then oriented collinear with the polarization of the diffusing spin current (typically by an external magnetic field), so that the effective magnetic damping becomes controllable by the current density within the HM. For the case of this collinear alignment of the polarization \mathbf{P} and the effective field \mathbf{H}_{eff} , if g is approximated to be constant, the intrinsic damping torque and the spin transfer torque obey the exact same symmetry and are identical to an enhanced or reduced damping coefficient. Then these two torques can be related by a scalar, here denoted as κ . In the literature the following form for the simplified STT τ_S in connection with the SHE is found [149, 150]:

$$\tau_S = \gamma \frac{1}{t_{FM}} \frac{\hbar}{2e} j_{\parallel}^c \cdot \theta_{SH} (\mathbf{m} \times (\mathbf{m} \times \mathbf{P})) = \gamma \frac{1}{t_{FM}} \frac{\hbar}{2e} j_{\parallel}^c \cdot \theta_{SH} \cdot \kappa (\mathbf{m} \times (\mathbf{m} \times \mathbf{H}_{\text{eff}})) \quad (2.22)$$

where the interface nature is expressed by the inverse scaling with the ferromagnet thickness t_{FM} , the product $(\hbar/2e) j_{\parallel}^c \cdot \theta_{SH}$ describes the spin current generated by the SHE and κ takes the spin-polarization and efficiency of the injection process into account. The main point here is the linear scaling with the current density j_{\parallel}^c allowing to control the effective damping λ_{LL}^{eff} in the Landau-Lifshitz notation:

$$\lambda_{LL}^{eff} = \lambda_{LL} - \gamma \frac{1}{t_{FM}} \frac{\hbar}{2e} j_{\parallel}^c \cdot \theta_{SH} \cdot \kappa \quad (2.23)$$

If the arising STT overcompensates the intrinsic magnetic damping, the magnetic systems becomes effectively anti-damped. It is noted here, that for positive spin Hall angles in the anti-damped configuration the Oersted field around the HM is oriented anti-parallel to the effective field in the ferromagnet.

In analogy to a LASER, the HM spin current injector can be seen as a pumping laser, while the ferromagnetic material acts as a pumped active medium. In the magnetic layer arbitrary magnetization dynamics are amplified by the "pumped" spin current until intrinsic non-linearities (such as non-linear damping contributions) limit the amplitude of the magnetization oscillations. These oscillations are also referred to as magnetization auto-oscillations and the next section is devoted to the dynamics and their characteristics in such devices.

2.3.2 Characteristics of magnetization auto-oscillations

Here the main characteristics of auto-oscillations for the investigated bilayer (Pt / Ni₈₁Fe₁₉) of quasi one dimensional tapered wire geometry are presented. As was discussed in the previous section, the effective damping \mathbf{R}_{eff} quantified by $\lambda_{LL}^{\text{eff}}$ can be electrically controlled in such devices utilizing conversion of charge- into spin currents by the spin Hall effect (SHE) and subsequent spin transfer torque (STT) on the magnetization up to complete compensation of the dissipation losses (equation 2.23).

For illustration, imagine the situation of a (e.g., spontaneously created) spin wave passing through such a region of effectively negative damping. This scenario is similar to a photon passing through the active medium of a LASER with amplification (negative losses) by stimulated emission. Analogous the spin wave amplitude c_k is amplified until the losses are equal to the inserted convertible power limited by non-linearities:

$$\lambda_{LL}^{\text{eff}} = \lambda_{LL} + Q|c_k|^2 - \gamma \frac{1}{t_{FM}} \frac{\hbar}{2e} j_{\parallel}^c \cdot \theta_{SH} \kappa \quad (2.24)$$

where the non-linearity can be phenomenologically introduced according to Slavin [31] by Q as an effective constant resulting from non-linear effects both present in the exciting STT as well as increasing damping. This can either lead to full reversal of the magnetization for too high currents (entering the highly damped regime, by switching to the spin-polarization-direction), or results in steady state precession stabilized by non-linearities to a spin-wave amplitude c_k so that $\lambda_{LL}^{\text{eff}} = 0$. This creation of such a limit cycle at finite amplitude of oscillation, on a steady trajectory, where neighboring trajectories spiral towards it, is also referred to as a supercritical Hopf bifurcation [151] and known from LASERS.

However, despite the great similarities to LASER-systems, there is a key difference to the optical amplification case: While the stimulated emission, as the amplification source, is wavelength (and hence frequency) as well as phase selective, the corresponding spin transfer torque term takes the same form as the general intrinsic damping. Therefore it is phase, wavelength and frequency independent. This allows to amplify arbitrary modes, which is promising for utilization of this mechanism for microwave sources. However, for the case of a dense mode spectrum, such as for an

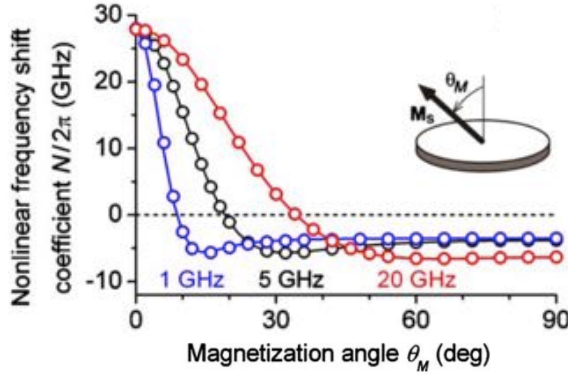


Figure 2.8: Non-linear frequency shift as obtained by calculations using the Hamiltonian formalism (lines) and numerical integration of the magnetization torques (dots) for different out-of-plane angles θ_M of the magnetization and uniform precession frequencies. For large angles (towards in-plane configuration) the frequency shift becomes negative. graph taken from [42].

extended thin film, the pump-energy distributes within the whole magnetic spectra, populating all spin-wave frequencies, demanding too high or even infinite pumping powers for auto-oscillations. Connected to this reason, it has been reported, that auto-oscillations can not be excited by a homogeneous spin current in an infinite thin film [152].

The situation changes, when the magnetic system or the pump area gets spatially confined and the spin-wave frequency red-shifts with increasing oscillation-amplitude. In this case auto-oscillation are excited and form spin-wave bullets. This state is found for the inplane magnetized SHO investigated within this thesis and will be discussed in the following:

Regarding the non-linear frequency shift (NLFS) a sophisticated, but not analytically solvable description is given in [153], for in-plane magnetized thin film systems under the assumption of non-resonant 3-wave but resonant 4-wave processes governed by W' in (according to equation 2.19 in section 2.2.2). This has been approximated for the uniform precession 1994 by Slavin [122] and refined to elliptical precession by Slavin and Tiberkevich in 2008 [154] to be:

$$\omega = \omega^0 - \frac{\gamma\mu_0 M}{2} \frac{4H + M}{4H + 4M} |c_k|^2 \quad (2.25)$$

This connects the frequency to the spin-wave amplitude c_k , so that with increasing auto-oscillation amplitude, tunable by the electrical current, the frequency red-shifts. This result was reproduced in 2010 by Krivosik [42] giving also the non-linear frequency shift for obliquely magnetized films as shown in Fig. 2.8, where a very good agreement to numerical macro-spin models was found.

Next to this frequency-amplitude coupling (NLFS), a confining geometry plays an important role in the formation of the spin-wave bullets. This is due to the fact, that the spin-wave spectrum becomes separated due to quantization, so that the pumping energy is spread to less modes resulting in higher spin-wave amplitudes, so that non-linearities become important.

To describe the bullet formation one can consider an area of locally lower spin-wave spectra within the SHO. Higher frequency contributions will leave this area at a higher rate, due to the higher spin-wave group velocity, so that they are effectively suppressed by radiation losses [31]. Such areas of

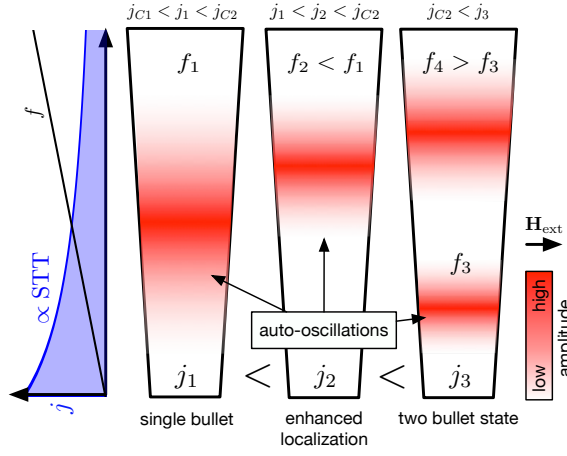


Figure 2.9: Schematic of auto-oscillations in SHO of tapered nanowire geometry. Spin-wave bullets (red regions) are created according to a Ginzburg-Landau-model [159]. In the tapered geometry, the spin-wave frequencies and current density varies along the SHO, indicated left of the sketched structure. This connects the frequency with the local position of the spin-wave bullet. With increasing current density, the bullet localization increases permitting the simultaneous formation of a second spin-wave bullet at a different position of non-equal frequencies ($f_3 \neq f_4$).

locally lower spin-wave spectra can either be induced by lower effective fields (such as the edges of microstructures) or arise from spontaneous fluctuations of the spin-wave amplitude in connection with the NLFS. This promotes the “localized” low-frequency dynamics. As a consequence, within this area the spin-wave amplitude c_k increases, and the effective field well deepens further by the NLFS. In contrast to the static wells, these self-induced wells are variable in size and position depending on the spin-wave amplitude. At the edges of this well, low frequency spin-wave radiation is directed towards the inside with already higher spin-wave amplitude (since it is of lower spectra). As a consequence, the well continues to shrink in size and the auto-oscillation increases in amplitude. This non-linear compression or self-contraction would indefinitely continue and lead to a bullet collapse, close to infinite amplitude and minimal size. However, dissipation losses and dispersion broadening are limiting this self-localization [155–158].

This general mechanism is now considered in the tapered geometry studied within this thesis. The tapered SHO is sketched in Fig. 2.9 and transversally magnetized. Its short width of around 200 nm quantizes the spin-wave spectra sufficiently to allow the excitation of auto-oscillations. Due to the tapered geometry, the spin-wave spectra varies along the SHO, so that the wider end exhibits higher frequency spin-wave dynamics. Simultaneously, the current density and directly connected spin transfer torque decreases towards the wider end. For this scenario a one-dimensional Ginzburg-Landau model is proposed to describe the auto-oscillations in agreement with the mechanism explained before [159]. The predictions for different driving currents j are sketched in Fig. 2.9.

Once the current density exceeds a critical value j_{C1} (left side of Fig. 2.9), the system becomes anti-damped and auto-oscillations emerge as a weakly localized spin-wave bullet. With increasing current density the bullet-mode increases in amplitude and shrinks in size by self-contraction. This is accompanied by stabilization of the bullet position and a shift of its center towards the wider end of the structure, attributed to the lower current density (see current j_2 in Fig. 2.9). Above a

second critical value j_{C2} (right side of Fig. 2.9) a second bullet mode forms at the narrow end. By shrinking the bullet size with driving current, the system becomes large enough to host two separate bullets at different frequencies. For higher current densities this process is predicted to continue in a similar fashion, resulting in the formation of an increasing number of spin-wave bullets.

Their mutual coupling behavior and controllability is an interesting target for research, from an application as well as fundamental point of view. The controllability and enhanced auto-oscillatory output is addressed in the next section, assessing “injection-locking” to enhance, tune or suppress formed spin-wave bullets. It should be noted, that while the number of bullets seems to be only limited by the pumping power and natural size of a spin-wave bullet, practically ohmic losses limited the working range of devices, so that, these schemes were tested in the two-bullet regime.

2.3.3 Improvement of monochromaticity, coherence and output power by injection locking

From an application point of view, a well defined output in terms of a tunable single-frequency operation with high output power and coherence of spin Hall oscillator devices is preferred. However, in typical devices auto-oscillations are at least partially incoherent, limiting their overall output power and spectral quality. The output power is additionally limited by thermal destruction or reversal of the magnetization for too strong spin transfer torques, the incoherence stems from noise/fluctuations in auto-oscillations [36, 160]. This is connected to the non-linearity of these devices, which allows to tune the operating frequency in a wide range, but in turn also renders them sensitive to ambient noise contributions reducing their coherency. This is due to the fact that the driving STT only determines the amplitudes of the stable limit-cycles but not its phase and frequency of the dynamics, so that these two quantities are still allowed to fluctuate in the system (see last section 2.3.2).

Experimentally, these fluctuations are commonly observed by the linewidth of the output signal, corresponding to measuring the phase-noise in the system. One noise-contribution to this linewidth directly stems from fluctuations in the precession phase. Considering a macrospin the magnetization is free to fluctuate between different points on the limit-cycle in the presence of thermal or environmental noise. Another noise source is due to amplitude fluctuations. Even though the linewidth does not directly depend on the amplitude in the auto-oscillation, the NLFS will indirectly convert any amplitude noise to a phase noise [160]. These two processes are illustrated in Fig. 2.10, where **a** shows the two principle fluctuations in phase and amplitude (yellow and pink arrow) and **b** the corresponding output signal. That the amplitude-noise is converted into a phase noise can be understood, when imagining an amplitude deviation away from the limit cycle, of steady state frequency f_0 at some time t_0 . Now the trajectory will spiral towards the limit-cycle

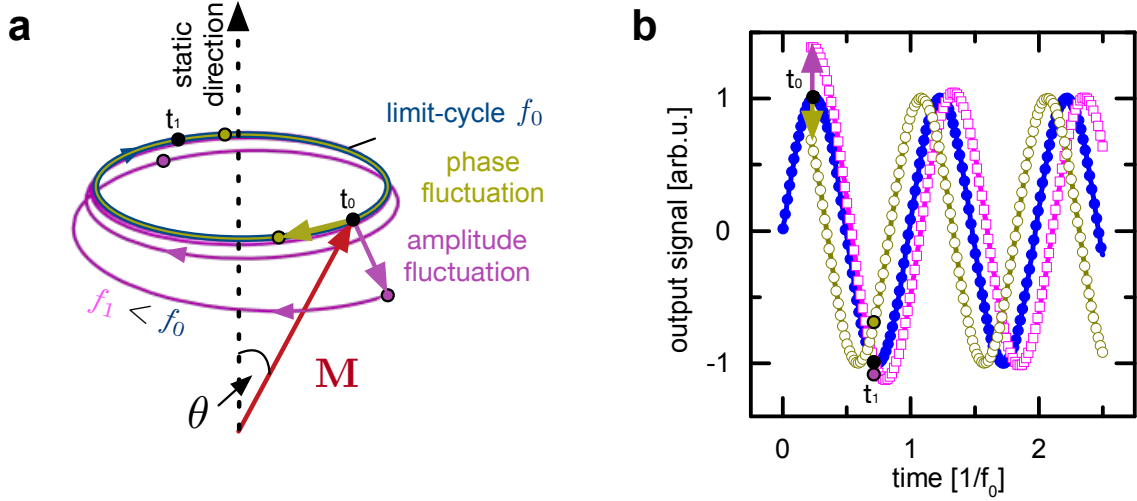


Figure 2.10: **a**, Schematic of amplitude- and phase-fluctuations contributing both to the phase-noise of the auto-oscillation steady-state precession, due to the amplitude-frequency coupling. At time t_0 the initial direction of the magnetization (red arrow, black dot) fluctuates either in the phase on the limit-cycle of frequency f_0 (yellow arrow, phase fluctuation) or in amplitude (pink arrow). Both of these "jumps" at t_0 result in a phase difference at a later time t_1 , when the limit-cycle is reached again (colored dots) with respect to the unperturbed trajectory. **b**, Corresponding auto-oscillatory output, represented by the oscillating transversal component to illustrate this effect.

amplitude again, but with a lowered frequency f_1 due to the NLFS. This results in an accumulated phase difference of the unperturbed auto-oscillation, when the steady-state amplitude is restored again at a later time $t_1 > t_0$.

A third type of noise contribution is mode-hopping [161–163] also known from LASER-systems [164, 165]. This occurs when more than one stable limit-cycle or auto-oscillating modes exist simultaneously and describes telegraphic switching between the different states. If the two modes share the same magnetization volume their competition over the supplied pumping-power, only allows one of the modes to auto-oscillate at the same time. However, if they are distinct in space, e.g., the bullet-modes in the two-bullet-regime, they likely do not compete for the pumping power and are, hence, allowed to auto-oscillate simultaneously. However, the spatial fluctuations of the bullet positions can decohere the output signal. For the case of the tapered wire geometry it is shown, that the symmetry-break stabilizes a fixed bullet position eliminating the decoherence from this source [159].

To reduce these noise contribution and improve the spectral properties in this thesis a method called "injection-locking" is tested on the SHO. Injection-locking dates back further than 1940 [166] and is commonly known and advanced in the field of electronic oscillators or LASERS [167].

To lock the spin Hall oscillators a coherent monochromatic signal at f_{MW} (RF-Signal) is super-

posed on the driving current by a signal generator, creating a phase-selectivity by periodic torque variations (arising from stray-fields and pumping power) synchronizing the dynamics to the externally imprinted phase and frequency. This resembles a master-slave principle, where the externally fed monochromatic signal is fixed experimentally. This imprinted signal then dominates over the ambient or internal random fluctuations and forces the frequency of the SHO f_{AO} to synchronize, in a frequency-interval $|f_{AO} - f_{MW}| < \Delta$. However, depending on the exact interaction between the RF-Signal and the auto-oscillations also locking for conditions $n^* \cdot f_{MW} = n \cdot f_{AO}$, where either n^* or n take integer values has been reported [168–175]. One example is the condition $2f_{MW} = f_{AO}$, when the parametric amplification (section 2.2.2) is used as the interaction for locking [176, 177]. Moreover the injection locking can present hysteretic behavior, when the external master-frequency is swept over the locking interval Δ [178]. The "locking-time" needed to reach this condition is also interesting from a fundamental and application point of view, where a few works have started to address this topic [179].

This effect is also observable if the "master"-signal stems from a second spin Hall oscillator and is then referred to as "mutual injection locking". This principle was perhaps first suspected by Huygens, when two pendulum clocks were connected by a wooden beam, synchronizing their frequency to each other [180]. Closely related to this is replacing the second spin Hall oscillator by a feedback loop, which uses the auto-oscillators output itself for injection under a time- or phase-delay [181]. Another aspect of these injection locking-mechanisms, which describes frequency synchronization, is the so called frequency modulation (first demonstrated for magnetization auto-oscillation in 2005 [182]). The frequency modulation is identical to the injection locking, but frequencies much lower than the auto-oscillation frequency are injected. This results in multiple side-bands spaced at the modulation frequency from the main one and gives a complementary manipulation possibility. In addition to refining the coherence of the output-signals by locking, also the output-power increases. When thinking about the electromagnetic power the RMS will increase quadratically (quadratic in the fields) at synchronization. Meaning, that for constructive interference, which can be achieved by phase-locking, the output power $n \cdot P_{\text{single}}$ of an uncorrelated array of n oscillators, increases by a factor of n to $n^2 \cdot P_{\text{single}}$.

This argument is expected to hold also for the large spin Hall oscillator locking to itself, when considering it as an array of n segments in direct connection to each other. This means for the one-dimensional wire case (as investigated here) ideally one would aim to achieve a scaling quadratically with its length l^2 . The presented study on these systems and their performance enhancement by injection-locking is therefore of general interest to all of the above mentioned different synchronization schemes of such SHO as a study on the reaction to external signals.

CHAPTER 3

Materials and Methods

This section provides an overview of the fabrication processes and experimental methods utilized to conduct the studies on tapered spin Hall auto-oscillators and spin-wave propagation in domain wall channels presented in the thesis. The main characteristics and properties of the samples and their underlying fabrication, as well as descriptions of the used experimental μ BLS set-up are presented. While the $\text{Ni}_{81}\text{Fe}_{19}$ microstructures involved in the study of spin-wave transport within magnetic domain walls were processed by the author in the NanoFaRo facility of the Helmholtz-Zentrum Dresden - Rossendorf, the Fe microstructures and tapered SHO have been fabricated within the group of Dr. Matthieu Bailleul (IPCMS, Strasbourg, France) and in the group of Prof. Dr. Ilya Krivorotov (University of California, California, USA), respectively.

First, sample production by electron beam lithography (EBL) is addressed, presenting general ideas used for fabrication. Subsequently, the processing steps as well as magnetic parameters of the studied samples are documented. In the last section the experimental set-up and measurement method is addressed, referencing more detailed descriptions for the interested reader.

3.1 Electron Beam Lithography, EBL

The microstructures investigated in the framework of this thesis were patterned by the use of Electron Beam Lithography (EBL). This method is well established and widely used to create nanostructures out of a target material for research or prototype purposes due to its high accuracy and flexibility, despite its rather low throughput. It is based on scanning electron microscopy (SEM, e.g. described in [183]). A substantial overview about EBL, its limitation and applications can be found here [184]. Generally speaking, in a first step, a stencil with the required pattern is created out of an often sacrificial mask-layer called "resist" on top of the working material.

While there are many different ways of creating a sacrificial mask, EBL-processes utilize scanning a focussed electron beam over resist-layers formulated to alter their chemistry, when exposed to electron irradiation. Once the chemistry of the resist layer has been locally modified in the desired pattern, chemical solutions, so called “developer”, are used to selectively remove either irradiated (positive resist) or non-irradiated (negative resist) areas. In either case this results in a structured mask defined by the exposure of the electron beam irradiation.

Subsequently the pattern in the mask-layer is transferred to the target material. This is achieved either by removing (e.g., chemical or dry etching processes) or depositing (e.g., evaporation processes) the material at areas unprotected from the resist-mask, resulting in patterned structures out of the target material. Subsequently the mask and any material on top of it, can be removed, referred to as “lift-off”. A good description and further information is given in [185].

3.2 Ni₈₁Fe₁₉ microstructures

For the fabrication of microstructures involved in the study of the spin-wave dynamics in domain walls the ferromagnetic nickel-iron compound Ni₈₁Fe₁₉ has been used. This material is a candidate system for fundamental research in the field of magnon-spintronics, due to its robustness, good reproducibility and reliability, as well as the possibility to traverse currents of acceptable spin-polarization around 30% - 48% through it [186, 187]. Especially the absence of magneto-crystalline anisotropies in this material allows studying the influence of microstructure geometries on the magnetic texture and its dynamics, isolated from distortions by such anisotropies.

For their fabrication, EBL with two sequential positive resist steps has been deployed, to separately process the microstructures and electrical contacts. The first step **A** for microstructure-fabrication and second step **B** for the electrical contacts are sketched in the following:

1. Step **A**: A 150-nm-thin high resolution resist-layer is patterned into a resist-mask by EBL. Subsequently electron beam deposition of 35-nm-thick Ni₈₁Fe₁₉ and “lift-off” is utilized to create the microstructures and additional micron-crosses for automated alignment purposes of the following step B.
2. Step **B**: A mask of two stacked resist layers of different solubility, referred to as “copoly” resist covered by thin PMMA is used to create a rather thick (450 nm + 50 nm) but still well defined resist mask for the 100-nm-thick Au structures. The position of the earlier fabricated micron crosses is read out, to recover the alignment parameters of step A (such as sample position and writefield parameters) allowing to create an additional accurately positioned mask for the current line and antenna fabrication. The idea of using a double-resist step is to create an enhanced undercut-profile

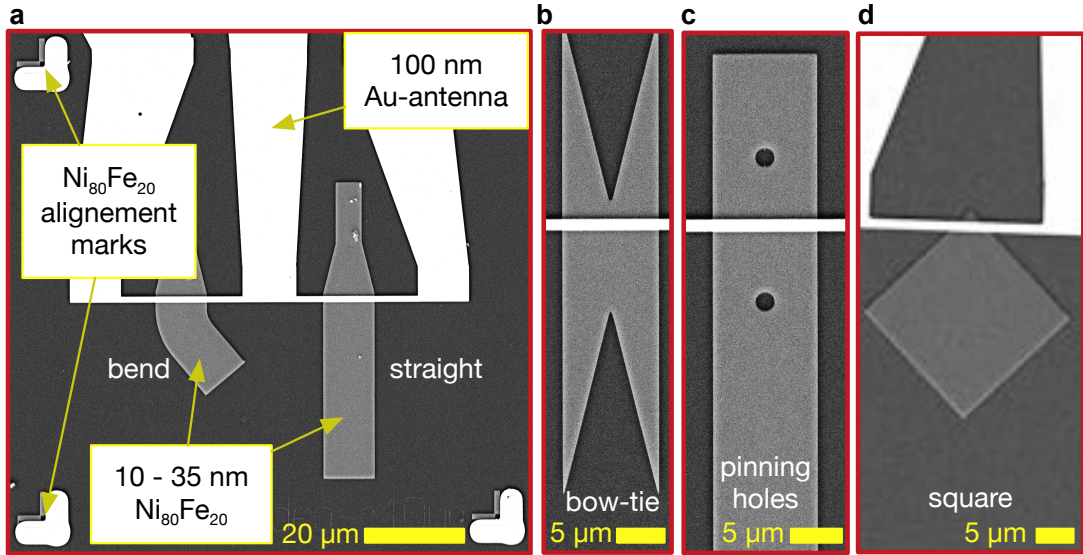


Figure 3.1: a) SEM-micrograph of the “bottle-shaped” spin-wave waveguide structures fabricated out of nominally 35-nm-thick Ni₈₁Fe₁₉. The simultaneously fabricated “alignment crosses” are used to position the subsequent fabrication of Au antennas to excite spin-wave transport. Exemplary sample structures are presented, such as the straight and bended structures shown in **a**, as well as bow-tie **b**, rectangular guides with “pinning holes” **c** and differently sized square structures **d**.

by combining a high sensitivity resist topped by a high resolution resist allowing for eased “lift-off” even for high structures, while maintaining accuracy [184]. The antennae are 100-nm-thick Au coplanar waveguides or micro-strip lines used to excite spin-wave dynamics.

In both of these processes additional 3-nm-thin Titanium layers have been used as an adhesion layer to ensure good adhesion of the Ni₈₁Fe₁₉ and Au structures to the Silicon substrate. The process parameters of step A and step B are documented in the appendix in section A.7. Exemplary SEM micrographs of the resulting fabricated structures are shown in Fig. 3.1.

Magnetic and optical material parameters

The nominally 35-nm-thick Ni₈₁Fe₁₉ films have been deposited by electron beam deposition. Based on previous characterization of similar 30-nm-thick Ni₈₁Fe₁₉ films produced at the same facility and measured by the author regarding their magnetic parameters using FMR [188] the values of a saturation magnetization of $M_S \approx 800 \text{ kA/m}$, a Gilbert damping parameter of $\alpha_G \approx 0.007$, a g-factor of 2.13 and an exchange length of 5 nm are adapted. These parameters agree with the broader variation found in the literature [189–193]. The magnetic and optical parameters (refractive index n and extinction coefficient k) are concluded in Tab. 3.1.

parameter	value	unit	taken from
M_S	$800 \pm 10\%$	kA/m	[188]
α_G	$0.007 \pm 15\%$		
g-factor	$2.13 \pm 10\%$		
A	$8.5 \pm 20\%$	pJ/m	
l_{ex}	5	nm	
thickness	32 ± 2	nm	[194]
n	1.76		
k	3.24		
n	3.596		[195]
k	5.796		

Table 3.1: Top part: Adopted magnetic parameters for the $\text{Ni}_{81}\text{Fe}_{19}$ microstructures based on broadband FMR measurements (3 - 20 GHz) thin film references from the same facility. Bottom part: literature values of optical parameters for thin $\text{Ni}_{81}\text{Fe}_{19}$ films.

3.3 Fe microstructures

The investigated 10- μm -wide Fe wire has been fabricated in the group of Dr. Matthieu Bailleul (IPCMS, Strasbourg, France). It consists of epitaxially grown Fe (base-centered-cubic structure) on a MgO substrate. The nominal layer stack is MgO(001)/Fe(20nm)/MgO(8.5nm) (Substrate / magnetic film / capping) and deposited using molecular beam epitaxy. The fabrication details are documented in [196]. Compared to $\text{Ni}_{81}\text{Fe}_{19}$ microstructures, Fe has a lower damping and higher magnetization, which offers larger attenuation length of spin wave propagation. This distance over which the spin-wave amplitude decays is an important quantity in the realization of energy efficient magnonic circuitry. Moreover, the crystalline anisotropy raises the zero-field spin-wave frequency to about 10 GHz and is expected to reduce the width of the domain wall channels down to about 12 nm (section 2.1). This frequency separation of the domain and domain wall dynamics renders Fe a promising candidate system for improved performance of the domain wall channels and eases their investigation. To excite spin-wave dynamics the devices were covered by a 75-nm-thick insulating layer of SiO_2 before additionally fabricating spin-wave antennae out of 120-nm-thick Al (10nm Ti as adhesion layer) by EBL. The distribution of wave vectors of the spin-waves generated by these antennae is given by the Fourier transform of the spatial distribution of the microwaves magnetic field, which has a main peak at $k_1 = 3.8 \text{ rad}/\mu\text{m}$ and a secondary peak at $k_2 = 1.5 \text{ rad}/\mu\text{m}$ [197]. A microscope image of the investigated Fe microstructure is shown in Fig. 3.2.

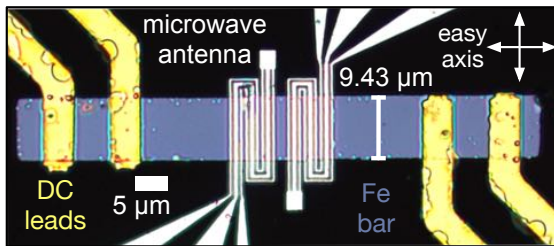


Figure 3.2: Microscope image of the rectangular 20-nm-thick Fe microwire. Two meander-shaped antennae are fabricated on top to excite (and detect) spin-wave dynamics. Four additional DC leads allow for 4-point resistance measurements, as well as to apply currents.

Magnetic material parameters

Characterization of the Fe wires by broadband FMR ¹ and propagating spin-wave spectroscopy, performed in the group of Dr. M. Bailleul [196] resulted in the magnetic parameters concluded in Tab. 3.2. An anisotropy of $\mu_0 H_U = 70$ mT with easy axis out of plane and a four-fold cubic anisotropy constant of $K_1 = 50$ kJ/m³ was found. The cubic anisotropy is oriented with one of its easy axis out-of-plane ([001]) and the structure principle axes are chosen to coincide with the easy directions in-plane ([100] and [010] axis). Since Fe has compared to Ni₈₁Fe₁₉ a lower damping of about $\alpha_G \approx 0.0023$ ([78, 198–200]) and typically higher group velocities (higher saturation magnetization) an attenuation length up to 6 μ m was observed. Together with large spin-polarization of about 83% investigation of such Fe microstructures are important in testing their suitability in magnonic circuitry and domain wall logic.

parameter	value	unit	taken from
M_S	1711	kA/m	[196]
α_G	0.0023		
g-factor	2.07		
K_1	50	kJ/m ³	
l_{ex}	3.2	nm	
A	19	pJ/m	
$\mu_0 H_U$	70	mT	[201]
n	2.8954		
k	2.9179		

Table 3.2: Adopted magnetic and optical parameters for the Fe microstructures investigated in this thesis.

3.4 Tapered spin Hall oscillators

The studied spin Hall oscillators were fabricated within the group of Prof. Dr. Ilya Krivorotov (University of California, California, USA) and are devices of tapered wire geometry. Details about the sample fabrication are given in [202]. The oscillators are fabricated on a c-plane sapphire substrate with a layer-stack of Pt (7 nm)/ Ni₈₁Fe₁₉ (5 nm) (spin Hall metal / ferromagnet) and capped by a 2-nm-thick protective oxide AlO_x layer.

A SEM micrograph of the investigated spin Hall oscillator is shown in Fig. 3.3 together with the principle electrical circuit. A bias Tee is used to combine a constant current (supplied by a DC source) and a microwave signal (supplied by a signal generator), which is then injected into the spin Hall oscillator to excite (DC current) and synchronize (microwave signal) auto-oscillations.

¹private communication with Yves Henry

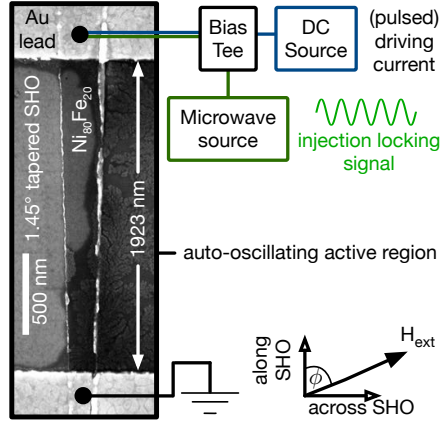


Figure 3.3: SEM micrograph of the studied SHO. For the tapered wire geometry a tapering angle of 1.45° is chosen. Au contacts restrict its active region to around $1.9 \mu\text{m}$ length and a mean width of 220 nm . A bias Tee is used to superpose a constant or pulsed driving current and a high frequency injection locking signal, which is applied to the SHO to excite and synchronize auto-oscillations. The auto-oscillations are optically detected by μ BLS.

Magnetic material parameters

Even though conventional magnetron sputtering has been used for material deposition, the determined magnetic parameters of these samples deviate from the expected literature values [203], namely:

saturation magnetization $M_S = 530 \text{ kA/m}$, exchange constant $A = 5 \cdot 10^{-12} \text{ J/m}$,
Landé factor $g = 2.03$

where the Landé factor was adapted from [203] and the remaining parameters are taken from [202] and determined from AMR measurements in different field geometries and broadband FMR measurements.

This lowered values for the saturation magnetization and exchange constant are very likely attributed to the increasingly complex extraction of magnetic parameters by a description of magnetization dynamics of microstructured samples combined with increasing deviations of sample geometry and magnetization from the ideal case, due to patterning limitations. In the fabrication the utilized plasma etching supposedly influenced the magnetic parameters of these samples, in particular to the heavier exposed structure edges. In prior studies the auto-oscillations are simulated to be localized at the edges of the tapered wire, which are suspected to be subjected to dilution of the magnetization, due to the etching process [204], rendering it the most likely cause for the reduced magnetic parameters.

3.5 Micro-focused Brillouin Light Scattering Spectroscopy, μ BLS

For the experimental detection of magnetization dynamics presented in this thesis a measurement technique referred to as micro-focused Brillouin Light Scattering (μ BLS) was utilized. A recent overview can, e.g., be found in [205]. This non-destructive and optical technique uses the detection

of momentum- and energy-exchange between photons and spin-waves in inelastic scattering processes by analysis of the scattered photons. Generally speaking, a focussed laser beam is scanned over the sample typically by a high numerical aperture objective lens, which collects the back-reflected photons and directs them to a Tandem-Fabry-Perot-Interferometer (TFPI) for frequency-analysis. The frequency analysis by the TFPI is performed by resonant transmission through two variable optical cavities, creating a tunable very narrow frequency band-pass for the photon beam, before it impinges on a highly sensitive single photon detector. In the majority of measurements, spin waves are excited by electrical means (in form of coplanar waveguides, microstrip antennas or DC current lines) enabling to define and record the spin-wave dynamics in the space-, frequency-, phase- as well as time domain. This technique is nowadays widely used, due to its high flexibility and well developed status [206]. The actual experimental set-up was constructed together with Andreas Henschke, Thomas Sebastian and Helmut Schultheiss, during the initial phase of the authors thesis followed by implementation of out-of-plane fields by permanent magnets, time-, frequency-, phase-resolution, pairing with a focussed femtosecond LASER-system to excite pulsed magnetization dynamics, stability against vibrations and extension of flexibility on the automation software.

Before stating the current capabilities and devices used in this particular set-up at the end of this section, first the general measurement method is explained in more detail, to explain the resolution and limits of the set-up, since they are reached in the presented studies:

As mentioned before, μ BLS relies on detecting the energy-shift of photons when scattering inelastically with spin waves (magnons) of the investigated magnet. Therefore in the case of metals it is surface-sensitive on the order of nanometer-depth. The analyzed type of scattering is named “Brillouin scattering” after Léon Brillouin and mediated by a periodic change of the permittivity tensor ϵ by material waves, such as phonons, polarons or magnons. In principle, all scattering processes with these quasi-particles can be detected in the scattered photons simultaneously. For magnons the coupling of the dielectric tensor to the local magnetic orientation (often described by optical Voigt constant or Kerr rotation angles) is the basis of this effect. In a simplified way, a spin wave can be seen as a periodically modulated deflection of the magnetization away from its equilibrium orientation traveling through the magnetic carrier (see also section 2.2.1). This resembles a traveling diffraction grating probed by the incoming photons, adding or subtracting the oscillation frequency of this grating to the one of the Photon (Stokes, or Anti-Stokes process). This is the equivalent of the energy- (and momentum-) conservation in the quantum picture, where one spin wave is either created or annihilated by the incoming photon, as schematically depicted in figure 3.4, giving:

$$(k_{\parallel}, \omega)_{\text{photon}}^{\text{scattered}} = (k_{\parallel}, \omega)_{\text{photon}}^{\text{incoming}} \pm (k_{\parallel}, \omega)_{\text{spin wave}} \quad (3.1)$$

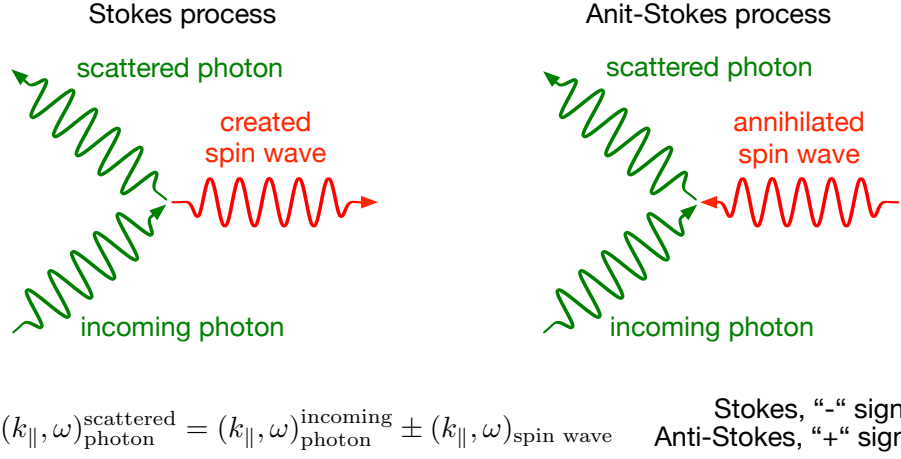


Figure 3.4: Stokes and Anti-Stokes magnon-photon scattering process analyzed in a μ BLS set-up. The left-hand side illustrates the creation of a spin wave (Stokes-process), while the right hand side shows annihilation (Anti-Stokes process). The scattered photons are re-collected by an objective lens and their energy-change is analyzed by a Tandem-Fabry-Perot-Interferometer (TFPI), acting as a tunable optical band-pass filter.

Where k_{\parallel} is the wave vector component in the plane of the investigated magnetic thin film. From these selection rules it becomes apparent that the geometry of μ BLS set-ups, focussing a laser beam on the sample by normal incidence, determines its detection limits. A main important aspect here is the conservation of the total in-plane momentum of magnons and photons in this scattering processes, as a result from the translational invariance of a thin film magnetic system in the sample plane. For this reason the change in angle of back reflected photons is connected to the magnons momentum. This is however limited by the angle-range θ^{\max} that can be re-collected by the used objective, given by its numerical aperture NA, which results in:

$$k_{\text{SW}}^{\max} = 2k_{\parallel, \text{photon}} = 2k_{\text{photon}} \cdot \sin \theta_{\text{photon}}^{\max} \underset{n_{\text{air}} \approx 1}{=} 2k_{\text{photon}} \cdot \text{NA} \underset{\text{NA} \rightarrow 0.75}{=} 17.7 \text{ rad}/\mu\text{m} \hat{=} 355 \text{ nm} \quad (3.2)$$

where k_{photon} is the incoming photons wave vector under an angle θ_{photon} and hence $k_{\parallel, \text{photon}}$ its in-plane projection. Since a numerical aperture of 0.75 and a wavelength of 532 nm were used in the presented experiments, this results in an **upper limit of the wave-vector component** of detectable plane-wave magnons of $k_{\text{SW}}^{\max} \approx 17.7 \text{ rad}/\mu\text{m}$ or **355 nm wavelength** respectively. However, for spatially localized spin waves the wave vector distribution broadens according to the uncertainty principle, allowing to probe spin waves confined to smaller length scales, if the wave-vector components extend into the detectable regime. Apart from the aforementioned selection rules scattering cross-sections of the magnon-photon interaction is complex and mainly treated

numerically. Furthermore, due to the material equations the cross-section depends on the photons wavelength as well as magnetic material. More detailed and extensive discussion are, e.g., given in [207–210]. However a few key characteristics can still be discussed:

As a rule of thumb the μ BLS-intensity is proportional to the squared amplitude (intensity) of the spin wave dynamics at the laser spot position. Furthermore, one can intuitively assume a main sensitivity to the dynamics occurring in the out-of-plane component of the magnetization in thin films in a μ BLS measurement. This is a result of the rotation symmetry around the out-of-plane axis for the incoming focussed photon beam superposing photons within a wide angle range of the different planes of incidence. Note that this detection scheme is similar to a polar (TR-)MOKE set-up resembling the same symmetry resulting also in an isolated out-of-plane sensitivity.

Another important aspect of the magnon-photon interaction is its qualitative difference to the simultaneously occurring Brillouin-scattering events of the incoming photons with the phonons within the magnetic carrier. Since the off-diagonal elements of the permittivity tensor are influenced by the magnetic orientation, the photons undergo a 90° rotation of their incoming polarization when scattering on spin waves. This is in contrast to the phonon-photon interaction which occurs mainly in the diagonal tensor elements. This qualitative difference allows to discriminate these two quasi-particles by polarization filters in front of the detector.

While the detectable wave vector range is defined by the scattering geometry, the energy/frequency-shift is limited by the band-width of the TFPI. Depending on the the cavity-length d and finesse F used in the experiment its single-pass **frequency resolution** Δf is given by $\Delta f = 150 \text{ GHz/mm} \cdot 1/(F d)$ and lies typically between **50 to 300 MHz**. The effective resolution for $d = 6 \text{ mm}$ was measured to be FWHM of $192 \pm 11 \text{ MHz}$. Connected to this frequency resolution there is also a **low frequency limit** set by the damage threshold of the detector. Even though the contrast of the TFPI is estimated greater than 10^{15} (manufacturer) the ratio between directly reflected photons and scattered photons can exceed 10^{17} for example in measurements of purely thermally excited dynamics [211]. Discriminating between this large number of elastically scattered photons of around 574 THz frequency (2.37 eV) and much fewer inelastically scattered photons away from this main frequency showed to be at the limit of the performance for a spin-wave frequency of **400 MHz** ($1.65 \mu\text{eV}$). The upper frequency limit is also governed by the interferometer used for discrimination and enables detection of spin-wave frequencies up to several hundreds of GHz.

The spatial limitation is assumed to be determined mainly by integral measurement over the laser spot size on the sample surface. The **detection function** is estimated to be a **Gaussian of FWHM of $340 \text{ nm} \pm 10 \%$** and its determination is described in the following section 3.5.1.

In its current status, the set-up uses a 532 nm single-mode laser (Torus 532, Quantum Physics) to supply the probing photons together with a TFP-2HC (improved high contrast Interferometer from JRS [206]) to probe photons scattered on the magnetization dynamics. For final photon-detection

a high efficient single-photon detector with a quantum efficiency greater than 70 % at 532 nm has been chosen (LaserComponents Count-10 module). 4 contact needles and 2 picoprobe mountings allow for 6 independent contacting possibilities either connected to a DC-Source (Keithley, 2614B), microwave (Agilent, E8257D) or pulse generator (Stanford research, DG645). Illumination of the sample with a Ti:Sa fs-Laser (Femtosome XL 500) and/or a second 532 nm CW Beam with controllable position relative to the BLS Laserspot has also been implemented during the framework of this thesis. The automation software programmed mainly by Helmut Schultheiß together with a simultaneous microscope image of the sample allows for active stabilization and precise positioning (1 nm minimum incremental motion of the XMS linear modules from Newport, while active stabilization is limited by the image recognition and the image resolution to about 20 nm). A traveling wave electro optical modulator (EO-TWK3-VIS from QUBIG) is utilized for the phase-resolved BLS measurements with an operating range at least between 0.5 and 30 GHz. A fast acquisition electronic circuitry logs the photon-arrival times (FAST ComTEC, MCSA6) allowing for time-resolved measurements with a resolution down to 100 ps.

3.5.1 μ BLS spatial resolution

To determine the spatial resolution of the μ BLS set-up the “knife-edge-method” was utilized [212]. For this, the laser beam is scanned over a steep edge, while the back-reflected light intensity is measured. Following the approach in the given reference, direct inversion on “knife-edge data” was used to determine the FWHM of the μ BLS detection function under the assumption of a Gaussian profile to be $340 \text{ nm} \pm 10\%$. Calculations of Quabis [213] suggest an elliptical shape of the laser spot with 287 nm along the short axis (perpendicular to the polarization) and 487 nm along the long axis, so that the experimental result lies within this range and seems reasonable. However, it should be noted that this experimental result is in disagreement with a spatial resolution of around 250 nm found in the literature for similar μ BLS set-ups [205, 214]. Therefore, additional effects arising from the spin-wave phase and at least resulting partial destructive interference or unintended systematic errors either in this work or in the given references are indicated.

In the following, the experiment and calculations used for determination of the spot-size are described in more detail:

In the experiment, the intensity of a side-band created by an electro-optical modulator at 5 GHz frequency-shift to the laser frequency, serving as an “artificial spin-wave signal” was measured. This experimental modelling of a spin-wave intensity measurement, has the advantage of including the complete detection scheme (objective lense, apertures, Tandem-Fabry-Perot-Interferometer, detector, ...) for a direct determination of the FWHM of the set-up detection function. It is assumed, that the detection-function is of Gaussian-shape.

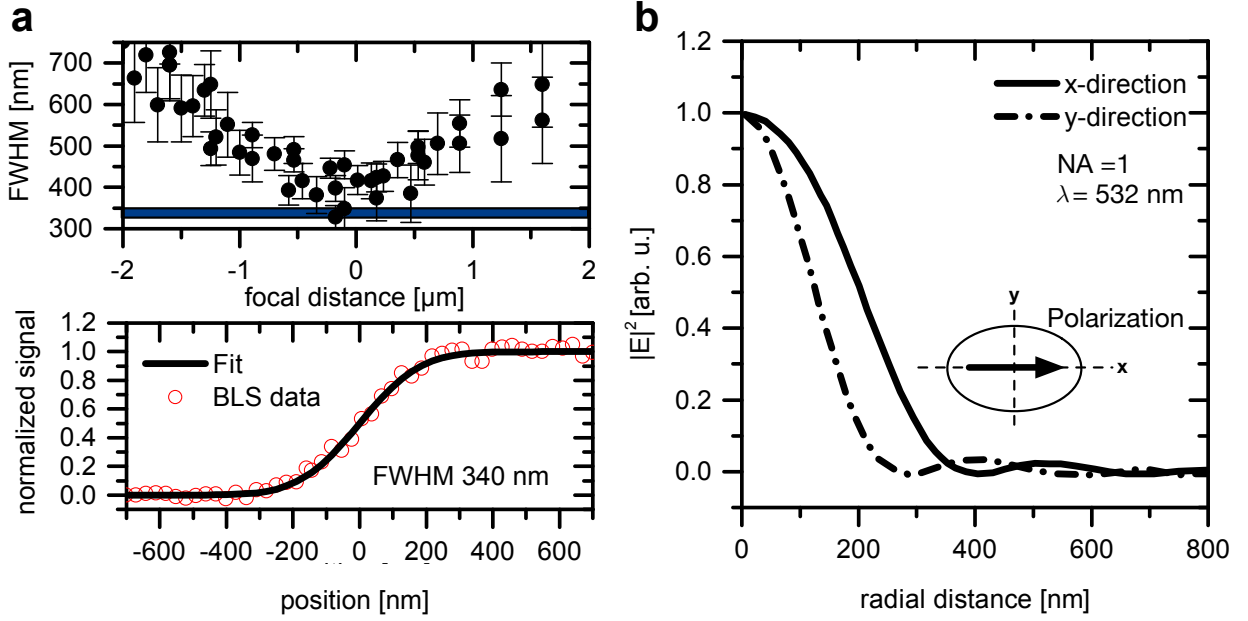


Figure 3.5: **a**, Experimental determination of the detection-function by the “knife-edge-method” and evaluation according to [212]. Several measurements for different focal-planes with minimal FWHM-value of ~ 340 nm (blue line) were performed (top graph). The measured signal (red hollow dots, bottom graph) is treated as a convolution of the detection-function with an “ideally” steep edge (black line). **b**, Calculation of the elliptical laser intensity-profile over radial distance ρ for linearly polarized homogeneous illumination of an objective with NA = 1, data taken from [212].

For its determination by the “knife-edge-method”, the laser beam is swept over a steep sample edge, from substrate and material. The different reflection coefficient, as well as change of focal-plane lead to a step-like intensity increase, when plotted over the edge position. To minimize interference effects², an edge of a 1- μ m-wide and 15-nm-thick $\text{Ni}_{81}\text{Fe}_{19}$ microstructure on a transparent (ideally reflectionless) substrate (sapphire) was chosen as the “knife-edge”. The measured signal is then treated as a convolution of the detection function with the sample edge-profile. Approximating the edge profile as ideal step-like allows then to calculate the detection function, which is here interpreted as the laserspot profile. Detailed explanation of the analysis of such a data-set to estimate the Gaussian-beam-diameter is given in [212]. To determine the best focus-position the FWHM of the assumed Gaussian detection-function was evaluated for different focal-planes, as shown in the top part of Fig. 3.5 **a**. The experimentally smallest repeatedly determined FWHM is around 339 nm.

The corresponding measurement data (red hollow dots) is displayed together with the fit by the cumulative distribution function (black line) in the bottom graph of Fig. 3.5 **a**. The parameters

²Initial experiments by the author showed, that interference effects lead to unaccounted destructive and constructive interference near the sample edge

resulted from application of the method of least squares to a linear fit of equation (10) of [212]. Even though in the publication an accuracy of 0.05% was reached the experimental data shows higher statistical noise. Moreover, systematic errors connected to stage vibrations (incorrectly high FWHM), non-ideal edge structure (incorrectly high FWHM), as well as focus depth influences (also leading to incorrectly high FWHM) are not taken into account in this approach. It is stressed, that in measurements of the spin-wave intensity in flat magnetic microstructures the latter two systematic error sources can be excluded. For this reason, the FWHM in the spin-wave measurements is expected to be smaller and here the lower limit of the FWHM is adapted as the spatial resolution. Importantly next to these systematic influences, wave-vector calculations [213] lead to polarization-dependent elliptical spot-profiles as shown in Fig. 3.5. In the reference spot-profiles are calculated for a linearly polarized input beam and several numerical apertures under homogeneous input illumination of the objective. The spot-area x defined by the radius of half maximum value is given in units of λ^2 , which translates for the FWHM as:

$$\text{FWHM} = \frac{2\lambda}{\sqrt{\pi}} \sqrt{x} \approx 1.128 \cdot 532\text{nm} \cdot \sqrt{x} = 600.1 \text{ nm} \cdot \sqrt{x}$$

so that the values in [213] give:

$$\text{FWHM} = 407 \text{ nm for NA} = 0.7$$

$$\text{FWHM} = 365 \text{ nm for NA} = 0.8$$

$$\text{FWHM} = 316 \text{ nm for NA} = 1.0 \quad \text{short-axis} = 235 \text{ nm, long axis} = 399 \text{ nm}$$

Interpolation:

$$\text{FWHM} = 386 \text{ nm for NA} = 0.75 \quad \text{short-axis} = 287 \text{ nm, long axis} = 487 \text{ nm}$$

Where the last result for NA = 0.75 was estimated by the author. Considering linear interpolation between the given values for NA = 0.8 and 0.7 yields an average FWHM of 386 nm with respect to spot-area. Assuming an identical ellipticity as for a numerical aperture of 1 to the spot-profile calculated for a numerical aperture of 0.75, a spot geometry with short-axis of 287 nm perpendicular to the linear polarization and 487 nm perpendicular to it can be estimated. This range covers the experimentally determined value of $340\text{nm} \pm 10\%$.

Potential ways for increasing the spatial resolution of μ BLS set-ups are using annular apertures, annular polarized light or superposition of two different TEM modes. This also holds the promise to modify the sensitivity to magnetic directions. A detailed explanation is given in [213]. In this context utilizing plasmon enhancement or near-field geometries seems also promising.

CHAPTER 4

Experimental results

The following section covers experimental results obtained within the framework of this thesis. It is split into two different topics:

The first part discusses strongly confined spin-wave propagation along magnetic domain walls in thin film elements. It is shown by μ BLS measurements as well as micromagnetic simulations, that the nanometer-wide effective potential well formed by 90° and 180° Néel walls lead to sub-wavelength confined one-dimensional spin-wave transport along them. Here, possibilities of steering spin-wave propagation via magnetic fields and magnetic configuration as well as non-linear effects and domain wall networks are further explored.

In the second part, starting from section 4.2, auto-oscillations and microwave amplification in micron sized tapered spin Hall oscillators in the anti-damped regime is addressed. The influence of injection locking of the oscillator to an external microwave signal superposed on a DC driving current on the spatio-spectral properties of the auto-oscillation generation is studied.

Therefore, regarding spin-wave circuitry, the first part deals with confining, miniaturizing and controlling spin-wave transport, while the second part discusses spin Hall oscillators as sources for magnetization dynamics and their controllability by the oscillator geometry and externally imprinted periodic signals.

4.1 Spin-wave dynamics in multi-domain magnetic configurations

Preliminary thoughts

In the following sections, spin-wave dynamics in magnetic textures comprised of several domains (regions of identical magnetic orientation) and domain walls, which form as interfaces at their

boundaries, are discussed. Such magnetic configurations naturally result from the minimization of energy by local magnetic orientation (section 2.1) and occur as remanent ground states of micro structured waveguides. The main important energy contributions governing the static equilibrium texture are the exchange and dipolar interactions as well as crystalline anisotropies. They determine size and orientation of the magnetic domains and also width of the domain walls forming between them. This domain wall width is typically on the order of tens of nanometers and determined mainly by the material parameters. The short-scale reorientation of the magnetization creates corresponding narrow effective field wells along the domain walls. Due to the pronounced dependence of the spin-wave dispersion relation on the effective field (section 2.2.1), these field wells locally lower the frequency of the magnetization dynamics with respect to the surrounding domains. Their effect on spin-wave propagation and controllable confining potential is the focus of the following study.

4.1.1 Spin-wave dynamics of 180° Néel walls in rectangular elements

First, the magnetic ground state and, subsequently, the confined spin-wave propagation in rectangular structures based on 40-nm-thick $\text{Ni}_{81}\text{Fe}_{19}$ is investigated experimentally and by micromagnetic simulations. In this subsection the characteristics of 180° Néel wall channels are assessed and the focus is restricted to a particular “bottle-shaped” geometry with an extending 180° Néel wall forming in the center, which covers all relevant aspects and allows discussion in greater detail.

4.1.1.1 Magnetic configuration and domain wall formation

Figure 4.1 **a** shows a SEM micrograph of the investigated “bottle-shaped” structure and introduces the coordinate system, where the x-axis coincides with the short axis and the y-axis with the long axis of the structure. The 6- μm -wide “bottle-neck” part (indicated by the dashed rectangle) added to one end of the 10- μm -wide rectangular structure aids in preparing the desired remanent state and stabilizing a domain wall along the waveguides centre. Additionally, to excite spin-wave propagation a microwave antenna has been patterned on top of the 10- μm -wide part of the structure (section 3.2). To initialize the magnetic state, a sinusoidal exponentially decaying magnetic field was applied parallel to the short axis, while imaging the magnetic configuration by magneto-optical dual Kerr microscopy (technique described in [215]) as shown in Fig. 4.1 **b**. A Landau-like pattern with a 180° Néel wall running along the center of the structure separating two domains of opposite magnetization is observed. Figure 4.1 **c** shows the schematic magnetic configuration of such a 180° Néel wall. The rotation of the magnetic moments within the sample plane give rise to magnetic volume charges ∇M as well as resulting effective field wells due to the exchange and demagnetization fields accompanied by the domain walls (section 2.1). Micromagnetic simulations

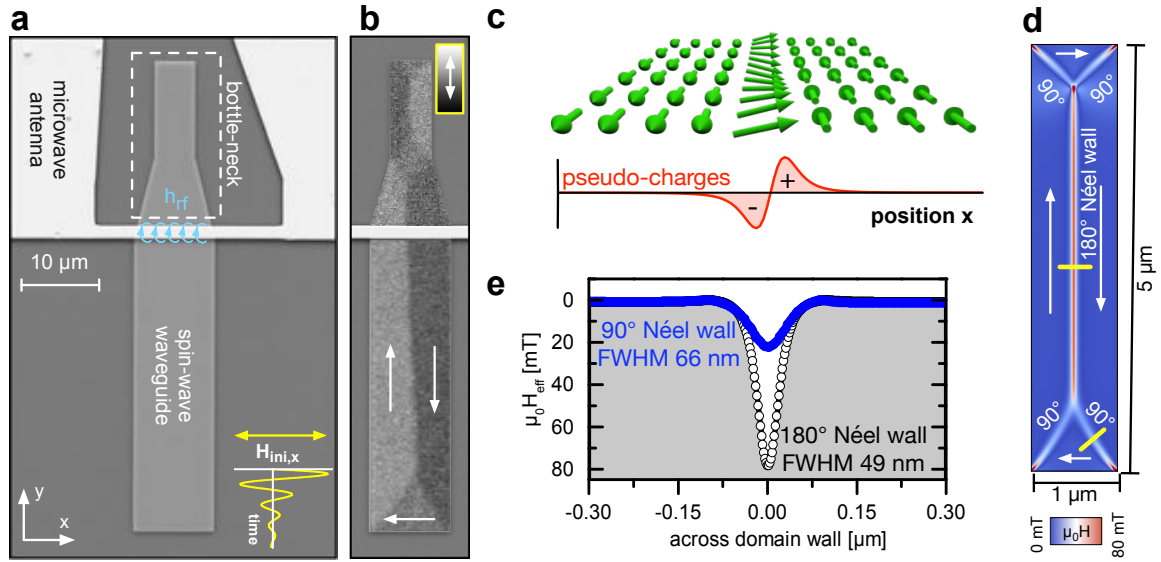


Figure 4.1: **a**, SEM micrograph of the “bottle-shaped” $\text{Ni}_{81}\text{Fe}_{19}$ waveguide and microwave antenna for excitation of spin-wave dynamics. In the lower right inset, the exponentially decaying magnetic field used to initialize the domain configuration is depicted. **b**, Kerr micrograph (magnetic contrast in y-direction, black-white color-coded) of the stabilized Landau-like domain pattern, with a 180° domain wall formed in the center of the structure. White arrows indicate the magnetization direction in the domains. **c**, Schematic of a 180° Néel wall and corresponding magnetic charge distribution, proportional to ∇M . **d**, Micromagnetic simulation of the domain configuration in a rectangular $\text{Ni}_{81}\text{Fe}_{19}$ thin-film element. The magnitude of the effective field is shown color-coded (red-white-blue), revealing the potential wells situated at the domain wall positions. Yellow lines mark the position for extraction of the effective field well profile as shown in **e** for the two different types of wall nucleating from the corner (90°) and in its center (180°).

were carried out to analyze the domain wall width and specific magnetic orientation in rectangular geometries. The system was modeled as a 5- μm -long, 1- μm -wide and 10-nm-thick $\text{Ni}_{81}\text{Fe}_{19}$ rectangle. This reduction in size allowed for a sufficiently fine discretization required to numerically resolve the nano-sized domain wall and proved necessary to reduce the needed computational time (details in appendix section A.5).

It is expected, that this reduction does not affect the magnetization and effective field profile, which is primarily determined by the material parameters and not the dimensions of the system. Figure 4.1 **d** shows the simulated structure, its magnetic orientation (white arrows) and effective field strength color-coded (blue-white-red) revealing effective field channels at the domain wall positions. The potential well profiles of the 180° and the 90° domain walls are shown in Fig 4.1 **e** and have been extracted along the yellow lines indicated in **d**. The potential wells of the 180° and 90° walls exhibit a full width half maximum (FWHM) of 49 nm and 66 nm, respectively.

As additional experimental analysis of the magnetic configuration, magnetic force microscopy

(MFM) was used to measure the out-of-plane stray fields for 50 nm tip-distance above the microstructure surface. These measurements and simulated MFM signals are discussed in the appendix in section A.4 and substantiate the formation of a 180° Néel wall at the microstrip-antenna used for spin-wave excitation as well as a cross-tie-domain structure in the remaining parts of the waveguide. In combination with the Kerr micrographs this concludes the preparation and observation on the magnetic configuration as a suited ground state for channeled spin-wave excitation within Néel walls.

Before proceeding, an intuitive view on these domain walls and their characteristics is presented to the reader to provide a simplified way of understanding the following experimental results. It can be very helpful to picture the resulting magnetic pseudo-charge distribution $\nabla\mathbf{M}$ and effective fields in analogy to the more familiar scenario of an electrically charged capacitor. For the idealized charged capacitor (infinite surface), the resulting electric field is homogeneous between the two charged surfaces, while vanishing on its outside. The domain wall charge-configuration, is, except for a gradual (or smeared out) change in the charge distribution, close to this ideal case of two separated oppositely charged surfaces, as shown in Fig. 4.1 c. Consequently, similar to the capacitor case, the field outside the domain wall vanishes and a field extrema inside the wall is found Fig. 4.1 e. Moreover, the two pseudo-charged surfaces attract each other, due to the dipolar interaction, favoring to decrease the domain wall width towards an instantaneous flip of the magnetization. This is analogous to the force acting on the charged plates of the capacitor and bringing these two into contact would resemble charge recombination. However, while for the capacitor the two surfaces are mechanically kept from moving towards each other, for the case of the domain wall, the exchange interaction does not allow for such a rapid magnetic reorientation. Instead it increases with decreasing domain wall width until it balances with the charge attraction for distances on the nanoscale. In this picture one can intuitively understand why domain walls form naturally, when starting from a non-uniform magnetic configuration with given volume charges moving towards each other and that their distance or domain wall width respectively is determined mainly by the interplay of material parameters. Furthermore, while the domain wall structure is stabilized by these two competing interactions, its position is determined by different and typically weaker interactions with the structure edges or indirectly by a domain-domain interaction. This promotes, that they can be moved through a magnetic material by a variety of means, such as electrical currents, ion implantation, small magnetic fields or laser dragging, while maintaining their characteristics. They form very narrow spin-wave waveguides, due to their drastically changed field inside the wall, where crystalline anisotropies can be utilized to further shrinking the domain wall width. This allows for even further miniaturization, while still allowing the wall to be moved across the magnetic carrier.

4.1.1.2 Thermal spin-wave spectrum

As a starting point on the investigation of spin-wave dynamics in this magnetic configuration thermally excited magnetic spectra have been recorded for the domain and domain wall by μ BLS. Since typical spin-wave energies are a few tens of μ eV and much lower than the thermal energies at ambient temperatures of ≈ 25.7 meV, the thermal excitation can be viewed as a stochastic, in time delta-correlated field (white noise), exciting all spin waves equally with random phase at random positions. Due to this, the measured magnetic spectra are free of distortions introduced when actively exciting, such as pumping field geometries, standing wave formation in the transmission lines or other frequency and phase selective measurement means. Therefore, even though thermal measurements typically have a poorer signal intensity, the recorded spectra are complementary and directly proportional to the density of states and scattering cross-section.

Figure 4.2 displays the μ BLS-Intensity recorded on the expected domain wall (blue dots, in the center of the structure) and domain (black squares) position. The data reveals clearly different magnetic spectra for the two measurement positions. Importantly, the spectrum recorded on the domain wall is of main intensity below 1 GHz, while the domain spectrum is of maximum intensity above 1.6 GHz. The higher intensity detected at low frequencies for both spectra around 0.5 GHz is a background signal from the elastically scattered light related to the set-up (section 3.5). The data agrees with the imaged domain wall position at the center of the structure and suggests two important assumptions: Firstly, the frequency onset of the spin-wave band in the domain is around 1.6 GHz, which is very likely attributed to spin-wave quantization, since the effective field vanishes in the domains. Secondly, spin waves with frequencies below 1.6 GHz are mainly contained in the domain wall spectrum. Therefore, confined spin-wave propagation within the domain wall is already suggested by these measurements for spin-wave frequencies below 1 GHz.

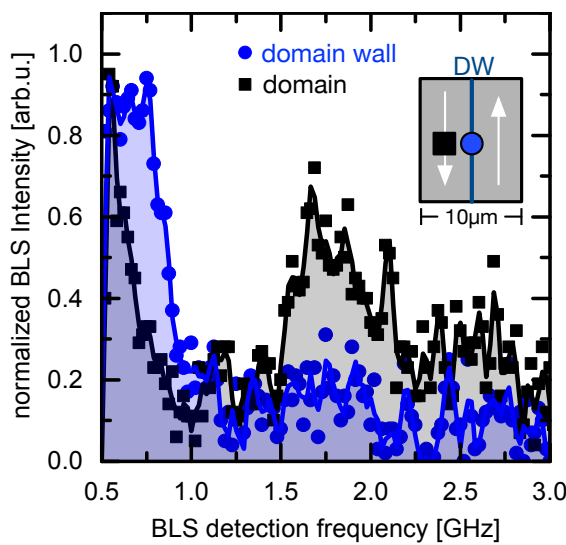


Figure 4.2: Thermally excited spin-wave spectra recorded by μ BLS on the 180° Néel wall (blue dots) and neighbouring domain (black squares). The different frequencies of main intensity in the spectra suggest confined transport for low frequency spin-wave excitations below 1 GHz. Positions for the measurements on x-axis with origin in the center of the structure: domain $-2 \mu\text{m}$; domain wall $0 \mu\text{m}$.

4.1.1.3 Direct excitation of spin waves

As aforementioned a 100-nm-thick Au microwave antenna has been patterned on top of the structure to excite spin waves and probe the resulting spin-wave transport by μ BLS. The discussion starts by presenting the spin-wave excitation efficiencies recorded for different positions on the waveguide, while sweeping the excitation frequency for constant source power $P = -1$ dBm. Figure 4.3 shows the spin-wave intensities measured in $1\ \mu\text{m}$ distance to the exciting antenna for the domain wall (blue dots), as well as on the domains (black squares, red triangles). Despite the small domain wall “volume” compared to the one of the domains, pronounced excitation and detection of spin-wave dynamics for frequencies below 1 GHz is observed. As expected, the excitation efficiency is similar to the previously shown thermal spectra. The spin-wave intensity at the domain wall increases with decreasing frequency below 1 GHz. In contrast to this, the domain spectra (black squares, red triangles) exhibit the highest spin-wave intensities for frequencies above 1 GHz. They are shifted in frequency with respect to each other and exhibit their intensity-maxima at around 2 GHz (domain A) and 2.8 GHz (domain B), respectively. This is assumed to be attributed to the domain wall displacement out of the exact center of the structure estimated to be around $0.75\ \mu\text{m}$. This results in different spin-wave quantization conditions for domain A and domain B. Calculations according to the thin film dispersion relation (section 2.2.1) for the expected domain sizes of around $4\ \mu\text{m}$ (domain A) and $6\ \mu\text{m}$ (domain B) were performed for comparison. Assuming pinned conditions at the structure edge and the domain wall boundary, resulted in lowest frequencies of the spin-wave band around 2.25 GHz (domain A) and 1.75 GHz (domain B). This is in contrast to the experimental result, where domain A is found to have a lower onset-frequency of the spin-wave band. However, special care was taken to ensure, that domain A is correctly identified in the experiment to be the smaller sized domain. Therefore, it is believed that deviations from pinned boundary conditions lead to the observed difference. Considering the results shown in

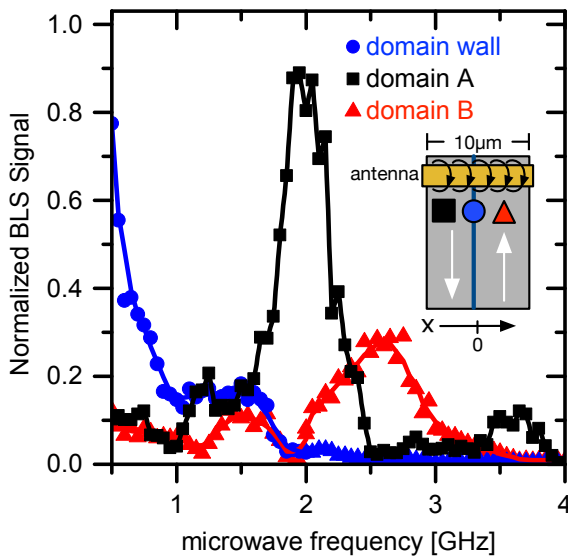


Figure 4.3: Normalized spin-wave intensities recorded in $1\ \mu\text{m}$ distance to the exciting antenna for the domain wall (blue dots) and neighboring domains, labeled A (black squares) and B (red triangles). Measurement positions with respect to x-axis with origin in the center of the structure (schematically shown in the inset): domain A: $-3\ \mu\text{m}$; domain B: $3\ \mu\text{m}$; domain wall: $-0.75\ \mu\text{m}$.

the following sections, the boundary conditions imposed by the domain wall seem to be frequency dependent. Additionally, the influence of spin-wave excitation on the domain wall position, when exciting spin waves in the domains has been reported before [216, 217] so that changes in domain size, while sweeping the excitation frequency can not be excluded and seem indicated for higher spin-wave frequencies and higher laser powers as discussed later. Moreover, the asymmetric probing positions relative to the domain boundaries could have influenced the shape of the recorded spectra, due to the transversal localization of the spin wave dynamics [105].

Here, it is of main importance, that the spectra when actively exciting confirm for both domains higher spin-wave frequencies, than for spin waves within the enclosed domain wall suggesting channeling. The next section discusses the role of the antenna geometry on the excitation efficiencies of spin waves within this magnetic configuration. Additionally, parametric pumping and second harmonic generation revealing frequency dependent quantization conditions for spin waves in the domains is presented. Afterwards the discussion continues on the spin-wave propagation confined within the domain wall.

4.1.1.4 Parametric pumping and spin-wave confinement in the domains

The antenna geometry plays a significant role for the spin-wave excitation efficiency in the presented experiments and is worth to be discussed in more detail before proceeding. The antenna, a wire with rectangular cross-section, is translation invariant parallel to the antenna axis across the structure (x-direction, see also Fig. 4.1). Consequently, its excitation field \mathbf{h}_P has only two components, being in-plane (y-component) and out-of-plane (z-component). To discuss the excitation efficiency of \mathbf{h}_P to the magnetization dynamics \mathbf{m}_{dyn} the time derivative of the corresponding Zeeman-energy can be considered:

$$\text{excitation strength} \propto \frac{d}{dt} \int_V \mathbf{h}_P \cdot \mathbf{m}_{\text{dyn}} dV \quad (4.1)$$

Implying that for great excitation efficiencies the averaged scalar product needs to be maximized. This means, that for infinite sample dimensions (V), only spin-wave modes of identical Fourier components as the pumping field are excited (see e.g. [218]). For the microstructure, this restricts spin-wave excitation to modes of non-vanishing averaged dynamic magnetization component across the structure (typically "uneven" modes). An important additional point to consider in the studied thin film geometry, is the elliptical precession trajectory of the magnetization dynamics (section 2.2.1). Since the out-of-plane component is reduced with respect to the in-plane one, this renders excitation of the in-plane pumping field in general to be more efficient. This has special implications for excitation of spin waves in a domain wall and surrounding domains. While the smaller z-component of the dynamics is excited equally in domains and domain wall, the in-plane

component is efficiently driven only at the domain wall. This is due to the fact, that the magnetization rotates around the z -axis across the wall, so that the plane of the precession trajectory depends on the position. For the magnetization in the domains this trajectory lies within the xz -plane (in-plane component perpendicular on the one of the pumping field), while in the middle of the domain wall the dynamic magnetization lies within the yz -plane matching the one of the pumping field. Hence, as the first conclusion, the highest excitation efficiency of spin waves is expected at the domain wall, which aids in particularly injecting spin waves at the domain wall channel experimentally.

Next to this, the pumping geometry can also be utilized to dominantly excite spin waves in the domains. This is connected to the fact, that the in-plane component of the pumping field is identical to the magnetization direction in the domains. For this geometry “parametric pumping” [128,129] (section 2.2.2) can be utilized, to excite spin waves at half the pumping frequency primarily within the domains. Figure 4.4 **a** shows a μ BLS-measurement on one of the domains, when detecting not only the directly pumped (blue hollow dots), but also the parametrically excited spin waves at half of the excitation frequency (black hollow dots) illustrating this point.

As can be seen from this data, for frequencies above 2 GHz the efficiency of the parametric pumping in the domain even exceeds the one for direct excitation. However, it has to be kept in mind, that due to the transmission lines the microwave excitation might change in power at twice the frequency, so that the comparison is not strictly quantitative. Moreover, this observation of parametric pumping is in agreement with a domain orientation parallel to the pumping field and the magnetic state imaged earlier in Fig. 4.1 **b** and can, therefore, serve to additionally distinguish between domains and domain wall.

To conclude: Considering the excitation field geometry, the direct excitation efficiency is highest for spin-waves in the domain wall, while the parametric pumping of spin waves at half the microwave frequency is most efficient in the domains, helping in selecting their dynamics separately. Together with the differences in the frequency spectra of domains and domain wall the μ BLS experiments allow to indicate the magnetic state and domain wall position even in the absence of additional magnetic contrast measurements. This is of great practical help to determine the wall position before recording magnetic spectra.

Besides the efficiency variation induced by the pumping field geometry, the simplest way to excite spin waves separately in the domain or the domain wall is by selection of the microwave frequency. In this context Fig. 4.4 **b** presents spin-wave excitation in the domains, for a microwave frequency lying within the domain spectra and a restriction on spin-wave propagation by the domain wall in the center. In the top part for two subsequent measurements labeled “M1” and “M2” the spin-wave intensity at the pumping frequency (1.4 GHz, direct excitation, top part) is recorded across the structure. Spin waves are mainly excited in the domain starting from a position around 5 μm and bound to this domain. This suggests, that the onset frequency of the neighboring domain

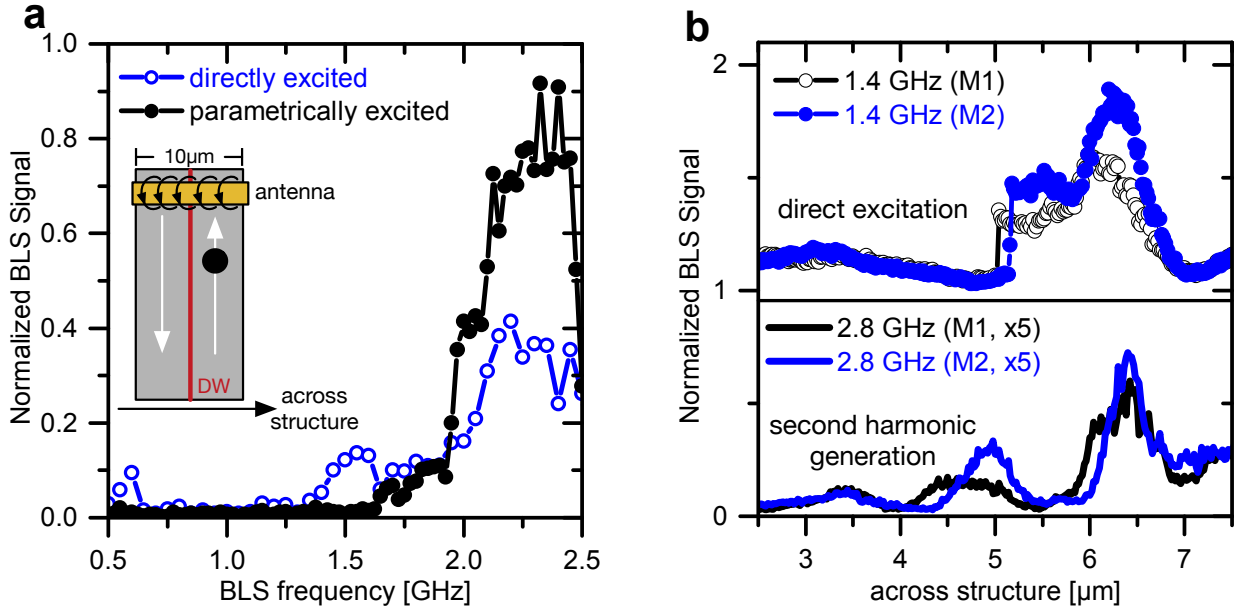


Figure 4.4: **a**, Simultaneously recorded direct and parametrically excited spin-wave spectra on one of the domains. For frequencies above 2 GHz the pronounced parametric excitation efficiency suggests an anti-/parallel orientation of the magnetization to the pumping field of the antenna (schematically shown in inset). **b**, Top graph: Spatial Intensity-profile of directly excited spin waves for an excitation frequency of 1.4 GHz (blue and black dots). The domain wall position presents itself as a sudden drop in the spin-wave intensities and its slight change in position for the two separate measurements M1 and M2. Bottom graph: Simultaneously recorded spin-wave intensities excited by second harmonic generation (SHG) detected at twice the excitation frequency (2.8 GHz).

is above 1.4 GHz and, therefore, does not allow spin-wave propagation below its onset. Hence, the domain wall position manifests itself as a sudden rise/drop in the directly excited spin-wave intensity when crossing from one domain to the other. This measurement suggests that the size of the individual domains, connected to the domain wall position, acts as to separate spin-wave dynamics and confirms that spin waves can be selectively excited in only one of the domains (if they are differently sized) depending on the microwave frequency.

Simultaneously for both measurements the spin-wave intensities generated by second harmonic generation (SHG) at twice the excitation frequency are additionally recorded. SHG is known from many non-linear systems. In magnetic systems it can be formulated as a confluence process of two magnons at the excitation frequency, as observed, e.g., in [117]. The spin waves excited by SHG can be detected in both domains. Interestingly, as indicated by the amplitude-decay when going from right to left domain, these spin waves propagate across the domain wall border. Therefore, this data excludes that the domain wall is mainly reflecting impinging spin waves at 2.8 GHz. It becomes evident, that the boundary conditions are more complex in this scenario, since otherwise

standing wave profiles could be expected. Furthermore, it is indicated that the confinement (as seen for 1.4 GHz) is a consequence of the individual domain spin-wave frequency onset (connected to the domain size) and not the domain boundary formed by the wall, since it differs for spin waves at 2.8 GHz and 1.4 GHz. Another important aspect, is the slightly changed domain wall position for these two nominally identical measurements, inferring induced motion by either thermal or magnon gradients. This is likely attributed to shifting the domain wall by magnon gradient [216] (agreeing with the result of the following section) in combination with exerting a dragging force on the domain wall by the thermal gradient induced by the swept laser (see section A.3 in the appendix). Meaning, that for high pumping powers of spin waves in the domains or high laser powers the domain wall channel position can be manipulated.

This confinement, or boundary conditions imposed by the domain size holds its own promise for future studies on spin-wave confinement and pinning conditions at a domain wall to be measured in one and the same sample for different domain wall positions. In this context, splitting processes, as recently simulated for confined geometries [219] were for the first time experimentally supported. The data is presented in the appendix (section A.1). Even though the quantization due to confinement in micrometer-sized waveguides has already been studied extensively (e.g. [102–104]), domain walls form more complex and material parameter dependent boundaries, which are controllable in position for example by small magnetic fields as presented later. Since in the analysis of spin-wave confinement the exact geometries and edge roughnesses, which typically deviate from sample to sample, play a major role, domain walls might provide a possibility to conduct systematic studies on spin-wave quantization not restricted by the fabricated geometry. However, this goes beyond the scope of this thesis, which continues with the spin-wave modes confined to the domain wall channel.

4.1.1.5 Spin-wave propagation along domain wall nanochannels

Now the focus is put on spin waves which travel confined to the effective field well formed by the 180° Néel wall. Part of these results and a rather concise presentation can be found in the authors publication in [O9].

As a start of this discussion, Fig. 4.5 shows the recorded spin-wave intensity profiles across the 10- μm -wide structure. Measurements were carried out for several frequencies including the two frequencies, that showed maximum spin-wave intensity in the larger domain (2.8 GHz) and domain wall (0.5 GHz) in the previous frequency dependent measurements (Fig. 4.3). The data clearly reveals the different mode character. While the higher frequency spin-waves are excited in the domains and drop in intensity at the domain wall position, the low frequency mode is strongly confined to the domain wall channel.

The slight asymmetry in the intensity-profile for the higher-frequency mode with respect to the

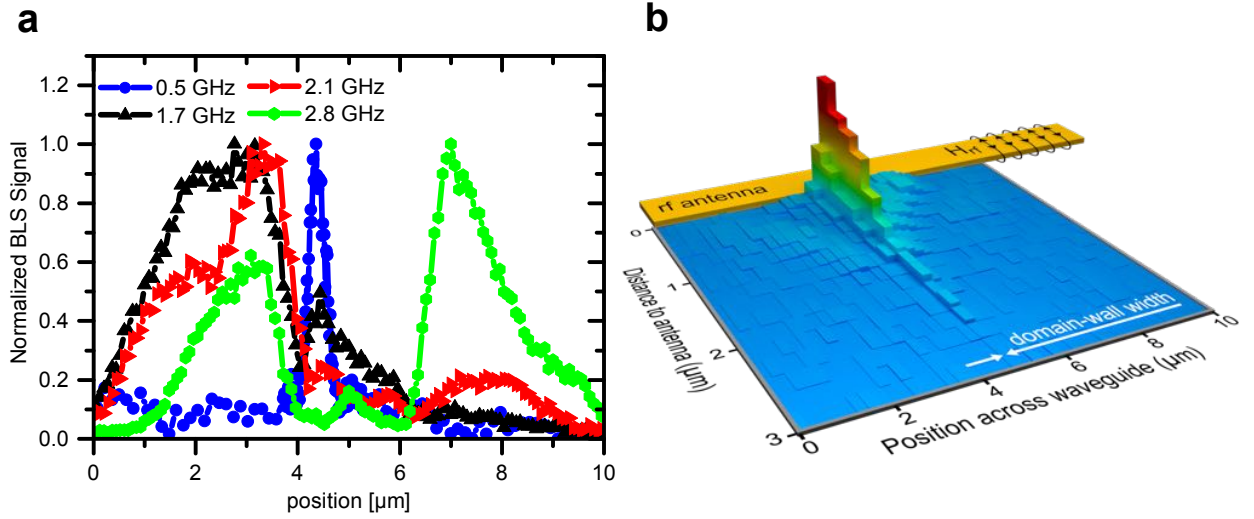


Figure 4.5: **a**, Spin-wave intensity-profiles across the structure for different excitation frequencies and 1 μm distance to the antenna. Mainly, three different types of mode-profiles are observed, which have their intensity maxima either within the domain wall (0.5 GHz), in one of the domains (2.1 GHz), or almost equal intensity in both domains (2.8 GHz). **b**, Two-dimensional spin-wave intensity map recorded by μBLS . Low-frequency spin waves (500 MHz) propagate, while staying confined, along the nanochannel formed by the domain wall in the center of the waveguide, as presented in [O9].

domains is likely attributed to their different size and, hence, shifted spectra, due to the spin-wave quantization, as addressed in the previous section. In the chronology of the experiment, the excitation frequency was kept constant while recording the spin-wave intensity profile across the structure and subsequently the frequency was increased starting from 0.5 GHz. In the experiment the domain wall position presents itself as a sharply confined 0.5 GHz mode profile to a position of approximately 4.36 μm (local maximum) and for higher frequencies as an intensity drop at this position for the spin-wave domain-modes for 1.7 GHz and 2.1 GHz, respectively. When increasing the frequency to 2.8 GHz, the data suggest that the domain wall changed its position by approximately 800 nm towards the exact centre of the structure during the measurement cycles. For this frequency a new symmetry around the center of the structure (5 μm) and rather equal spin-wave intensity in both domains is observed. This substantiates the point raised in the earlier section of a domain wall motion induced, when actively exciting spin waves in the domains combined a thermal gradient of the swept laser.

The lower frequency localized spin-wave transport within the domain wall becomes more evident from two-dimensional μBLS -measurements as presented in Fig. 4.5 **b** for an excitation frequency of 500 MHz. As can be seen from this data, these spin waves remain sharply confined to the domain wall channel, while propagating away from the exciting antenna.

To obtain a deeper insight into the spin-wave transport properties within this channel, the previously introduced micromagnetic simulations of a 5- μm -long, 1- μm -wide and 10-nm-thin $\text{Ni}_{81}\text{Fe}_{19}$ rectangle were extended to include time dependent magnetic fields to investigate magnetization dynamics. The magnetic field utilized for excitation is oriented out-of-plane and of Gaussian spatial profile with a FWHM of 100 nm. It is positioned on one end of the domain wall as shown in Fig. 4.6 a. The time dependent amplitude of the excitation pulse was chosen to be a superposition of equally strong fields oscillating at frequencies covering the range from 0 up to 40 GHz. Its representation is given by $\sin(2\pi f_{\text{grenz}} \cdot t)/(2\pi f_{\text{grenz}} \cdot t)$ with f_{grenz} being 40 GHz. The simulated dynamic magnetic response was then recorded every 10 ps for a duration of 25 ns for each cell. In the linear regime, the time dependencies allow to analyze the dynamic response separately for a frequency selected by windowed backward Fourier transformation [112, 220]. A more detailed description of the methodology can be found in the appendix in section A.5. Exemplary results for a continuous wave excitation are shown in Fig. 4.6 b for three spin-wave modes transversally confined to the domain wall (0.52 GHz, 1.28 GHz and 2.1 GHz) as well as for a higher frequency above the onset of the spin-wave band of the domains. For the higher frequency modes loss of channeling capability of the domain wall and increased radiation into the neighboring domains, attributed to the availability of spin-wave states at this frequency, is observed.

As another important observation, the simulations suggest that vortices effectively block spin-wave propagation. This can be inferred from the spin-wave transmittance at the top and bottom domain wall junction from the simulated dynamics, e.g., for 2.16 GHz. While spin waves confined to the domain wall seem to be fully reflected at the vortex situated on the top junction, at the lower junction a partial transmittance is observed. This suggests, that the strong effective field variation at the vortex-core blocks transmission of spin waves. The difference in the effective field channels for the 180° Néel and the 90° Néel walls (see earlier figure 4.1 e) is not as drastic as for the vortex core resulting in partial transmission in analogy to the impedance matching of transmission lines in microwave technology. This is in agreement with the results on iron based system and domain wall junction as addressed in the later presented section 4.1.3.2.

The spin-wave dispersion as determined by subsequent spatial Fourier analysis of the dynamic magnetization along the domain wall for several frequencies is shown in Fig. 4.6 c. A more detailed description of its derivation is given after this paragraph. A positive dispersion with group velocities about 1.75 $\mu\text{m}/\text{ns}$ is found. Despite the strong transversal confinement of the spin-wave flow on length scales given by the domain wall width, their dispersion is dominated by dipolar interactions resulting initially in an almost linear relation between wave vector and frequency, which is an important property, to allow for transmittance of signals without dispersion induced broadening. The exchange energy stems mainly from the quantization across the width of the domain wall channel and, therefore, does not significantly influence the wave vector in propagation direction. For this reason the term can be seen as a constant offset, compensating the anti-parallel effective

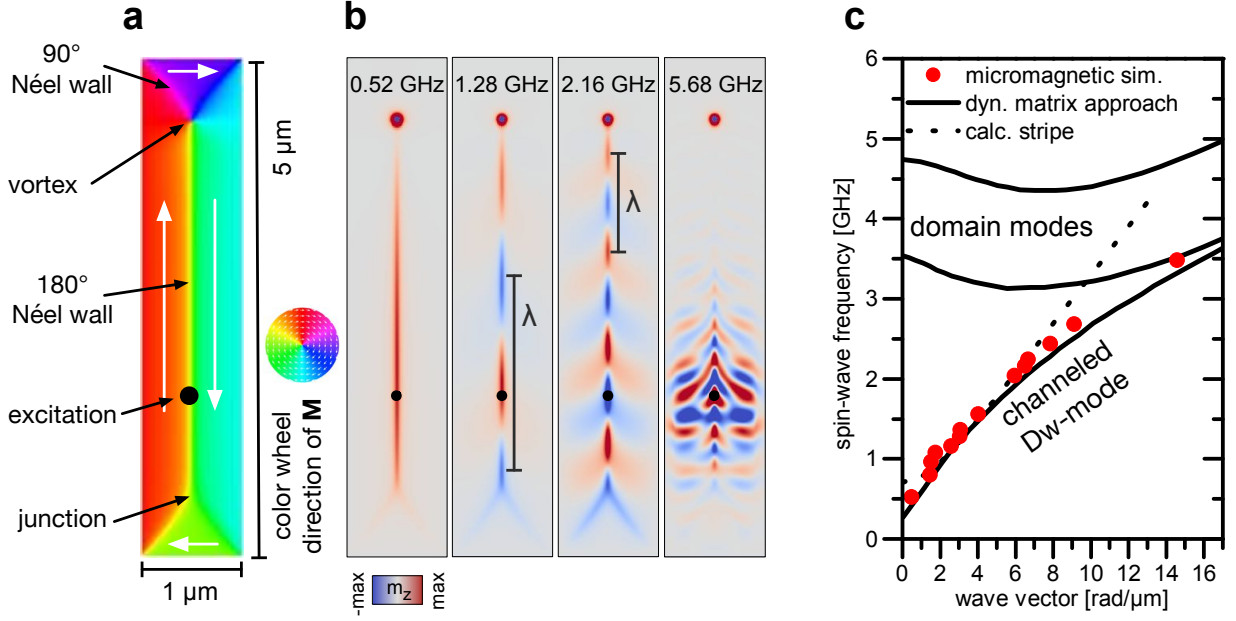


Figure 4.6: **a**, Magnetic ground state together with the position of point-source for spin-wave excitation in the micromagnetic simulations. The direction of the magnetization is shown color-coded (see color wheel) and by white arrows. **b**, Simulated spin-wave response to a localized continuous wave excitation visualized by a snapshot of the dynamic out-of-plane magnetization for exemplary frequencies. **c**, Dispersion relation along the domain wall as derived from the micromagnetic simulations (red dots) and according to a dynamical matrix approach, described in [221] (black lines). Additionally, the calculated dispersion-relation according to equation 2.14 (black dashed line) is shown for a transversally magnetized wire with effective width of 60 nm and an average effective field strength of -80 mT inside the wall, assuming pinned boundary conditions.

field inside the well. For comparison, calculations based on a dynamical matrix approach [221] (black lines), as well as the for the dispersion relation according to the thin-film dispersion equation 2.14 (dashed black line) assuming pinned boundary conditions for a transversally magnetized 60 nm-wide wire with an average effective field strength of -80 mT are shown. A good agreement between the dynamical matrix approach with the micromagnetic simulation is observed validating these two numerical approaches. However, regarding the analytical approach, even though some agreement of the calculated dispersion-relation for a transversally magnetized wire is found for these parameters, it is very sensitive on small variations and there is no support for choosing these particular values. Nevertheless, it is presented here, since main characteristics of the initial linear dispersion relation are recovered by this ansatz, illustrating the idea, that the exchange energy compensates for a negative field inside the well, which leads to a linear dispersion dominated by the dipolar interaction.

The derivation of the dispersion relation is now explained in a bit more detail and indicates, that

the dynamic part of the dipolar energy originating from the spin waves is by a factor of three to five larger than the dynamic exchange energy, depending on the frequency considered. For illustration, the derivation is exemplarily shown for a spin-wave frequency of 1.28 GHz. Figure 4.7 **a** displays the dynamic out-of-plane magnetization δm_z along the domain wall situated at the centre of the simulated structure and the section chosen for analysis (blue line). This part of the dynamic out-of-plane component of the spin wave is then Fourier-transformed (using a Gaussian windowing function and zero-padding) to calculate the wave vector distribution shown in Fig. 4.6 **b**. The weighted average of this distribution is then taken as the mean wave-vector in the dispersion relation and yields 3.14 rad/ μm for this particular frequency. Finally, Fig. 4.7 **c** presents the dynamic exchange and dipolar contributions averaged over the simulated system for one period. The mean values of the energies have been subtracted, so that the energies oscillate around 0 and give a factor of 3.38 higher variation of the dipolar energy, suggesting its stronger influence on the spin-wave dispersion.

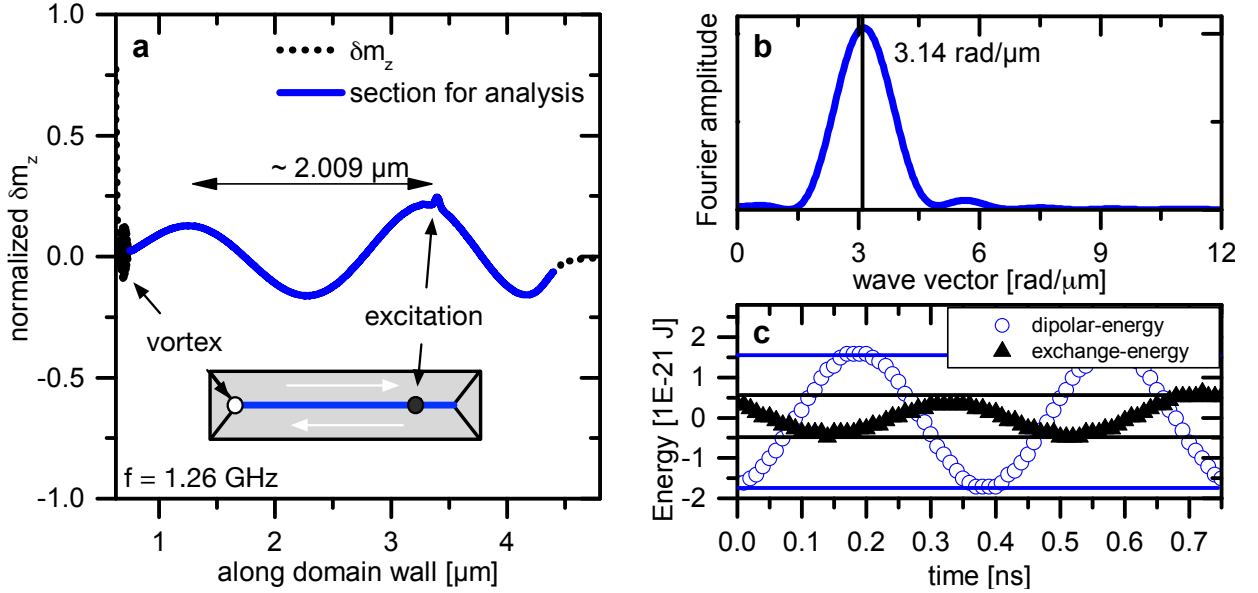


Figure 4.7: Analysis of the dispersion relation and dynamic energy contributions: **a**, Line profile, extracted along the center long-axis (see also schematic inset) of the simulated spin-wave response presented by the dynamic out-of-plane magnetization for an excitation frequency of 1.28 GHz (black dotted line) and the section chosen for analysis (blue line). **b**, Spatial Fourier transformation of the section presented in **a** using a gaussian windowing function and zero-padding to yield the presented wave vector distribution. The weighted average is taken as the mean wave vector for the dispersion relation giving a value of $k = 3.14 \text{ rad}/\mu\text{m}$. **c**, Oscillations of the exchange- and dipolar-energy in the simulated structure around their equilibrium value, when a spin-wave of 1.28 GHz is excited over one period. The variation of the dipolar energy is a factor of 3.38 higher than it's exchange counterpart. Similar analysis for all other frequencies result in the dispersion relation shown in Fig. 4.6.

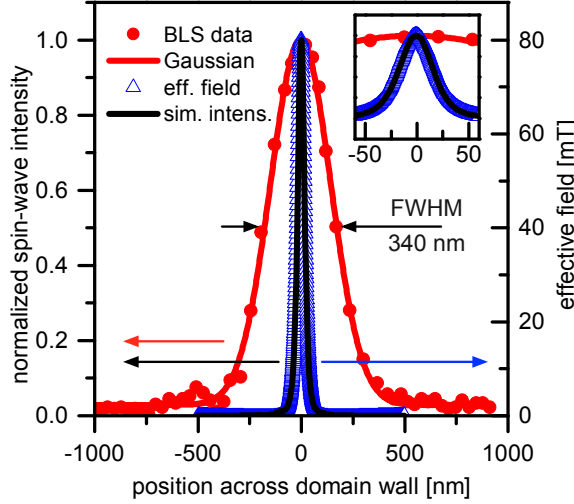


Figure 4.8: Simulated effective field well (blue triangles, right y-axis) and spin-wave intensity (black line) across the domain wall channel. A lateral confinement to 40 nm (FWHM) and high degree of correlation (magnified in inset, identical axes) is observed. Additionally, the experimentally measured μ BLS-intensity (red dots) is shown together with a Gaussian fit (red line). The signal is a convolution of the spin-wave intensity with a detection-function of the μ BLS set-up suggesting strong confinement of several tens of nanometre or less experimentally.

The correlation of the confinement and the effective field well is finally demonstrated by the simulation as seen in Fig. 4.8, which shows the simulated effective field well (blue line) together with the simulated intensity profile (black dotted line) of the channeled spin-wave mode of frequency 0.52 GHz. The direct comparison reveals the strict confinement to the potential well formed by the domain wall matching in FWHM of 40 nm. For comparison with the experiment the recorded spin-wave intensity profile in 1 μ m distance to the antenna (red dots) by μ BLS is shown, which is well reproduced by a Gaussian fit (red line) of 340 ± 30 nm FWHM. Even though the experimentally recorded μ BLS-signal is proportional to the spin-wave intensity, it is additionally convoluted with previously measured set-up specific detection function (section 3.5.1). Since the recorded spin-wave intensity-profile and detection function are equal in FWHM, it is concluded that the spatial resolution limit of the set-up is reached. This confirms a pronounced transversal confinement experimentally to length scales of a few tens of nanometers or below agreeing with the micromagnetic prediction.

4.1.1.6 Active steering of spin-wave flow by controlling the domain wall nanochannel

This section discusses the possibilities to steer spin-wave flow utilizing channeled spin waves in domain walls. In contrast to waveguide designs based on geometric confinement, where the initial fabrication fixes the spin-wave propagation, domain walls can be manipulated by several means in one and the same waveguide. For instance, by magnetic fields [222], laser dragging [223–225], ion implantation [226], thermal gradients [217, 223] or spin currents [227, 228]. Within the framework of this thesis, small external magnetic fields are chosen to proof the concept of displacing the domain wall nano-channel to steer the spin-wave flow within it. The fields on the order of only a few Oersted were applied along the long-axis of the bottle-shaped structure favoring the growth of either the left or right domain depending on the field polarity. This resulted in a shifted domain wall position over several microns. Figure 4.9 shows the experimentally measured spin-wave intensity in 1 μm distance to the antenna exciting spin waves with a frequency of 0.52 GHz, for four differently displaced domain wall channels by small magnetic field values of -0.15, -0.05, 0.05 and 0.23 mT. For each field value, a sharply confined spin-wave channel of different position is observed. Hence, it can be concluded that the channeling capability of the domain wall channel is robust against small fields, even though its position in the waveguide changes in the micron range. The slight left-right asymmetry of the spin-wave intensity-peak is believed to be attributed to the differing domain spectra on the left and right side of the domain wall (section 4.1.1.5). When correlating the position of the confined spin-wave transport and, hence, the domain wall position, with the applied field a proportionality constant between displacement and field strength as large as $5.57 \pm 0.75 \mu\text{m}/\text{mT}$ is found. An accuracy in determining the channel position of $\pm 70 \text{ nm}$ was estimated and the fields were determined with an statistical accuracy of 0.02 mT. This establishes an interesting mechanism of active steering of spin-wave transport over several microns and may pave the way for reprogrammable and yet non-volatile spin-wave based logic circuitry.

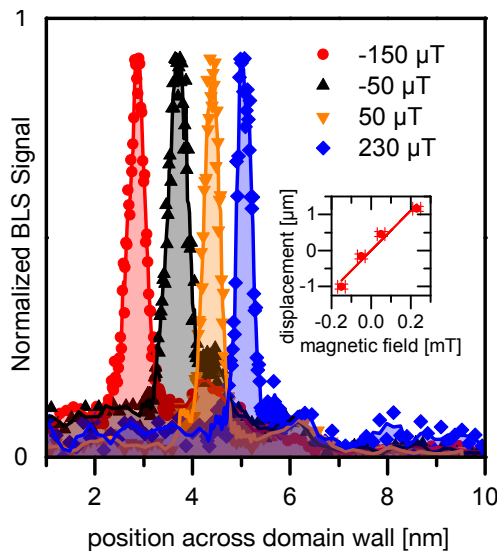


Figure 4.9: Steering spin-wave propagation by moving the domain wall channel. The spin-wave transport was recorded by μBLS across the structure. Small external magnetic fields along the long axis of the bottle-shaped structure are used to control the domain wall position in the micron-range. The channeling capability of the domain wall maintains intact despite the applied fields. A large proportionality constant between displacement and field strength of $5.57 \mu\text{m}/\text{mT}$ is found experimentally.

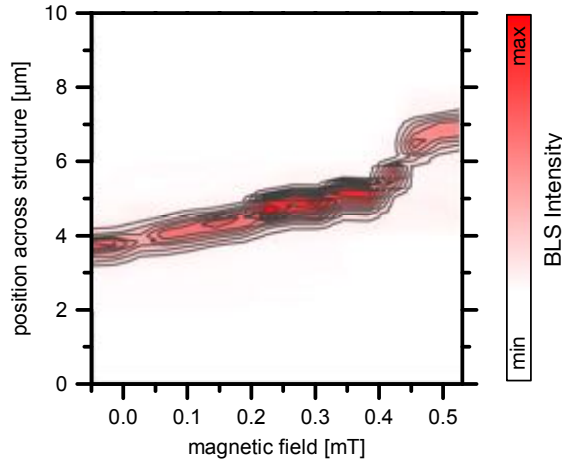


Figure 4.10: Domain wall positioning influenced by sample impurities. In this nominally identical structure the displacement of the domain wall by small external magnetic fields along the long axis of the bottle-shaped structure exhibits a rather ratchet-like motion. The spin-wave intensity measured inside the wall changes without a clear trend, indicating influences of pinning sites on the channel.

Nevertheless, it is indicated, that sample impurities exert pinning forces on the domain wall and influence its free positioning. Additionally, since they are a type of inhomogeneity, they can be expected to hamper spin-wave transport along the channel. The influence of such pinning sites was more clearly observed for a second nominally identical sample structure, expected to have a higher density of these sites. In Fig. 4.10 the recorded spin-wave intensity profile across the structure is shown for a range of magnetic fields. As a consequence of pinning effects a rather ratchet-like motion of the domain wall channel with the applied field is confirmed by imaging of the spin-wave transport.

To deepen the insight on field manipulation on the domain wall channel, in the next step magnetic fields, rotated by 90° to point along the short axis of the bottle-shaped structure, are applied. This is expected to have two pronounced effects on the magnetic state: Firstly, the domain wall (where the magnetization is collinear with the magnetic field) is supposed to broaden or contract depending on the field polarity, as well as to shift the channel spectrum to higher and lower frequencies. Secondly, the vortices and anti-vortices, which can be situated at the domain wall in the cross-tie pattern (see section 2.1 and section A.4), should move in opposite directions by the applied field, resulting in their eventual annihilation. Since the effective field changes rapidly within the core radius of (anti-)vortices, they are expected to hamper/block spin-wave propagation (see also previous subsection 4.1.1.5).

For this reasons, it is believed that improved spin-wave propagation could be achieved by applying small fields along the short-axis. To this end, sample structures of the same geometry were first studied by Kerr microscopy in respect to the interaction between their magnetic configurations and small external fields applied along the short direction, as shown in Fig. 4.11. Two different structures are shown referred to as “structure A” and “structure B” and the magnetic contrast was simultaneously recorded for the x- (bottom half, red frames) and y-direction (upper half, blue frames). As can be seen from the micrograph, some of the vortices and anti-vortices annihilate each other, while the domain wall remains in its position in the centre of the structure. For instance,

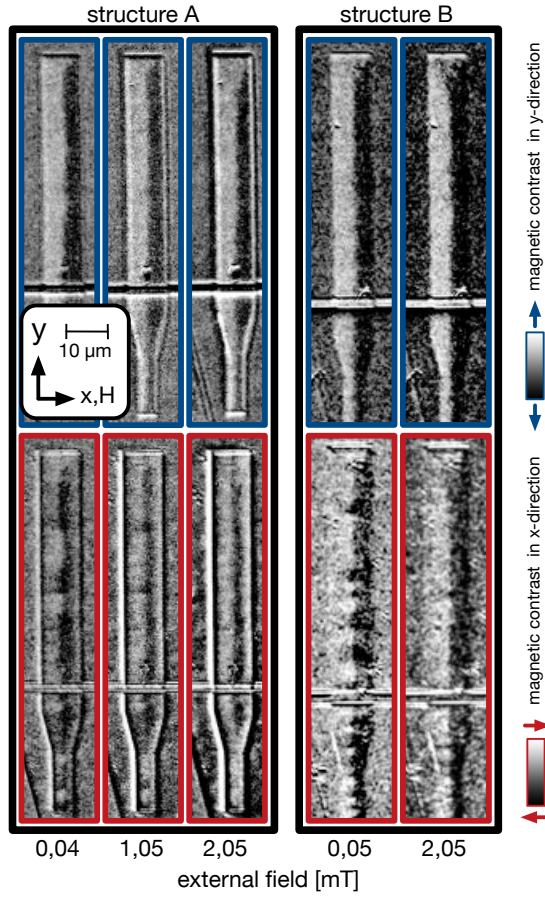


Figure 4.11: Variation of the remanent state with cross-tie-domain wall structure by applying fields along the short axis (x -direction) for two different structures referred to as structure A and B. The Dual-Kerr micrographs are separated by the direction of the magnetic contrast (y -direction in top panel, x -direction in bottom panels). In the top panel the two oppositely magnetized domains are seen (black-to-white contrast). In the simultaneously recorded bottom row vortices and anti-vortices can be visualized as well as their partial annihilation.

structure B exhibits less vortices when a field of 2.5mT is applied along the short axis (bottom right part of the graphs). This is accompanied by a slight reduction in contrast, which could indicate a tilting of the domain magnetization towards the field direction softening the wall.

Figure 4.12 **a** now presents the experimentally detected intensity of the channeled spin-wave modes of 600 MHz in $1\mu\text{m}$ distance to the antenna for different field strength between -2 and 2 mT. An increase in channeled spin-wave intensity is observed for only one of the field polarities. For the opposite field direction the spin-wave intensity is either reduced or detection of channeled spin-wave propagation was not possible. This agrees with the previous assumption, that the spin-wave spectrum in the domain wall depends on the external field and that the wall is contracting or broadening depending on the field polarity. When recording the spin-wave propagation by μBLS , the intensity-decay away from the antenna did not resemble a clear exponential decay or reveal an increased decay length. This is exemplarily shown by a measurement for a spin-wave frequency of 600 MHz as presented in 4.12 **b**. Future studies are needed to explore the possible control over the operating spectra of domain wall channels by small fields and for answering the delicate question of field dependence of the decay length. The impossibility to enhance the spin-wave decay length with this approach on these structures imposes the interesting challenge, if other means can be found to reduce the cross-tie formation and reduce the density of propagation hampering vortex anti-vortex configurations. A promising and simple way to suppress their formation is the reduction

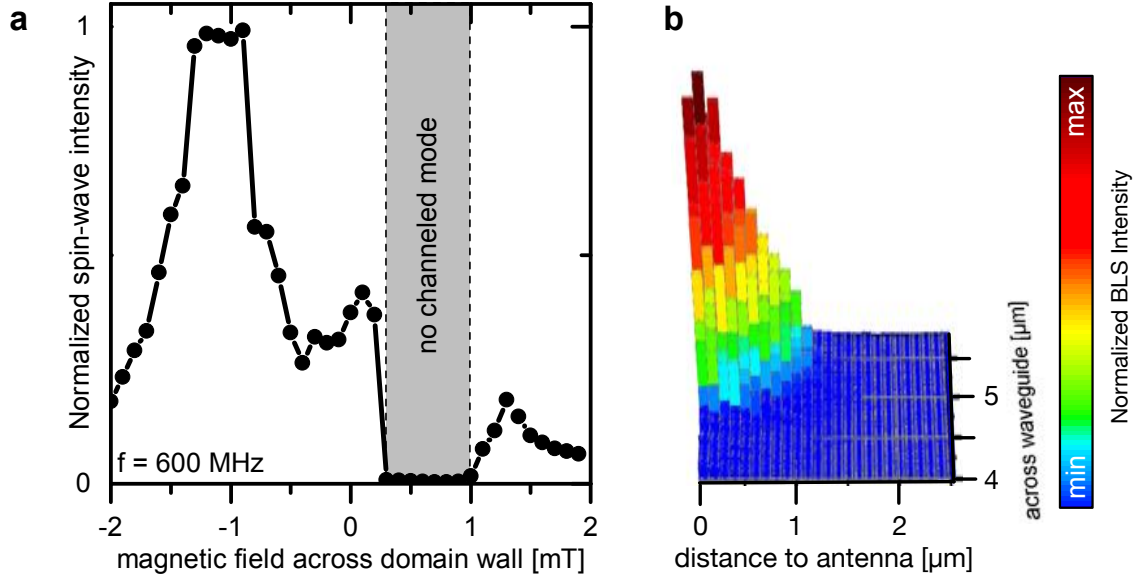


Figure 4.12: **a**, Normalized experimentally recorded spin-wave intensity for a frequency of 600 MHz integrated across the domain wall nanochannel, when subjected to small external magnetic fields along the short axis of the structure. The integrated intensities across the structure are normalized to the elastically scattered reference laser-light for comparison. **b**, Spatially mapped spin-wave intensity for an external field of -1.1mT. No clear exponential or enhanced propagation of the channelled spin waves is observed.

of the sample size in particular the microstructure thickness and recommended to be pursuit in future research.

4.1.1.7 Non-reciprocity of spin-wave propagation

For completeness, the non-reciprocity of the dispersion relation for domain walls and domains is briefly described in the sense of any change in propagation characteristics when inverting the spin-wave vector (and hence opposite propagation direction of the spin waves.) A more detailed analysis can be found in the co-authored publication [O1]. As can be seen from the simulated snapshots for lower spin-wave frequencies (figure 4.6), the symmetry with respect to mirroring the y-axis is broken. The underlying reason is the chirality of the domain wall, which breaks the symmetry in the magnetic texture itself and is also represented by the position of the vortex core and its vorticity (here situated on the upper of the two domain wall junctions). This curling of the magnetization leads to a situation, where the spin-wave wave vector encloses a different angle with the magnetization at the side of the domain wall for opposite travel directions. Since their dispersion relation is inherently anisotropic (section 2.2.1) this is expected to result in different transport properties depending on the travel direction along the wall or domain. As can be seen

from the dynamic response (for instance for 2.16 GHz of excitation frequency) "v-shaped" unidirectional phase fronts emerge. In this respect the spin-wave propagation in the domains differs depending on the travel direction. However, for the channeled spin-wave modes within the domain wall, reciprocity is found regarding the dispersion relation [O1]. This is in contrast to the observed non-reciprocity according to simulations from Garcia-Sanchez [26] where the interfacial DMI additionally broke the symmetry.

4.1.2 Spin-wave dynamics of 90° Néel walls in square elements

In this section, the magnetic remanent configuration and resulting spin-wave dynamics of thin film square elements based on $\text{Ni}_{81}\text{Fe}_{19}$ is investigated. Similar to the rectangular case the spin-wave transport is analyzed both experimentally and by micromagnetics. Even though the geometry has only been slightly changed from rectangular to square structures, the important key difference is that in the square geometry the 90° domain walls nucleating at the corners are better defined and easier to study in contrast to the 180° domain walls running along the middle of elongated rectangular structures. Due to the closeness to the previous investigation for the rectangular geometry, the focus is put on the differences and additional observations for this slightly different wall and potential well, such as results for non-linear excitations at large angle precessions and possible higher order modes.

4.1.2.1 Magnetic configuration and domain wall formation

For the study, 40-nm-thick $\text{Ni}_{81}\text{Fe}_{19}$ structures of square geometry with different side length of 4 μm up to 20 μm were fabricated by electron beam lithography (EBL, see section 3.1). A SEM micrograph of a structure with a side-length of nominally 12 μm is shown in Fig. 4.13 **a**. For active excitation of spin-wave flow, additionally a 100-nm-thick Au antenna was fabricated over one of the square corners in a second step. Following the approach for the rectangular structures (section 4.1.1.1), an alternating decaying magnetic field was applied along the square's diagonal to initialize the magnetic configuration in the Landau-state. Subsequently, the remanent state was confirmed by Kerr microscopy (black-white contrast overlay) and substantiated by micromagnetic simulation for this geometry. Additionally, the simulations were used to analyze the expected profile and width of the effective field wells created by the 90° Néel walls. Figure 4.13 **b** presents the Kerr-micrograph and the simulated magnetic configuration together with the effective field wells (bottom). The first notable difference of the 90° Néel walls in square structures with respect to the 180° Néel walls, is that the effective field well depth varies with the distance from the vortex situated in the center as shown in Fig. 4.13 **c**. This variation in the effective field well depth is expected to result in a variation of the spin-wave spectrum, which suggests wave-vector changes or reduced propagation length for spin-waves traveling along these wells. Another difference to the previously studied case of the 180° Néel walls is the reduction of the total angle and therefore transition between the domains magnetic orientation by 90°. Since the spin-wave dispersion is strongly anisotropic, the additional confinement effect based on the changing angle could be reduced and lead to a slightly larger FWHM of the channeled spin-wave modes and rather smoothed transition between domain and domain wall spectra. The bottom part of Fig. 4.13 **c** shows the effective field well across one domain wall half-way between the vortex and the corner of the structure. The

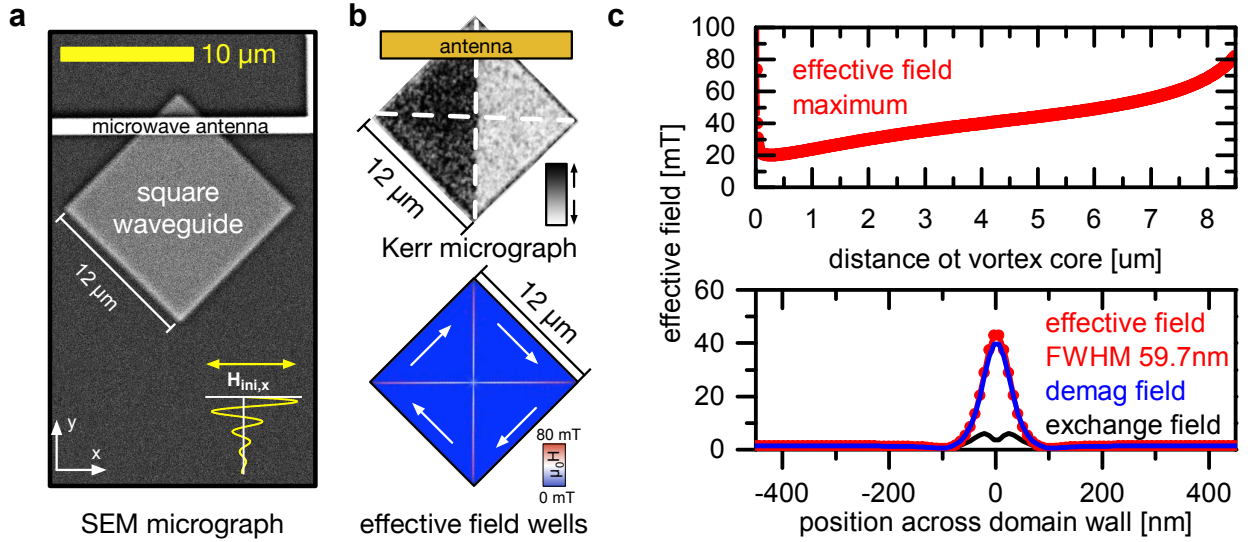


Figure 4.13: **a**, SEM micrograph of the $\text{Ni}_{81}\text{Fe}_{19}$ square and microwave antenna fabricated for external excitation of spin-wave dynamics. An exponentially decaying magnetic field H_{ini} is applied along the diagonals of the square to initialize the domain configuration (depicted in inset). **b**, Top part: Kerr micrograph with magnetic contrast along y-direction (black-white). A Landau-state is observed with four 90° Néel walls forming along the diagonals of the square structure. Bottom part: Micromagnetic simulation of the domain configuration in a corresponding $\text{Ni}_{81}\text{Fe}_{19}$ square together with the magnitude of the effective field (blue-white-red color), revealing the potential wells situated at the domain walls and the vortex-core in the center of the structure. White arrows give the magnetic orientation of the domains. **c**, Top graph: Effective field maximum along the domain wall as a function of the distance to the vortex core. The field well depth varies almost steadily from 20 mT to 80 mT with increasing distance. Bottom graph: Effective field well profile across the 90° Néel wall in half the distance between the center and corner of the square structure ($4.25 \mu\text{m}$) is shown. The effective field well (red dots) is well approximated by a Lorentzian profile (red line) with FWHM $\approx 60 \text{ nm}$. Visualization of the demagnetization field (blue line) and exchange field (black line) reveals the dominant contributions of the dipolar interaction for the formation of these potential wells.

well-profile (red dots) is well approximated by a Lorentzian profile of 59.64 nm FWHM (red line). As for the 180° Néel walls in the rectangular geometry the field well is dominated by the dipolar contributions, while the exchange field plays only a minor role.

4.1.2.2 Thermal spin-wave spectrum

Following the study on the 180° Néel wall (section 4.1.1.2), the spatial dependence of the thermally excited magnetic spectrum across the 90° Néel wall was investigated by μBLS . As discussed for the 180° case, this is complementary to excitation of spin-wave dynamics by an antenna, since the purely thermal excitation excludes distortions present in active excitation efficiencies, such as

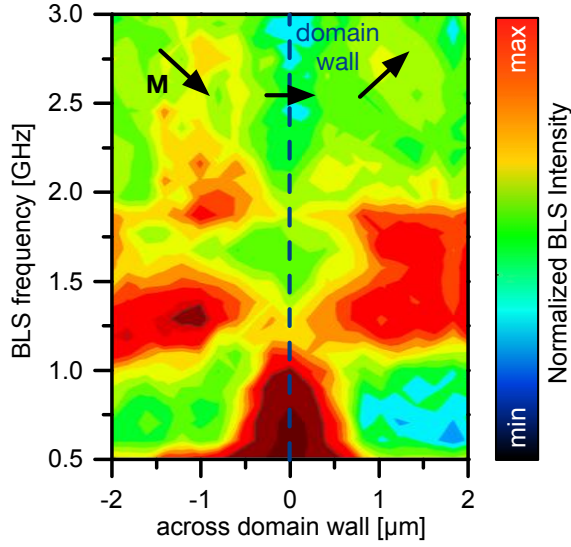


Figure 4.14: Spatially resolved thermal spin-wave spectra recorded by μ BLS across the 90° Néel wall. Magnetic configuration and domain wall position indicated by black arrows and blue dashed line, respectively. Reduced frequencies at the domain wall position are observed, while the frequency onset of the domain spectra is around 1.25 GHz. For the domain wall, the spin-wave signal is found to increase with decreasing frequency down to the experimentally accessible lower limit of 0.5 GHz.

pumping field geometries. Figure 4.14 displays the μ BLS-intensity recorded across the domain wall at $1\ \mu\text{m}$ distance to the in-active antenna in the corner of the square structure. Note, that the frequencies of the spectra are strongly reduced in the center of the structure compared to its surrounding. This correlates well to the expected domain wall position and previous observations. Firstly, the data indicates that the frequency onset of the domains is around 1.25 GHz and due to quantization will depend on the exact wall position. Secondly, for spin waves with frequencies below that onset dynamics are only contained within the domain wall spectrum, suggesting already spin-wave propagation confined to the domain wall. For instance, this can be seen from the spatial spin-wave profile across the domain wall, when considering the recorded spin-wave intensity for a constant frequency of 0.6 GHz. Furthermore, a rather smooth adoption of the spin-wave spectra of domain wall and domains is observed experimentally at the sides of the wall. This is most likely attributed to the reduced total rotation of the magnetization of 90° , which could allow additional confined modes in the effective field gradients at the side, as will be discussed in the presence of active excitation at higher pumping powers.

4.1.2.3 Direct excitation of spin waves

A 100-nm-thick Au microwave antenna was patterned on top of one corner of the square structure (see Fig. 4.13 a). Figure 4.15 shows the spin-wave intensities measured by μ BLS in $1\ \mu\text{m}$ distance to the exciting antenna in one domain (black triangles) and on the domain wall (blue dots). For comparison, each spectra has been normalized by the number of scans. Subsequently, the domain spectra was multiplied 20 times for better visibility. The recorded spectra are in good agreement with the thermally detected spin-wave spectra from before and confirm again, that despite the small domain wall “volume”-part compared to the domains, efficient excitation and detection proved possible for the nano channel, attributed to its preferred magnetization orientation. The

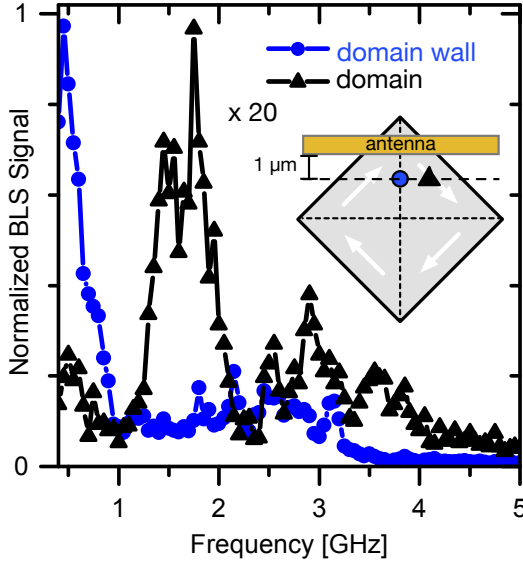


Figure 4.15: Spin-wave excitation efficiency of the 90° Néel wall (blue dots) and surrounding domain (black triangles) for a nominal microwave power of $P = -1$ dBm recorded by μ BLS. Inset: Schematic of measurement position (black and blue markers) and microwave antenna. Besides the measurement position identical conditions are chosen. Good agreement with the previously recorded thermal spectra is observed.

reduced spin-wave intensity in the domains is believed to be associated with the lowered group velocity (and, hence, less spin-waves propagating into the measured region) and reduced excitation efficiency by the antenna for the magnetic orientation in the domain.

4.1.2.4 Simulated spin-wave dispersion of 90° Néel walls

In this section the focus is put on spin waves which travel confined to the effective field well formed by the 90° Néel walls. The discussion starts by micromagnetic analysis of a simulated square structure of $12\ \mu\text{m}$ side length in the Landau-state. A Gaussian field pulse identical to the approach already described in section 4.1.1.5 is utilized to investigate the spin-wave dynamics. This localized excitation field was positioned on one end of the 90° Néel wall nucleated at the corner and the emerging spin-wave dynamics analyzed by Fourier Transformation. The resulting integral power spectra of the whole structure is shown in the left part of figure 4.16 **a**. In the spectrum a frequency gap is observed between 2 and 3 GHz separating the spin-wave dynamics into two branches. Additionally, a schematic of the simulation geometry and ROI used (dashed line) for the magnetization snapshots given in 4.16 **b** is shown. The right part of Fig. 4.16 **a** then presents the dispersion relation.

The dispersion has been derived identical to the rectangular case (section 4.1.1.5), using the the dynamic out-of-plane component (δm_z) of spin waves connecting the spin-wave frequencies with their wave vector k along the domain wall channel (yellow line along square-diagonal shown in inset). The two different branches are found to have a linear dispersion with typical group velocities of $2.82\ \mu\text{m}/\text{ns}$ for the lower frequency branch (up to 2 GHz) and $2.43\ \mu\text{m}/\text{ns}$ for the higher frequency one starting at 3 GHz. Figure 4.16 **b** presents snapshots of (δm_z) for modes of both branches revealing a sub wavelength confinement to the domain wall and a well defined wave

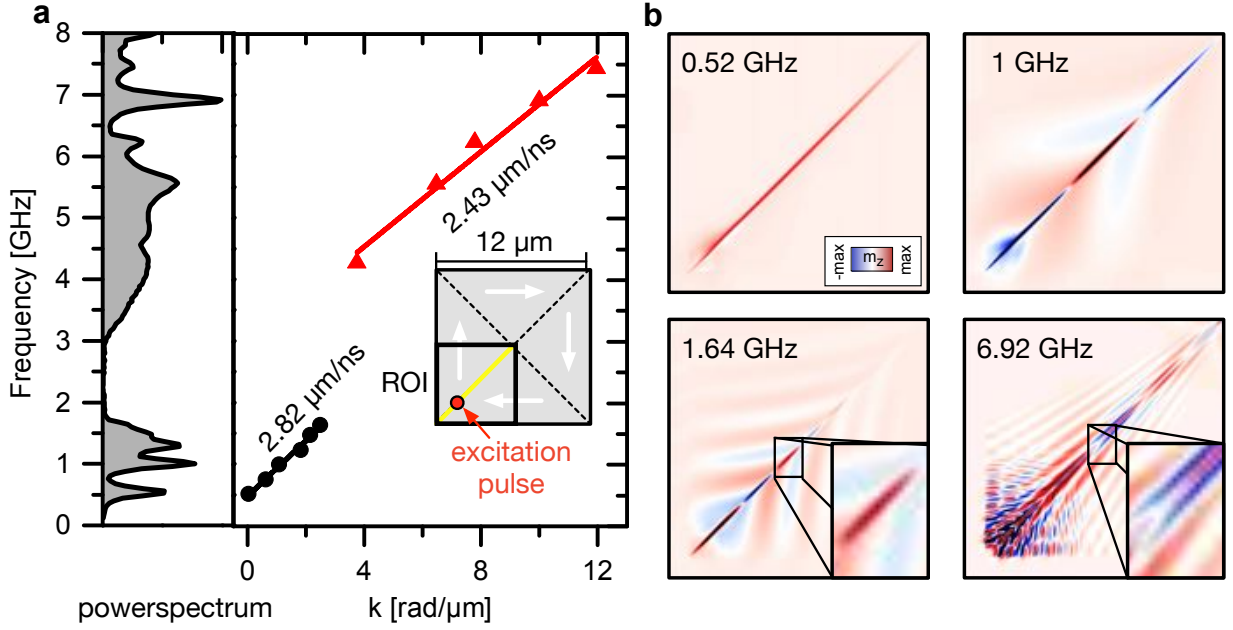


Figure 4.16: Micromagnetic simulation of the spin-wave dynamics for a 90° Néel wall induced by a localized pulsed excitation on one end of the domain wall as schematically shown in the inset of **a**. The magnetic configuration, position of the excitation pulse as well as region of interest (ROI) used for analysis is shown. The left part of **a** presents the integral power spectra of the whole structure. A frequency gap located between 2 and 3 GHz is observed, separating the spin-wave dynamics into two branches. The right part of **a** shows the extracted dispersion relation connecting the spin-wave frequency to the wave vector along the domain wall k . A linear dispersion with group velocities of $2.82 \mu\text{m/ns}$ and $2.43 \mu\text{m/ns}$ for lower and upper branch are found, respectively. **b** Spin-wave profiles for both branches, visualized by snapshots of the dynamic out-of-plane component (δm_z), revealing their transversal confinement to the domain wall and well defined wave vector along the channel direction.

vector along the channel direction. The small wavelength “wiggles” for 6.92 GHz near the source-point (bottom left corner) are assumed to originate from numerical artifacts connected to the increasing frequency. However, it seems likely that their presence alters the channeled spin waves and their dispersion relation only to a minimal extend, so that the simulations still allow to capture the main characteristics and confinement of these higher frequency spin waves. To illustrate the qualitative difference of the modes of these two branches for the spin-wave frequencies of 1.64 GHz and 6.92 GHz a small part of the snapshot at the domain wall position is magnified and presented in the lower right corner, revealing a rapid variation of the spin wave along the confinement direction. This will be discussed more deeply in comparison with the experimental data in the later section 4.1.2.6, while in the next section the channeled propagation in the lower frequency branch is demonstrated experimentally.

4.1.2.5 Spin-wave propagation along 90° Néel walls in the linear regime

To experimentally probe the channeled spin-wave propagation within 90° Néel walls, the spin-wave intensity is recorded for an excitation frequency of 0.5 GHz, across the square structure, as shown in Fig. 4.17. The inset gives a schematic of the measurement positions, for the line profile in 1 μm distance to the antenna shown in **a** (along black dashed line), as well as for the spatial map in **b** (blue rectangular overlay). The experimentally recorded spin-wave intensity (red dots) shown in Fig. 4.17 **a** is well reproduced by a Gaussian of 368 nm FWHM (red line). Additionally, the simulated effective field well together with the simulated intensity profile (represented by the squared dynamic out-of-plane magnetization) of the channeled spin-wave mode of frequency 0.5 GHz are presented. Direct comparison of effective field well and simulated intensity suggests almost identical FWHM ≈ 55 nm with only slight deviations of their respective profiles at the side of the wall of the wall.

As discussed for the measurements on the 180° Néel wall, the experimentally recorded μBLS signals is a convolution of the spin-wave intensity with a set-up specific detection function. The FWHM of this detection function was determined to be $340 \pm 10\%$ nm (section 3.5.1), so that the

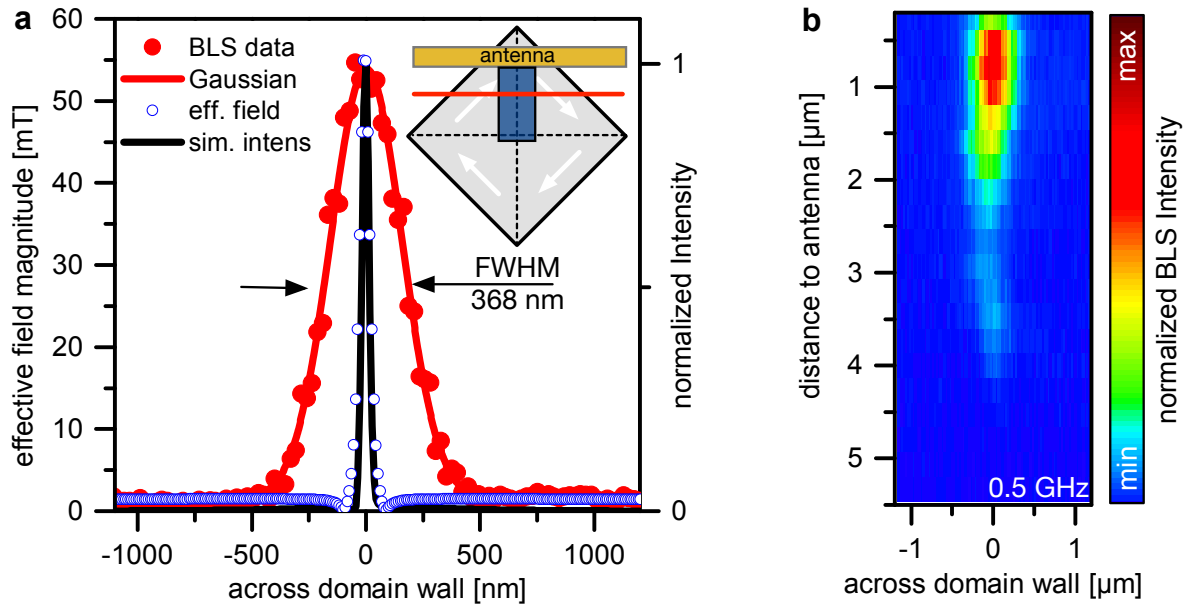


Figure 4.17: **a**, Simulated spin-wave intensity profile (black line) together with the simulated effective field well (blue dots) with FWHM = 55 nm. Additionally, the experimentally recorded spin-wave intensity profile (red dots), and corresponding Gaussian profile (red line) of increased FWHM of 368 nm, measured in 1 μm distance to the exciting antenna (inset red line) is shown. **b**, Two-dimensional spin-wave propagation away from the exciting antenna measured in an area sketched in the inset of **a** (blue rectangle). A confined spin-wave beam along the domain wall channel is observed.

FWHM of 368 nm lies within the accuracy of the set-up. Hence, a confinement to a few tens of nanometers or less can also be concluded for this type of wall channel. Nevertheless, since for the 180° wall a FWHM of 340 nm was observed, this measurement might indicate a broader channel for the 90° case.

The channeled propagation can be more clearly seen in the spatial map presented in Fig. 4.17 **b**. Surprisingly a slight increase in the spin-wave intensity is observed in this particular experiment at around $3.5\ \mu\text{m}$ instead of the simple expected exponential decay of the spin-wave intensity with increasing distance to the antenna. A possible explanation for this observations, could be attributed to excitation of spin-waves at the position of the vortex core, which is outside the region of interest and standing wave formation on top of an exponential decay. This hypothesis would imply, that the antenna's Oersted field is able to induce gyrotropic motion on the vortex-core possibly by domain distortion or domain wall displacements. However studying this effect in more detail is beyond the scope of this thesis, but hints on spin-wave excitation in the domain wall channel by vortex gyration.

When taking a closer look at the propagation path, also a slight “kink” situated around $2.9\ \mu\text{m}$ distance can be seen. This could be considered as the result of laser dragging of the domain wall (discussed in section A.3 in the appendix), when scanning the laser spot over the domain wall and, thereby, influencing the wall position as well as the resulting spin-wave propagation. This also allows for an alternative explanation, that the standing-wave formation is observed, due to the presence of a “barrier” for the spin-wave flow at a distance around $4\ \mu\text{m}$. Such a “barrier” could be formed by pinning sites or kinks of the domain wall or the intrinsic variation of effective field well depth towards the vortex core (as shown in figure 4.13 **c**) resulting in reflection.

For future experiments the author recommends to measure the spin-wave flow within the domain wall near the vortex on the opposite side to the exciting antenna to investigate possible spin-wave excitation from the vortex core.

4.1.2.6 Non-linear spin-wave transport and higher harmonic generation

To study the non-linear spin-wave spectra and mode profiles in the presence of a 90° Néel wall μ BLS-experiments at higher pumping powers and larger precession angles of the magnetization dynamic were performed. In the non-linear regime several effects, such as higher harmonic generation and magnon-magnon-interactions occur (see section 2.2.2). This is a first investigation of the additional possibilities and limitations of the spin-wave transport along domain walls introduced by non-linear effects. An additional class of spin-wave mode, which can not be excited directly is observed connecting excitation power with distinct localization and frequency of the excited spin waves. Complementary to the observed non-linearities in the domains at the example of parametric pumping and second harmonic generation (section 4.1.1.4), here the non-linearity of the domain wall channel is assessed.

In contrast to the previous measurements, the studied square has an extended side length of $20\ \mu\text{m}$, which was explored to investigate channeling by domain walls also in larger geometries. For higher pumping powers additional spin-wave signals emerged at frequencies distinct from the excitation frequency defined by the microwave source, which are attributed to higher harmonic generation. To start the discussion an exemplary recorded μ BLS-spectrum, when channeled spin waves of $0.5\ \text{GHz}$ are directly excited, is presented in Fig. 4.18 **a** on a logarithmic intensity scale. A distance of $0.2\ \mu\text{m}$ was chosen to the exciting antenna and several spectra were integrated across the domain wall channel for a microwave power of $0\ \text{dBm}$. Pronounced spin-wave intensities appear at twice ($1\ \text{GHz}$, second harmonic generation, SHG) and thrice ($1.5\ \text{GHz}$, third harmonic generation, THG) of the excitation frequency. Figure 4.18 **b** shows the spatial dependence of this higher harmonic generation process. The data reveals a distinct localization for the direct ($500\ \text{MHz}$) and SHG ($1\ \text{GHz}$) and THG ($1.5\ \text{GHz}$), when scanning across the domain wall channel.

Identical measurements were performed for a range of excitation frequency ($0.4\ \text{GHz}$ up to $3.5\ \text{GHz}$) across the domain wall channel for nominally constant power covering also higher frequency modes. From each of these measurements the spin-wave intensities have been extracted for $0.5\ \text{GHz}$ -wide windows around the excitation frequency and twice this frequency for the SHG. The resulting spin-wave signals arising only from the direct excitation are shown in Fig. 4.19 **a**, separate to the indirectly excited SHG contribution presented in **b**. Focusing first on the directly excited modes in the low frequency regime below $0.7\ \text{GHz}$ (bottom part of Fig. 4.19 **a**) as for the previously presented cases the channeled mode with a Gaussian profile is observed. As expected with increasing excitation frequency the signal intensity reduces until it almost vanishes for frequencies close to $1\ \text{GHz}$. However, interestingly for higher frequencies it reappears with different spatial modulation exhibiting mainly three intensity maxima until the situation becomes more elusive for frequencies above $2.5\ \text{GHz}$, either showing two or one maxima. Such an observation is somewhat similar to geometrical spin-wave confinement in transversal waveguides [229].

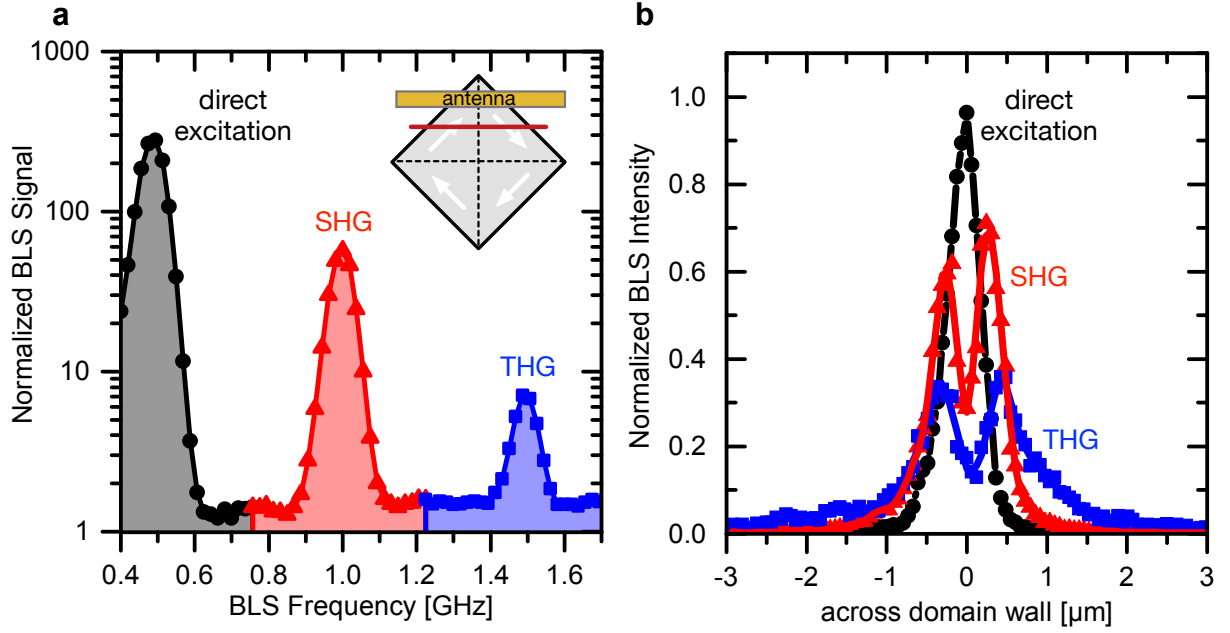


Figure 4.18: **a**, Experimentally recorded spin-wave excitation efficiency integrated across the domain wall (red line in the schematic shown in inset). Next to the directly excited channeled spin waves of 0.5 GHz, simultaneously higher harmonic generation resulting in spin-wave signal-intensities at 1 GHz and 1.5 GHz is observed. **b**, Corresponding intensity profiles, when scanning across the domain wall. The detected spin-wave signals are separated by their spectral contribution to the total recorded spin-wave intensities and individually plotted for the direct excitation (black dots), second harmonic generation (SHG, red triangles) and third harmonic generation (THG, blue squares).

Despite this similarity, the situation here is more complex, since the spin waves are bound to the effective field well created by the domain wall combining magnetic charges and rotation of the magnetization. Pinning conditions and confinement effects for this situation of simultaneously acting effective field gradients and magnetization rotation are to the authors knowledge not included in the present theories. Additionally, as indicated by the previously presented experiments, these boundary conditions seems to be frequency dependent.

Nevertheless, it seems reasonable to assume an asymptotically similar behavior to a transversally magnetized waveguide the sharper the effective field well and rotation become. This agrees with the rather smooth variation of the spectra in the thermal measurements from Fig. 4.14, and formation of transversal standing spin-waves similar to a waveguide behavior. For this reason, in the following discussion these channeled spin waves are indexed by their “quantization” transversal to the domain wall channel as first order (one maxima), second order (two maxima) and third order (three maxima) modes. That only first and third order modes are observed in the direct excitation can be attributed to the pumping field geometry, which is homogeneous across the channel and can, therefore, only couple to uneven modes. This is in agreement with the possibility to excite

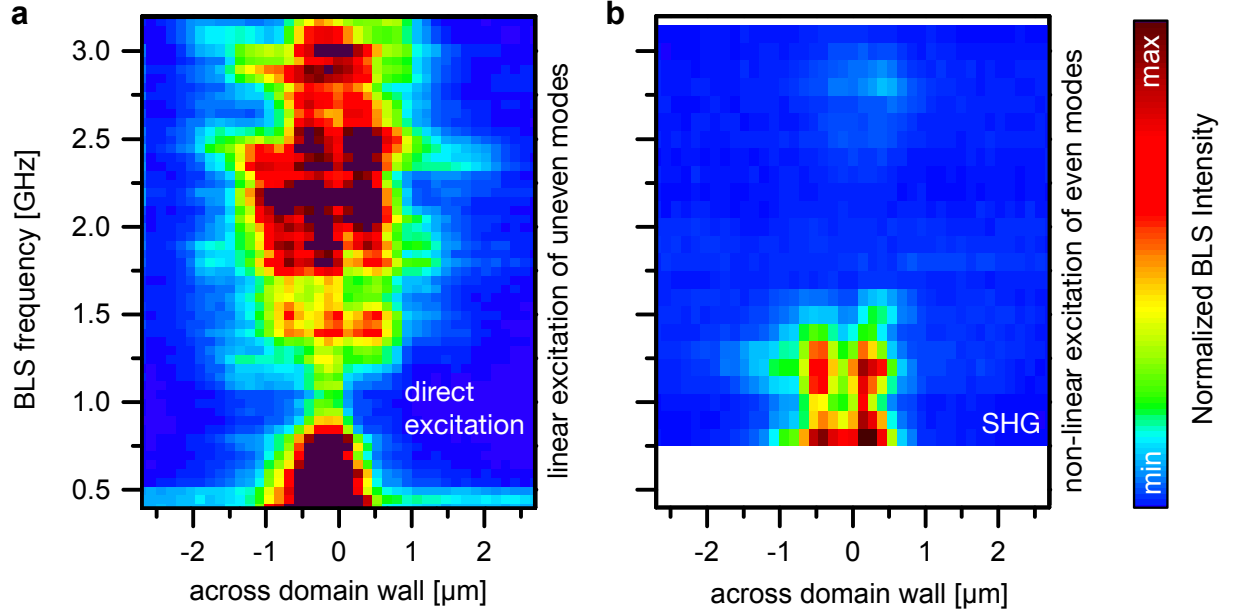


Figure 4.19: **a**, Spin-wave intensity-profiles across the domain wall as a function of the excitation frequency in $0.2\ \mu\text{m}$ distance to the RF-antenna. The intensity profile of the directly excited spin-wave modes reveal the channelled mode with Gaussian profile in the low frequency regime below $0.7\ \text{GHz}$, as demonstrated before. For a frequency around $1\ \text{GHz}$ a “gap” in spin-wave excitation is found, while for higher spin-wave frequencies 3 intensity maxima across the channel are observed. **b**, Simultaneously recorded spin-wave intensities arising from second harmonic generation (SHG). Two intensity maxima in the frequency gap for the direct excitation around $1\ \text{GHz}$ is observed.

additional even modes by the second harmonic (SHG) shown in Fig. 4.19 **b**. Here, located in the low intensity regime between the first and third order mode from the direct excitation, two intensity maxima corresponding to the second order mode are found, overlapping partially in frequency with the first and third order modes. Importantly, the observation, that the frequencies of the modes of different order overlap (simultaneous excitation for identical frequency but different transversal quantization), confirms the existence of spin-wave branches for each transversal confinement. Otherwise only discrete frequencies and no overlap would be expected, hence, indicating that different wave vectors along the nano channel and propagation direction are allowed for each branch. This marks a clear distinction to models based solely on domain wall resonance in contrast to channelled transport substantiating the different character of the propagating mode.

To further shed light on this first observation of these type of modes, the simulation of the dispersion relation for a $12\ \mu\text{m}$ side length square is revisited. In the simulation also two frequency branches along the domain wall channel were observed (Fig. 4.16), raising the question on comparison of their nature and transversal confinement. Figure 4.20 presents the simulated intensity profiles for the upper and lower frequency branch for exemplary frequencies of $1.64\ \text{GHz}$ and

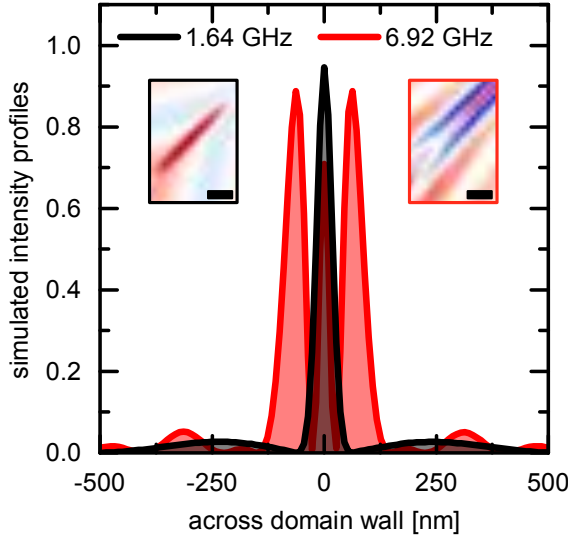


Figure 4.20: Spin-wave intensity profiles across a 90° Néel wall for upper (red line) and lower frequency branch (black line) as derived from micromagnetic simulations. Snapshots of the dynamic magnetization in a small region around the domain wall are shown as insets (200nm black scale-bar). The different mode character is seen by their distinct transversal quantization across the domain wall, exhibiting either one intensity-maxima (black line, lower frequency branch, 1.64 GHz) or three intensity maxima (red line, upper frequency branch, 6.92 GHz).

6.92 GHz. As in the experiment, in the simulations they exhibit 3 maxima, third order mode, for the upper frequency branch and a single one, first order mode, for the lower frequency modes and are confined to the domain wall channel. As an important difference to the experiment, in the simulation a pulse of even field symmetry (gaussian) is used to excite spin-wave dynamics of small-angle deflections in the linear regime. Therefore, in the simulations only the first and third order modes of the domain wall are excited, while coupling to the second order modes is expected to be only accessible by non-linear scattering in the experiments performed in the non-linear regime. That the spin-wave mode with 2 intensity maxima can not be excited directly, agrees well with the hypothesis of the second order transversally confined mode of the domain wall channel or two separate channels at the side of the domain wall, which are optically coupled. The observation, that the experimentally detected second order spin-wave branch lies between the first and third order branches in the experiment suggests, that the “frequency-gap” in the simulated dispersion relation is attributed to this second order branch of modes propagating confined to the domain wall.

However, even though a satisfactory qualitative agreement of simulation and experiment of higher order domain wall modes is found, where in both cases transversal spin-wave profiles with 1 and 3 maxima for lower and upper frequency branch and a “gap” in the regime of the even modes between them is observed, quantitative agreement is not observed. While the third order branch in the experiment has a lowest frequency of around 1.25 GHz and the spacing of the 3 spin-wave intensity-maxima is around 550 nm (see Fig. 4.19 a), in the simulation this frequency-onset is around 3 GHz and the spacing of the maxima is only 63 nm. This spacing is well below the FWHM of the detection function (section 3.5.1) and corresponding Rayleigh criteria for the μ BLS set-up and, therefore, would be expected to be not accessible.

Nevertheless, there are candidate reasons for quantitative differences between simulation and experiment. The main points to consider are the different side length (domain size) of the structure

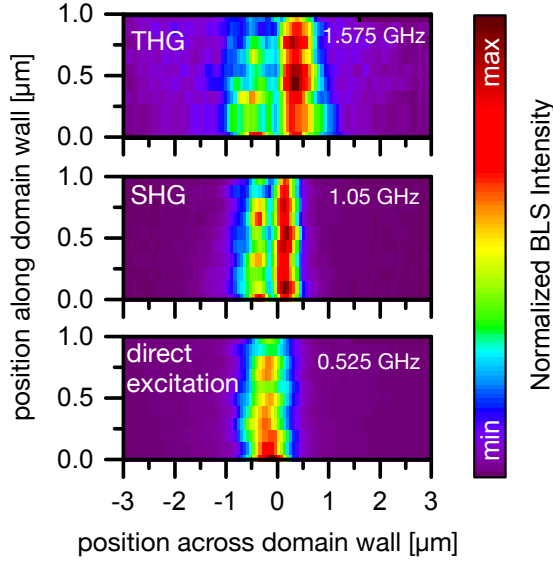


Figure 4.21: Two-dimensional μ BLS-measurement of the directly and indirectly excited spin waves for an excitation frequency of 0.525 GHz. The antenna is situated at the bottom of the intensity maps. The simultaneously recorded different spectral contributions are separated for the direct excitation (bottom graph, 0.525 GHz), second harmonic generation (middle graph, 1.05 GHz) and third harmonic generation (upper graph, 1.575 GHz). Two guided spin-wave beams of different intensity at the side of the domain wall are excited by the higher harmonic generation process.

and deviations between the magnetic parameters used in the simulation and in the real sample. Even though the domain size is not expected to influence the domain wall character strongly (such as its width), the domains onset-frequency will depend on its size and decrease for larger domains. This lowers the domain spin-wave spectrum in frequency for the experimentally studied larger square with respect to the simulation (in agreement with the thermal measurement, Fig. 4.14) and decreases channeling capability due to the reduced frequency-gap between domain wall and domain spectra. This also agrees well with the reduced domain onset frequency in the experiment. As the next candidate reason variations in the magnetic parameters would change the domain wall width and, hence, also width of the channeled propagation. This also suggests that heating by the probing laser spot might contribute to widening the domain wall and local change of the magnetic parameters in the measurement scenario (e.g. reduction of the saturation magnetization results in an increase in wall width).

Investigation on the propagation characteristics of these modes presented in the following shows that the current hypothesis needs to be extended, as discussed next. To study the propagation of the non-linearly excited modes the spin-wave flow is recorded by μ BLS for an excitation frequency of 0.525 GHz away from the exciting antenna for the direct excitation, second harmonic (SHG) and third harmonic generation (THG) simultaneously. The recorded spin-wave intensity is shown in Fig. 4.21. As before, the first order channeled spin wave is directly excited and for the indirectly excited second harmonic (SHG), the main intensity is found in two spin-wave beams which remain guided at both sides of the domain wall, agreeing with a second order mode. However, surprisingly, also 2 intensity maxima, but with an increased spatial spacing are observed for a frequency of 1.575 GHz for the THG. Such an increase is not expected from simply transversally quantized modes. Moreover, for both the SHG and THG a pronounced asymmetry in intensity is observed.

These experiments point towards an additional influence of the domains on the channeled transport more complex than for transversal waveguides. Both of which could potentially be attributed to mode hybridization of the channeled modes with the domain modes. Since the domains are likely to differ in size, they would also exhibit a different spectral separation to the channeled modes and, hence, degree of hybridization. This would then be reflected in the asymmetry of the intensity profiles. Furthermore, the increased spacing of the two intensity maxima for the THG (1.575 GHz) would agree with this hypothesis. This is due to the fact, that the channeled modes of higher frequency are spectrally less separated to the domain spectra and, hence, expected to shift their localization towards the domain (right channel in the THG process in Fig. 4.21). It is stressed here, that for the same frequency of 1.575 GHz the directly driven spin-wave mode exhibits 3 intensity maxima (see Fig. 4.21 **a**). This further marks the differences in the directly and indirectly excited modes, which exhibit different localization and a frequency overlap of their respective branches. The third hypothesis, that channeled spin wave modes are subjected to a non-linear frequency conversion and radiate out of the potential well between domain and domain wall can very likely be excluded here, since one would assume the main intensities in the middle of the channel for the direct excitation as well as SHG and THG.

To summarize: To the author's knowledge, this is the first time, that such modes guided along the sides of domain walls have been observed either experimentally or by simulation. It remains intriguing for future studies to question their nature and test whether they are related to the following hypothesis: 1) hybridization between spin-wave modes of the domain and domain wall channel; 2) softened quantization in an (asymmetric) effective field well or 3) non-linear frequency conversion effects. A promising way to start such investigations is to utilize asymmetric out-of-plane or in-plane dynamic fields to excite and analyze the anti-symmetric spin-wave response. This could be studied in their relation to varying the magnetic parameters and, therefore, domain wall width (for the quantization condition) as well as differing domain sizes, resulting in shifted domain spectra influencing hybridization with the domain wall modes. As a last remark on this, it should be noted, that the observations in microstripes [117] showed second harmonic generation of two optically coupled spin-wave beams by a directly excited single spin-wave in the center of the wire. The results of similar, but macroscopic observation, were interpreted by second order transversally confined spin-wave modes. However, these two beams contracted with propagation distance towards the center of the wire, which can not be explained solely by this explanation. This indicates also some "guidance" of the second harmonic generation by the direct excitation beam, rendering this phenomenon an interesting topic, which may also apply to general waveguides.

4.1.3 Spin-wave dynamics of interconnected Néel walls in Fe wires

In the following section, the spin-wave dynamics in a 9.4- μm -wide, 80- μm -long and 20-nm-thick rectangular element made out of crystalline Iron (Fe) grown on MgO(001) is investigated. Compared to the previously discussed domain walls in the $\text{Ni}_{81}\text{Fe}_{19}$ microstructures, different domain wall characteristics are expected for this material system due to the higher saturation magnetization of Fe and presence of additional crystalline anisotropies (section 3.3). Connected to the different material parameter, the domain wall width in these systems, which scales proportional to $(1/2 \cdot \mu_0 M_s^2 + K_C)^{-1/2}$ is expected to shrink and to confine the spin-wave transport to even smaller length scales. Moreover, the gilbert damping induced dissipative losses are reduced compared to $\text{Ni}_{81}\text{Fe}_{19}$ and the crystalline anisotropy blue-shifts the domain-spectra to higher frequencies. This separates domain and domain wall dynamics in frequency, easing experimental observations on the individual dynamics and increases the frequency range of the channel and spin-wave decay length. Since the underlying principle arguments and hypothesis about this channeled transport have already been discussed, this section focuses on the observed differences and the experimental recorded spin-wave propagation in different domain wall patterns.

As a starting point, Fig. 4.22 **a** presents a microscope image of the investigated Fe wire. The easy axis of the four-fold crystalline anisotropy (sketched by the white arrows in the upper left corner) of the Fe-phase is chosen to coincide with the principal axes of the structure (here referred to as x- and y-direction respectively) stabilizing Landau- oder diamond-like states. Additional meander-shaped Au antennas are patterned on top of the structure allowing to excite spin-wave dynamics, as well as DC contacts at the end of the structure which can be used to traverse currents through the magnetic layer. For orientation, the two antennas (also referred to as antenna A and B)

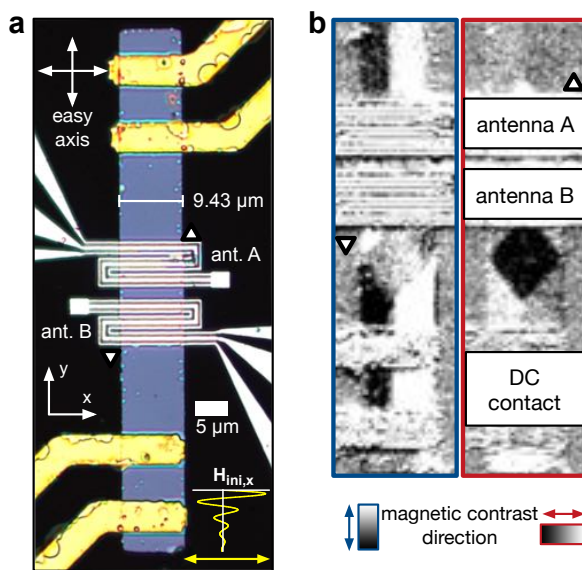


Figure 4.22: **a**, Microscope image of the investigated crystalline Fe wire. The easy axes of the crystalline four-fold anisotropy coincide with the principal axes of the structure as depicted in the upper left corner. A decaying alternating magnetic field (depicted in the bottom right corner) was utilized to set the magnetic configuration. **b**, Dual-Kerr micrograph presenting the simultaneously recorded magnetic contrast along y-direction (left part, blue border) and x-direction (right part, red boarder). For orientation: Upper and downwards pointing white triangles surrounded by a black line are included in **a** and **b**.

are marked with an upwards and downwards pointing white triangle, separating a “top” (upwards pointing triangle), “bottom” (downwards pointing triangle) and “middle” section between the two antennas.

For initialization of the domain state, a decaying alternating field was applied along the short axis of the rectangular element (x-direction) and, subsequently, imaged by Dual-Kerr microscopy as shown in Fig. 4.22 **b** for the two independent magnetic contrast directions. This magnetic state will be referred to as “diamond-state”, where the magnetic orientation is given below the images in black-to-white color for the two contrast directions. The recorded spectra and spin-wave propagation, shown in the following, are able to support the presence of this magnetic state during measurements. It is pointed out, that at the “top” antenna two 90° Néel walls are interconnected to a 180° Néel wall (note the x-direction contrast, revealing the white triangular shaped domain at antenna A). In the “bottom” section a diamond domain, where antenna B extends across one of its tips is observed. As will be indicated by later shown spin-wave intensity measurements in the remaining region between both antenna, four 90° Néel walls are expected to be linked together.

4.1.3.1 Thermal spin-wave spectra in a 180° wall

Prior to active excitation of spin-waves, thermal μ BLS-spectra were recorded across the Fe wire in the “top” part. This is particularly useful, for comparison with the studies of different geometries based on $\text{Ni}_{81}\text{Fe}_{19}$ in the earlier sections, since the thermal excitation is independent of the different antenna design and pumping field geometries. Figure 4.23 presents the measured spectra, while sweeping across the 180° Néel wall in $3.5\ \mu\text{m}$ distance to the top antenna.

The data shows the spin-wave band in the domains, with an onset frequency of around 9.7 GHz and a pronounced local reduction at the domain wall position ($\approx 0.1\ \mu\text{m}$) down to below 3 GHz.

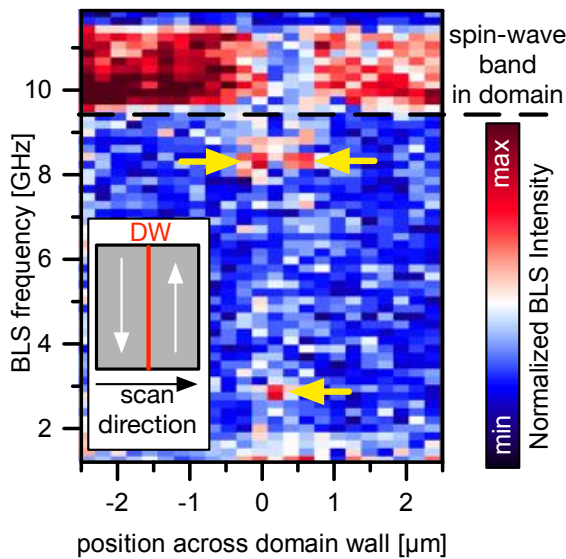


Figure 4.23: Thermally excited spin-wave spectra recorded by μ BLS across the 180° Néel wall in $3.5\ \mu\text{m}$ distance to the top antenna (antenna A). The domain spin-wave band, with an onset frequency of around 9.7 GHz is observed, while at the domain wall position the spin-wave spectra drastically decreases in frequency (position approx. $0.1\ \mu\text{m}$.) down to frequencies below 3 GHz. Additionally, an intermediate spectra is observed next to the domain wall position with an onset frequency around 8.1 GHz.

Interestingly, at the side of the domain wall an intermediate spectra with a distinct onset frequency of around 8.1 GHz (yellow arrows) is observed, which is clearly not a superposition of domain and domain wall spectrum. These intermediate frequencies have neither been predicted or observed so far and seem to favor the hypothesis of hybridization between the domain and domain wall modes resulting in intermediate spin-wave frequencies at both sides of the domain wall formulated in the previous section. Due to the additional crystalline anisotropy in Fe both domain and domain wall modes are blue-shifted in frequency and separated by a wider frequency-gap, when compared to the $\text{Ni}_{81}\text{Fe}_{19}$ -cases (where the onset frequencies are about 1.2 GHz to 2 GHz in the domains).

4.1.3.2 Active excitation of spin wave modes in merging domain walls

Two 120-nm-thick meander-shaped Al antennae (Fig. 4.22 a) were fabricated for local excitation of spin-wave dynamics and to measure the resulting spin-wave transport by μBLS . In contrast to the antenna microstrip-design from the previously presented studies, the meander-shaped antenna's pumping field couples mainly to spin waves with a wave vector of $k_1 = 3.8 \text{ rad}/\mu\text{m}$ (and less pronounced for $k_2 = 1.5 \text{ rad}/\mu\text{m}$), due to the pumping fields periodicity (section 3.3).

Figure 4.24 a shows the recorded spin-wave spectra in $3.05 \mu\text{m}$ distance to the "top" antenna (upwards pointing triangle) close to the previous measurement distance ($3.5\mu\text{m}$) of the thermal line-scan across the structure. The distance was reduced to $3.05 \mu\text{m}$, since for the previously chosen $3.5 \mu\text{m}$ distance to the antenna on the 180° wall only an impractical small spin-wave signal resulting from active pumping could be detected. The main intensities of the domain wall channel at this position are found for 2 distinct frequencies of 1.95 and 3.25 GHz respectively. Close to this position, two 90° Néel walls are interconnected to each other and merge into a 180° Néel wall in form of a domain wall junction in about 3 to $3.5 \mu\text{m}$ distance. This is also indicated by the Kerr-micrographs (see the inset in figure 4.24 a or figure 4.22 b) and can be more clearly seen, when the intensity of channeled spin waves was recorded in a two dimensional area around the antenna having an excitation frequency of 1.977 GHz as presented in Fig. 4.24 b.

The data clearly reveals two confined spin-wave beams, which are attributed to the channeled spin-wave propagation within the two 90° Néel wall. For the following discussion the domain wall positions at the microwave antenna are labeled as point "1" and point "3", and the estimated point of the three linked domain walls labeled as "2" (previous spectrum recorded at this position) as well as the point behind the junction labeled as "4" have been indicated in Fig. 4.24 b. The recorded spin-wave intensity is now analyzed in greater detail, starting with the observations in the measurement. Next to the appearance of two spin-wave beams, a periodic modulation of the spin-wave intensity signal with propagation along the domain wall channels is observed, which suggests interference effect. Moreover, only minimal spin-wave intensity is recorded behind the junction (point 4) and the spin-wave intensity in the left and right 90° Néel wall differ quantitatively and

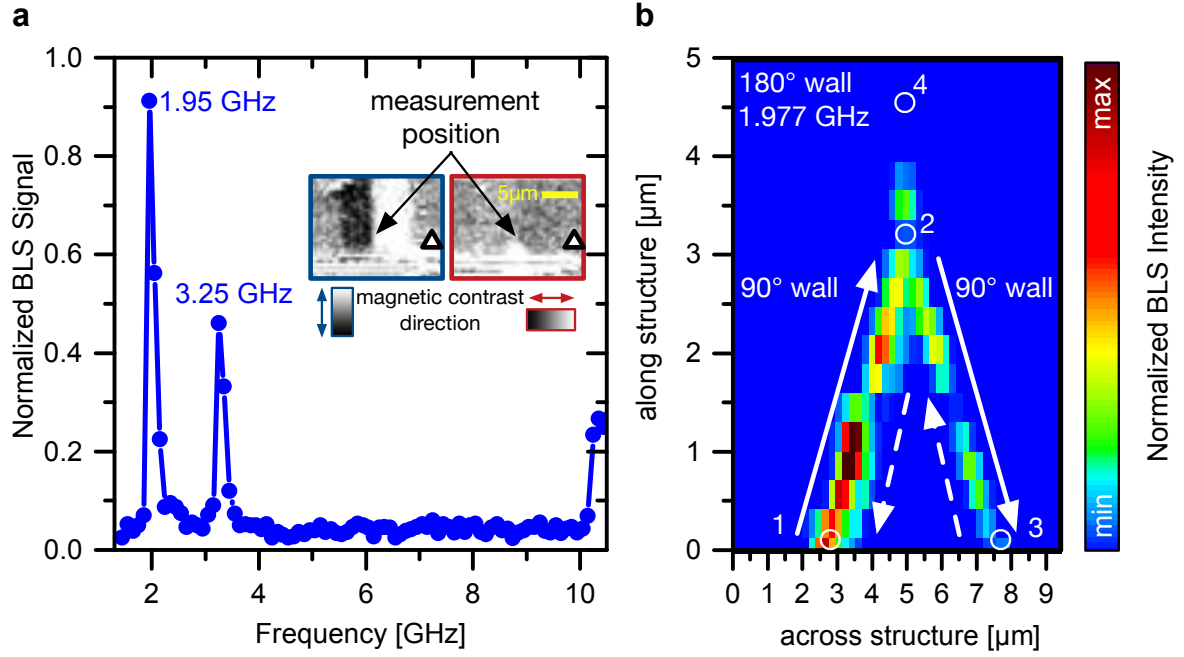


Figure 4.24: **a** Spin-wave excitation efficiency measured in 3.05 μm distance to antenna A. The main spin-wave intensities are observed for excitation frequencies of 1.977 GHz and 3.25 GHz. **b** Spin-wave intensity recorded for an excitation frequency of 1.977 GHz, revealing two spin-wave beams following the two 90° walls merging into a 180° wall of supposedly 3 GHz onset frequency (thermal measurements). White arrows indicate the possible propagation direction from “left-to-right” domain wall (solid arrows, along points 1 to 2 to 3) as well as weaker spin-wave propagation from “right-to-left” domain wall (dashed arrows).

qualitatively (left arm between point 1 and 2, right arm between point 3 and 2). Even though in both “domain wall arms” the periodic modulation persists, the intensity in the left domain wall starts at a higher intensity (point 1), which decreases towards the junction (point 2), while for the intensity in the right wall the opposite behavior of a lower starting intensity (point 3), which increases towards the junction is observed. The author proposes the following hypothesis and assumptions to explain these findings:

The difference in spin-wave intensity measured for the “left” and “right” domain wall directly at the antenna, suggests a difference in excitation efficiency. Even though active excitation of spin waves in the Damon-Eshbach-geometry is known to be asymmetric for two opposite propagation directions [230], in this particular geometry no asymmetry attributed to the pumping field geometry is expected and can, therefore, very likely be excluded. Preliminary micromagnetic simulations of differently oriented antennas with respect to the domain wall orientation showed no difference in excitation efficiency. It seems indicated, that the two domain walls have a slightly different spectra and for this reason differ in excitation efficiency. The origin of the shifted spectra remains an open

question, but is consistently seen also in the later presented results. It is hypothesized that this difference is attributed to a different angle of the domain wall normal (here 3° difference) with respect to its magnetization orientation. Meaning, that since the orientation of the magnetization for the domains and domain wall is fixed by the anisotropy, the angle of the path along which the domain wall forms will alter the effective fields within the channel. However, additional effects of pinning sites besides influencing the path can not be fully excluded here.

Interestingly, if only an asymmetric excitation would occur a smooth exponential decay is expected. In contrast to this, a periodic intensity-modulation is observed and indicates interference effects of oppositely propagating spin waves. This requires the existence of spin waves propagating from the junction (point 2) towards the antenna (point 1 and 3). Such spin waves are likely the result of reflectance of spin wave flow at the junction. This would also imply, that reflection of spin waves towards their original point of excitation (meaning spin waves traveling in the "left" wall are back-reflected into the "left" wall, path 1 to 2 and back reflection to 1) is not dominant, since then the increasing intensity in the "right" domain wall towards the junction (from point 3 towards point 1) could not be explained. Instead, the periodic modulation of the spin-wave intensity, and simultaneous increase in intensity towards the junction for the "right" wall agrees with reflection of spin waves from the "left" into the "right" wall at the junction and vice versa. This reflection is furthermore in agreement with the observed minimal transmission of spin waves into the 180° wall at the junction point (point 4). The suppressed transmission between this different type of walls can likely be attributed to dispersion mismatch, since a lower spectrum of the 90° walls (which support spin-wave propagation at 1.97 GHz) compared to the higher onset-frequency of the linked 180° wall channel of 3 GHz as determined from the previous thermal scan on the 180° wall is expected. Another point to consider is the assumption of a vortex-core situated at the junction (point 2) blocking propagation. However, this would be expected to separate the domain wall channels and favor back-reflection in contrast to the experimental indications.

To summarize: Two spin-wave beams propagating along two 90° Néel walls are excited at the antenna with different initial intensity. The asymmetric excitation efficiency of channeled spin waves for the two domain wall arms indicate different domain wall spectra. This is hypothesized be connected to their slightly different angle between the domain wall normal and its magnetization orientation (3° difference). When the spin waves impinge on the interconnection point of the two 90° walls and a 180° wall, mainly reflection of channeled spin waves between the 90° walls is observed (path along points 1-2-3 and 3-2-1), which is favored over simple back-reflection. For optical reflection, as consequence of conservation of momentum/wave vector a similar observation would be expected. Transmission of spin waves into the 180° wall is not observed and seems prohibited. This is believed to be attributed to the different spectra of 90° and 180° channels. The increasing intensity in the right wall towards the junction (point 3 towards point 2), confirms the direction of the main spin-wave flow from the left wall to the right wall (path along points

1-2-3). The periodic modulation of the spin-wave intensity in both “domain wall arms” arises from simultaneously exciting channeled modes in both walls. This is the first study on spin-wave propagation along interconnected domain walls with a domain wall junction as well as the first observation of asymmetric excitation of spin-wave flow in domain walls. The here presented points will be raised again, when considering a remanent magnetic configuration of a domain wall junction of four 90° Néel wall crossing in section 4.1.3.4.

4.1.3.3 Active excitation of channeled spin-wave modes in a diamond state

The discussion continues with the spin-wave flow in the “diamond” magnetic configuration observed at the “bottom” region. At this position 90° Néel walls form a square (diamond) pattern. Figure 4.25 **a** shows a schematic of the domain configuration and the region of interest for the

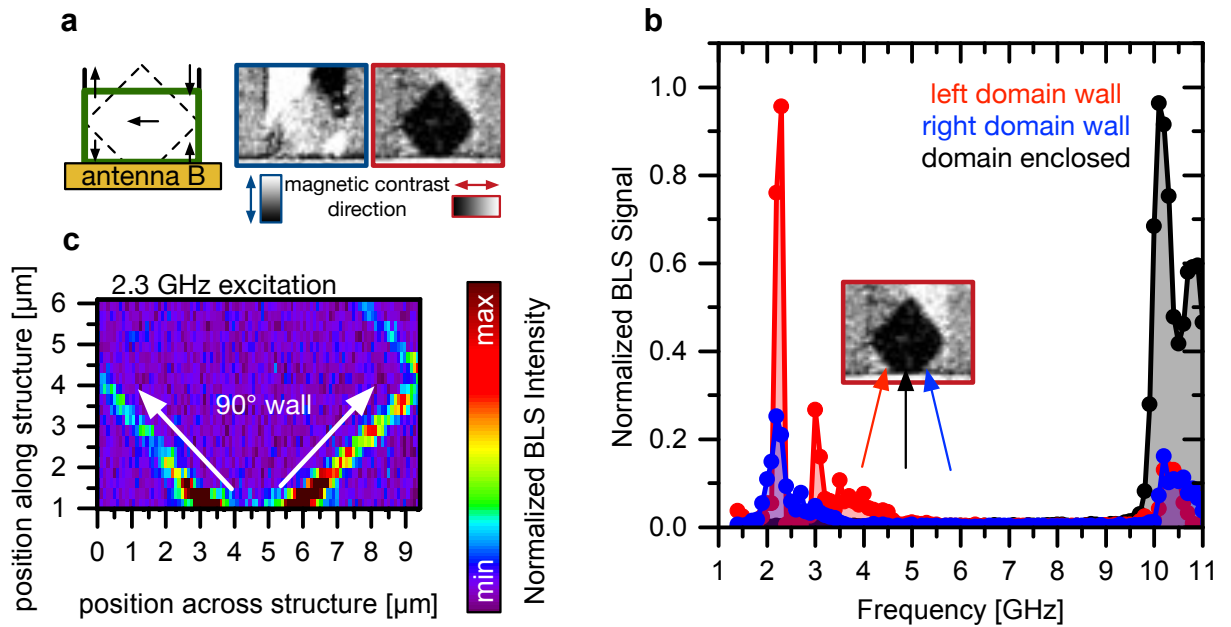


Figure 4.25: **a**, Schematic domain configuration (arrows indicating the local magnetization orientation, black lines domain boundaries) and region of interest for the spatial map presented in **c** (green rectangle). On the right hand side the magnetic contrast around the bottom antenna B is shown. **b**, Spin-wave excitation recorded in 640 nm distance to the antenna on the two domain walls and enclosed domain for excitation frequencies in the range between 1.4 and 11 GHz. Three different spectra are observed, separating the domain walls, with main intensity of spin-wave dynamics for frequencies below 4 GHz from the domain with an onset frequency of around 9.7 GHz. Additionally differences in the spin-wave spectra of the left and right domain wall are seen. **c**, Spin-wave intensity-map for a frequency of 2.3 GHz revealing two spin-wave beams propagating confined to the domain walls, and “turning the corner” at the structure edges.

spatially-resolved measurements together with a corresponding region of the Kerr micrographs. With increasing distance to the antenna the two domain walls separate laterally and turn in direction at the structure edges.

For this configuration the spin-wave intensities were measured for different excitation frequencies in a range between 1.4 and 11 GHz in 640 nm distance to the exciting antenna on both domain walls and the domain enclosed as shown in figure 4.25 b. Importantly, the distinct spectra confirm the different excitation efficiencies of the antenna for the two domain walls. The similarity in the shape of the spectra, seems to indicate that for the right domain wall (blue data points) the spectrum is red-shifted with respect to the spectrum of the left domain wall (red dots). According to this hypothesis a second peak in the spectra recorded on the right domain wall would be expected for lower excitation frequencies around 1 GHz, outside of the experimentally covered range. As was suggested in the previous chapter, this shift in spectra might be attributed to the different path of the domain walls with respect to the crystallographic/structure axes. In the following the angle between the line along which the domain wall is formed and the short-axis of the structure will be referred to as lateral wall angle.

To investigate this further, the spin-wave intensity was then measured by μ BLS for an excitation frequency of 2.3 GHz, in an area around the lower antenna. The recorded intensity is presented in Fig. 4.25 c and clearly shows two distinct spin-wave beams confined to the domain walls (region of interest depicted in Fig. 4.25 a, green rectangle). This evidences the underlying magnetic configuration. The lateral wall angles measured with respect to the short-axis of the structure are determined to be $50 \pm 2^\circ$ and $45 \pm 2^\circ$ degree for the “left” and “right” wall (LW and RW), respectively. The data confirms spin-wave propagation even “turning” with the domain wall “corner”.

The asymmetric dependency of the spin-wave excitation for the two distinct walls is promising as a direct possibility of multiplexing spin-wave signals (field and current free) by selection of the

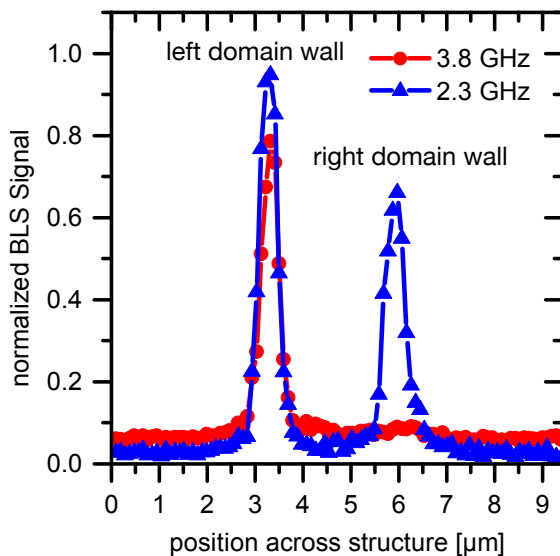


Figure 4.26: Spin-wave Intensity measured by μ BLS across the two 90° Néel walls for the diamond configuration for two exemplary excitation frequencies. The difference in spin-wave excitation efficiency for the two domain walls results in selective transport for spin-wave signals of different frequencies, such that for 2.3 GHz in both channels spin-wave intensity can be detected, while for a higher frequency of 3.8 GHz the spin-wave intensity stays confined only to one domain wall.

spin-wave frequency. An exemplary measurement of this "multiplexing capability" recorded in 0.8 μm distance to the antenna is presented for excitation frequencies of 2.3 GHz and 3.8 GHz in Fig. 4.26.

As can be seen from the data, selective spin-wave transport either along one channel or both channels based on the different excitation efficiencies can be realized. This indicates the intriguing possibilities offered by domain wall channels if these effects can be analyzed, explained and finally utilized in devices. In this context, the hypothesis, if the spectra differences can be attributed to the 5° difference in the lateral wall angle should be tested. Since the magnetic orientation in the domains and domain wall is fixed by the shape- and crystalline anisotropies, the lateral angle is expected to change the domain wall channel properties. This assumption and also the effect of pinning sites could be systematically studied using local ion implantation, serving to stabilize different lateral wall angles but also inducing well defined pinning sites in ongoing research. A prototype structure and scheme to investigate these effects is presented in the appendix (A.2).

In the next step, the spin-wave intensities were spatially mapped for excitation frequencies of 3.65 GHz (Fig. 4.27 a) and 10.4625 GHz (Fig. 4.27 b), respectively. For the measurements the spectral contributions (including the thermal background of the domains) have been separated to reveal the different localization of the spin-wave dynamics and non-linear processes.

For these measurements, a variety of effects, such as spin-wave frequency conversion is observed. For instance, for an excitation of spin waves at 3.65 GHz (Fig. 4.27 a), as shown earlier two spin-wave beams are excited at this frequency. However, simultaneously channeled spin waves are detected having a frequency of 2.1 GHz (left panel). Interestingly, their intensity increases in the "right" domain wall (marked as RW) with increasing distance to the antenna. This implies, that the 2.1 GHz signal is not only excited at the antenna itself, but even stronger near the turning point of RW and additionally requires frequency-conversion since its distinct from the driving frequency. This could be explained by initial excitation of spin waves having a frequency of 3.65 GHz, which then scatter into spin waves of 2.1 GHz at the points of inflection from the right wall. Such a frequency conversion effect is even more pronounced for an excitation frequency of 10.4625 GHz shown in Fig. 4.27 b. When first focusing on the direct excitation, spin waves are efficiently excited in the left domain marked in the graph as "D". Simultaneously, spin waves are detected at a much lower frequency of 4.8 GHz in the adjacent left wall ("LW" in left graph of Fig. 4.27 b). Therefore, this observation suggests for the first time that the directly excited spin waves in domains (domain D) are converted to channeled modes of lower frequency, when impinging on the domain wall channel.

Another peculiarity, is the observed gas-like spin-wave intensity distribution for a frequency of 10.1 GHz at the lowest frequency of the spin-wave band in the domains is observed. To determine its origin and possible connection to magnon condensates remains an interesting question to be addressed in future studies.

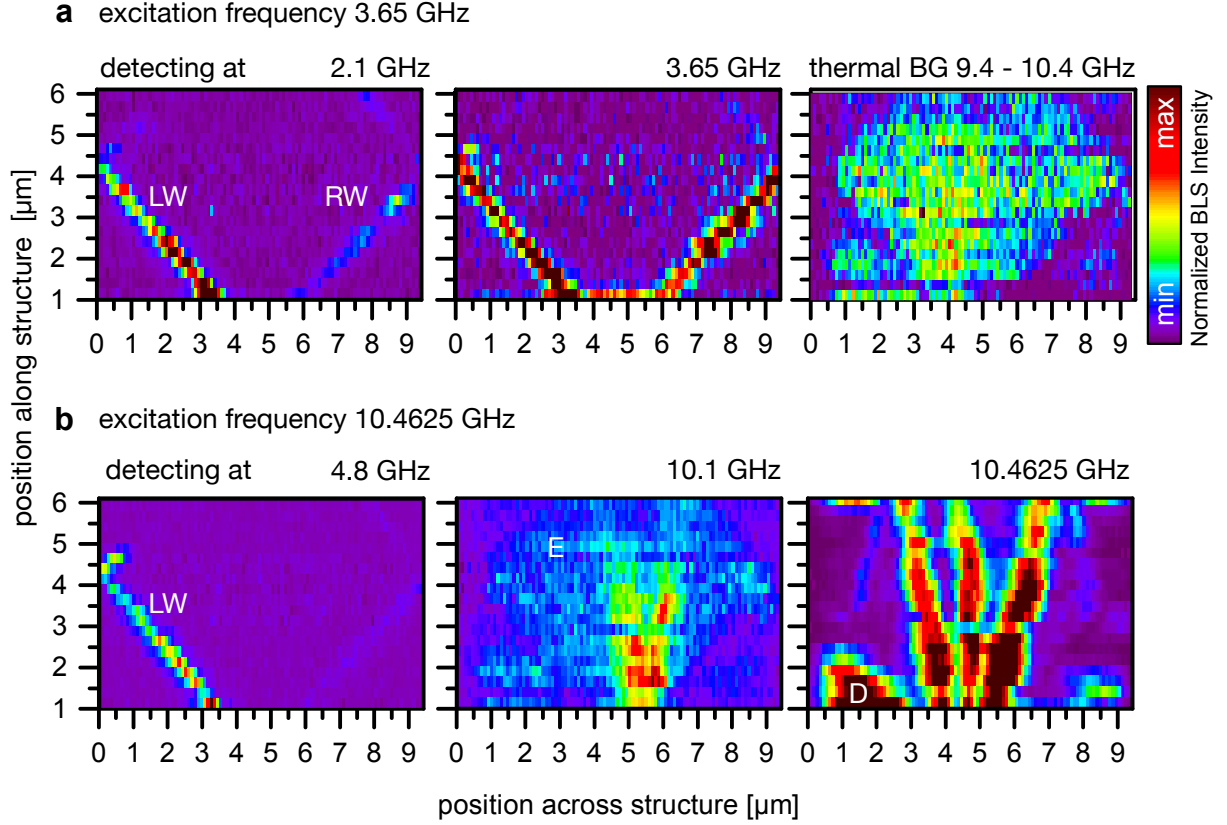


Figure 4.27: Non-linear spin-wave excitation and transport in a diamond domain and surrounding Néel walls. Spin-wave intensity-maps are separated for different spectral contributions when exciting channeled spin waves (3.65 GHz in **a**) and spin waves in the domains (10.4625 GHz in **b**). The spin-wave frequency is stated in the top right corner of each graph. A variety of effects, for instance, frequency conversion, asymmetric excitation and wave-vector adjustment of spin waves is observed. The domain thermal spectra (right sub-graph in **a**), shows vanishing intensities at the domain wall positions (LW and RW). The indirectly excited spin-wave beams at a frequency of 2.1 GHz are converted from directly excited spin waves (3.65 GHz) and have asymmetric intensities, while staying within the domain wall channels. **b** Excitation of spin waves in the domains: Conversion of directly excited spin waves in domain “D” (right sub-graph) scattering into channeled spin waves with frequency of around 4.8 GHz (left sub-graph). More detailed discussion given in the text.

Additionally, in the experiment an adiabatic wave-vector adjustment or caustic-formation for spin-waves traveling in the domains is observed. This time considering the spin waves having a frequency of 10.4625 GHz in Fig. 4.27 **b** directly excited in the diamond domain. The transversal wave vector of the spin waves spin waves traveling through the widening domain changes gradually but interestingly not proportional to the local width of the diamond domain.

Regarding this rich variety of effects, development of theories for the observed phenomena is

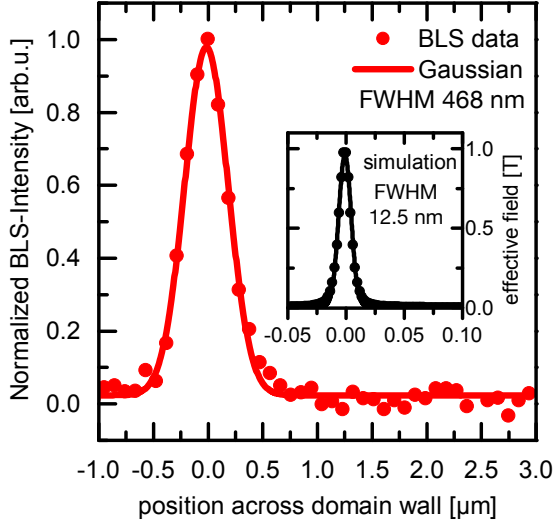


Figure 4.28: Spin-wave intensity profile measured across the domain wall for a frequency of 2.3 GHz (red dots) by μ BLS. The recorded intensities are well reproduced by a Gaussian of FWHM of 468 nm (red line). However, the simulated effective field wells for material parameters of Fe, are expected to be as narrow as 12.5 nm FWHM.

beyond the scope of this thesis. The results are presented here to provide experimental data for further research and to test against models to be developed. The author suggests that systematic studies in particular of swept excitation power and hence magnon density as well as time resolved μ BLS should be conducted to investigate these different mechanisms based on a larger variety of different sample geometries and scenario. The data clearly shows the promising flexibility of guiding spin-waves in different magnetic configurations in more complex domain wall networks.

The section closes with the confinement of the spin waves in this diamond state. Figure 4.28 shows the exemplary intensity profile for a frequency of 2.3 GHz across the domain wall (red dots) and a Gaussian Fit to the data (red line). Additionally, the effective field well profile was simulated for the material parameters of the crystalline Iron sample (gyrotropic splitting factor $\gamma = 29$ GHz / T, exchange constant $A = 19$ pJ/m, first cubic anisotropy constant $K_1 = 5 \cdot 10^4$ J/m³, saturation magnetization $M_S = 1711$ kA/m) as shown in the inset. Fitting a Gaussian to the simulated effective field well profile resulted in a FWHM of 12.5 nm, which is narrower than the effective field well width for the case of $\text{Ni}_{81}\text{Fe}_{19}$ (49 nm). This is expected from the increased dipolar and magnetocrystalline energies contracting the wall, compared to the exchange energies. This reduction in channel width is also accompanied by an increasing depth of the well, with maximum effective field values of 0.98 T. For this reason, even narrower confinement in Fe-based systems was expected. In contrast to this, the experimental data resulted in FWHM between 420 nm and 464 nm of the channeled spin-wave mode profile. This is surprisingly wider than FWHM of the spin-wave intensity in the domain wall channels in $\text{Ni}_{81}\text{Fe}_{19}$ (368 nm for 90 ° wall and 340 nm for 180° wall) and seems to indicate additional unaccounted effects.

Candidate sources of such an observation are the locally changed magnetic parameters due to heating by the set-up laser, but also laser dragging of the domain wall (and hence channeled mode) in the created thermal gradient and pinning site effects. However, there seems to be no indication, that such effects should be more pronounced in Fe based systems than compared to $\text{Ni}_{81}\text{Fe}_{19}$ based

structures, except for the reduced heat conductivity of the MgO substrate compared to Si. Moreover, even when assuming a completely vanishing magnetocrystalline anisotropy under the laser spot, still a narrower channel due to the increased magnetic moment and higher Curie-temperature of Fe would be expected. Additionally, in contrast to $\text{Ni}_{81}\text{Fe}_{19}$ microstructures (appendix A.3) dragging effects by the laser could not be confirmed by measurements, where the positional-sweep-direction of the measurement was reverted, but no observable difference could be detected. Further studies are recommended and required to investigate this delicate subject.

4.1.3.4 Active excitation of channeled spin-wave modes - merging domain walls

At the third remaining optically accessible “middle” region situated between the two antenna structures, the case of four crossing 90° Néel walls could be studied. This result is shown, despite its rather poor spatial resolution, since it serves as an interconnect between the two previously investigated regions and observation of spin-wave propagation in linked domain walls of identical type. The assumed magnetic configuration with a connection point of the two square shaped domains in the diamond state situated under the antenna is sketched in the top part of figure 4.29. This reasonable hypothesis (since the diamond state is observed on both other sides of the antennae) could not be investigated by Kerr microscopy due to the strongly restricted optical access between the antennae and resolution of the white-field microscope, so that the magnetic configuration is inferred from the spin-wave intensity measurements. However, bearing the already presented results about spin waves traveling along domain walls in mind, it seems justified to base the assumption of the magnetic configuration on the experimentally recorded spin-wave flow.

The resulting spin-wave intensity is measured across the structure for 5 different distances between the antennae when exciting at a frequency of 1.8 GHz shown in the bottom part of Fig. 4.29. In contrast to the previously presented measurements, the intensity has been normalized to compensate the exponential decay (with decay constant of 236 nm) to aid in identifying the transmission through the junction and underlying domain configuration. Importantly, this measurement was reproducible in several individual area scans in this region including the vanishing/undetectable spin-wave intensities at a distance of about $1.06\text{ }\mu\text{m}$.

The absence of a spin-wave intensity signal at the junction point might be connected to the reflectance of spin-wave intensity at the vortex core (due to the strongly changing effective fields) situated there. In this hypothesis, spin waves would either tunnel by their long-range dipolar fields across the barrier formed by the vortex or would be excited by the far field of the antenna on the other side of the vortex. A third possibility might be given by assuming, that the spin-wave signal is rendered inaccessible, when the static magnetization points out-of-plane or that vortex gyration is induced by the impinging spin waves leading to excitation of spin waves by the vortex core on the other side. Importantly, an asymmetry in spin-wave intensity is observed and again hints on

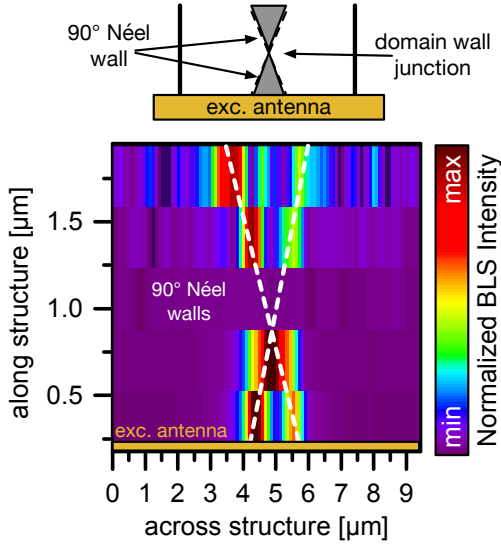


Figure 4.29: Spin-wave intensity measured between antennae A and B, when actively exciting at antenna B. Four 90° Néel walls are expected to be linked together (dashed white lines). The spin-wave intensity has been normalized to compensate an exponential decay. For these identical wall types, spin-wave beams are detected even behind the junction point.

the idea of asymmetric excitation efficiency. The fact, that a non vanishing spin-wave intensity is observed behind the junction point indicates the difference in the wall spectra for 90° walls and 180° Néel walls.

This concludes the study on spin-wave propagation in magnetic domain walls within this thesis. The presented results substantiate the possibility to confine and control spin-wave propagation in micro-magnets utilizing domain wall networks. Next to their characterization for different domain wall types, unexpected phenomena connected to higher harmonic generation and frequency-conversion as well as different spectra for the spin waves channeled within domain walls of identical type but different orientation of the domain wall plane (lateral wall angle) are observed. The latest shown result hints on the idea of transmittance across junctions of identical walls. A final conclusion and summary of the study is given in chapter 5.

4.2 Auto-oscillation in tapered wire geometries

In a loss-free magnetic system, deviations from the ground state result in a precessional motion of the magnetic moments on iso-energy trajectories. However, simultaneously, the moments relax towards the ground-state due to energy dissipation by coupling to the electronic, phononic and photonic system (section 2.2). If those loss channels could be turned off, any initial precessional motion or spin-wave dynamics would persist indefinitely. However, such material systems or magnetic phases have not been observed so far and tailoring the magnetic damping remains a delicate challenge. Nevertheless, it is possible to compensate the losses by pumping additional energy into the system via spin currents and corresponding spin-transfer-torque (STT) (section 2.3.2). In this case, the angular momentum transferred by the spin current is chosen anti-parallel to the magnetization, resulting in persisting precession. For this dynamic equilibrium, the system is said to be anti-damped and the resulting steady-state precessional motion are referred to as auto-oscillations or self-sustained oscillations (section 2.3.2).

Since the spin-orbit torque counterbalances the damping torque regardless of phase, frequency or wave vector of the precessional dynamic, in principal, arbitrary modes of the magnetic spectra, without restrictions on the wave vector or frequency can be amplified, rendering this mechanism a promising candidate for highly flexible spin-wave sources [231].

The non-linearity of the dynamics within the magnetic material is, thereby, both the boon and bane of their performance. While it allows for a wide range of tunability by the magnetic fields as well as by strength of driving spin-current, it also promotes multi-magnon scattering. As a consequence, when increasing the active area of a SHO non-linear spin-wave interactions distribute energy and angular momentum amongst an increasing number of modes, since the spin-wave spectra increases in density of available states. Their simultaneous excitation or mode hopping restrict spectral qualities and output-power of larger SHOs, hampering them from becoming competitive sources of microwave signals or spin-wave dynamics. To reduce such scattering and yield better heat-management for sufficiently high spin-current densities, the active region of devices is typically limited to the nanoscale. However, recent works showed, that quasi one-dimensional systems of micron long nanowire geometry still sufficiently restrict the magnetic spectrum to suppress spin-wave interactions such as four-magnon-scattering in these devices and allow for auto-oscillations [204] in much larger active regions. In a subsequent study the geometry was refined to a slightly tapered nanowire geometry to break the translational symmetry [159].

This symmetry breaking resulted in a wider regime of single mode operation and reduced phase noise. However, even in this quasi-one-dimensional cases, the precessional phase of the auto-oscillation remains in principal undefined (section 2.3.3), so that they are expected to be not fully coherent. Additionally, the effect of self-contraction or \pm -focussing of the auto-oscillations into

spin-wave bullets is predicted to allow a simultaneous existence of bullets with different frequencies within the same wire (section 2.3.2). This simultaneous formation of bullet-modes and their manipulation is studied. In this regime, the influence of a phase sensitive periodic external locking-signals on the auto-oscillation amplitude and spectrum are of interest, particularly with respect to the possible increase of spectral coherency and/or synchronized auto-oscillation amplitudes, for large SHO or SHO-arrays (section 2.3.3). Such questions are addressed in the following chapter and are the basis for synchronization of arrays of small spin Hall oscillators, enabling large output powers while staying in the single-mode regime.

4.2.1 Initial static magnetic configuration and effective field

The tapered nanowire SHO, based on a Pt(7 nm)/Ni₈₁Fe₁₉(5 nm) bilayer, is a semi one dimensional system of short width and height compared to its length. More precisely, the magnetic wire has a mean width of 220 nm, while it is 6 μm -long along the long-axis. Its active auto-oscillatory region is restricted to a length of 1.92 μm by Au electrodes. The tapering angle is chosen to be 1.45° . As a result the geometric width increases from 171 nm up to 268 nm along the active region and the related spin-wave spectrum varies along the SHO. A SEM-micrograph of the SHO is shown in Fig. 4.30 **a** together with the used coordinate system. The direction along the long-axis of the tapered wire, oriented towards the wider end is referred to as “along the SHO” and the perpendicular short-axis as “across the SHO”. Further information about sample production, magnetic parameters and geometry are given in section 3.4 and in [202].

To define the magnetic state, a saturating field of 300 mT is applied at an angle of $\phi = 80^\circ$ and then gradually decreased in strength to 70 mT. This 10° deviation from a perpendicular magnetization along the short-axis is chosen in order to still efficiently drive auto-oscillations (anti-damping torque $\propto \sin\phi$), but simultaneously permits direct coupling of an injected microwave signal (H_{RF} , polarized across the SHO) to the magnetization dynamics (excitation efficiency $\propto \cos\phi$).

For this geometry, the magnetic configuration and effective magnetic field in the tapered nanowire was calculated by micromagnetic simulations (details in appendix A.5). The magnitude and direction of the effective field are depicted in Fig. 4.30 **b** via color-code and black arrows, respectively. In the static configuration both magnetization and effective field are everywhere collinear¹ revealing the magnetic configuration. As can be seen, the external magnetic field is not sufficiently strong to fully overcome the shape anisotropy, which forces the magnetic moments to partially line up along the sample edges. Hence, the internal magnetic field is reduced to zero along the edges of the SHO creating potential wells, where the magnetization is canted. To illustrate this, the magnetization angle and effective field strength profile across the SHO for the narrow (171 nm wide) and

¹This can be seen by the equilibrium condition of vanishing torque $\dot{\mathbf{M}} \propto \mathbf{M} \times \mathbf{H}_{\text{eff}} = 0$ (see section 2.2)

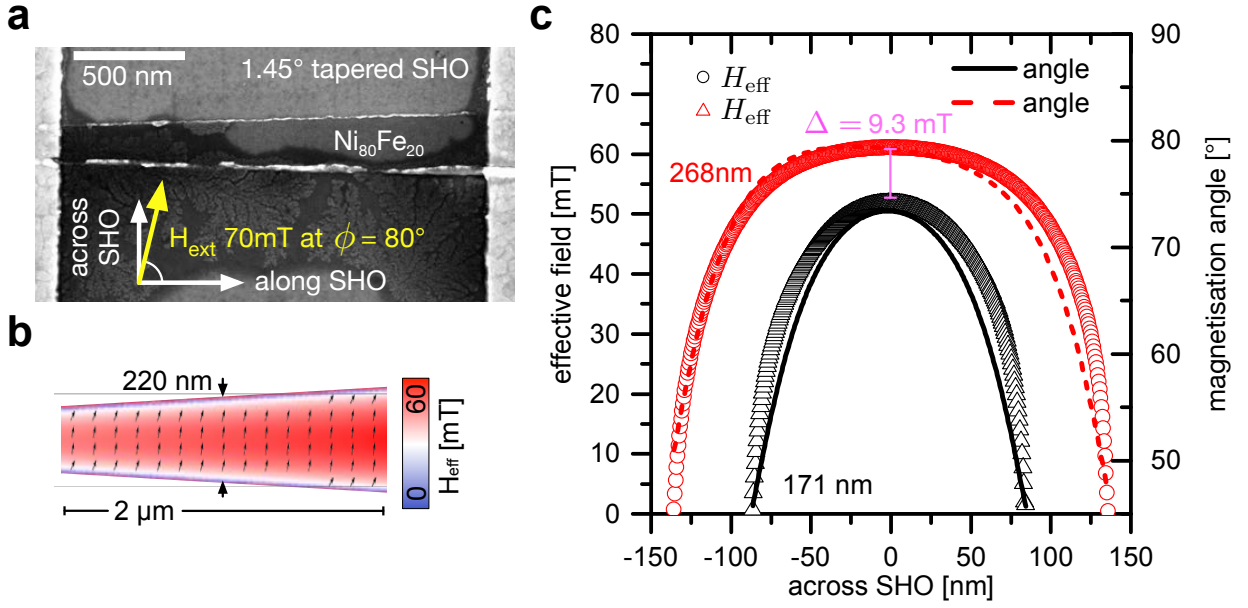


Figure 4.30: **a**, SEM-micrograph of the spin Hall oscillator. **b**, Simulated magnetic configuration and resulting effective field inside the tapered SHO. Arrows indicate the direction of the magnetization and effective field. The magnitude of the effective field is displayed color-coded. For better visibility axes are scaled. **c**, Spatial variation of the effective field and magnetization angle across the SHO at different positions, as determined by micromagnetic simulations. The magnetization is canted at the edges of the structure, compensating the external field of 70 mT resulting in effective field free edges. The effective field maximum is found to differ by 9.3 mT along the active region of the tapered wire geometry (extracted in the middle of the structure with respect to the x-direction) with a higher effective field of 61.1 mT at the wider end of the structure.

wider end (268 nm wide) of the active region is shown in Fig. 4.30 **c**. This dependency also reveals the increase of the internal magnetic field with increasing width of the nanowire. Across the SHO the effective field strength (dots, left y-axis) and the magnetization angle (line, right y-axis) mainly correlate with each other. Only a slight “left-right”- asymmetry ($< 3\text{ mT}$) of the two effective field wells at the opposite edges is observed. Even though this asymmetry, which stems from the different angle enclosed by the external field and surface normal for the two edges, is observable in idealized micromagnetic simulations, as in [202], it is expected to be negligible in experiments in real samples. This seems indicated by the SEM-micrograph, where the contrast change at the edges implies deviations from the ideal case in terms of sidewall damage, edge-roughness and slightly changed geometry, which are assumed to dominate the local resonance conditions for spin waves with main intensity at the edges.

4.2.2 Thermally excited dynamics and spectral properties

Due to the tapering of the SHO, the width increase along the active region is expected to influence the related spin-wave spectra locally. To study this effect, the spatial dependence of the thermally excited magnetic spectrum was recorded by μ BLS. As in the previous studies the thermal excitation (typical energy ≈ 25 meV) can be thought of as a stochastic, delta-correlated (and hence random) field, exciting all spin waves (typical energy $\approx 10\mu\text{eV}$) equally with random phase at random positions. This enables one to measure magnetic spectra free of distortions by excitation efficiencies or frequency and phase selective measurement means. As a side remark, the sensitivity of the μ BLS is limited to spin waves of wave-length contributions longer than 355 nm (section 3.5). This reduces the sensitivity for spin waves localized to length scales below 177 nm, but still renders them detectable, since they span a wider range in wave vector space due to localization.

Thermal μ BLS-spectra were recorded for several positions along the SHO of the tapered wire. The data is presented in Fig. 4.31 **a**. In each measured spectrum, a position dependent sharp

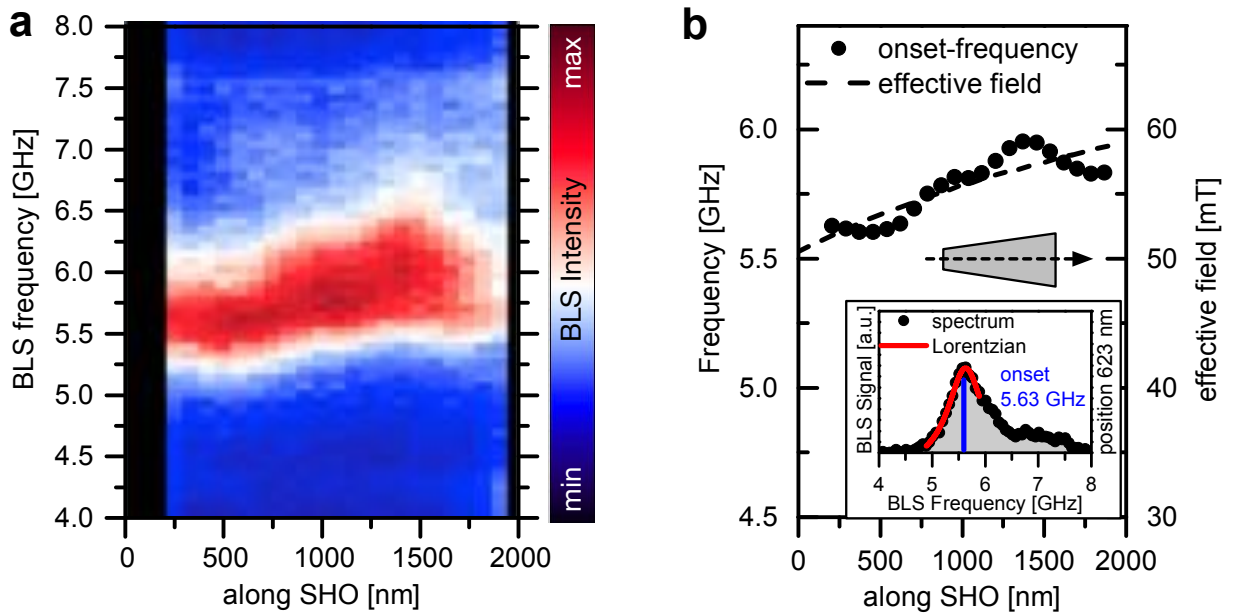


Figure 4.31: **a**, Thermal μ BLS spectra recorded for different positions along the SHNO. The rising edge of the BLS Spectra (intensity shown color coded), indicates the spatial dependent frequency-onset of the spin-wave band. **b**, Extracted onset-frequency (black dots) along the SHO by fitting a Lorentzian to the low-frequency side of the spectrum. An exemplary spectrum for a position of 623 nm along the SHO is shown in the inset together. The onset-frequency increases along the tapered wire. This is in qualitative agreement with the increasing effective field, as determined by micromagnetic simulations for this wire geometry (dashed black line) and quantization conditions.

increase in signal intensity around 5 to 6 GHz is observed, which then gradually decreases again for higher frequencies. The local maxima correlates with the lowest frequency of the spin-wave band, connected to the abrupt increase in density of states available for frequencies above the magnetic band gap [232, 233]. To estimate this onset-frequency the low-frequency-side of the signal was fitted by a Lorentzian and its maxima position was used as an estimate of the spatial dependent spin-wave spectra as shown in Fig. 4.31 **b**. Additionally, the effective field magnitude along the middle of the wire is shown by a dashed line, as extracted from the simulations shown in Fig. 4.30 **b**. Using the effective field as a guide to the eye, the onset-frequencies increase by ~ 300 MHz from ≈ 5.6 GHz to around ≈ 5.9 GHz along the active region of the tapered wire, which corresponds to around 3.1 GHz/ μm with respect to the width change. The variation of the onset-frequency from a simple linear spatial dependence can most likely be attributed to deviations from the idealized structure geometry. Hence, the experimental observation confirms the locally changing magnetic spectra and quantization of spin waves across the SHO.

Discussing these spin-wave spectra quantitatively by theory is challenging for several reasons, such as the inhomogeneous ground state and broken translation invariance, however the author would like to provide a starting assessment: Geometrical boundary conditions and effective field wells confine spin waves, discretizing their wave vector (see, e.g., [104]). In the tapered geometry, this confinement along the short-axis depends on the position along the SHO and has to be considered. Next to this confinement, the effective field increases along the SHO. When averaged across the SHO for the inner 80% part of the wire, this field points in the 75° -direction with a mean magnitude of 46 mT for the narrow and 56 mT for the wider end. Neglecting the edge-regions by assuming a homogeneously almost transversally (75°) magnetized stripe one can virtually divide the SHO into individual segments of increasing width and discuss the local spectra. In a first step, a global effective field of 56 mT is considered throughout the system, to analyze the effects of quantization separately. Calculations are based on the linear thin-film spin-wave dispersion (section 2.2.1).

Calculating the frequency of a spin wave quantized by pinned boundary conditions for the narrow end ($\lambda/2 = 171$ nm) yields a lowest spin-wave frequency onset of 8.01 GHz, while the decreased quantization for the wider end ($\lambda/2 = 268$ nm) results in a reduced onset-frequency of 7.61 GHz. This quantization induced frequency red-shift along the SHO (oriented from narrow to wider) of 400 MHz evidences the exchange regime, despite the low spin-wave angle ($\approx 15^\circ$) between magnetization and wave vector. Therefore, if geometrical quantization is considered the spin-wave frequency is predicted to decrease along the SHO contrary to the experimental observations and can not alone explain the findings.

When in a second step, the effective field variation of around 10 mT (from 46 mT to 56 mT) along the SHO is separately considered (neglecting the tapering and assuming a constant average width of 220 nm), a field-induced blue-shift of around 686 MHz is calculated. Taking in the next step simultaneously the decreasing spin-wave localization and increase of effective field along the

SHO into account yields a frequency blue-shift of ~ 233 MHz along the gradually widening SHO. Which is in reasonable qualitative agreement with the measured 300 ± 100 MHz.

Similar considerations apply for an effective field well quantization hypothesis. Studies on the closely related geometry of straight wires with an external magnetic field applied along the short-axis are, e.g., given in [104, 234]. In the μm -wide straight wires, mainly two different spin-wave modes are observed being localized in the wire center (“bulk modes”) and at the wire-edges (“edge modes”) with two distinct resonance frequencies separated in the GHz regime. In the experiment only a single branch (single Lorentzian) is observed in the spin-wave spectrum, contrary to the previously mentioned studies [104, 234], but as observed in 300 nm wide wires in [235]. Since the tapered SHO is of similar average width of 220 nm and the thermal spectrum has only one peak it is indicated that separation into edge- and bulk-modes seems not applicable in this case. Moreover, if despite this reasoning modes localized to the edges would be assumed, one has to take into account, that these modes are expected to strongly depend on the edge-properties, such as local roughness and profile [236] aggravating theoretical treatment of real samples. In particular, such a localized edge mode assumption is put into question by earlier studies on a similar system indicating dilution (reduction) of the magnetization at the edges [204] and side-wall damage.

To conclude, a general frequency blue-shift along the SHO of around 300 MHz and a single, dense or closely spaced, spatially continuously varying spin-wave band is observed. Calculations suggest, that the increasing effective field along the SHO causes a dominating blue-shift, overcompensating a red-shift due to decreased quantization. In agreement with the thin-film spin-wave dispersion relation (section 2.2.1) the simulated increase in effective field strength by ≈ 10 mT (averaged for 80% of the middle of the wire, see also figure 4.30) yields a spin-wave field-sensitivity of ≈ 69 GHz/T.

4.2.3 Direct microwave excitation of spin-wave dynamics

In the next step, the excitation of spin waves by injecting a microwave current flowing through the SHO is studied. The current I generates an Oersted field \mathbf{H}_{RF} , which is polarized across the SHO according to the Biot-Savart law [49]. Its magnitude and orientation is presented in Fig. 4.32 **a** for a cross-section of the SHO in the middle of the active region. To calculate the Oersted field, in a first step, the current density j along the widening nanowire has been estimated. For this, the two thin layers are treated as parallel resistances and the thin film resistances of $\text{Ni}_{81}\text{Fe}_{19}$ and Platinum of $36 \mu\Omega \text{ cm}$ and $28 \mu\Omega \text{ cm}$ are adopted, respectively [237]. The calculations yield 64% of the total current I flowing in the Pt-layer and a decrease in current density j along the SHO, due to the increasing cross section of the nanowire as shown in Fig. 4.32 **b** (black line). Based on this current density the Oersted field is calculated by modeling infinitely long rectangular conducting wires changing in width (see e.g. equation 32 in [238]) as additionally shown by hollow black dots.

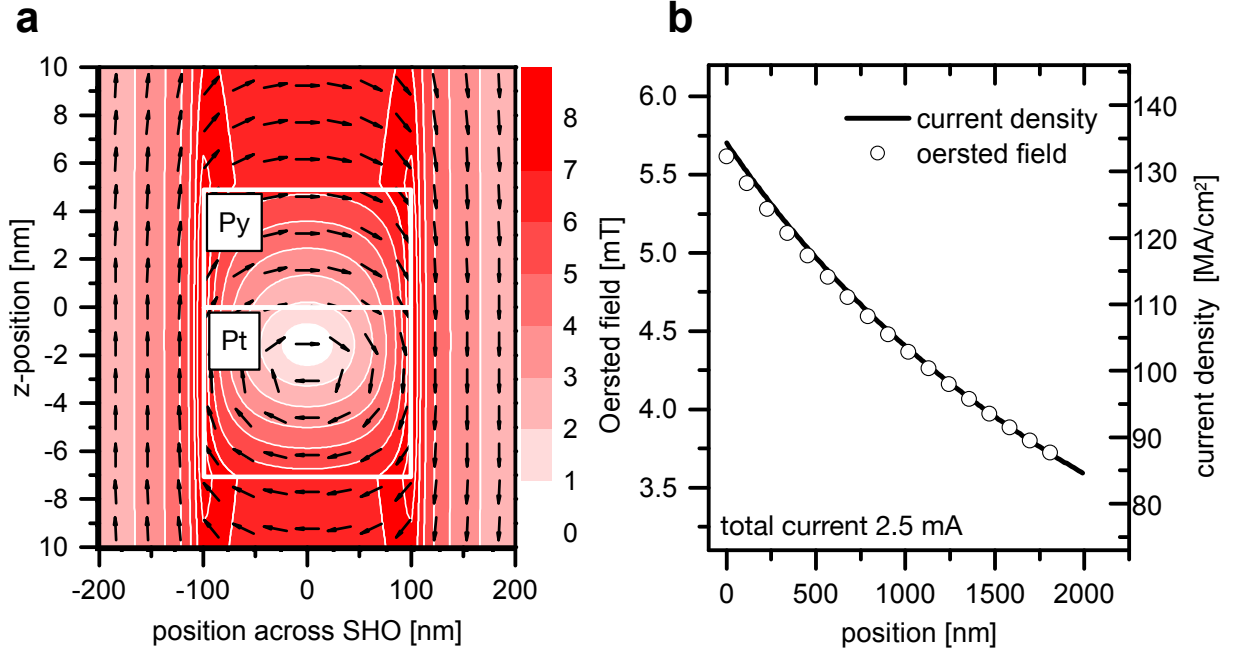


Figure 4.32: **a** Oersted field created by a current of 2.5 mA flowing through the 7-nm-thick Pt (64%) and 5-nm-thick $\text{Ni}_{81}\text{Fe}_{19}$ (36%) bilayer for a width of 200 nm. The strength of the field is color-coded while arrows point towards the field-direction. **b** Oersted field strength in the middle of the magnetic $\text{Ni}_{81}\text{Fe}_{19}$ layer and average current density within the Pt-layer for different positions along the SHO.

The Oersted field correlates almost perfectly with the current density ($\propto 1/\text{width}$) and decreases by around 36% along the SHO towards the wider part. Hence, the current density itself and not the geometry change by the width-variation dominates the Oersted field strength in the middle of the wire. When considering the excitation of spin waves the angle enclosed by this Oersted field and the magnetization $\phi_{H,M}$ determines the excitation efficiency $\propto \sin \phi_{H,M}$. Due to the tilted magnetic moments (presented earlier in Fig. 4.30 c) this predominantly excites spin waves at the SHO edges where the angle is up to 45° , while it is only around 10° in the center of the nanowire (reduction to 70%). Since the excitation also scales linearly with the Oersted field strength the spin-wave excitation is expected to additionally decrease towards the wider part of the SHO by 64%.

It should be mentioned that there exists a broad variation in the actual thin film sheet resistances in literature. For example, for Platinum ranging from $10.2 - 62 \mu\Omega \text{ cm}$ [237, 239–245] with critical dependence on the thickness and used evaporation method. However, calculating for a range of Pt-values (not shown) the Oersted field kept its characteristics and shifted its point of radial symmetry. As expected, in particular the reduction of 36% towards the wider part was consistently confirmed, which is the important point in the later discussion.

Now the focus is put on the experimental study of spin-wave excitation, when injecting microwave currents. Figure 4.33 **a** shows a spin-wave spectrum measured 500 nm away from the narrow end

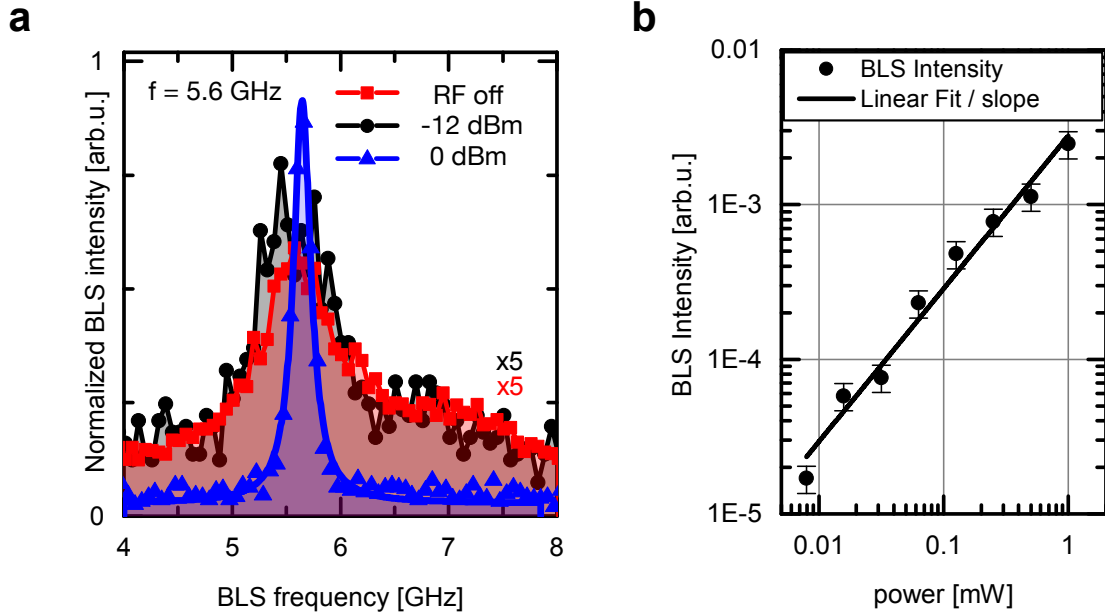


Figure 4.33: **a**, BLS Spectra for different nominal powers of microwave excitation with 5.6 GHz. The thermal spectrum (red squares) is plotted together with a nominal power of -12 dBm (black dots) and a 16 times higher pumping power of 0 dBm (blue triangles). For the pumping power of -12 dBm almost no additionally excited magnetization dynamic was detected compared to the thermal background. **b**, Logarithmic dependence of the BLS-Intensity on the microwave power after subtraction of the thermal background. A linear relation with the expected slope of 0.99 ± 0.06 [arb. u./mW] is observed.

of the SHO by μ BLS when exciting by a microwave with 5.6 GHz frequency and nominal power of -12 dBm (black dots) and 0 dBm (blue triangles), respectively, together with a purely thermal spectra (red squares).

For powers of -12 dBm and below, even for this position of close to expected largest excitation efficiency, almost no spin waves are excited above the thermal background (black dots). As presented in Fig. 4.33 **b** up to 0 dBm the signal amplitude increases linear with applied power as expected [246]. This confirms that the excitation of spin waves by the injected microwave-current remains in the linear regime up to 0 dBm and that for pumping powers of -12 dBm or below almost no differences to the thermal background are indicated. The linewidth of the spin-wave intensity peak is determined to be around 192 ± 11 MHz by Lorentzian fitting of the experimental data (blue line), giving the frequency resolution limit of the μ BLS-setup used in the following experiments (frequency resolution of microwave generator 10^{-3} Hz and, hence, negligible). These points are raised again, when studying the effect of the injected microwave signal on the auto-oscillation frequency, linewidth, power amplification and mode structure (section 4.2.5).

4.2.4 Auto-oscillatory response

This section is now devoted to the auto-oscillatory response, and the influence on it from the continuously varying spin-wave spectra along the SHO. DC currents I of different strength and polarity are applied to the SHO to excite auto-oscillations (working principle described in section 2.3.1, schematic set-up in section 3.4). The polarization of the spin current is parallel to the short axis of the wire. Hence, it encloses a 10° angle with the magnetic moments close to the optimal configuration, except for the wire-edges, where the magnetization rotates up to 40° away from the spin-polarization. In contrast to the spin-wave excitation by the Oersted field the damping-torque compensation by the STT is expected to scale $\propto I \cdot \cos \phi_{\mathbf{M},\mathbf{P}}$ [247–249], where $\phi_{\mathbf{M},\mathbf{P}}$ is the angle between magnetization and polarization of the spin current. Due to this the torque-compensation drops by about 36 % along the SHO (with current density) and an additional 28% towards the edges (due to the canted moments). This also suggests that the damping-torque compensation is strongest near the center axis of the tapered wire in the narrow part, in contrast to the microwave excitation assumed to be greatest at the edges.

The magnetic auto-oscillations, experimentally recorded by μ BLS along the SHO, are shown in Fig. 4.34 a, where a constant current of $I = 2$ mA was applied to the SHO, resulting in a current density within the Pt-layer ranging from $j = 107 - 68$ MA/cm² (narrow to wider part). Each spectrum was fitted by a single Lorentzian to estimate frequency, linewidth and amplitude of the auto-oscillations. It is challenging to give an exact error estimate for single parameters of a multi-parameter fit. However, e.g., with respect to frequency the set-up resolution (FWHM) was measured to be 192 ± 11 MHz (previous section) and the accuracy in determining peak frequencies connected to the signal to noise ratio and number of channels is estimated to be about ± 50 MHz. As can be seen later from the data, this estimate is rather conservative and intended to cover systematic errors, since it is larger than the noise of the measured frequency-data being in the range of about 10 MHz.

The amplitude of a peak (maximum value) is estimated to be accurate within 5%. In the following the point size is always chosen to cover the estimated error bars in these experiments if not stated otherwise explicitly. The determined auto-oscillation frequencies are shown in Fig. 4.34 a (pink dots) together with the previously determined onset-frequencies of the thermal spectra (green triangles). The data reveals a global red-shift in auto-oscillation frequency as expected from the non-linear frequency shift (NLFS, section 2.3.2, equation 2.25). However, the spatial dependence of the auto-oscillation amplitude (pink dots) and magnitude of the red-shift (hollow black dots) is peculiar and presented in Fig. 4.34 b. As will be further supported by later presented measurements, the 500 nm-long segment between the positions 1500 nm to 2000 nm along the SHO (marked by a grey background of the data) shows qualitative differences to the remaining SHO. In this particular measurement a sudden drop in amplitude is observed for this part.

For the remaining SHO (up to 1500 nm) the analysis reveals an almost constant amplitude and frequency red-shift of the auto-oscillation. On first glance, this is a surprising result. The Oersted field and STT drop in total by 36% along the SHO towards the wider end (section 4.2.3) and, additionally, the needed STT increases with increasing effective field (see equation 2.12). This is expected to manifest itself as a pronounced continuous intensity drop and decreasing frequency shift towards the wider part. Both is not observed experimentally.

For elucidation, let us consider the SHO to be comprised of several shorter connected SHO-slabs of increasing width (SHO-segments). When including the varying Oersted field the difference in effective field along the SHO will increase by 1.4 mT resulting in a total difference of 11.4 mT (41.6 mT in the narrow part and 53 mT in the wider part) and a mean lowering of the effective field by 4.5 mT. Therefore, the previously measured frequency shift variation along the SHO of around 300 MHz (due to the quantization and effective field) is expected to increase due to the Oersted field. Using the previously suggested field dependence of around 69 MHz/mT this can be estimated as an additional frequency difference (due to the additional 1.4 mT difference) of 100 MHz and an additional global red-shift of 250 MHz. Though the constant red-shift is in reasonable agreement with the experimental observation of ≈ 200 MHz (linear fit in Fig. 4.34 **b**), the increasing 100 MHz difference between wide and narrow part can not be confirmed from the frequency shift data. As presented later the estimation of this global frequency shift based on the auto-oscillation amplitude for several driving currents, suggest an Oersted field contribution of 130

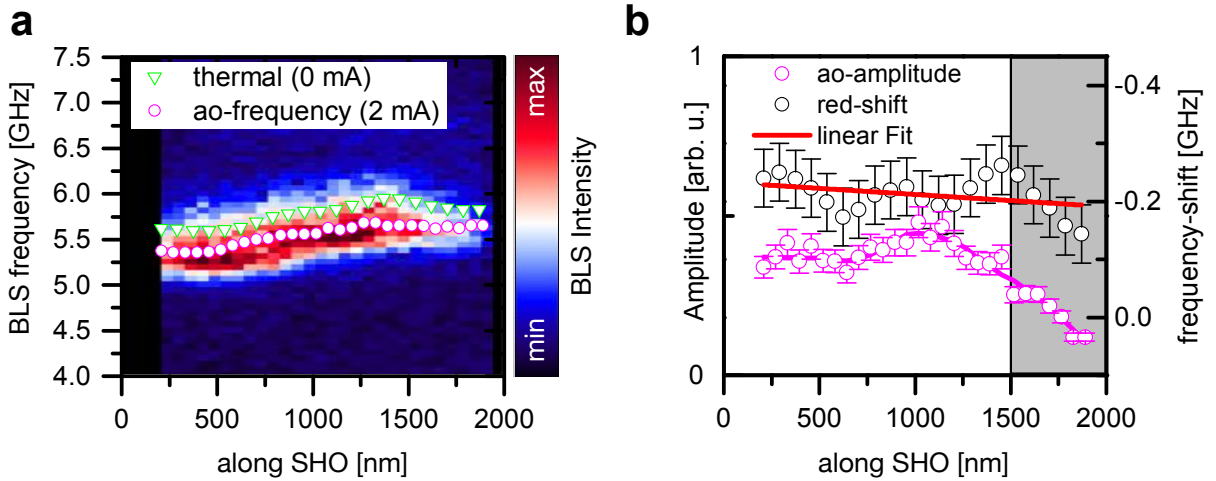


Figure 4.34: **a**, Auto-oscillation spectra along the SHO for $I = 2$ mA recorded by μ BLS (BLS-intensity color-coded). The auto-oscillation frequencies (pink dots) and thermal onset-frequencies (green triangles) as determined by Lorentzian fitting are additionally shown. **b**, Auto-oscillation amplitude (pink dots) and frequency shift (black dots) with respect to the onset-frequency of the thermal spin-wave spectra. The auto-oscillation amplitude and its frequency red-shift show a less pronounced variation along the tapered SHO as would be expected.

MHz for this measurement, where the remainder is attributed to the NLFS.

Considering the amplitude of the auto-oscillation (pink dots) in Fig. 4.34 **b**, the increased effective field along the SHO should require an increasing STT to compensate for the damping. Since the damping torque scales linearly with the effective field (equation 2.12) and the STT is linear in current density, one would require a 27% higher current density in the wider SHO segments to compensate the dissipative losses. Combined with the geometry-induced current density drop by 36% along the SHO, this suggests, that about a factor of 1.6 higher current ($I = 3.2$ mA) is needed to achieve identical conditions for the wide end SHO-segment with respect to the narrowest segment for a current of $I = 2$ mA. This should lead to a pronounced exponential drop of auto-oscillation amplitude along the SHO. The constant frequency shift and amplitude do not agree with this prediction, but mutually with each other, since they are coupled by the NLFS. The absence of the variation of amplitude and increased frequency shift of the auto-oscillations along the SHO is not expected and indicates two important assumptions:

Firstly, since the magnetic spectrum exhibits a continuous spatial dependence similar to the thermal spectra and no discrete energy-levels, the segments of the SHO do not couple or hybridize into a fixed set of eigenmodes with discretized frequency, shared throughout the whole active region.

Secondly, the almost constant amplitude of auto-oscillation, observed over $1.5\ \mu\text{m}$ of the narrower part of the SHO, suggest some form of a frequency-independent coupling, compensating the expected strong amplitude dependence on the STT strength in relation to the damping along the SHO. Furthermore, the amplitude drop over the remaining 500 nm of the SHO indicates, that the wider end is still effectively damped and the applied current only sufficient to drive the narrower part of the SHO.

4.2.4.1 Spin-wave bullet formation for higher driving currents

In the next step, the changes in auto-oscillations are investigated for higher driving currents in order to observe the expected spin-wave bullet formation. For this, a current of $I = 2.5$ mA corresponding to current-densities in the Pt-layer of $134 - 85\ \text{MA}/\text{cm}^2$ was applied to the SHO. As a consequence of the increased STT the auto-oscillation amplitude increases. This should intensify self-contraction and, hence, result in double bullet formation as predicted by a Ginzburg-Landau model [159] (see section 2.3.2). Additionally, the coherence length of spin waves, due to the reduced effective damping is expected to be enhanced, potentially allowing discretization along the SHO for these higher current densities.

The μBLS measurements along the SHO are presented in Fig. 4.35 **a** (BLS-intensity color-coded with logarithmic scale) and show qualitative differences to the measurements for lower driving currents. In each spectrum three auto-oscillation peaks occur simultaneously. Along the SHO two

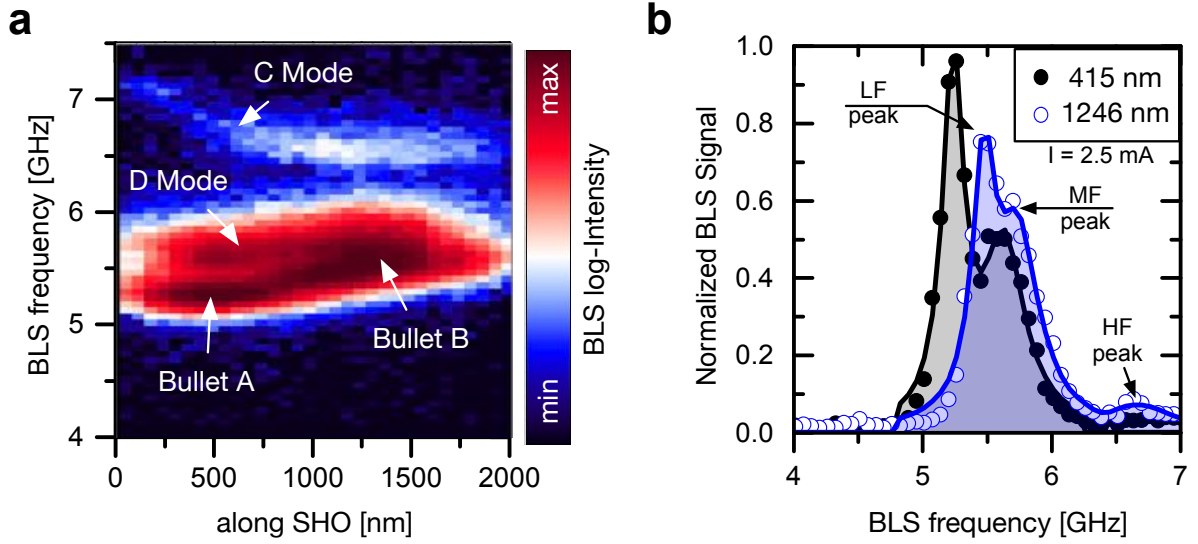


Figure 4.35: **a**, Spatially dependent contributions to the auto-oscillations in the SHO for a current of 2.5 mA as measured by μ BLS. Each spectra contains 3 signals, which are fitted by 3 Lorentzian and labeled LF, MF and HF to determine frequency and amplitude of the auto-oscillations, as shown for exemplary spectra in **b**. The points of main intensity in the auto-oscillation spectrum are classified as two spin-wave bullets labeled “Bullet A” and “Bullet B” together with two additional observed modes labeled “C mode” and “D mode”.

points of main auto-oscillation intensity, identified as “Bullet A” and “Bullet B”, are observed. Two additional modes appear for higher frequencies and lower signal intensities labeled as “C Mode” and “D Mode”. To discuss the validity of this classification into two spin-wave bullets and additional mode C and D, each spectrum was fitted by three Lorentzian to extract their frequency and amplitude. The three signals are labeled according to their frequency as low frequency (LF), middle frequency (MF) and high frequency (HF) peak. For illustration, two exemplary spectra for a position of 415 nm (black dots) and 1246 nm (blue hollow dots) along the SHO are presented in Fig. 4.35 **b** together with the fit by three Lorentzian (solid lines). From this exemplary measurements, the spectral overlap of the different auto-oscillation signals can be seen in particular for the LF and MF signal. Figure 4.36 **a** and **b** present the extracted frequencies and auto-oscillation amplitudes, respectively. Additionally, the spin-wave eigenfrequencies as calculated by micromagnetic simulations (white-filled symbols) are shown. The three modes exhibit different qualitative spatial dependences. Their nature and classification will be discussed in the following:

The lowest frequency auto-oscillation signal (LF-peak) generally contributes with the highest intensity to the auto-oscillation signal. Similar to the single-mode auto-oscillation for $I = 2$ mA it exhibits a global frequency red-shift along the SHO with respect to the thermal spectra as shown in the inset of Fig. 4.36 **a**. This indicates that this LF-signal can be identified as the continuation from the auto-oscillation signal for $I = 2$ mA. Interestingly, with respect to the auto-oscillations for

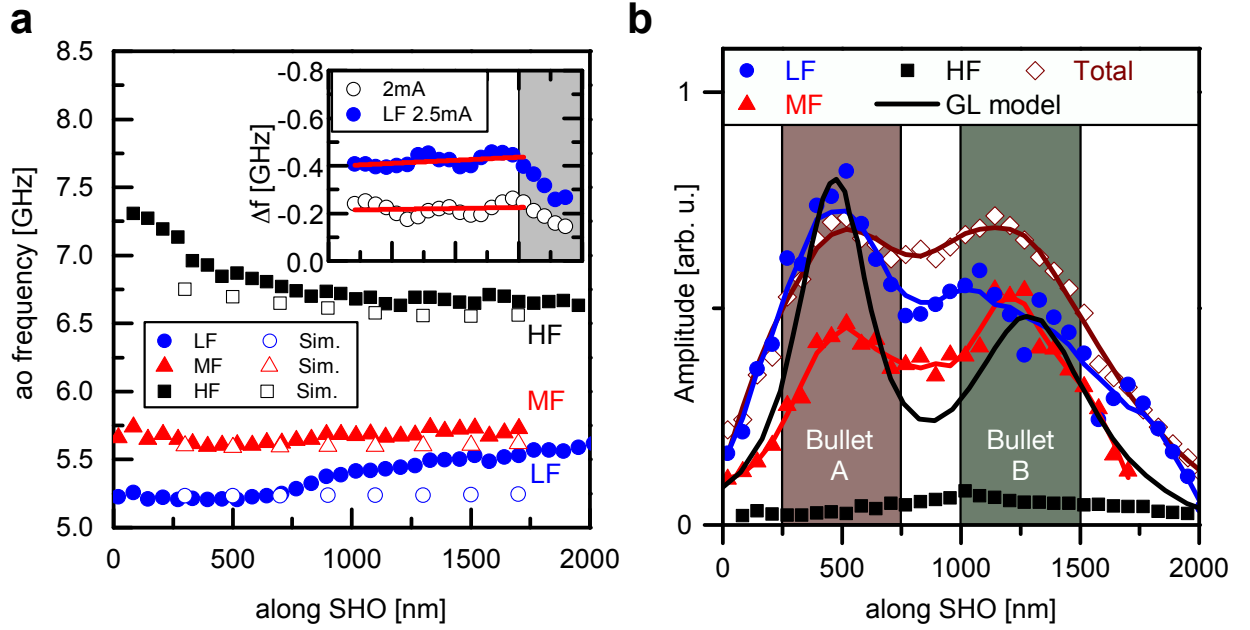


Figure 4.36: **a**, frequency of the three auto-oscillation signals (LF blue dots, MF red triangles, HF black squares) observed for a current of $I = 2.5$ mA. Calculations of the linear spin-wave spectra by micromagnetic simulations are also shown as corresponding white filled symbols. The inset (identical x-axis) shows the position dependency of the frequency red-shift with respect to the thermal spin-wave spectra for the LF-signal (blue dots) and for a current of $I = 2$ mA (white dots). Red lines are linear fits and serve as guide to the eye. **b**, Amplitude of the different spectral contributions together with the total intensity integrated over the entire auto-oscillation spectrum (brown diamonds) and the auto-oscillation amplitude in the two Bullet state predicted by a Ginzburg-Landau model (GL model, black line, Yang:2015hf).

$I = 2$ mA the frequency red-shift is approximately constant and about twice its previous value (400 MHz), while the Oersted field is only increased by 25%. This confirms a non-linear relation of the shift with current density. This is further substantiated by the absence of an increasing frequency difference along the SHO as would otherwise be expected (slope on red-shift). Calculations for the frequency shift assuming a linear relation with the current (Oersted field linear in current density) and linear in auto-oscillation intensity (non-linear frequency shift, NLFS), suggest that 130 MHz ($I = 2$ mA) and 165 MHz ($I = 2.5$ mA) stem from the Oersted field.

The remaining red-shift of ≈ 230 MHz ($I = 2.5$ mA) originates from the NLFS due to the increase in auto-oscillation amplitude (section 2.3.2). Its amplitude is shown in Fig. 4.36 **b** (blue dots) and is highest at a position of about 500 nm along the SHO and exhibits a second less localized/pronounced maximum around 1250 nm. In particular at the position of 1250 nm it becomes difficult to unambiguously separate the contributions from the LF and MF signal, since they are close in frequency and overlap spectrally. As will be picked up in the later discussion, also the

total signal, integrated over the complete spectrum, is shown in Fig. 4.36 **b** (brown diamonds) and is almost perfectly symmetric around the center of the SHO. The auto-oscillation amplitude and frequency dependence of the LF-signal along the SHO fit well to the two bullet state prediction of the Ginzburg-Landau model. The amplitude according to this model is shown as a black line, exhibiting two similar intensity maxima, with larger deviations, where the LF and MF signal overlap spectrally. The frequency separation of the two bullet modes is expected to be around 190 MHz. From the experiment the bullet frequencies are determined at the position of highest intensities (500 nm and 1250 nm) to be 5.2 GHz and 5.45 GHz, respectively, resulting in a frequency difference around 260 MHz in reasonable agreement with this prediction.

The middle frequency auto-oscillation signal (MF-peak) is of almost constant frequency of 5.65 GHz along the entire SHO with two intensity maxima symmetrically spaced from the middle position of the active region. The corresponding mode labeled as “D mode”, is not expected and marks the necessity to extend current auto-oscillation theories. Since this D Mode has a higher frequency with respect to the two bullets, it seems reasonable to assume that this mode is allowed to propagate along the SHO. Such an assumption fits well to the lower intensity (due to radiation losses) and that this mode exists throughout the structure. It can be seen, that in the simulation of the linear spin-wave spectra a mode of similar frequency is found, which is localized at one of the tapered edges of the SHO. The simulated mode-profiles are given in the appendix (section A.5). This hints on the idea of an increase in the coherence length of spin waves by the anti-damping STT, allowing for standing wave formation along the SHO in contrast to the result for lower driving currents ($I = 2$ mA). However, auto-oscillations are strongly non-linear excitations, so that a strict comparison with the linear spin-wave spectra is only well justified for the C Mode, since it is of much lower intensity.

This third mode labeled as “C Mode” (about a factor of 10 lower in intensity with respect to the LF signal) has a frequency around 7 GHz, which decreases along the SHO. According to the simulations and observations in [235] such a mode is attributed to a mode localized in the center of the wire. Here, the main focus is not put on this additional low intensity mode, but on the auto-oscillatory state determined mainly by the two spin-wave bullets and the propagating D Mode. As best seen by the total auto-oscillation intensity in Fig. 4.36 **b** (brown diamonds), no systematical decrease in intensity along the SHO is observed. This agrees with the previous absence of such a tendency for $I = 2$ mA and substantiates the presence of additional coupling or energy flow along the SHO to counteract the expected intensity variations. Such a coupling similar to the observed D mode is not predicted, rendering this mode a candidate to mediate the coupling.

To conclude and briefly summarize: the auto-oscillatory state is likely best understood as two spin-wave bullets (Bullet A and Bullet B) oscillating at different frequencies (5.2 GHz and 5.45 GHz) at two distinct positions (500 nm and 1250 nm) localized to about $1\mu\text{m}$ length scale. This agrees well with the theoretical predictions presented in [204], as inferred from electrical measurements

and the simultaneous occurrence of 2 auto-oscillation frequencies. Next to the spin-wave bullets, two additional modes “C mode” and “D mode” are observed, which have a higher frequency and lower intensity. The “C mode” is of negligible intensity and attributed to a linear mode from the spin-wave spectrum localized in the center of the wire. The appearance of the “D mode” is unexpected and suggested to be a mode propagating along the SHO. It exhibits comparable intensity to the two bullets and extends with a constant frequency along the entire SHO. Suprisingly, the auto-oscillation amplitude shows no tendency to drop together with the decreasing STT along the SHO. This substantiates a coupling mechanism or energy flow along the SHO for both currents of $I = 2.5$ mA and $I = 2$ mA compensating the expected drop in amplitude along the SHO.

To further investigate this coupling and threshold-current behavior of the auto-oscillatory state, μ BLS-spectra were recorded for four equidistant positions along the SHO, while sweeping the driving current I . Figure 4.37 **a** presents the measured integrated auto-oscillation intensity (integrated over the measurement positions, black dots) and its inverse (blue triangles). The intensity is compared with the calculated output power (blue and black line) according to equation 84b in [250], including the critical current ζ , the non-linear damping coefficient Q and noise background η :

$$\text{Output-power / Intensity} \propto \frac{\eta Q}{\zeta + Q} \left(\frac{e^{\frac{-\zeta - Q}{\eta Q^2}}}{E_{\beta(\eta, \zeta, Q)} \left(\frac{Q + \zeta}{Q^2 \eta} \right)} + 1 \right) + \frac{\zeta - 1}{\zeta + Q} \quad (4.2)$$

Where $E_{\beta(\eta, \zeta, Q)}$ denotes the exponential integral-function. The calculation fits the data well for the values $\zeta = 2.28$ mA, $Q = 0.8$ and $\eta = 1$, as shown in Figure 4.37 **a**. This corresponds to an averaged critical current density in the Pt-layer of around 95 MA/cm², under the assumption of 64% of the current flowing in the Pt-layer. This value is considerably lower than, e.g., 300MA/cm² reported in [214] on a very similar system, but close to values ≈ 100 MA/cm² indicated by measurements in [152] and [240]. This likely results from differences in spin-transparencies and qualities of the HM/FM interface depending on the exact growth conditions. While the integrated auto-oscillation intensity is well explained by the theory, its spatial dependence contradicts the expected increase in critical current along the SHO, due to the current density variation.

This can be well seen, when analyzing the data according to [38, 152], approximating the BLS intensity to be proportional to the inverse damping $\propto 1/\lambda_{\text{eff}}$, so that its inverse scales linearly with the current density. This model is used to determine the critical current density in similar studies by extrapolation towards diverging intensity (crossing of inverse intensity with the current-axis). This is presented as a guide to the eye for the four separate positions along the SHO in Fig. 4.37 **b**. As can be seen from this qualitative extrapolation, the inverse SHO auto-oscillations indicate similar critical currents for the first three positions up to 1246 nm. A qualitative difference for the wider part (position 1662 nm) is revealed by the higher critical current estimate (dashed line).

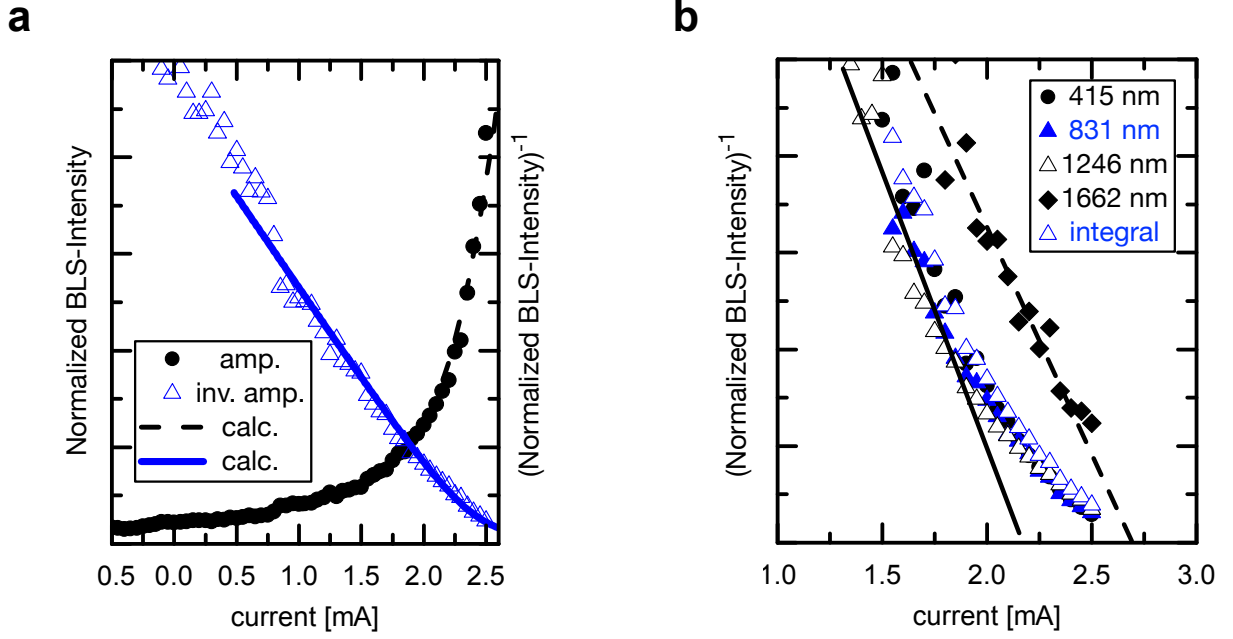


Figure 4.37: **a**, Total auto-oscillation intensity (black dots) and theoretically expected output power (black intermitted line) according to equation 4.2 from [250]. Additionally, the inverse intensity (blue triangles) is shown yielding a good agreement with the model (blue line) over the whole investigated range for the values $\zeta = 2.28$ mA, $Q = 0.8$ and $\eta = 1$. **b**, Inverse auto-oscillation intensity for different positions along the SHO. When approximating the critical current density, by linear extrapolation of the inverse intensity dependence (dashed and solid line, crossing with the x-axis, see e.g. [152]) the qualitative difference of the wider part of the SHO is clearly seen.

This agrees with the previous absence of a decrease in amplitude along the SHO of the earlier measurements for $I = 2$ mA and $I = 2.5$ mA (Fig 4.34 and Fig. 4.35) and the change in characteristics for positions exceeding 1500 nm. This further substantiates the presence of an unpredicted coupling mechanism along the SHO resulting in similar critical currents and amplitudes of the auto-oscillation, despite the current density variation along the tapered SHO. Furthermore, this coupling-mechanism seems to be present only up to a position of 1500 nm along the SHO.

One possibility to consider, is the reoccurring generation of an auto-oscillatory bullet-mode in the narrow end of the structure (highest current density) and subsequent travel along the SHO active region. This would explain the identical critical currents along the SHO and the finite spatial extend of this regime (up to 1500 nm), if combined with the assumption of a finite bullet-lifetime. Even though this model agrees with the measurements for lower driving currents of 2 mA, it can not describe the two measured intensity maxima for a higher current of 2.5 mA. Additionally, the qualitative different behavior for the mode frequencies is hard to understand within this model. Therefore, generation of laterally flowing spin-currents by spin-wave propagation is considered. In this hypothesis, the previously mentioned “D mode” (attributed to the MF signal) represents

spin-wave radiation, interacting with the two bullet modes. This is substantiated by its similar intensity, in particular at Bullet B. Its slightly lower intensity at the position of Bullet A, suggests its creation at Bullet B and travel direction towards Bullet A. The observation that only the narrower 1500 nm long part is coupled, reflects that radiation is hampered towards the wider segment (opposite direction) by the increase in spin-wave frequency. In this scenario, the STT would need to compensate the damping across the entire active region and suffice to explain the common threshold of auto-oscillation. This assumption would allow for an extended mode and the occurrence of different oscillation frequencies, as well as a rather constant amplitude of the auto-oscillations. Therefore, it agrees with and fits best with the experimental findings, but has not been predicted earlier and was not expected. The author suggests, that future studies should address if extension of current theories will allow to predict such a coupling and to record additional evidence for this effect.

To conclude, in context of auto-oscillation intensity it seems best to characterize the system as coupled with respect to amplitude of the auto-oscillation, but not with respect to frequency. The auto-oscillatory state and output power is best viewed in the perspective of the two-bullet-mode hypothesis (Bullet A and Bullet B, separately localized) including additional spin-wave radiation along the SHO, possibly mediated by the aforementioned D mode. Further measurements of output-power and frequency of the auto-oscillation in dependence on the driving current are presented in the appendix to complete the documentation for future studies (section A.6).

4.2.5 Microwave amplification and injection locking

In the next step injection-locking of the SHO to an external microwave signal is studied for the two bullet when applying $I = 2.5$ mA. While excitation by the STT allows for the oscillations to be incoherent and broad in spectral range, imprinting an additional periodic microwave signal with well defined phase should serve to select and enhance those auto-oscillatory dynamics matching in frequency and phase. This is expected to result in coherent auto-oscillations with higher amplitude and reduced linewidth. The ability of injection-locking SHO (section 2.3.3) is closely related to its general locking behavior, such as mutual (locked to another SHO) or self-locking of the SHO [251] as a requirement for sufficient performance (spectral coherence, linewidth, power) of SHO-arrays. Moreover, in this specific geometry the interesting question on the effect and possible control of the spin-wave bullets arises. Therefore, in the following study the driving current remains at $I = 2.5$ mA to set the SHO in the two-bullet state.

As a starting point of the discussion, the auto-oscillation are recorded at the position of Bullet A (500 nm along SHO, 5.2 GHz), when adding a microwave signal with a nominal power of -12 dBm for different frequencies, as shown in Fig. 4.38. As shown earlier (section 4.2.3) for these

low microwave powers no direct excitation of spin waves is expected, so that the influence of the microwave signal on the spin-wave dynamics is restricted to synchronization of the SHO.

For comparison, the thermal spectrum of the unpowered SHO (orange hollow dots), the effect of isolated microwave excitation (orange dots) and the pure excitation by a DC current (black crosses) are additionally shown in the graph. The two spectra of the unpowered SHO ($I = 0$) are identical within the noise of the measurement and confirm no detectable direct excitation of magnetization dynamics by the microwave current. This remains the case for the active SHO $I = 2.5$ mA, for microwave frequencies not matching the auto-oscillation frequencies. Such a spectrum is exemplarily shown for a microwave-frequency of 4.7 GHz, where the auto-oscillation spectra is unaltered with and without injected microwave current (black dots and black crosses).

However, if the microwave frequency is chosen to lie within the auto-oscillation spectra with Bullet A (5.2 GHz) or D mode (5.6 GHz), the spectrum changes significantly due to injection locking. For a frequency matching the one of Bullet A (red hollow dots) its intensity is increased by more than a factor of 4 in amplitude, while the amplitude for the D mode is simultaneously slightly reduced (to about 85%). This reduction of auto-oscillations not matching the microwave frequency is an important indication of successful injection locking and excludes simply adding directly excited dynamics by the microwave source to the existing auto-oscillations. This supports the idea that the energy supplied by the STT is partly redirected into the amplified mode. This behavior is mirrored, when the microwave frequency matches the D mode (blue triangles, 5.6 GHz), supporting a systematic influence.

This synchronization and its effect on the spectra were then studied for a broader range of external frequencies covering the entire auto-oscillatory spectrum. For each spectrum, the two signals from Bullet A and from the D mode have been fitted by two Lorentzian to analyze the individual signal contributions. Figure 4.39 shows the extracted dependences of amplitude (a), linewidth (b) and

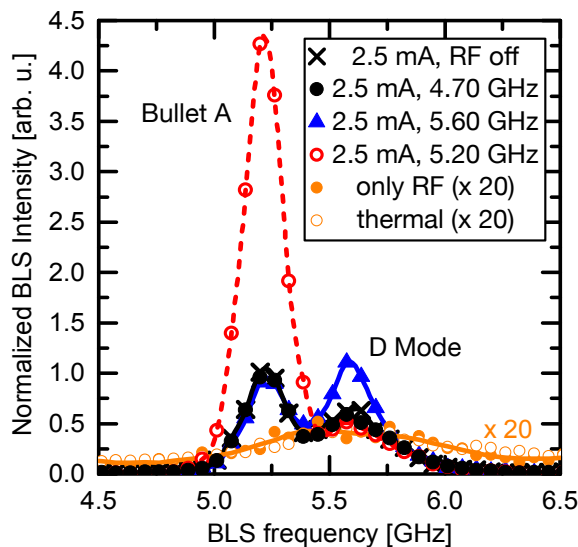


Figure 4.38: μ BLS-spectra on the injection-locked SHO: thermal excitation (orange hollow dots), pure DC excitation (black crosses), pure microwave excitation (orange dots, frequency 5.6 GHz) and injection-locking on the driven auto-oscillating SHO for $I=2.5$ mA (red dots and blue triangles) to different microwave signals of -12 dBm nominal power. For better visibility the μ BLS-spectra for thermal and pure microwave excitation have been multiplied by a factor of 20.

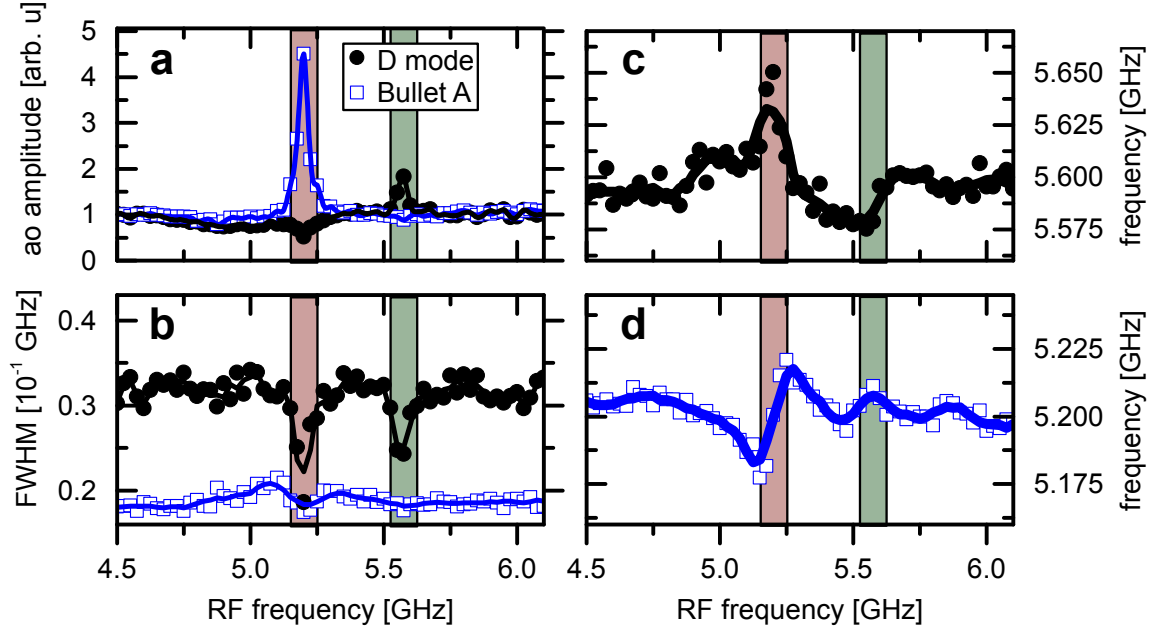


Figure 4.39: Injection locking of the SHO to microwave frequencies in the range between 4.5 GHz and 6.2 GHz for a nominal power of -12 dBm. The amplitude **a**, FWHM **b**, and frequencies **c**, **d** are shown for the main two auto-oscillatory modes (Bullet A and D mode), extracted by fitting each spectrum with two Lorentzian. The estimated locking-intervals of about 100 MHz width around the auto-oscillation frequencies of 5.2 GHz and 5.6 GHz are marked by brown and green squares, respectively. Frequency-locking, amplification and linewidth reduction for the Bullet and propagating D mode are observed.

mode frequencies (**c** and **d**) on the microwave frequency for a nominal microwave power of -12 dBm.

First, the observations for a microwave signal having a frequency of 5.2 GHz are assessed. As aforementioned, amplification and suppression of the Bullet A and D mode, respectively, is observed. The amplitude of the bullet mode (having an intrinsic frequency of 5.2 GHz) is increased by a factor of about 4.5 and accompanied by a suppression of the D mode to about half its amplitude. Simultaneously, the linewidths of both auto-oscillation signals drop down to the spectral resolution of $\text{FWHM} = 190 \pm 11$ MHz of the μBLS set-up. On first glance, it is surprising, that this reduction in linewidth is observed for both modes. For the bullet mode this was expected, since its FWHM has been electrically characterized to be around 20 MHz [159], well below the detection limit and it additionally locks to the external frequency. However, in contrast to this, the line width reduction for the D mode was not expected. This mode does not match the microwave frequency and, therefore, is not directly synchronized to the microwave signal. This is clearly seen from the extracted frequencies as shown in Fig. 4.39 **c** (D mode) and **d** (Bullet A). While the Bullet exhibits

frequency-locking adopting the frequency of the microwave signal in 100 MHz-wide locking window as indicated by the brown square in the background of the data, the D mode has a frequency of around 5.65 GHz distinct from the microwave frequency of 5.2 GHz. The corresponding 100 MHz wide locking-window for the D mode is located at higher frequencies 5.575 GHz as indicated by a green background distinct from the microwave signal of 5.2 GHz. Consequently, the reduction in linewidth of the D mode can not be traced back to direct synchronization.

Therefore, the existence of an interaction between these two modes seems implied, so that they simultaneously reduce in line width within both locking windows (see Fig. 4.39 **b**). Such a behavior is also observed for the amplitude reduction of the D mode and supports the hypothesis of a coupling mechanism as indicated by the earlier presented spatial dependence of the frequency shift and amplitude along the SHO. The simplest and most likely explanation of this effect is a general stabilization of the auto-oscillations. For instance, a substantial increase in line width, when more than one auto-oscillatory mode is excited has been reported before and is attributed to mode-hopping [252, 253]. Combined with the reasonable assumption, that mode-hopping is reduced during injection-locking, for example by stabilizing the bullet mode, also the linewidth of the D mode would reduce simultaneously. Next to this, the thermal fluctuations of the spatial position of Bullet A should be considered as an additional influence on the spectral noise equivalent to the mode-hopping. It seems reasonable to assume, that these fluctuations will be suppressed during injection locking, since the imprinted bullet frequency defines its position in the tapered SHO due to the spatial variation in spectra. However, there is an additional point to consider: As will be shown later in the spatial resolved measurements of the locked states for this frequency around 5.2 GHz Bullet B is suppressed and of low intensity. In case of an interaction/scattering of the D mode with bullet B (indicated in the measurements of the free-running SHO) its lowered intensity will reduce scattering events also resulting in the here observed linewidth reduction.

As is expected close to the locking regime frequency pulling is observed. This is seen as a change in auto-oscillator frequency towards the external microwave frequency, but not matching it. Simultaneously, in this regime, the linewidth of the auto-oscillation is increased attributed to the stability transition between locked and unlocked state, as reported e.g. in [254].

In short, for the tapered SHO two frequency windows are observed, in which frequency locking and amplitude enhancement of the auto-oscillation is confirmed. The two windows are approximately 100 MHz wide and centered around the bullet frequency of 5.2 GHz and the D Mode for an external frequency of 5.575 GHz. Surprisingly, inside the separate locking windows, a line width reduction is observed for both modes simultaneously, which is attributed to decreased mode-hopping and general increased mode stability.

Now the focus is put on the signal/mode amplification within the first locking-window of Bullet A at 5.2 GHz for a microwave power range from -21 dBm up to 0 dBm. As for the previous measurements, the driving current was kept constant at $I = 2.5$ mA and the position remained on

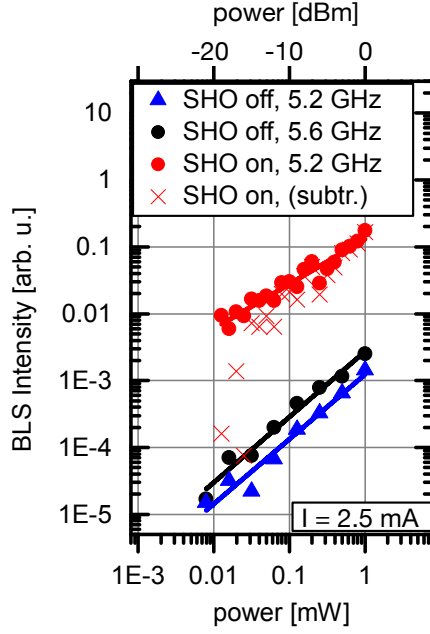


Figure 4.40: Auto-oscillation intensity in dependence on the injected microwave power measured by μ BLS at a position of 500 nm along the SHO (red dots). Additionally, the increase in auto-oscillation intensity after subtraction of the constant auto-oscillation background is shown (red crosses). For comparison, the directly excited spin-wave signal for $I = 0$ mA (SHO off) is presented for an identical microwave frequency of 5.2 GHz (blue triangles) and the microwave frequency of maximum excitation efficiency at 5.6 GHz (black dots). While the directly excited spin-wave signal exhibits a linear dependence on the microwave power P , the Intensity for $I = 2.5$ mA scales as $P^{2/3}$.

Bullet A, situated 500 nm along the SHO and the microwave frequency was chosen to match the 5.2 GHz of the bullet. Figure 4.40 presents the extracted auto-oscillation amplitude of the locked Bullet A (red dots). The intensity of the signal consists of the initial auto-oscillation intensity and an enhancement by the injected microwave signal. The enhancement after subtraction of the constant initial auto-oscillation power is marked by red crosses. Interestingly, the relation of the signal-increase with applied microwave power differs from the expected power law. The exponent is predicted to be 0.5 [255], while linear fitting of the unsubtracted signal results in a power-exponent of 0.67 ± 0.04 close to $2/3$ and even larger values after subtraction. The author is not aware of any experimental work on this exponent, so that this experiment could indicate the necessity to rework current theories, with the prospect of greater amplification than assumed so far.

For comparison, the directly excited spin-wave signal in the unpowered SHO $I = 0$ mA is presented for an identical microwave frequency of 5.2 GHz and the microwave frequency of maximum excitation efficiency at 5.6 GHz in the unpowered SHO (black and blue dots). The linear fits of the data in the double logarithmic plot confirm the expected linear dependence of the directly excited dynamics with microwave power. The slopes are 0.97 ± 0.08 and 0.98 ± 0.06 covering the expected value of 1. This signal amplification and line width reduction might enable the usage of the SHO as a microwave amplifier or detector within the locking regime and as controllable coherent dynamic sources. Due to the tapering a broader tuneability by auto-tuning the bullet position can be expected, but has been beyond the scope of this thesis and remains an interesting question for future studies to address.

In the final step, the auto-oscillations in the tapered SHO during injection locking are spatially

mapped by μ BLS for different frequencies of the imprinted microwave signal and nominal power of $P = 0$ dBm. In the locked-regime, three different states are observed. Depending on the chosen microwave frequency either Bullet A (having a frequency of ~ 5.2 GHz) or Bullet B (~ 5.45 GHz) are selected by injection locking, in terms of their individual amplification and reduction in linewidth. The opposing bullet with greater spectral separation to the imprinted microwave signal is simultaneously suppressed resulting in a single-bullet operation of the SHO. For abbreviation these two states will be classified as single-bullet state A or B (SB A and SB B).

Exemplary measurements for these two states are shown for microwave frequencies of 5.255 GHz (SB A) in Fig. 4.41 **a** to **c** and 5.4 GHz (SB B) in Fig. 4.41 **d** to **f**. The recorded signal intensities of the auto-oscillation spectra along the SHO are shown on a logarithmic color-scale in **a** and **d**. Each spectrum has been fitted by a single Lorentzian to extract the frequency (Fig. 4.41 **b** to **e**), as

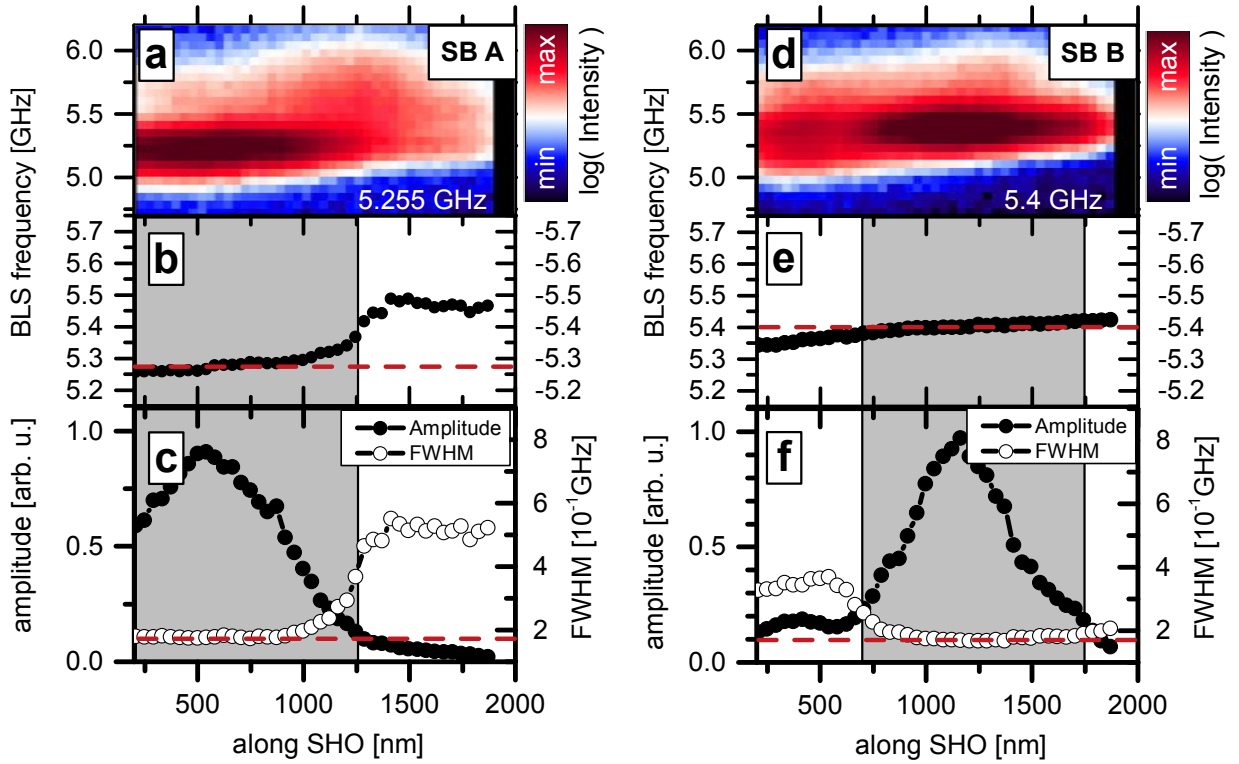


Figure 4.41: Injection locked auto-oscillations measured spatially resolved by μ BLS along the SHO for microwave frequencies of 5.255 GHz and 5.4 GHz. The measured spectra **a** and **d**, frequency **b** and **e**, as well as amplitudes and FWHM, **c** and **f** as extracted by fitting each spectrum by a single Lorentzian are displayed. As a reference the average auto-oscillation intensity prior to microwave injection and microwave frequency is indicated by a dashed line in **b,c** and **e,f**. Single bullet states (SB A in **a** to **c** and SB B in **d** to **e**) are observed, enhancing either one of the bullet modes. The estimated spatial extend of the locked regime (marked by grey background as guide to the eye) is clearly seen by the transition of the FWHM down to the spectral resolution of the set-up.

well as FWHM and amplitude (Fig. 4.41 **d** to **f**) of the auto-oscillation signal.

Focusing on the SB A state shown in **a** to **c**, Bullet A is localized in the narrow part of the SHO at a position $\sim 500 \pm 100$ nm and adopts the external microwave frequency (marked by a dashed red line in **b**). It is amplified in intensity about a factor of 8 to 10. For comparison the average auto-oscillation intensity prior to the microwave injection (free-running) is indicated by a dashed red line in **c** as a guide to the eye. Simultaneously, the remaining Bullet B, previously localized at a position around 1250 nm is suppressed and outputs a considerably lower signal (about a factor of 13 compared to Bullet A), with a clear frequency-difference. As indicated by the spatial dependence of the frequency and line width (FWHM) in Fig. 4.41 **b** and **c**, the spatial extend of the locked regime extends to an estimated position around 1250 nm along the SHO. Up to this position, the frequency is pulled towards the one of the locking signal accompanied by a reduction of the FWHM below the μ BLS resolution limit (192 ± 11 MHz). Additionally, the auto-oscillation amplitude is reduced when proceeding further along the SHO > 1250 μ m to about 50% to 60% compared to the free-running auto-oscillator and the FWHM increases to about 500 MHz. Therefore, this state is classified as a single-bullet operation of bullet A, which is located at a position of 500 nm and enhanced by the injected signal, while competing modes such as Bullet B and the D mode are suppressed.

The complementary SB B state is measured for a higher microwave frequency of 5.4 GHz shown in Fig. 4.41 **d** to **f**. Treatment of the data and presentation are similar as the previously discussed SB A state in Fig. 4.41 **a** to **c**. For the SB B state, the locking-regime is estimated to extend over the wider part of the wire down to a position of around 700 nm and enhances Bullet B with main intensity at a position around 1160 ± 50 nm. This is close to the free-running bullet position of 1250 nm, but points towards the possibility of a slightly changed bullet position by injection locking. As before, inside the locked part of the SHO the FWHM is reduced to the detection limit of the set-up.

Besides the two single-bullet states (SB A and SB B) another type of auto-oscillatory state is observed in the experiments, which will in the following be referred to as injection locked “double bullet state” (DBS). The DBS shows locking and fairly equal intensities of both bullets simultaneously, but with less pronounced amplitude enhancements and linewidth reduction. In the same manner as in the previous analysis and presentation, this state is shown exemplarily for the injected frequencies of 5.35 GHz (between the frequencies of each bullet) and 5.625 GHz (above both bullet frequencies) in Figure 4.42 **a** to **f**, respectively.

These measurements reveal two intensity maxima situated in the narrow and in the wider part of the wire. Interestingly, the position of the maxima is not identical to the prior bullet positions (500 nm and 1250 nm), but are now situated at ~ 375 nm and ~ 1120 nm for an injected frequency of 5.35 GHz, while being at a position of ~ 415 nm and ~ 1250 nm for a frequency of 5.625 GHz. Since by comparison of the spectral background with the recorded data an accidental

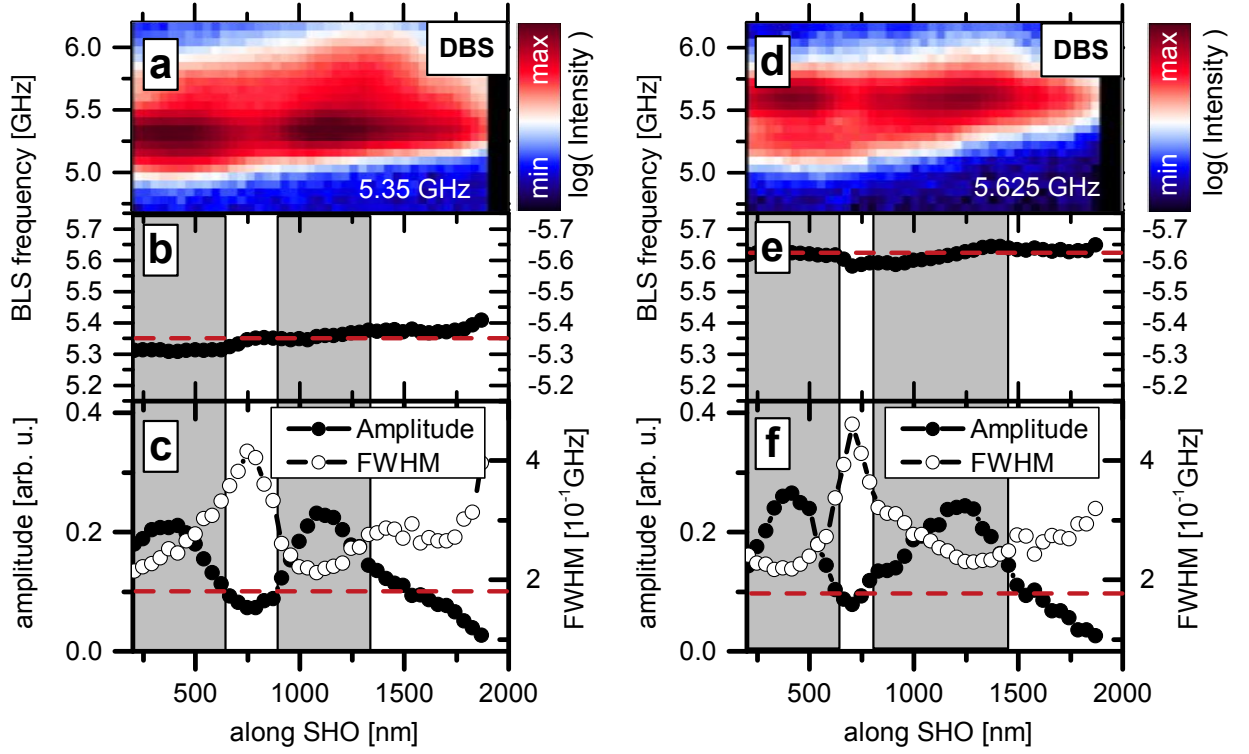


Figure 4.42: Injection locked auto-oscillations measured spatially resolved by μ BLS along the SHO for microwave frequencies of 5.255 GHz and 5.4 GHz at a nominal power of 0 dBm. The measured spectra **a** and **d**, frequencies **b** and **e** as well as amplitudes and FWHM, **c**, **f** as extracted by fitting each spectrum by a single Lorentzian are displayed. As a reference, the average auto-oscillation intensity prior to microwave injection and microwave frequency are indicated by dashed lines in **b,c** and **e,f**. A locked double bullet states (DBS) is observed. The amplitudes of both bullets is found to be of equal intensity (within 10%) substantiating a coupling between the bullets. The FWHM reveals an unlocked region of increased linewidth separating two locked bullets.

shift in measurement position can be excluded, these measurements further point towards the earlier hypothesis of auto-tuning of the bullet frequency by adjusting its position in the tapered SHO, enabled by the spatial dependence of the spectra. This remains an open question for future studies but indicates the possibility to control the bullet positions by the injected frequency.

Regarding this state, when considering the amplitude and FWHM shown in Fig. 4.42 **c** and **f**, it can further be seen, that the extracted auto-oscillation amplitudes are identical for both modes, while the linewidth increases between the two separate bullets. Note that this spatial dependency of the FWHM excludes models suggesting standing wave formation, since the linewidth would then be expected to be constant throughout the SHO. Nevertheless, the FWHM does not decrease below the detection limit and takes a value around 230 ± 20 MHz. Such observations can be explained by mode-hopping between the states SB A and SB B. This hints on the idea that in the DBS, the

SHO switches between the two different SB A and SB B operations rendering them less stable. This agrees with the fact of the changed bullet position with respect to the free running one and would suffice to explain the higher linewidth (since of the shorter life-time) as well as the reduced amplitude. Such a scenario fits well to the situation of the DBS observed for a frequency between the bullets of 5.35 GHz. However, the appearance of this state for frequencies above the two bullets (5.625 GHz) can not be readily interpreted in this way, since it seems unlikely that locking of Bullet A (5.2 GHz) can be achieved for such a large spectral separation and is not dominated by locking of Bullet B. This state seems to rather indicate a standing wave formation along the SHO. This is supported by the second weak maximum created in the SB B state at a position of 400 nm (Fig. 4.41 f) as a possible signature of this standing wave contribution. These two hypothesis could be tested against each other in future experiments, by similar measurements for different injected powers. In the higher pumping power regime such measurements should reveal if the increase of FWHM between the proposed bullet positions originates from the lorentzian fitting of the reduced oscillation amplitude agreeing with standing wave formation. In the lower power regime transitions between the SB A and SB B state could be revealed by a gradual change in the amplitude relations and frequency pulling.

In conclusion, the frequency of an externally imprinted microwave signal can be used to select between different auto-oscillatory states in a tapered SHO, which are classified into single-bullet operation states (SB A and SB B), as well as a mixed state (DBS). For frequencies between the single bullet states the DBS is attributed to switching between the SB A and SB B with time showing a greater line width and less enhancement of the auto-oscillation amplitude. Different localizations of the auto-oscillation maxima are found depending on the microwave frequency. With respect to practical application of such SHO-arrays for electrical signals, this provides a control possibility on output power, spatial localization of the auto-oscillations and reduction of their generation linewidth. These SHO and their synchronization is of particular interest, since their intrinsic spin-wave spectra is already broader in frequency promising an enhanced locking window with respect to single-mode nano-contact SHO. When considering the bullet formation, this is another step towards the investigation of non-linear spin-wave emission by bullets as well as spin-wave interaction with bullets.

CHAPTER 5

Summary and outlook

This thesis on "Spin-wave generation and transport in magnetic microstructures" was devoted to the field of magnonics. In particular, the first part focussed on the challenge of miniaturization and control of spin waves on the sub-micron scale in thin film microstructures. A novel approach, which allows confining spin-wave transport to nanometre-wide channels by utilizing magnetic domain walls is demonstrated experimentally for the first time by μ BLS and further analyzed by micromagnetic simulations for two material systems $\text{Ni}_{81}\text{Fe}_{19}$ and crystalline Fe. This has a great potential for spin-wave circuitry with high integration density, but is also of fundamental interest with regard to understanding the link between spin-wave dynamics and the magnetic texture of a microstructure.

It is found, that the waveguides formed by domain walls confine spin waves transversally to sub-wavelength wide beams with a well-defined wave vector along the wall. Furthermore, they allow field-free operation and are tunable in width by material parameters down below a few tens of nanometers. The propagation characteristics of the modes channeled within domain walls are studied for 90° as well as 180° Néel walls for both material systems in the thermal, linear and non-linear regime. In $\text{Ni}_{81}\text{Fe}_{19}$ microstructures a gapless, initially linear and dipolar dominated relation between the spin-wave wave vector and frequency is found with typical group velocities of around 2 to 4 $\mu\text{m}/\text{ns}$. This linearity minimizes dispersion broadening and is, thus, promising for spin-wave signal transmission. The operating range of the channel seems limited to frequencies below the spin-wave band of the domains, since for higher frequencies radiation losses are indicated. Hence, exploring different materials with stronger anisotropies and smaller domains is suggested to extend the operating regime and further reduce the channel width.

The broad variety of means to manipulate domain walls and their networks opens up extensive possibilities in combination with the channeled spin-wave transport. For instance, domain walls can be controlled electrically [256], optically [257], by spin or charge currents [258, 259], thermal

gradients [260], pinning sites [261] or spin waves themselves [262]. This can not only be utilized to define and shape the spin-wave transport but also to probe changes in the magnetic texture via spin waves. Thus, paving the way for sensors, data storage and reconfigurable circuitry. In this regard, a lateral control of the spin-wave propagation path via manipulation of the domain wall position over several microns by small magnetic fields is demonstrated. The proportionality constant is found to be as large as $5.57 \pm 0.75 \mu\text{m/mT}$. This serves as a proof of concept for utilizing these domain wall channels as highly flexible waveguides independent from the specific geometry of a microstructure.

In addition to this, the experimental results on Fe microstructures indicate a dependency of the domain wall spectra on the orientation of the domain wall plane. This interesting modification of the spectrum by the angle of the path along which the domain walls form has not been predicted or studied before. Two $\sim 5^\circ$ differently oriented 90° Néel wall channels were investigated and showed distinct experimentally recorded spin-wave spectra. This difference was then utilized to selectively send spin waves along one or both of the channels by choosing different spin-wave frequencies. Pinning sites are expected to stabilize these slightly different orientations, but it remains unclear if they affect the guided spin waves additionally. Nevertheless, this complementary possibility to alter the channel properties is particularly promising for passing spin waves between several receivers and senders by tailoring domain wall networks by their position, orientation and chosen operating frequency.

Moreover, guiding spin waves through linked 90° Néel walls, which suddenly turn in direction, is confirmed experimentally within Fe. In the experiment on spin-wave transmission between interconnected 90° and 180° walls mainly spin-wave reflection was observed. This is believed to be attributed to mismatches between the spectra of the different type of walls and the presence of vortices at the linking points. However, a better understanding of these effects still needs to be developed. Their future investigation is of great prospect in designing mismatch-free junctions, e.g. interconnection-angles, to uncover the full potential of these domain wall networks.

Localized ion irradiation is a uniquely suited tool to systematically study such details on configuring domain wall channels. This is due to the fact, that pinning sites or material modifications can be introduced locally with high precision. Thus, it is not only possible to stabilize different domain wall networks, but also to induce targeted changes in the local magnetic properties for individual channels. The possibility to switch between distinct remanent domain wall configurations in one and the same microstructure stabilized by localized ion irradiation is demonstrated as an outlook and proof of principle in the appendix (section A.2).

In the non-linear regime, an unpredicted second class of higher harmonic generated spin waves is observed in the experiments. These second and third harmonic spin waves are confined to the sides of the domain wall and have doubled or tripled frequency of the channeled mode. The two observed beams could not be directly excited suggesting an anti-phase relation with respect to each

other. A full understanding of these modes still remains to be developed. Three hypotheses are presented and suggested to be tested by future studies: 1) transversal confinement of spin waves to a softened potential well created by the domain wall; 2) hybridization of domain modes and channeled domain wall modes at the side of the channel; and 3) non-linear frequency conversion of spin waves at the side of the domain wall.

Amongst other non-linear effects, in particular, a conversion between spin waves excited in the domains and channeled spin waves of lower frequency is indicated in the experiments. This implies, that spin waves in the bounded domains are injected into the domain wall channel changing their frequency as well as direction. Extensive systematic studies are strongly suggested to unravel these phenomena. This is fundamentally very intriguing but could also potentially allow future devices to use such non-linearities to control frequency and position of spin-wave signals by applied input power and conversion effects.

The second part of the thesis addressed the generation and control of spin-wave bullets by the spin transfer torque (STT) in tapered nanowire spin Hall oscillators (SHO). The active region of these oscillators is larger than typically studied nano-contact devices and as long as 2- μm . Earlier electrical characterization and calculations based on a non-linear Ginzburg-Landau model indicated, that this allows the formation of two differently localized spin-wave bullets simultaneously. This has been directly observed in the present work by μBLS measurements. The two spin-wave bullets have a size of about 1 μm and oscillate at distinct frequencies and positions creating a polychromatic total output.

In the context of modifying the SHO and bullet formation, imprinting external microwave signals by injection-locking is shown to synchronize the SHO. To the authors knowledge, this is the first time that auto-oscillations are recorded spatially resolved during injection-locking. The synchronization results in linewidth reduction reaching below the experimental resolution of ~ 192 MHz and frequency-locking of the individual bullets within approximately 100 MHz wide windows centered around their free-running frequency. Additionally, in the injection-locked regime their amplitude is enhanced and scales as $P^{3/2}$ with the injected microwave power P . The different states can be selected by the frequency of the external microwave signal. Thus, this defines the frequency of the SHO output, which is of key-importance for modulation in telecommunication applications. These results are a first step towards the control of localization, amplitude and frequency of spin-wave bullets, so that, for example their interaction with spin waves can be systematically tested. The observed amplitude enhancement of an external microwave signal might also pave the way for utilizing these devices as microwave amplifiers or detectors.

Next to the expected bullet formation an additional mode extending along the entire SHO having a constant frequency is observed. The presence of this mode and details of the spatial variation of the auto-oscillation amplitude for different driving currents seem not explainable by current models. The experiments suggest a coupling mechanism influencing the auto-oscillation ampli-

tude along the SHO. It is hypothesized, that the coupling is due to spin-currents pumped by the auto-oscillating modes, but clearly further research and evidence is needed. For this pulsed current sources can be utilized to investigate the SHO characteristics for higher driving currents and on an increasing number of bullet modes. Combined with time-dependent BLS-studies the bullet formation process, and transient times of injection locking can be studied in the time-domain to solidify the current understanding. Due to the high degree of analogy of SHOs to LASERs, the author would like to suggest research on similar concepts not only for injection-locking but also, for instance, spin-wave amplifiers [263], spectral/spatial hole burning [264], mode-hopping, utilization of Q-switches [265] and so forth. These concepts are promising for creating miniaturized coherent continuous or pulsed spin-wave sources.

Lastly, there is great potential in combining the channeling of spin waves by domain walls with the flexible SHO excitation mechanism. Utilizing injected spin currents for excitation of spin waves in domain walls promises scaling capability down to point-contacts and coverage of broader spin-wave wavelength and frequency range compared to excitation by microstrip antennas. As an important improvement, due to the angular dependency of the STT, a spatially selective excitation of spin waves and auto-oscillations only within the domain wall, but not in the surrounding domain is expected. Furthermore, domain walls are promising candidates to form nanowire spin Hall oscillators, which form spontaneously, and are of unprecedented nanoscale width tuneable by material parameters. These would be even reconfigurable and controllable in position. Besides this anticipated excitation of channeled spin waves, analytical treatment, micromagnetic simulations and experiments demonstrated, that current-driven domain wall oscillations can excite short wavelength spin waves in the surrounding domains [266–269]. In these studies the fast oscillation of the potential well functions as a nano-sized antenna both for domain wall resonances and radiating modes. Therefore, it seems very promising for future studies to explore the rich possibilities in the interplay of spin currents with the magnetization dynamics and auto-oscillations in domain wall networks and spin waves channeled within it.

Own publications

- [O1] L. Korber, K. Wagner, A. Kákay, H. Schultheiß, *Spin-wave reciprocity in the presence of Néel walls*, IEEE Magnetics Letters **8**, 1–4 (2017).
- [O2] F. M. Römer, M. Möller, K. Wagner, L. Gathmann, R. Narkowicz, H. Zähres, B. R. Salles, P. Torelli, R. Meckenstock, J. Lindner, M. Farle, *In situ multifrequency ferromagnetic resonance and x-ray magnetic circular dichroism investigations on Fe/GaAs(110): Enhanced g-factor*, Applied Physics Letters **100**, 092402 (2012).
- [O3] K. Schultheiss, K. Wagner, A. Kákay, H. Schultheiß, *Chapter 9: Steering Magnons by Non-collinear Spin Textures*, in K. Schultheiss, K. Wagner, A. Kákay, H. Schultheiß (Hg.), *Spin Wave Confinement*, 261–294, CRC Press, 6000 Broken Sound Parkway NW, Suite 300 Boca Raton, FL 33487-2742 (2017).
- [O4] R. A. Gallardo, A. Banholzer, K. Wagner, M. Körner, K. Lenz, M. Farle, J. Lindner, J. Fassbender, P. Landeros, *Splitting of spin-wave modes in thin films with arrays of periodic perturbations: theory and experiment*, New Journal of Physics **16**, 023015 (2014).
- [O5] C. Schoeppner, K. Wagner, S. Stienen, R. Meckenstock, M. Farle, R. Narkowicz, D. Suter, J. Lindner, *Angular dependent ferromagnetic resonance analysis in a single micron sized cobalt stripe*, Journal of Applied Physics **116**, 033913 (2014).
- [O6] G. Hlawacek and R. Bali F. Röder, Y. Aleksandrov, A. Semisalova, S. Wintz, K. Wagner, H. Schultheiß, S. Facsko, J. Fassbender, *Tailoring magnetic nanostructures with neon in the ion microscope*, Microscopy and Microanalysis **22**, S3 1716-1717 (2016).
- [O7] M. Langer, K. Wagner, T. Sebastian, R. Hübner, J. Grenzer, Y. Wang, T. Kubota, T. Schneider, S. Stienen, K. Lenz, H. Schultheiss, J. Lindner, K. Takanashi, R. E. Arias, J. Fassbender, *Parameter-free determination of the exchange constant in thin films using magnonic patterning*, Applied Physics Letters **108**, 102402 (2016).
- [O8] K. Wagner, S. Stienen, M. Farle, *Continuous wave approach for simulating Ferromagnetic Resonance in nanosized elements*, arXiv:1611.06153 (2016).

- [O9] K. Wagner, A. Kákay, K. Schultheiss, A. Henschke, T. Sebastian, H. Schultheiss, *Magnetic domain walls as reconfigurable spin-wave nanochannels*, Nature Nanotechnology **11**, 432 (2016).
- [O10] H. Schultheiss, K. Wagner, A. Kákay, K. Schultheiss, A. Henschke, T. Sebastian, *Magnetic domain walls as controllable spin-wave nanochannels*, SPIE Newsroom (2017).
- [O11] K. Wagner, *Charakterisierung periodisch strukturierter magnetischer dünner Filme mittels Ferromagnetischer Resonanz*, Master-Arbeit, University Duisburg-Essen (2013).

Bibliography

- [1] A. Fert, *Nobel Lecture: Origin, development, and future of spintronics*, Reviews of Modern Physics **80**, 1517 (2008).
- [2] S. A. Wolf, *Spintronics: A Spin-Based Electronics Vision for the Future*, Science **294**, 1488 (2001).
- [3] G. Binasch, P. Grünberg, F. Saurenbach, W. Zinn, *Enhanced magnetoresistance in layered magnetic structures with antiferromagnetic interlayer exchange*, Physical Review B **39**, 4828 (1989).
- [4] M. N. Baibich, J. M. Broto, A. Fert, F. N. Van Dau, F. Petroff, P. Etienne, G. Creuzet, A. Friederich, J. Chazelas, *Giant Magnetoresistance of (001)Fe/(001)Cr Magnetic Superlattices*, Physical Review Letters **61**, 2472 (1988).
- [5] M. Julliere, *Tunneling between ferromagnetic films*, Physics Letters A **54**, 225 (1975).
- [6] L. Berger, *Emission of spin waves by a magnetic multilayer traversed by a current*, Physical Review B **54**, 9353 (1996).
- [7] J. C. Slonczewski, *Current-driven excitation of magnetic multilayers*, Journal of Magnetism and Magnetic Materials **159**, L1 (1996).
- [8] J. J. Nowak, R. P. Robertazzi, J. Z. Sun, G. Hu, J.-H. Park, J. Lee, A. J. Annunziata, G. P. Lauer, R. Kothandaraman, E. J. O'Sullivan, P. L. Trouilloud, Y. Kim, D. C. Worledge, *Dependence of Voltage and Size on Write Error Rates in Spin-Transfer Torque Magnetic Random-Access Memory*, IEEE Magnetics Letters **7**, 1 (2016).
- [9] Z. Diao, M. Pakala, A. Panchula, Y. Ding, D. Apalkov, L.-C. Wang, E. Chen, Y. Huai, *Spin-transfer switching in MgO-based magnetic tunnel junctions (invited)*, Journal of Applied Physics **99**, 08G510 (2006).
- [10] C. Mathieu, J. Jorzick, A. Frank, S. O. Demokritov, A. N. Slavin, B. Hillebrands, B. Bartenlian, C. Chappert, D. Decanini, F. Rousseaux, E. Cambril, *Lateral Quantization of Spin Waves in Micron Size Magnetic Wires*, Physical Review Letters **81**, 3968 (1998).

-
- [11] J. Jorzick, S. O. Demokritov, B. Hillebrands, M. Bailleul, C. Fermon, K. Y. Guslienko, A. N. Slavin, D. V. Berkov, N. L. Gorn, *Spin Wave Wells in Nonellipsoidal Micrometer Size Magnetic Elements*, Physical Review Letters **88**, 047204 (2002).
- [12] M. Bailleul, D. Olligs, C. Fermon, S. O. Demokritov, *Spin waves propagation and confinement in conducting films at the micrometer scale*, EPL (Europhysics Letters) **56**, 741 (2001).
- [13] G. de Loubens, V. V. Naletov, O. Klein, J. B. Youssef, F. Boust, N. Vukadinovic, *Magnetic Resonance Studies of the Fundamental Spin-Wave Modes in Individual Submicron Cu/NiFe/CuPerpendicularly Magnetized Disks*, Physical Review Letters **98**, 127601 (2007).
- [14] G. Gubbiotti, G. Carlotti, T. Okuno, M. Grimsditch, L. Giovannini, F. Montoncello, F. Nizzoli, *Spin dynamics in thin nanometric elliptical Permalloy dots: A Brillouin light scattering investigation as a function of dot eccentricity*, Physical Review B **72**, 184419 (2005).
- [15] M. A. W. Schoen, D. Thonig, M. L. Schneider, T. J. Silva, H. T. Nembach, O. Eriksson, O. Karis, J. M. Shaw, *Ultra-low magnetic damping of a metallic ferromagnet*, Nature Physics **12**, 839 (2016).
- [16] C. Hauser, T. Richter, N. Homonnay, C. Eisenschmidt, M. Qaid, H. Deniz, D. Hesse, M. Sawicki, S. G. Ebbinghaus, G. Schmidt, *Yttrium Iron Garnet Thin Films with Very Low Damping Obtained by Recrystallization of Amorphous Material*, Scientific Reports **6**, 082408 (2016).
- [17] B. Pfau, C. M. Günther, T. Hauet, S. Eisebitt, O. Hellwig, *Thermally induced magnetic switching in bit-patterned media*, Journal of Applied Physics **122**, 043907 (2017).
- [18] A. Deschenes, S. Muneer, M. Akbulut, A. Gokirmak, H. Silva, *Analysis of self-heating of thermally assisted spin-transfer torque magnetic random access memory*, Beilstein Journal of Nanotechnology **7**, 1676 (2016).
- [19] A. V. Kimel, *All-optical switching: Three rules of design*, Nature Materials **13**, 225 (2014).
- [20] E. B. Myers, *Current-Induced Switching of Domains in Magnetic Multilayer Devices*, Science **285**, 867 (1999).
- [21] D. Grundler, *Reconfigurable magnonics heats up*, Nature Physics **11**, 438 (2015).
- [22] A. V. Chumak, V. I. Vasyuchka, A. A. Serga, B. Hillebrands, *Magnon spintronics*, Nature Physics **11**, 453 (2015).
- [23] A. Lara, J. R. Moreno, K. Y. Guslienko, F. G. Aliev, *Information processing in patterned magnetic nanostructures with edge spin waves*, Scientific Reports **7**, 5597 (2017).
- [24] J. M. Winter, *Bloch Wall Excitation. Application to Nuclear Resonance in a Bloch Wall*, Physical Review **124**, 452 (1961).
-

- [25] J.-C. S. Lévy, *Bloch wall spin waves*, Journal of Applied Physics **50**, 7418 (2008).
- [26] F. Garcia-Sanchez, P. Borys, R. Soucaille, J.-P. Adam, R. L. Stamps, J.-V. Kim, *Narrow Magnonic Waveguides Based on Domain Walls*, Physical Review Letters **114**, 247206 (2015).
- [27] V. E. Demidov, S. Urazhdin, S. O. Demokritov, *Direct observation and mapping of spin waves emitted by spin-torque nano-oscillators*, Nature Materials **9**, 984 (2010).
- [28] S. Bonetti, V. Tiberkevich, G. Consolo, G. Finocchio, P. Muduli, F. Mancoff, A. Slavin, J. Åkerman, *Experimental Evidence of Self-Localized and Propagating Spin Wave Modes in Obliquely Magnetized Current-Driven Nanocontacts*, Physical Review Letters **105**, 217204 (2010).
- [29] J. C. Slonczewski, *Excitation of spin waves by an electric current*, Journal of Magnetism and Magnetic Materials **195**, L261 (1999).
- [30] M. Madami, S. Bonetti, G. Consolo, S. Tacchi, G. Carlotti, G. Gubbiotti, F. B. Mancoff, M. A. Yar, J. Åkerman, *Direct observation of a propagating spin wave induced by spin-transfer torque*, Nature Nanotechnology **6**, 635 (2011).
- [31] A. Slavin, V. Tiberkevich, *Spin Wave Mode Excited by Spin-Polarized Current in a Magnetic Nanocontact is a Standing Self-Localized Wave Bullet*, Physical Review Letters **95**, 237201 (2005).
- [32] M. A. Hoefer, T. J. Silva, M. W. Keller, *Theory for a dissipative droplet soliton excited by a spin torque nanocontact*, Physical Review B **82**, 2000 (2010).
- [33] Q. Mistral, M. van Kampen, G. Hrkac, J.-V. Kim, T. Devolder, P. Crozat, C. Chappert, L. Lagae, T. Schrefl, *Current-Driven Vortex Oscillations in Metallic Nanocontacts*, Physical Review Letters **100** (2008).
- [34] M. Tsoi, A. G. M. Jansen, J. Bass, W. C. Chiang, M. Seck, V. Tsoi, P. Wyder, *Excitation of a Magnetic Multilayer by an Electric Current*, Physical Review Letters **80**, 4281 (1998).
- [35] O. Boulle, V. Cros, J. Grollier, L. G. Pereira, C. Deranlot, F. Petroff, G. Faini, J. Barnaś, A. Fert, *Shaped angular dependence of the spin-transfer torque and microwave generation without magnetic field*, Nature Physics **3**, 492 (2007).
- [36] T. Chen, R. K. Dumas, A. Eklund, P. K. Muduli, A. Houshang, A. A. Awad, P. Dürrenfeld, B. G. Malm, A. Rusu, J. Åkerman, *Spin-Torque and Spin-Hall Nano-Oscillators*, Proceedings of the IEEE **104**, 1919 (2016).
- [37] D. D. Stancil, A. Prabhakar, *Spin waves* (2009).

- [38] A. G. Gurevich, G. A. Melkov, *Magnetization oscillations and waves* (1996).
- [39] S. O. Demokritov (Hg.), *Chapter 9: Steering Magnons by Noncollinear Spin Textures*, CRC Press, 6000 Broken Sound Parkway NW, Suite 300 Boca Raton, FL 33487-2742 (2017).
- [40] A. Hubert, R. Schäfer, *Magnetic domains: the analysis of magnetic microstructure*, Magnetic domains: the analysis of magnetic ... (1998).
- [41] J.-V. Kim, *Chapter Four - Spin-Torque Oscillators*, Band 63 von *Solid State Physics*, Academic Press (2012).
- [42] P. Krivosik, C. E. Patton, *Hamiltonian formulation of nonlinear spin-wave dynamics: Theory and applications*, Physical Review B **82**, 184428 (2010).
- [43] L. V., *Wave Turbulence Under Parametric Excitation*, World Scientific Publishing Company (1994), ISBN 978-3-642-75297-1.
- [44] H. Suhl, *The theory of ferromagnetic resonance at high signal powers*, Journal of Physics and Chemistry of Solids **1**, 209 (1957).
- [45] T. L. Gilbert, *Classics in Magnetism A Phenomenological Theory of Damping in Ferromagnetic Materials*, IEEE Transactions on Magnetism **40**, 3443 (2004).
- [46] L. Landau, E. Lifshitz, *On the theory of the dispersion of magnetic permeability in ferromagnetic bodies*, Phys Z Sowjetunion (1935).
- [47] B. A. Kalinikos, A. N. Slavin, *Theory of dipole-exchange spin wave spectrum for ferromagnetic films with mixed exchange boundary conditions*, Journal of Physics C: Solid State ... (1986).
- [48] R. Arias, D. L. Mills, *Extrinsic contributions to the ferromagnetic resonance response of ultrathin films*, Physical Review B **60**, 7395 (1999).
- [49] J. D. Jackson, *Classical electrodynamics*, Wiley, New York, NY, dritte Auflage (1999), ISBN 9780471309321.
- [50] P. Bruno, C. Chappert, *Oscillatory coupling between ferromagnetic layers separated by a nonmagnetic metal spacer*, Physical Review Letters **67**, 1602 (1991).
- [51] W. H. Meiklejohn, *Exchange Anisotropy—A Review*, Journal of Applied Physics **33**, 1328 (2004).
- [52] N. M. Kreines, D. I. Kholin, S. O. Demokritov, *The interlayer exchange interaction in multi-layer magnetic systems Fe/Cr/Fe (Review Article)*, Low Temperature Physics **38**, 826 (2012).

- [53] R. Q. Wu, L. J. Chen, A. Shick, A. J. Freeman, *First-principles determinations of magneto-crystalline anisotropy and magnetostriction in bulk and thin-film transition metals*, Journal of Magnetism and Magnetic Materials **177-181**, 1216 (1998).
- [54] W. F. Brown Jr, *Theory of Magnetoelastic Effects in Ferromagnetism*, Journal of Applied Physics **36**, 994 (2004).
- [55] P. Dirac, *On the theory of quantum mechanics*, ... of the Royal Society of London A: ... (1926).
- [56] W. Heisenberg, *Mehrkörperproblem und Resonanz in der Quantenmechanik*, Zeitschrift für Physik A Hadrons and Nuclei (1926).
- [57] J. J. Novoa, M. Deumal, J. Jornet-Somoza, *Calculation of microscopic exchange interactions and modelling of macroscopic magnetic properties in molecule-based magnets*, Chemical Society Reviews **40**, 3182 (2011).
- [58] A. Aharoni, A. Arrott, *Introduction to the Theory of Ferromagnetism* (1997).
- [59] A. Aharoni, *Magnetostatic energy calculations*, IEEE Transactions on Magnetics (1991).
- [60] L. K. Bogart, D. Atkinson, K. O'Shea, D. McGrouther, S. McVitie, *Dependence of domain wall pinning potential landscapes on domain wall chirality and pinning site geometry in planar nanowires*, Physical Review B **79**, 054414 (2009).
- [61] M. Laufenberg, D. Bedau, H. Ehrke, M. Kläui, U. Rüdiger, D. Backes, L. J. Heyderman, F. Nolting, C. A. F. Vaz, J. A. C. Bland, T. Kasama, R. E. Dunin-Borkowski, S. Cherifi, A. Locatelli, S. Heun, *Quantitative determination of domain wall coupling energetics*, Applied Physics Letters **88**, 212510 (2006).
- [62] L. Thomas, M. Hayashi, R. Moriya, C. Rettner, S. Parkin, *Topological repulsion between domain walls in magnetic nanowires leading to the formation of bound states*, Nature Communications **3**, 810 (2012).
- [63] L. O'Brien, D. Petit, H. T. Zeng, E. R. Lewis, J. Sampaio, A.-V. Jausovec, D. E. Read, R. P. Cowburn, *Near-Field Interaction between Domain Walls in Adjacent Permalloy Nanowires*, Physical Review Letters **103**, 077206 (2009).
- [64] S. T. Bramwell, S. R. Giblin, S. Calder, R. Aldus, D. Prabhakaran, T. Fennell, *Measurement of the charge and current of magnetic monopoles in spin ice*, Nature **461**, 956 (2009).
- [65] K. Ramstöck, W. Hartung, A. Hubert, *The phase diagram of domain walls in narrow magnetic strips*, physica status solidi (a) **155**, 505 (1996).

- [66] L. Néel, *Energie des parois de Bloch dans les couches minces*, ... Des Seances De L Academie Des ... (1955).
- [67] R. Kirchner, W. Döring, *Structure and Energy of a Néel Wall*, Journal of Applied Physics **39**, 855 (1968).
- [68] E. E. Huber Jr, D. O. Smith, *Domain-Wall Structure in Permalloy Films*, Journal of Applied ... (1958).
- [69] E. E. Huber Jr, D. O. Smith, J. B. Goodenough, *Domain-Wall Structure in Permalloy Films*, Journal of Applied Physics **29**, 294 (2004).
- [70] B. A. Lilley, *LXXI. Energies and widths of domain boundaries in ferromagnetics*, The London (1950).
- [71] T. Trunk, M. Redjda, A. Kákay, M. F. Ruane, *Domain wall structure in Permalloy films with decreasing thickness at the Bloch to Néel transition*, Journal of Applied ... (2001).
- [72] A. E. LaBonte, *Two-Dimensional Bloch-Type Domain Walls in Ferromagnetic Films*, Journal of Applied Physics **40**, 2450 (1969).
- [73] A. Hubert, *Stray-Field-Free and Related Domain Wall Configurations in Thin Magnetic Films (II)*, physica status solidi (b) **38**, 699 (1970).
- [74] H. A. M. van den Berg, *Self-consistent domain theory in soft-ferromagnetic media. II. Basic domain structures in thin-film objects*, Journal of Applied Physics **60**, 1104 (1998).
- [75] J. R. MacDonald, *Ferromagnetic Resonance and the Internal Field in Ferromagnetic Materials*, Proceedings of the Physical Society. Section A **64**, 968 (1951).
- [76] T. L. Gilbert, H. Ekstein, *Basis of the domain structure variational principle*, Bull. Amer. Phys. Soc. (1956).
- [77] D. D. Stancil, *Phenomenological propagation loss theory for magnetostatic waves in thin ferrite films*, Journal of Applied Physics **59**, 218 (1986).
- [78] L. Van Bockstal, F. Herlach, *Ferromagnetic relaxation in 3d metals at far infrared frequencies in high magnetic fields*, Journal of Physics: Condensed Matter **2**, 7187 (1990).
- [79] M. Fähnle, D. Steiauf, J. Seib, *The Gilbert equation revisited: anisotropic and nonlocal damping of magnetization dynamics*, Journal of Physics D: Applied Physics **41**, 164014 (2008).

- [80] M. Fähnle, D. Steiauf, C. Illg, *Generalized Gilbert equation including inertial damping: Derivation from an extended breathing Fermi surface model*, Physical Review B **84**, 172403 (2011).
- [81] M. C. Ciornei, J. M. Rubí, J. E. Wegrowe, *Magnetization dynamics in the inertial regime: Nutation predicted at short time scales*, Physical Review B **83**, 153 (2011).
- [82] R. Mondal, M. Berritta, A. K. Nandy, P. M. Oppeneer, *Relativistic theory of magnetic inertia in ultrafast spin dynamics*, Physical Review B **96**, 101 (2017).
- [83] B. Heinrich, D. J. Meredith, J. F. Cochran, *Wave number and temperature dependent Landau-Lifshitz damping in nickel*, Journal of Applied Physics (2008).
- [84] J. Kuneš, V. Kamberský, *First-principles investigation of the damping of fast magnetization precession in ferromagnetic metals*, Physical Review B **65**, 212411 (2002).
- [85] K. Gilmore, Y. U. Idzerda, M. D. Stiles, *Identification of the Dominant Precession-Damping Mechanism in Fe, Co, and Ni by First-Principles Calculations*, Physical Review Letters **99**, 027204 (2007).
- [86] V. Kamberský, *Spin-orbital Gilbert damping in common magnetic metals*, Physical Review B **76**, 134416 (2007).
- [87] F. Schreiber, J. Pflaum, Z. Frait, T. Mühge, J. Pelzl, *Gilbert damping and g-factor in $\text{Fe}_{1-x}\text{Co}_x$ alloy films*, Solid State Communications **93**, 965 (1995).
- [88] J. O. Rantschler, R. D. McMichael, A. Castillo, *Effect of 3d, 4d, and 5d transition metal doping on damping in permalloy thin films: Journal of Applied Physics: Vol 101, No 3, Journal of applied ...* (2007).
- [89] A. I. Akhiezer, V. G. Bar'yakhtar, S. V. Peletminskii, S. Chomet, *Spin waves* (1968).
- [90] M. Sparks, *Ferromagnetic Resonance in Thin Films. I. Theory of Normal-Mode Frequencies*, Physical Review B **1**, 3831 (1970).
- [91] R. E. De Wames, T. Wolfram, *Dipole-Exchange Spin Waves in Ferromagnetic Films*, Journal of Applied Physics **41**, 987 (2003).
- [92] T. Wolfram, R. E. De Wames, *Magnetoexchange Branches and Spin-Wave Resonance in Conducting and Insulating Films: Perpendicular Resonance*, Physical Review B **4**, 3125 (1971).
- [93] H. Puzkarski, *Theoretically predictable effects and new interpretations in spin wave resonance of thin films with asymmetric boundary conditions*, physica status solidi (b) **50**, 87 (1972).

- [94] K. Sekiguchi, K. Yamada, S. M. Seo, K. J. Lee, D. Chiba, K. Kobayashi, T. Ono, *Nonreciprocal emission of spin-wave packet in FeNi film*, Applied Physics Letters **97**, 022508 (2010).
- [95] M. Kostylev, *Non-reciprocity of dipole-exchange spin waves in thin ferromagnetic films*, Journal of Applied Physics **113**, 053907 (2013).
- [96] T. Schneider, A. A. Serga, T. Neumann, B. Hillebrands, M. P. Kostylev, *Phase reciprocity of spin-wave excitation by a microstrip antenna*, Physical Review B **77**, 214411 (2008).
- [97] K. J. Harte, *Theory of Magnetization Ripple in Ferromagnetic Films*, Journal of Applied Physics **39**, 1503 (1968).
- [98] S. Maendl, I. Stasinopoulos, D. Grundler, *Spin waves with large decay length and few 100 nm wavelengths in thin yttrium iron garnet grown at the wafer scale*, Applied Physics Letters **111**, 012403 (2017).
- [99] V. Veerakumar, R. E. Camley, *Magnon focusing in thin ferromagnetic films*, Physical Review B **74**, 214401 (2006).
- [100] V. E. Demidov, S. O. Demokritov, K. Rott, P. Krzysteczko, G. Reiss, *Self-focusing of spin waves in Permalloy microstripes*, Applied Physics Letters **91**, 252504 (2007).
- [101] V. E. Demidov, S. O. Demokritov, K. Rott, P. Krzysteczko, G. Reiss, *Mode interference and periodic self-focusing of spin waves in permalloy microstripes*, Physical Review B **77**, 064406 (2008).
- [102] Y. Roussigné, S. M. Chérif, C. Dugautier, P. Moch, *Experimental and theoretical study of quantized spin-wave modes in micrometer-size permalloy wires*, Physical Review B **63**, 134429 (2001).
- [103] J. Jorzick, C. Krämer, S. O. Demokritov, *Spin wave quantization in laterally confined magnetic structures*, Journal of Applied ... (2001).
- [104] J. P. Park, P. Eames, D. M. Engebretson, J. Berezovsky, P. A. Crowell, *Spatially Resolved Dynamics of Localized Spin-Wave Modes in Ferromagnetic Wires*, Physical Review Letters **89**, 277201 (2002).
- [105] S. O. Demokritov, B. Hillebrands, A. N. Slavin, *Confined dynamic excitations in structured magnetic media*, IEEE Transactions on Magnetics **38**, 2502 (2002).
- [106] G. T. Rado, J. R. Weertman, *Spin-wave resonance in a ferromagnetic metal*, Journal of Physics and Chemistry of Solids **11**, 315 (1959).

- [107] M. Kostylev, *Interface boundary conditions for dynamic magnetization and spin wave dynamics in a ferromagnetic layer with the interface Dzyaloshinskii-Moriya interaction*, Journal of Applied Physics **115**, 233902 (2014).
- [108] K. Y. Gusliencko, S. O. Demokritov, B. Hillebrands, A. N. Slavin, *Effective dipolar boundary conditions for dynamic magnetization in thin magnetic stripes*, Physical Review B **66**, 132402 (2002).
- [109] K. Y. Gusliencko, R. W. Chantrell, A. N. Slavin, *Dipolar localization of quantized spin-wave modes in thin rectangular magnetic elements*, Physical Review B **68**, 024422 (2003).
- [110] C. Bayer, J. Jorzick, B. Hillebrands, S. O. Demokritov, R. Kouba, R. Bozinoski, A. N. Slavin, K. Y. Gusliencko, D. V. Berkov, N. L. Gorn, M. P. Kostylev, *Spin-wave excitations in finite rectangular elements of Ni₈₀Fe₂₀*, Physical Review B **72**, 064427 (2005).
- [111] R. Huber, M. Krawczyk, T. Schwarze, H. Yu, G. Duerr, S. Albert, D. Grundler, *Reciprocal Damon-Eshbach-type spin wave excitation in a magnonic crystal due to tunable magnetic symmetry*, Applied Physics Letters **102**, 012403 (2013).
- [112] E. V. Tartakovskaya, M. Pardavi-Horvath, R. D. McMichael, *Spin-wave localization in tangentially magnetized films*, Physical Review B **93**, 214436 (2016).
- [113] K. Vogt, F. Y. Fradin, J. E. Pearson, T. Sebastian, S. D. Bader, B. Hillebrands, A. Hoffmann, H. Schultheiss, *Realization of a spin-wave multiplexer*, Nature Communications **5**, 1 (2014).
- [114] V. E. Demidov, S. O. Demokritov, K. Rott, P. Krzysteczko, G. Reiss, *Nano-optics with spin waves at microwave frequencies*, Applied Physics Letters **92**, 232503 (2008).
- [115] C. Bayer, J. Jorzick, S. Demokritov, A. Slavin, *Spin-wave excitations in finite rectangular elements*, Spin dynamics in ... (2006).
- [116] G. Gubbiotti, M. Conti, G. Carlotti, *Magnetic field dependence of quantized and localized spin wave modes in thin rectangular magnetic dots*, Journal of Physics: ... (2004).
- [117] V. E. Demidov, M. P. Kostylev, K. Rott, P. Krzysteczko, G. Reiss, S. O. Demokritov, *Generation of the second harmonic by spin waves propagating in microscopic stripes*, Physical Review B **83**, 054408 (2011).
- [118] T. Brächer, P. Pirro, B. Obry, B. Leven, A. A. Serga, B. Hillebrands, *Mode selective parametric excitation of spin waves in a Ni₈₁Fe₁₉microstripe*, Applied Physics Letters **99**, 162501 (2011).
- [119] A. Y. Dobin, R. H. Victora, *Intrinsic Nonlinear Ferromagnetic Relaxation in Thin Metallic Films*, Physical Review Letters **90**, 167203 (2003).

- [120] H. Schultheiss, K. Vogt, B. Hillebrands, *Direct observation of nonlinear four-magnon scattering in spin-wave microconduits*, Physical Review B **86**, 054414 (2012).
- [121] C. L. Ordóñez-Romero, B. A. Kalinikos, P. Krivosik, W. Tong, P. Kabos, C. E. Patton, *Three-magnon splitting and confluence processes for spin-wave excitations in yttrium iron garnet films: Wave vector selective Brillouin light scattering measurements and analysis*, Physical Review B **79**, 144428 (2009).
- [122] A. N. Slavin, I. V. Rojdestvenski, " *Bright*" and " *dark*" spin wave envelope solitons in magnetic films, IEEE Transactions on Magnetics (1994).
- [123] D. J. Seagle, S. H. Charap, J. O. Artman, *Foldover in YIG*, Journal of Applied Physics **57**, 3706 (1985).
- [124] M. Chen, C. E. Patton, G. Srinivasan, Y. T. Zhang, *Ferromagnetic resonance foldover and spin-wave instability in single-crystal YIG films*, IEEE Transactions on Magnetics **25**, 3485 (1989).
- [125] P. Wigen, *Nonlinear Phenomena and Chaos in Magnetic Materials*, World Scientific Publishing Company (1994), ISBN 9780471309321.
- [126] T. Holstein, H. Primakoff, *Field Dependence of the Intrinsic Domain Magnetization of a Ferromagnet*, Physical Review **58**, 1098 (1940).
- [127] E. Schlömann, *Fine Structure in the Decline of the Ferromagnetic Resonance Absorption with Increasing Power Level*, Physical Review **116**, 828 (1959).
- [128] E. Schlömann, J. J. Green, U. Milano, *Recent Developments in Ferromagnetic Resonance at High Power Levels*, Journal of Applied Physics **31**, S386 (1960).
- [129] E. Schlömann, J. J. Green, *Spin-Wave Growth Under Parallel Pumping*, Journal of Applied Physics **34**, 1291 (1963).
- [130] J. Sklenar, V. S. Bhat, C. C. Tsai, L. E. DeLong, J. B. Ketterson, *Generating wave vector specific Damon-Eshbach spin waves in Py using a diffraction grating*, Applied Physics Letters **101**, 052404 (2012).
- [131] M. Krawczyk, D. Grundler, *Review and prospects of magnonic crystals and devices with reprogrammable band structure*, Journal of Physics: Condensed Matter (2014).
- [132] F. Aryasetiawan, K. Karlsson, *Green's function formalism for calculating spin-wave spectra*, Physical Review B **60**, 7419 (1999).

-
- [133] A. V. Nazarov, C. E. Patton, R. G. Cox, L. Chen, P. Kabos, *General spin wave instability theory for anisotropic ferromagnetic insulators at high microwave power levels*, Journal of Magnetism and Magnetic Materials **248**, 164 (2002).
 - [134] N. Bogoliubov, *On the theory of superfluidity*, J Phys (1947).
 - [135] V. E. Zakharov, *The instability of waves in nonlinear dispersive media*, Sov Phys JETP (1967).
 - [136] V. P. Krasitskii, *On the canonical transformation of the theory of weakly nonlinear waves with nondecay dispersion law*, Sov Phys JETP (1990).
 - [137] E. H. Hall, *On a New Action of the Magnet on Electric Currents*, American Journal of Mathematics **2**, 287 (1879).
 - [138] E. H. H. P. D, XVIII. *On the “Rotational Coefficient” in nickel and cobalt*, The London, Edinburgh, and Dublin Philosophical Magazine and Journal of Science **12**, 157 (2010).
 - [139] E. H. Hall, XVIII. *On the “Rotational Coefficient” in nickel and cobalt*, Philosophical Magazine Series 5 **12**, 157 (1881).
 - [140] E. A. Stern, *Faraday Effect in Magnetized Solids*, Physical Review Letters **15**, 62 (1965).
 - [141] N. F. Mott, H. Massey, *The theory of atomic collisions* (1965).
 - [142] L. Berger, *Side-Jump Mechanism for the Hall Effect of Ferromagnets*, Physical Review B **2**, 4559 (1970).
 - [143] M. N. Baibich, J. M. Broto, A. Fert, F. N. Van Dau, F. Petroff, P. Etienne, G. Creuzet, A. Friederich, J. Chazelas, *Giant Magnetoresistance of (001)Fe/(001)Cr Magnetic Superlattices*, Physical Review Letters **61**, 2472 (1988).
 - [144] M. I. D'yakonov, V. I. Perel, *Possibility of Orienting Electron Spins with Current*, JETP Letters **13**, 467 (1971).
 - [145] Y. K. Kato, R. C. Myers, A. C. Gossard, D. D. Awschalom, *Observation of the Spin Hall Effect in Semiconductors*, Science **306**, 1910 (2004).
 - [146] A. Hoffmann, *Spin Hall Effects in Metals*, IEEE Transactions on Magnetics **49**, 5172 (2013).
 - [147] M. Schreier, G. E. W. Bauer, V. I. Vasyuchka, J. Flipse, K.-i. Uchida, J. Lotze, V. Lauer, A. V. Chumak, A. A. Serga, S. Daimon, T. Kikkawa, E. Saitoh, B. J. van Wees, B. Hillebrands, R. Gross, S. T. B. Goennenwein, *Sign of inverse spin Hall voltages generated by ferromagnetic resonance and temperature gradients in yttrium iron garnet platinum bilayers*, Journal of Physics D: Applied Physics **48**, 025001 (2014).
-

- [148] A. Hoffmann, *Spin Hall effects in metals*, IEEE transactions on magnetics (2013).
- [149] M. D. Stiles, J. Miltat, *Spin-transfer torque and dynamics*, Spin dynamics in confined magnetic structures III (2006).
- [150] L. Liu, R. A. Buhrman, D. C. Ralph, *Review and Analysis of Measurements of the Spin Hall Effect in Platinum*, arXiv.org (2011).
- [151] S. H. Strogatz, *Nonlinear dynamics and chaos: with applications to physics, biology, chemistry, and engineering* (2014).
- [152] V. E. Demidov, S. Urazhdin, E. R. J. Edwards, M. D. Stiles, R. D. McMichael, S. O. Demokritov, *Control of Magnetic Fluctuations by Spin Current*, Physical Review Letters **107**, 107204 (2011).
- [153] S. M. Rezende, F. M. de Aguiar, A. Azevedo, *Spin-Wave Theory for the Dynamics Induced by Direct Currents in Magnetic Multilayers*, Physical Review Letters **94**, 037202 (2005).
- [154] A. Slavin, V. Tiberkevich, *Excitation of Spin Waves by Spin-Polarized Current in Magnetic Nano-Structures*, IEEE Transactions on Magnetism **44**, 1916 (2008).
- [155] A. A. Serga, M. P. Kostylev, B. Hillebrands, *Formation of Guided Spin-Wave Bullets in Ferrimagnetic Film Stripes*, Physical Review Letters **101**, 137204 (2008).
- [156] A. N. Slavin, O. Büttner, M. Bauer, S. O. Demokritov, B. Hillebrands, M. P. Kostylev, B. A. Kalinikos, V. V. Grimalsky, Y. Rapoport, *Collision properties of quasi-one-dimensional spin wave solitons and two-dimensional spin wave bullets*, Chaos: An Interdisciplinary Journal of Nonlinear Science **13**, 693 (2003).
- [157] O. Büttner, M. Bauer, S. O. Demokritov, B. Hillebrands, Y. S. Kivshar, V. Grimalsky, Y. Rapoport, A. N. Slavin, *Linear and nonlinear diffraction of dipolar spin waves in yttrium iron garnet films observed by space- and time-resolved Brillouin light scattering*, Physical Review B **61**, 11576 (2000).
- [158] A. A. Serga, S. O. Demokritov, B. Hillebrands, A. N. Slavin, *Self-Generation of Two-Dimensional Spin-Wave Bullets*, Physical Review Letters **92**, 117203 (2004).
- [159] L. Yang, R. Verba, V. Tiberkevich, T. Schneider, A. Smith, Z. Duan, B. Youngblood, K. Lenz, J. Lindner, A. N. Slavin, I. N. Krivorotov, *Reduction of phase noise in nanowire spin orbit torque oscillators*, Scientific Reports **5**, 16942 (2015).
- [160] K. Kudo, T. Nagasawa, R. Sato, K. Mizushima, *Amplitude-phase coupling in a spin-torque nano-oscillator*, Journal of Applied Physics **105**, 07D105 (2009).

-
- [161] I. N. Krivorotov, N. C. Emley, R. A. Buhrman, D. C. Ralph, *Time-domain studies of very-large-angle magnetization dynamics excited by spin transfer torques*, Physical Review B **77**, 054440 (2008).
- [162] P. K. Muduli, O. G. Heinonen, J. Åkerman, *Decoherence and Mode Hopping in a Magnetic Tunnel Junction Based Spin Torque Oscillator*, Physical Review Letters **108**, 207203 (2012).
- [163] S. Bonetti, V. Tiberkevich, G. Consolo, G. Finocchio, P. Muduli, F. Mancoff, A. Slavin, J. Åkerman, *Experimental Evidence of Self-Localized and Propagating Spin Wave Modes in Obliquely Magnetized Current-Driven Nanocontacts*, Physical Review Letters **105**, 217204 (2010).
- [164] M. Ohtsu, Y. Otsuka, Y. Teramachi, *Precise measurements and computer simulations of mode-hopping phenomena in semiconductor lasers*, Applied Physics Letters **46**, 108 (1998).
- [165] M. Sciamanna, K. Panajotov, H. Thienpont, *Optical feedback induces polarization mode hopping in vertical-cavity surface-emitting lasers*, Optics ... (2003).
- [166] G. L. Beers, *A Frequency-Dividing Locked-in Oscillator Frequency-Modulation Receiver*, Proceedings of the IRE **32**, 730 (1940).
- [167] H. L. Stover, W. H. Steier, *LOCKING OF LASER OSCILLATORS BY LIGHT INJECTION*, Applied Physics Letters **8**, 91 (1966).
- [168] R. Lebrun, A. Jenkins, A. Dussaux, N. Locatelli, S. Tsunegi, E. Grimaldi, H. Kubota, P. Bortolotti, K. Yakushiji, J. Grollier, A. Fukushima, S. Yuasa, V. Cros, *Understanding of Phase Noise Squeezing Under Fractional Synchronization of a Nonlinear Spin Transfer Vortex Oscillator*, Physical Review Letters **115**, 017201 (2015).
- [169] W. H. Rippard, M. R. Pufall, S. Kaka, T. J. Silva, S. E. Russek, J. A. Katine, *Injection Locking and Phase Control of Spin Transfer Nano-oscillators*, Physical Review Letters **95**, 067203 (2005).
- [170] J. C. Sankey, P. M. Braganca, A. G. F. Garcia, I. N. Krivorotov, R. A. Buhrman, D. C. Ralph, *Spin-Transfer-Driven Ferromagnetic Resonance of Individual Nanomagnets*, Physical Review Letters **96**, 227601 (2006).
- [171] B. Georges, J. Grollier, M. Darques, V. Cros, C. Deranlot, B. Marcilhac, G. Faini, A. Fert, *Coupling Efficiency for Phase Locking of a Spin Transfer Nano-Oscillator to a Microwave Current*, Physical Review Letters **101**, 017201 (2008).
- [172] R. Lehdorff, D. E. Bürgler, C. M. Schneider, Z. Celinski, *Injection locking of the gyrotropic vortex motion in a nanopillar*, Applied Physics Letters **97**, 142503 (2010).
-

-
- [173] S. Urazhdin, P. Tabor, V. Tiberkevich, A. Slavin, *Fractional Synchronization of Spin-Torque Nano-Oscillators*, Physical Review Letters **105**, 104101 (2010).
- [174] S. Urazhdin, V. Tiberkevich, A. Slavin, *Parametric Excitation of a Magnetic Nanocontact by a Microwave Field*, Physical Review Letters **105**, 237204 (2010).
- [175] A. Dussaux, A. V. Khvalkovskiy, J. Grollier, V. Cros, A. Fukushima, M. Konoto, H. Kubota, K. Yakushiji, S. Yuasa, K. Ando, A. Fert, *Phase locking of vortex based spin transfer oscillators to a microwave current*, Applied Physics Letters **98**, 132506 (2011).
- [176] P. Dürrenfeld, E. Iacocca, J. Åkerman, P. K. Muduli, *Parametric excitation in a magnetic tunnel junction-based spin torque oscillator*, Applied Physics Letters **104**, 052410 (2014).
- [177] H. Ulrichs, S. V. Gurevich, S. O. Demokritov, V. S. Tiberkevich, A. N. Slavin, A. Zholud, S. Urazhdin, V. E. Demidov, *Synchronization of spin Hall nano-oscillators to external microwave signals*, Nature Communications **5**, 1 (2014).
- [178] P. Tabor, V. Tiberkevich, A. Slavin, S. Urazhdin, *Hysteretic synchronization of nonlinear spin-torque oscillators*, Physical Review B **82**, 020407 (2010).
- [179] W. Rippard, M. Pufall, A. Kos, *Time required to injection-lock spin torque nanoscale oscillators*, Applied Physics Letters **103**, 182403 (2013).
- [180] J. P. Ramirez, L. A. Olvera, H. Nijmeijer, J. Alvarez, *The sympathy of two pendulum clocks: beyond Huygens' observations*, Scientific Reports **6**, 126 (2016).
- [181] G. Khalsa, M. D. Stiles, J. Grollier, *Critical current and linewidth reduction in spin-torque nano-oscillators by delayed self-injection*, Applied Physics Letters **106**, 242402 (2015).
- [182] M. R. Pufall, W. H. Rippard, S. Kaka, T. J. Silva, S. E. Russek, *Frequency modulation of spin-transfer oscillators*, Applied Physics Letters **86**, 082506 (2005).
- [183] H. Seiler, *Secondary electron emission in the scanning electron microscope*, Journal of Applied Physics **54**, R1 (1998).
- [184] A. A. Tseng, K. Chen, C. D. Chen, K. J. Ma, *Electron beam lithography in nanoscale fabrication: recent development*, IEEE Transactions on Electronics Packaging Manufacturing **26**, 141 (2003).
- [185] C. Vieu, F. Carcenac, A. Pepin, Y. Chen, M. Mejias, A. Lebib, L. Manin-Ferlazzo, L. Couraud, H. Launois, *Electron beam lithography: resolution limits and applications*, Applied Surface Science **164**, 111 (2000).
- [186] J. S. Moodera, G. Mathon, *Spin polarized tunneling in ferromagnetic junctions*, Journal of Magnetism and Magnetic Materials **200**, 248 (1999).
-

-
- [187] E. Martinez, L. Torres, L. Lopez-Diaz, M. Carpentieri, G. Finocchio, *Spin-polarized current-driven switching in permalloy nanostructures*, Journal of Applied Physics **97**, 10E302 (2005).
- [188] K. Wagner, *Charakterisierung periodisch strukturierter magnetischer dünner Filme mittels Ferromagnetischer Resonanz*, Diplomarbeit, University Duisburg-Essen, Germany (2013).
- [189] G. C. Bailey, C. Vittoria, *Spin-Wave Resonance Fields, Linewidths, and Intensities of a Permalloy Film: Theory and Experiment*, Physical Review Letters **28**, 100 (1972).
- [190] M. Hennion, B. Hennion, A. Castets, D. Tocchetti, *Stiffness constant measurement in Ni-Fe alloys by neutron inelastic scattering*, Solid State Communications **17**, 899 (1975).
- [191] Z. Frait, *FMR in Thin Permalloy-Films with Small Surface Anisotropy*, Physica B & C **86**, 1241 (1977).
- [192] Y. Yin, F. Pan, M. Ahlberg, M. Ranjbar, P. Dürrenfeld, A. Houshang, M. Haidar, L. Bergqvist, Y. Zhai, R. K. Dumas, A. Delin, J. Åkerman, *Tunable permalloy-based films for magnonic devices*, Physical Review B - Condensed Matter and Materials Physics **92**, 024427 (2015).
- [193] R. K. Dumas, E. Iacocca, S. Bonetti, S. R. Sani, S. M. Mohseni, A. Eklund, J. Persson, O. Heinonen, J. Åkerman, *Spin-wave-mode coexistence on the nanoscale: A consequence of the oersted-field-induced asymmetric energy landscape*, Physical Review Letters **110**, 257202 (2013).
- [194] S.-i. Tanaka, *Longitudinal Kerr Magneto-Optic Effect in Permalloy Film*, Japanese Journal of Applied Physics **2**, 548 (1963).
- [195] V. W. Biricik, F. R. Nakatsukasa, *Magneto-optic response of a thin magnetic film on a transparent substrate*, Thin Solid Films (1989).
- [196] O. Gladii, D. Halley, Y. Henry, M. Bailleul, *Spin-wave propagation and spin-polarized electron transport in single-crystal iron films*, Physical Review B **96**, 174420 (2017).
- [197] V. Vlaminck, M. Bailleul, *Spin-wave transduction at the submicrometer scale: Experiment and modeling*, Phys. Rev. B **81**, 014425 (2010).
- [198] M. Oogane, T. Wakitani, S. Yakata, R. Yilgin, Y. Ando, A. Sakuma, T. Miyazaki, *Magnetic Damping in Ferromagnetic Thin Films*, Japanese Journal of Applied Physics **45**, 3889 (2006).
- [199] S. M. Bhagat, P. Lubitz, *Temperature variation of ferromagnetic relaxation in the 3d transition metals*, Physical Review B **10**, 179 (1974).
-

- [200] B. Heinrich, Z. Frait, *Temperature Dependence of the FMR Linewidth of Iron Single-Crystal Platelets*, physica status solidi (b) **16**, K11 (1966).
- [201] P. B. Johnson, R. W. Christy, *Optical constants of transition metals: Ti, V, Cr, Mn, Fe, Co, Ni, and Pd*, Physical Review B **9**, 5056 (1974).
- [202] L. Yang, R. Verba, V. Tiberkevich, T. Schneider, A. Smith, Z. Duan, B. Youngblood, K. Lenz, J. Lindner, A. N. Slavin, I. N. Krivorotov, *Reduction of phase noise in nanowire spin orbit torque oscillators*, Scientific Reports **5**, 16942 EP (2015).
- [203] J. P. Nibarger, R. Lopusnik, Z. Celinski, T. J. Silva, *Variation of magnetization and the Landé g factor with thickness in Ni-Fe films*, Applied Physics Letters **83**, 93 (2003).
- [204] Z. Duan, A. Smith, L. Yang, B. Youngblood, J. Lindner, V. E. Demidov, S. O. Demokritov, I. N. Krivorotov, *Nanowire spin torque oscillator driven by spin orbit torques*, Nature Communications **5**, 5616 (2014).
- [205] T. Sebastian, K. Schultheiss, B. Obry, B. Hillebrands, H. Schultheiß, *Micro-focused Brillouin light scattering: imaging spin waves at the nanoscale*, Frontiers in Physics **3**, 1589 (2015).
- [206] C. W. Sandweg, M. B. Jungfleisch, V. I. Vasyuchka, A. A. Serga, P. Clausen, H. Schultheiss, B. Hillebrands, A. Kreisel, P. Kopietz, *Wide-range wavevector selectivity of magnon gases in Brillouin light scattering spectroscopy*, Review of Scientific Instruments **81**, 073902 (2010).
- [207] J. F. Cochran, J. R. Dutcher, *Calculation of the intensity of light scattered from magnons in thin films*, Journal of Magnetism and Magnetic Materials **73**, 299 (1988).
- [208] J. Hamrle, J. Pištora, B. Hillebrands, B. Lenk, M. Münzenberg, *Analytical expression of the magneto-optical Kerr effect and Brillouin light scattering intensity arising from dynamic magnetization*, Journal of Physics D: Applied Physics **43**, 325004 (2010).
- [209] M. Buchmeier, H. Dassow, D. E. Bürgler, C. M. Schneider, *Intensity of Brillouin light scattering from spin waves in magnetic multilayers with noncollinear spin configurations: Theory and experiment*, Physical Review B **75**, 184436 (2007).
- [210] J. F. Cochran, J. R. Dutcher, *Calculation of Brillouin light scattering intensities from pairs of exchange-coupled thin films*, Journal of Applied Physics **64**, 6092 (1988).
- [211] H. Schultheiß, *Kohärenz und Dämpfungsverhalten von Spinwellen in magnetischen Mikrostrukturen* (2010).
- [212] B. A. Garetz, J. M. Khosrofian, *Measurement of a Gaussian laser beam diameter through the direct inversion of knife-edge data*, Applied Optics **22**, 3406 (1983).

-
- [213] S. Quabis, R. Dorn, M. Eberler, O. Glöckl, G. Leuchs, *Focusing light to a tighter spot*, Optics communications **179**, 1 (2000).
- [214] V. E. Demidov, S. Urazhdin, H. Ulrichs, V. Tiberkevich, A. Slavin, D. Baither, G. Schmitz, S. O. Demokritov, *Magnetic nano-oscillator driven by pure spin current*, Nature Materials **13**, 467 (2012).
- [215] T. von Hofe, N. O. Urs, B. Mozooni, T. Jansen, C. Kirchhof, D. E. Bürgler, E. Quandt, J. McCord, *Dual wavelength magneto-optical imaging of magnetic thin films*, Applied Physics Letters **103**, 142410 (2013).
- [216] D.-S. Han, S.-K. Kim, J.-Y. Lee, S. J. Hermsdoerfer, H. Schultheiß, B. Leven, B. Hillebrands, *Magnetic domain-wall motion by propagating spin waves*, Applied Physics Letters **94**, 112502 (2009).
- [217] D. Hinzke, U. Nowak, *Domain Wall Motion by the Magnonic Spin Seebeck Effect*, Physical Review Letters **107**, 027205 (2011).
- [218] B. A. Kalinikos, *Spectrum and linear excitation of spin waves in ferromagnetic films*, Soviet Physics Journal **24**, 718 (1981).
- [219] R. E. Camley, *Three-magnon processes in magnetic nanoelements: Quantization and localized mode effects*, Physical Review B **89**, 214402 (2014).
- [220] G. Venkat, D. Kumar, M. Franchin, O. Dmytriiev, M. Mruczkiewicz, H. Fangohr, A. Barman, M. Krawczyk, A. Prabhakar, *Proposal for a Standard Micromagnetic Problem: Spin Wave Dispersion in a Magnonic Waveguide*, IEEE Transactions on Magnetics **49**, 524 (2013).
- [221] Y. Henry, O. Gladii, M. Bailleul, *Propagating spin-wave normal modes: A dynamic matrix approach using plane-wave demagnetizing tensors*, arXiv:1611.06153 (2016).
- [222] N. L. Schryer, L. R. Walker, *The motion of 180° domain walls in uniform dc magnetic fields*, Journal of Applied Physics **45**, 5406 (2003).
- [223] A. Ashkin, J. M. Dziedzic, *Interaction of laser light with magnetic domains*, Applied Physics Letters **21**, 253 (2003).
- [224] O. Sandig, Y. A. Shokr, J. Vogel, S. Valencia, F. Kronast, W. Kuch, *Movement of magnetic domain walls induced by single femtosecond laser pulses*, Physical Review B **94**, 054414 (2016).
- [225] S. Moretti, V. Raposo, E. Martinez, L. Lopez-Diaz, *Domain wall motion by localized temperature gradients*, Physical Review B **95**, 064419 (2017).
-

- [226] J. Fassbender, J. McCord, *Magnetic patterning by means of ion irradiation and implantation*, Journal of Magnetism and Magnetic Materials **320**, 579 (2008).
- [227] I. M. Miron, T. Moore, H. Szambolics, *Fast current-induced domain-wall motion controlled by the Rashba effect*, Nature (2011).
- [228] M. Kläui, P. O. Jubert, R. Allenspach, A. Bischof, J. A. C. Bland, G. Faini, U. Rüdiger, C. A. F. Vaz, L. Vila, C. Vouille, *Direct Observation of Domain-Wall Configurations Transformed by Spin Currents*, Physical Review Letters **95**, 026601 (2005).
- [229] H. G. Bauer, J. Y. Chauleau, G. Woltersdorf, C. H. Back, *Coupling of spinwave modes in wire structures*, Applied Physics Letters **104**, 102404 (2014).
- [230] T. Schneider, A. A. Serga, T. Neumann, B. Hillebrands, M. P. Kostylev, *Phase reciprocity of spin-wave excitation by a microstrip antenna*, Physical Review B **77**, 214411 (2008).
- [231] S. Urazhdin, R. Liu, B. Divinskiy, A. Telegin, S. O. Demokritov, V. E. Demidov, *Excitation of coherent propagating spin waves by pure spin currents*, Nature Communications **7**, 1 (2016).
- [232] T. Meyer, T. Brächer, F. Heussner, A. A. Serga, H. Naganuma, K. Mukaiyama, M. Oogane, Y. Ando, B. Hillebrands, P. Pirro, *Experimental Investigation of the Temperature-Dependent Magnon Density and Its Influence on Studies of Spin-Transfer-Torque-Driven Systems*, IEEE Magnetism Letters **8**, 1 (2017).
- [233] M. Geilen, T. Meyer, F. Heussner, B. Hillebrands, P. Pirro, *Spin-wave density of states and microfocussed Brillouin light scattering spectra as a function of magnetic film thickness*, Annual Report AG Magnetism University Kaiserslautern **8**, 71 (2014).
- [234] M. Bailleul, D. Olligs, C. Fermon, *Micromagnetic Phase Transitions and Spin Wave Excitations in a Ferromagnetic Stripe*, Physical Review Letters **91**, 2041 (2003).
- [235] J. Topp, J. Podbielski, D. Heitmann, D. Grundler, *Internal spin-wave confinement in magnetic nanowires due to zig-zag shaped magnetization*, Physical Review B **78**, 024431 (2008).
- [236] R. D. McMichael, B. B. Maranville, *Edge saturation fields and dynamic edge modes in ideal and nonideal magnetic film edges*, Physical Review B **74**, 024414 (2006).
- [237] M. Avrekh, O. R. Monteiro, I. G. Brown, *Electrical resistivity of vacuum-arc-deposited platinum thin films*, Applied Surface Science **158**, 217 (2000).
- [238] V. F. Dmitriev, B. A. Kalinikos, *Excitation of propagating magnetization waves by microstrip antennas*, Soviet Physics Journal **31**, 875 (1988).

- [239] Z. Duan, C. T. Boone, X. Cheng, I. N. Krivorotov, N. Reckers, S. Stienen, M. Farle, J. Lindner, *Spin-wave modes in permalloy/platinum wires and tuning of the mode damping by spin Hall current*, Physical Review B **90**, 024427 (2014).
- [240] V. E. Demidov, S. Urazhdin, A. Zholud, A. V. Sadovnikov, S. O. Demokritov, *Nanoconstriction-based spin-Hall nano-oscillator*, Applied Physics Letters **105**, 172410 (2014).
- [241] T. Aaltonen, M. Ritala, T. Sajavaara, J. Keinonen, M. Leskelä, *Atomic Layer Deposition of Platinum Thin Films*, Chemistry of Materials **15**, 1924 (2003).
- [242] A. Ganguly, R. M. Rowan-Robinson, A. Haldar, S. Jaiswal, J. Sinha, A. T. Hindmarch, D. A. Atkinson, A. Barman, *Time-domain detection of current controlled magnetization damping in Pt/Ni81Fe19 bilayer and determination of Pt spin Hall angle*, Applied Physics Letters (2014).
- [243] P. Slepíčka, V. Švorčík, M. Šlouf, V. Rybka, M. Špírková, *Characterization of metal nanolayers sputtered on poly (ethyleneterephthalate)*, Optoelectronics and advanced materials - Rapid communications **2**, 153 (2008).
- [244] C. Hahn, G. de Loubens, O. Klein, M. Viret, V. V. Naletov, J. Ben Youssef, *Comparative measurements of inverse spin Hall effects and magnetoresistance in YIG/Pt and YIG/Ta*, Physical Review B **87**, 174417 (2013).
- [245] V. Castel, N. Vlietstra, J. Ben Youssef, B. J. van Wees, *Platinum thickness dependence of the inverse spin-Hall voltage from spin pumping in a hybrid yttrium iron garnet/platinum system*, Applied Physics Letters **101**, 132414 (2012).
- [246] A. A. Stashkevich, P. Djemia, Y. K. Fetisov, N. Bizière, C. Fermon, *High-intensity Brillouin light scattering by spin waves in a permalloy film under microwave resonance pumping*, Journal of Applied Physics **102**, 103905 (2007).
- [247] A. N. Slavini, P. Kabos, *Approximate theory of microwave generation in a current-driven magnetic nanocontact magnetized in an arbitrary direction*, IEEE Transactions on Magnetics **41**, 1264 (2005).
- [248] C. Safranski, I. Barsukov, H. K. Lee, T. Schneider, A. A. Jara, A. Smith, H. Chang, K. Lenz, J. Lindner, Y. Tserkovnyak, M. Wu, I. N. Krivorotov, *Spin caloritronic nano-oscillator*, Nature Communications **8**, 104411 (2017).
- [249] M. Collet, X. De Milly, O. d. Kelly, V. V. Naletov, R. Bernard, P. Bortolotti, J. Ben Youssef, V. E. Demidov, S. O. Demokritov, J. L. Prieto, M. Muñoz, V. Cros, A. Anane, G. de Loubens,

-
- O. Klein, *Generation of coherent spin-wave modes in yttrium iron garnet microdiscs by spin-orbit torque*, Nature Communications **7**, ncomms10377 (2016).
- [250] A. Slavin, V. Tiberkevich, *Nonlinear Auto-Oscillator Theory of Microwave Generation by Spin-Polarized Current*, IEEE Transactions on Magnetics **45**, 1875 (2009).
- [251] S. Tsunegi, E. Grimaldi, R. Lebrun, H. Kubota, A. S. Jenkins, K. Yakushiji, A. Fukushima, P. Bortolotti, J. Grollier, S. Yuasa, V. Cros, *Self-Injection Locking of a Vortex Spin Torque Oscillator by Delayed Feedback*, Scientific Reports **6**, 11 (2016).
- [252] E. Iacocca, O. Heinonen, P. K. Muduli, J. Åkerman, *Generation linewidth of mode-hopping spin torque oscillators*, Physical Review B **89**, 054402 (2014).
- [253] R. Sharma, P. Dürrenfeld, E. Iacocca, O. G. Heinonen, J. Åkerman, P. K. Muduli, *Mode-hopping mechanism generating colored noise in a magnetic tunnel junction based spin torque oscillator*, Applied Physics Letters **105**, 132404 (2014).
- [254] S. Urazhdin, P. Tabor, V. Tiberkevich, A. Slavin, *Fractional Synchronization of Spin-Torque Nano-Oscillators*, Physical Review Letters **105**, 104101 (2010).
- [255] A. N. Slavin, V. S. Tiberkevich, *Nonlinear self-phase-locking effect in an array of current-driven magnetic nanocontacts*, Physical Review B **72**, 092407 (2005).
- [256] T. H. E. Lahtinen, K. J. A. Franke, S. van Dijken, *Electric-field control of magnetic domain wall motion and local magnetization reversal*, Scientific Reports **2**, 813 (2012).
- [257] A. J. Ramsay, P. E. Roy, J. A. Haigh, R. M. Otxoa, A. C. Irvine, T. Janda, R. P. Campion, B. L. Gallagher, J. Wunderlich, *Optical Spin-Transfer-Torque-Driven Domain-Wall Motion in a Ferromagnetic Semiconductor*, Physical Review Letters **114** (2015).
- [258] A. W. Rushforth, *Domain wall motion driven by spin Hall effect—Tuning with in-plane magnetic anisotropy*, Applied Physics Letters **104**, 162408 (2014).
- [259] K.-J. Kim, Y. Yoshimura, T. Ono, *Current-driven magnetic domain wall motion and its real-time detection*, Japanese Journal of Applied Physics **56**, 0802A4 (2017).
- [260] X. S. Wang, X. R. Wang, *Thermodynamic theory for thermal-gradient-driven domain-wall motion*, Physical Review B **90** (2014).
- [261] V. D. Nguyen, W. S. Torres, P. Laczkowski, A. Marty, M. Jamet, C. Beigné, L. Notin, L. Vila, J. P. Attané, *Elementary depinning processes of magnetic domain walls under fields and currents*, Scientific Reports **4**, 147204 (2014).
- [262] S. Woo, T. Delaney, G. S. D. Beach, *Magnetic domain wall depinning assisted by spin wave bursts*, Nature Physics **13**, 448 (2017).
-

- [263] S.-M. Seo, K.-J. Lee, H. Yang, T. Ono, *Current-Induced Control of Spin-Wave Attenuation*, Physical Review Letters **102**, 147202 (2009).
- [264] C. H. Brito Cruz, J. P. Gordon, P. C. Becker, R. L. Fork, C. V. Shank, *Dynamics of spectral hole burning*, IEEE Journal of Quantum Electronics **24**, 261 (1988).
- [265] Y. Shimony, Z. Burshtein, *Cr/sup 4+/:YAG as passive Q-switch and Brewster plate in a pulsed Nd:YAG laser - IEEE Xplore Document*, IEEE journal of quantum ... (1995).
- [266] N. J. Whitehead, S. A. R. Horsley, T. G. Philbin, A. N. Kuchko, V. V. Kruglyak, *Theory of linear spin wave emission from a Bloch domain wall*, Physical Review B **96**, 064415 (2017).
- [267] E. Martinez, L. Torres, L. Lopez-Diaz, *Oscillator based on pinned domain walls driven by direct current*, Physical Review B **83**, 174444 (2011).
- [268] M. Voto, L. Lopez-Diaz, E. Martinez, *Pinned domain wall oscillator as a tuneable direct current spin wave emitter*, Scientific Reports **7**, 453 (2017).
- [269] B. Mozooni, J. McCord, *Direct observation of closure domain wall mediated spin waves*, Applied Physics Letters **107**, 042402 (2015).
- [270] A. Haldar, C. Banerjee, P. Laha, *Brillouin light scattering study of spin waves in NiFe/Co exchange spring bilayer films*, Journal of Applied ... (2014).
- [271] V. Warren Biricik, F. Russell Nakatsukasa, *Magneto-optic response of a thin magnetic film on a transparent substrate*, Thin Solid Films **181**, 141 (1989).
- [272] A. Vansteenkiste, J. Leliaert, M. Dvornik, M. Helsen, F. Garcia-Sanchez, B. van Waeyenberge, *The design and verification of MuMax3*, AIP Advances **4**, 107133 (2014).
- [273] R. Engel-Herbert, D. M. Schaadt, T. Hesjedal, *Analytical and numerical calculations of the magnetic force microscopy response: A comparison*, Journal of Applied Physics **99**, 113905 (2006).
- [274] J. McCord, R. Schäfer, *Domain wall asymmetries in Ni81Fe19/NiO: proof of variable anisotropies in exchange bias systems*, New Journal of Physics **11**, 083016 (2009).
- [275] G. S. Abo, Y.-K. Hong, J. Park, J. Lee, W. Lee, B.-C. Choi, *Definition of Magnetic Exchange Length*, IEEE Transactions on Magnetics **49**, 4937 (2013).
- [276] H. Kronmüller, *General Micromagnetic Theory*, John Wiley & Sons, Ltd, Chichester, UK (2007).

Acknowledgement

I would like to thank *all colleagues who contributed to this thesis* in one way or the other. But before addressing the colleagues in detail, i would like to express my special thanks to my dear *family* and *friends*, whose support and trust paved the way for my promotion and personal development aside from the scientific support.

From the Helmholtz-Zentrum Dresden-Rossendorf i want to thank *Prof. Dr. Jürgen Fassbender* for giving me the opportunity to perform my studies in the Institute of Ion Beam Physics and Material Research in a very interesting research field. In particular, I appreciate his advises and honest care to create a pleasant atmosphere and equitable working environment. His constant strive to keep the Institute a better place is a great quality and i wish that this inspiring attribute keeps with him.

Equal thanks to *Dr. Helmut Schultheiss*. I deeply appreciate our time working together. His scientific impulses contributed greatly to my scientific and personal development over the course of my time at the Helmholtz-Zentrum Dresden-Rossendorf. He stood at my side in scientific and organizational improvement, packed with lots of helpful critic and good times together.

Many thanks go to *Yves Henry* and *Matthieu Bailleul* at the IPCMS for the fruitful collaboration. The scientific discussions and work together was a great pleasure to me. I am looking forward to the ongoing research.

Equal thanks to *Ilya Krivorotov* and *Andi Smith*. Not only for the fabrication of the investigated spin Hall oscillators, but also for the scientific discussion and input during my PhD.

Jürgen Lindner, for his attentive eye on the division, cross-synergies and the constant pursuit of a refined atmosphere. Also for the nice chats and personal advices.

Special thanks to *Ciaran Fowley*, for all the laughter, fun and much more. You always had an open ear for me and scientific insight to share, but the most i thank you for your friendship.

Katrin Schultheiss for her support, discussions and general helpfulness. It was a pleasure to work together. Your advises and scientific insight helped me a lot on my way.

Attila Kákay not at least for enduring me as his desk-neighbour. For interesting and (un)helpful

scientific discussions, and teaching me in micromagnetics and beyond. Lots of laughter and good times.

To the post-docs within the group of magnonics: *Lorenzo Fallarino, Julia Osten* and *Nana Nishida*. It was a pleasure to work and discuss together with you.

To the *students/interns* within the group of magnonics (chronological order): *Eva Paprotzki, Tobias Hula, Cansu Canpolat, Franziska Wehrmann, Ek-In Surapat, Toni Hache, Christian Riedel, Lukas Körber, Peter Matthies, Tillman Weinhold, Dmitri Tolmachev, Dogukan Hazar Özbey*. Working together with you was a keystone during my promotion and helped me to develop and understand supervision and teamwork better, connected to my personal development. I enjoyed your drive and ideas deeply and are convinced you will make a good way in science.

My gratitude goes also to *all colleagues who directly supported me and my work in the laboratory*, clean room or electron beam facilities. Without your help and maintenance of the facilities this thesis would not have been possible as well. Last but not least my thanks to everyone who contributed to my promotion and is not specifically mentioned here.

APPENDIX A

Appendix

A.1 Splitting process in magnetic domains confined by domain walls

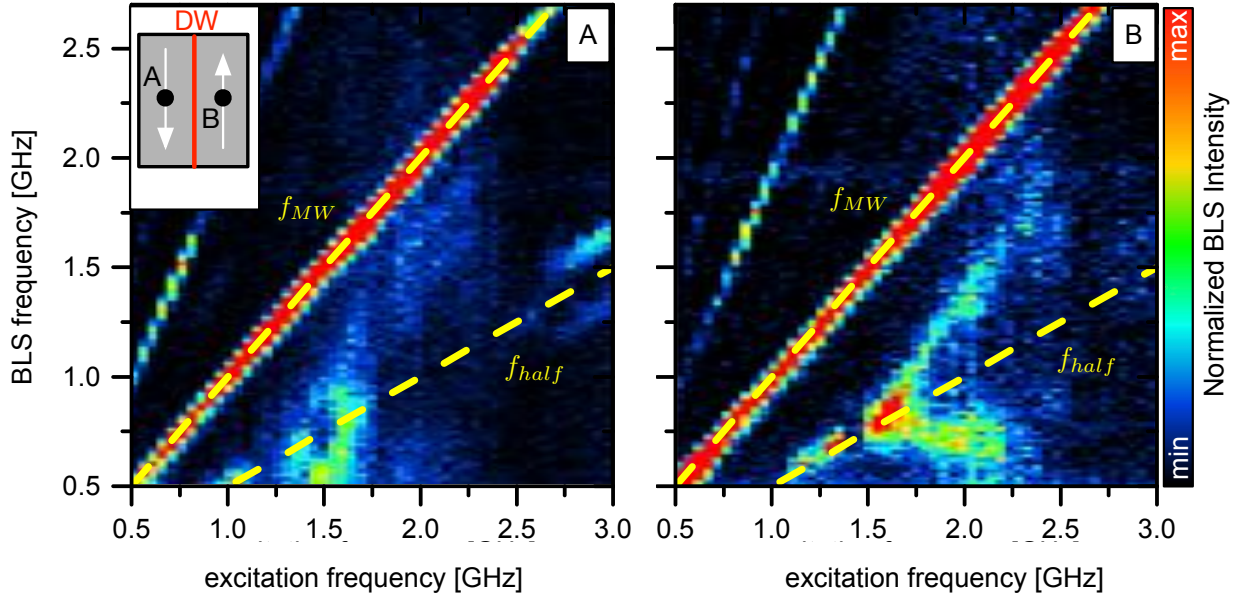


Figure A.1: μ BLS Intensity as recorded on a domain position (labeled A and B) in a rectangular $\text{Ni}_{81}\text{Fe}_{19}$ structure in a Landau-Like state. Positions are indicated in the inset. The splitting of strongly directly excited magnons at the source frequency (f_{MW}) into two separate and equidistant "satellites" around half the pumping frequency (f_{half}) is observed. This is clear indication of the confining nature of the Néel wall and first experimental support of the simulations in [219].

The experimentally recorded 3-magnon splitting process inside domains is presented for a 10- μm -

wide $\text{Ni}_{81}\text{Fe}_{19}$ wire, with two 5- μm -wide oppositely magnetized domains (geometry in section 4) in Fig. A.1. This observation evidences two important things. For one, the confinement of spin-wave dynamics to the individual domains and, hence, reflection of spin waves at the domain wall boundary. But furthermore, this is also the first experimental support to recent micromagnetic simulations [219] on the 3-magnon process in confined geometries. In the simulations a modification of the 3 magnon-splitting is predicted for thin film wires. In the unmodified process magnons created by a microwave having a source frequency f_{MW} scatter into two magnons at half the frequency $f_{\text{MW}}/2$ conserving both energy and momentum. However, for the confinement by the wire geometry differences to this rule were found and spin waves having frequencies symmetrically spaced around half the frequency (here referred to as “satellites”) were observed in the simulation.

This was attributed to the discrete and localized nature of the spin-wave spectrum in the presence of confining boundary conditions. The recorded spin-wave intensities reveal such a modified splitting process experimentally. The frequency dependence of this process is an interesting study on its own, but is just in the beginning of its research. The observation of this modification of the splitting-process, where the transition rule from the momentum conservation seems softened is clear indication of the confining nature of the Néel walls. This effect combined with the lateral control on the domain wall position, within the thesis exemplarily shown by small magnetic fields, may allow for studies on confined spin-wave dynamics, where the quantization conditions can be systematically varied in one and the same structure in future experiments.

A.2 reconfigurable remanent states in square structures stabilized by local ion irradiation

With the aim towards reconfigurable magnonic circuits based on domain walls, the possibility to stabilize different remanent magnetic configurations in square structures was investigated. For the study 30 nm-thick $\text{Ni}_{81}\text{Fe}_{19}$ squares of 20 μm side-length were fabricated by EBL. Non-irradiated, these structures exhibited a symmetric Landau-state as demonstrated for square structures within this thesis, featuring 4 domain walls and a vortex nucleated at the center. Subsequently, local Helium- and Neon-Ion irradiation performed via a Helium-Ion microscope (acceleration voltage 25 and 31 keV, respectively) was used to create artificial pinning sites by exposure of 4 circular spots (1 μm -diameter) regularly displaced by 4 μm from the middle position. After the modification mainly two stable remanent states (labeled A and B) of distinct vortex and domain wall configuration were confirmed by wide-field Kerr microscopy as shown in Fig. A.2 on the left hand side. For illustration the implantation-sites labeled from A to D are additionally marked as red dots in configuration A. To analyze the configurability of the magnetic state, the vortex position was then tracked by Kerr-microscopy, while sweeping an external magnetic field applied paral-

lel to the sides of the squares. The recorded positions are shown on the right hand side of Fig. A.2 for different doses and ion-types, where the two stable configuration are labeled as A and B. The hysteretic behaviour of the vortex displacement out of the center of the square structure can be clearly seen from the data. This demonstrates the possibility to prepare different domain wall orientations and, hence, potential spin-wave channels depending on the magnetic-field history to set the desired operation. In combination with the confirmation of spin-wave propagation within domain walls, this result may pave the way towards realization of a prototype magnonic circuitry allowing field-free operation paired with reprogrammability and non volatility in future studies.

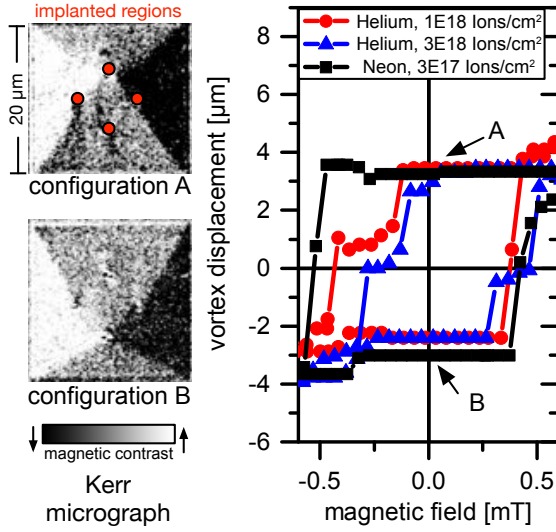


Figure A.2: Different remanent magnetic states in a square-structure. Two configurations labeled “A” and “B” of different domain wall path can be stabilized. Kerr micrographs of each configuration are shown on the left hand side. The four implanted regions are indicated by red dots. The symmetry of the structure implies stabilization of two additional states, pinning the vortex core to either of the two remaining implanted regions. The right hand graph presents the tracked vortex position, while sweeping an external magnetic field applied parallel to the squares sides confirming the hysteretic behaviour.

A.3 Domain wall displacements induced by a scanning laser beam

This section is devoted to the influence of the laser spot used for μ BLS-measurements on the detected spin-wave dynamics. Probing the sample is accompanied by thermal gradients, as well as possible excitation of spin-currents or spin-waves by heat. Shifting the domain wall has to be considered, due to the so called “entropic torque” as well as magnonic spin transfer torque (μ STT) and thermally induced dipolar fields (e.g. [225]). To test the presence of this effect, several measurements were repeated under nominally identical conditions, for different laser powers and while reverting the sweep direction.

For total laser powers exceeding around 1.8 mW impinging on the sample surface, such effects could be observed. This power equals to a laser-intensity at the sample surface of about 19.82 kW/mm² (taking the experimentally determined FWHM of 340nm as the effective diameter of the

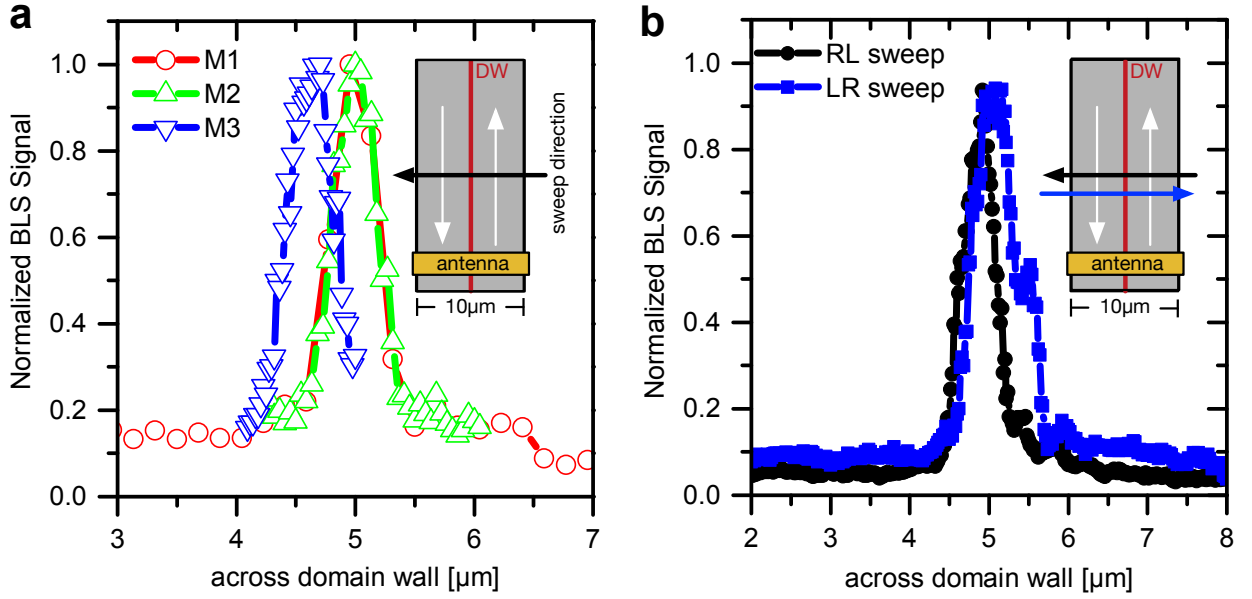


Figure A.3: **a** Consecutive μ BLS-measurements (denoted as M1 to M3) sweeping the laser spot position from right to left across the 10- μ m-wide structure and 180° domain wall situated at its center. The spin-wave flow excited at a frequency of 500 MHz is confined to the domain wall, which changes position between measurements M2 and M3 indicating the possibility to drag the domain wall by the measurement-beam. **b** Similar μ BLS-measurements when inverting the sweep direction from right to left (black line and dots) towards left-to-right (blue line and dots). The asymmetry between the two measurements and the irregular right flank of the left-to-right sweep directions peak confirm the distortion possibilities by the measurement-beam.

beam, see section 3.5.1). The optical skin depth of the 35 nm thick permalloy films is around 12 - 24 nm [270], so that here the reflection coefficient is reduced compared to the bulk value of permalloy [271]. Experimentally in the lab the coefficient of 36 % was determined, while calculations with the optical parameters given in section 3.2 yields 34 %. Assuming absorption of the remainder this results in 6.74 kW/mm².

Figure A.3 **a** shows three consecutive BLS-measurements at 2 mW of laser power, when sweeping the probing laser over the 10- μ m-wide structure and the 180° domain wall at its center, while exciting channeled spin-wave flow (see for example the experiments in section 4.1.1.5). Between the second and third measurement cycle (denoted as M2 and M3) the domain wall is displaced around 0.5 μ m away from the center towards the sweeping direction, indicating a changed domain wall position by laser dragging. A similar observation depending on the sweeping direction is presented in subfigure **b**. When sweeping the laser spot from left-to-right across the domain wall, the intensity-profile appears wider, than compared to the inverted sweep direction. The author suggests to perform purely electrical measurement schemes avoiding large thermal gradients to obtain deeper insight by comparison with the optical measurements presented here.

A.4 Magnetic Force Microscopy investigation of the domain wall type and width

In this section the Magnetic Force Microscopy (MFM) micrographs are presented for the case of the 10- μm -wide $\text{Ni}_{81}\text{Fe}_{19}$ based structure. The micrograph of the MFM signal phase is presented in figure A.4. For these measurements tips of the type "PPP-LM-MFMR" from NanoSensorsTM were scanned in 50 nm distance across the sample structure, while recording the cantilevers oscillation phase. These tips have a magnetic resolution of 35 nm or better, a magnetic moment of 150 emu/cm³ and a coercivity of 250 Oe according to the manufacturer. The tips are magnetized normal to the sample surface (z-direction) and hence sensitive on the out-of-plane stray fields, due to the interaction with the tips magnetic moment. The normalized phase of the MFM signal extracted across a line indicated in figure A.4 a) is shown in figure A.4 b). To further analyze this measurement, the frequency shift exerted on the MFM tip was simulated using mumax3 [272] as according to [273] for comparison with the experimental data in 50 nm distance to the sample, assuming the tip to be an ideal dipole. In the experiment the measurement geometry and tip radius as well as tip sensitivity, will influence the strayfield-forces acting on the real tip and therefore result in a convolution of the expected signal with some apparatus function. The simulated lateral distance

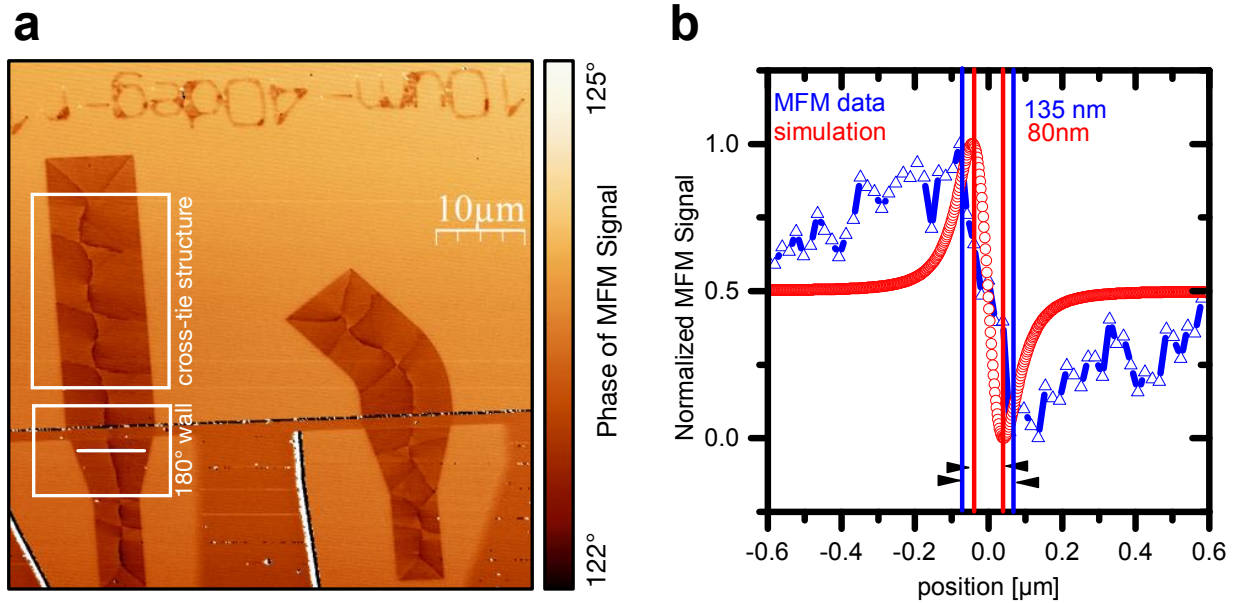


Figure A.4: a) Magnetic Force Microscopy micrograph for a 10- μm -wide $\text{Ni}_{81}\text{Fe}_{19}$ based structure. In larger areas a cross-tie domain wall structure and distortions on the wall formation by the magnetic tip used in the experiment are observed. b) Normalized phase of the MFM Signal extracted along the line given in a) in the vicinity of the exciting microwave antenna across the domain wall together with the expected MFM Signal according to micromagnetic simulations for a tip distance of 50 nm.

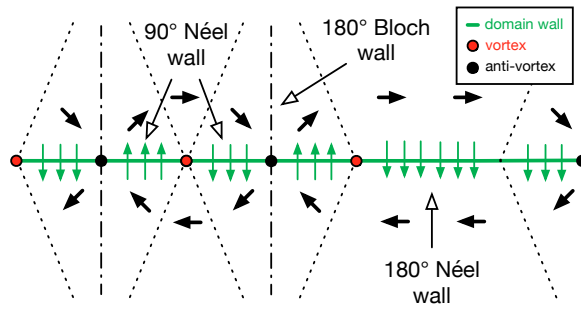


Figure A.5: Schematic magnetic configuration (arrows) for the cross-tie structure, as well as vortices (red dots) and anti-vortices (black dots) along the domain wall (green line) running along the centre of the structure. Sections with strict periodicity between anti-vortices and vortices are observed as well as sections of extended periodicity and domain wall configuration.

between the maximum forces acting on the tip, while scanning across the domain wall is about 80 nm, while experimentally the signal is found to be broadened, giving a lateral distance of about 135 nm. This result is plausible assuming some convolution in the real experiment and corroborates the assumed nanometre width potential well, created by the domain wall. Looking more close on the magnetic state imaged as shown in figure A.4 a suggests two important conclusions: First, the magnetic state indeed resembles a Landau-like state but with cross-tie domain wall structures (such as in [274]), where vortices and anti-vortices are formed along the 180° domain wall in larger regions with changing periodicity between them. Furthermore from the MFM-micrograph the influence on the magnetic state by the tip's magnetic field becomes apparent and results in distorted domain walls and sometimes discontinuities in the detected signal, when the domain wall is unintentionally moved. Near the exciting antenna for this particular remanent state a region with no vortices or anti-vortices can be identified, which is assumed to have the typical 180° wall structure. For illustration this configuration is schematically shown in figure A.5, which gives the magnetic configuration by arrows and vortex (red dot) and anti-vortex (black dot) positions along the domain wall in the centre of the structure.

A.5 Micromagnetic simulations: problem definition and analysis

In micromagnetic finite difference calculations, the magnetization dynamics is treated by discretizing the magnetic body into several small elements (cells) of assumed homogeneous magnetization. This discretization is mainly determined by the ratio between the exchange constant and other energy contributions, resulting in the definition of the so called exchange length:

$$\lambda_{\text{ex}} = \sqrt{\frac{A}{(K_{\text{dip}} + K_{\text{anisotropy}})}} \quad (\text{A.0})$$

which gives a measure for the cell size [275]. It is commonly agreed on, that the assumption of a homogeneous magnetization in cells of sizes smaller than this exchange length are of good approximation, where the exchange interaction transforms into a nearest-neighbour-cell interaction. A general overview about micromagnetism and the finite difference calculations is given in [276].

For solving the LLG-equation (equation 2.11) numerically by stepwise integration for each cell, we use mumax3 [272]. After initial relaxation of the system we excite magnetization dynamics by a locally defined time-dependent magnetic field (pulsed excitation). The time dependent amplitude of this excitation pulse was chosen to be a superposition of equal excitation strength from 0 up to 40 GHz and hence following the form $\sin(2\pi f_{\text{cut}} \cdot t)/(2\pi f_{\text{cut}} \cdot t)$ with f_{cut} being 40GHz. Spatially the excitation pulse is of Gaussian-profile of 200 nm full width half maximum. The magnetization response is then saved together with the calculated energies and effective fields for every 10ps yielding time trajectories for the magnetization within each cell of index i $m_i(t)$. Subsequently the static direction of the magnetization prior to the pulsed excitation is subtracted yielding the dynamic magnetization response $\delta m_i(t) = m_i(t) - m_i(0)$ and Fourier-Transformed to give $\delta m_i(\omega)$ in the frequency domain. For Fourier-Transformation the time-trajectory is “zero-padded” and different windows have been tried, where typically a “Hanning-window” or no window was utilized. In a first step the total powerspectrum is calculated from these time trajectories as the integral response of the system for a certain frequency ω as powerspectrum(ω) $\propto \sum_i \delta m_i(\omega)$ and chosen region of interest. The powerspectrum then contains peaks, where the magnetic system is resonantly excited by the magnetic field. To visualize the mode profile to different approaches are taken:

In the **first approach** a backward windowed Fourier Transformation can be used for the selected mode frequency ω as for example determined by the peak positions in the powerspectrum. This yields the cell-dependent response amplitude at the chosen frequency δm_i^* , which can then be visualized spatially and is open for further analysis, such as determining the wave vector, mode-profiles or phases of this magnetic response.

The **second approach** uses in contrast to the first one an additional simulation, where the time

dependent magnetic field is chosen as $\propto \sin(\omega \cdot t)$ to only excite dynamics at the selected frequency ω . This approach holds the advantage to be free of any distortions by a Fourier-Transformation or interaction with modes excited at different frequencies, as is the case for pulsed excitation. The spatial response of the system is then extracted by a simple snapshot in time of the magnetization of each cell. As an advantage over a pulsed excitation, in such simulations spin waves are excited only at the selected frequency, so that non-linear effects and frequency conversion can be studied.

In both cases To determine the wave vector of the resulting mode, an additional spatial Fourier-Transformation is performed along the direction of interest. For the case of the domain wall modes this direction was chosen along the propagation path (along the wall). The resulting peak in wave-vector space is then taken as the mean wave vector of the spin-wave mode.

A.5.0.0.1 Parameters of the spin-wave propagation in domain walls simulations In table A.1 the parameters of the micromagnetic simulation in the rectangular and square geometry for analysis on the spin-wave propagation in domain walls is listed. The coordinate system is always chosen, such that the modelled thin-film element lies in the xy-plane and the point of origin is in the center of the structure. In both geometries an absorbing boundary layer (ABS) of higher damping α_{ABS} and shell-width w_{ABS} was introduced at the structure edges.

parameter	rectangular geometry	square geometry
M_S	830 kA/m	830 kA/m
A	13 pJ/m	13 pJ/m
α_G	0.007	0.007
g-factor	2.13	2.13
dimension ($\mathbf{x} \times \mathbf{y} \times \mathbf{z}$)	$5 \times 1 \times 10^{-2} \mu\text{m}^{-3}$	$13 \times 13 \times 4 \cdot 10^{-2} \mu\text{m}^{-3}$
cell dimension ($\mathbf{x} \times \mathbf{y} \times \mathbf{z}$)	$2.44 \times 1.95 \times 10 \text{ nm}^{-3}$	$6.35 \times 6.35 \times 40 \text{ nm}^{-3}$
l_{ex}	5.3 nm	5.3 nm
field-pulse position (x, y, z)	(0.9, 0, 0) μm	(-5.4, -5.4, 0) μm
field-shape	Gaussian	Gaussian
field-pulse width (σ)	20 nm	250 nm
max. pulse-amplitude	50 mT	50 mT
f_{cut}	40 GHz	40 GHz
α_{ABS}	0.5	0.5
w_{ABS}	0.2 μm	1 μm
magnetic configuration	Landau-state (vortex at $x = -1.9 \mu\text{m}$)	Landau-state

Table A.1: Parameters of the micromagnetic simulations in the rectangular and square geometry, performed by mumax3 [272].

A.5.0.0.2 Magnetic configuration and spin-wave spectra in the tapered SHO A 2.9- μm -long tapered magnetic wire of 220 nm average width, 5 nm thickness and a tapering angle of 1.45° is modeled. The geometry is represented on a 1024 x 256 x 1 grid, resulting in approximate cell

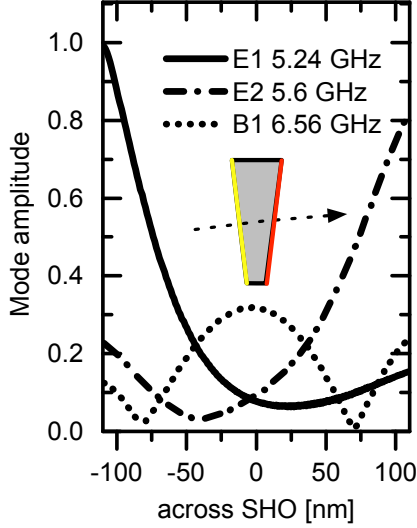


Figure A.6: Simulated spin-wave mode profiles across the spin Hall oscillator. Two modes with main intensities at the structure edges “E1” and “E2” are observed having a frequency of 5.24 GHz and 5.6 GHz, respectively. The third mode “B1” of higher frequency (6.56 GHz) is attributed to a mode with main intensity at the center of the nanowire.

sizes of $2.9 \times 1.2 \times 5 \text{ nm}^3$, below the exchange length of $\text{Ni}_{81}\text{Fe}_{19}$. The saturation magnetization $M_S = 530 \text{ kA/m}$ and exchange stiffness $A = 5 \text{ pJ/m}$ are set according to the experimentally determined values (section 3.4). To excite and study the spin-wave dynamics, a homogeneous out-of-plane pulse and a damping parameter $\alpha_G = 0.007$ are used. Subsequently, the time trajectory of the magnetization of each cell is Fourier transformed. For analysis the middle $2\text{-}\mu\text{m}$ -long section is divided into ten separate 200 nm segments to give the position dependent spin-wave spectra integrated across the SHO. Eigenfrequencies are then determined by the maxima-positions in the simulated spectra. To investigate the spatial profile of the spin-wave eigenmodes, a backward Fourier transform for the eigenfrequencies is calculated for each cell, giving the mode amplitude at each position. The spin-wave mode-profiles are presented in Fig.

A.6 Current dependence of auto-oscillations in the tapered SHO

The auto-oscillation frequency was recorded in dependence of the driving current and, hence, auto-oscillation intensity for the different positions, as shown in figure A.7. The frequency always red-shifts as expected, due to the oersted field, non-linear amplitude-frequency coupling (NLFS), as well as Joule heating. The qualitative different frequency shift for the different positions indicates a coupling between the regions, otherwise similar dependencies would be expected for all sample positions. The amplitude, has been discussed in the thesis.

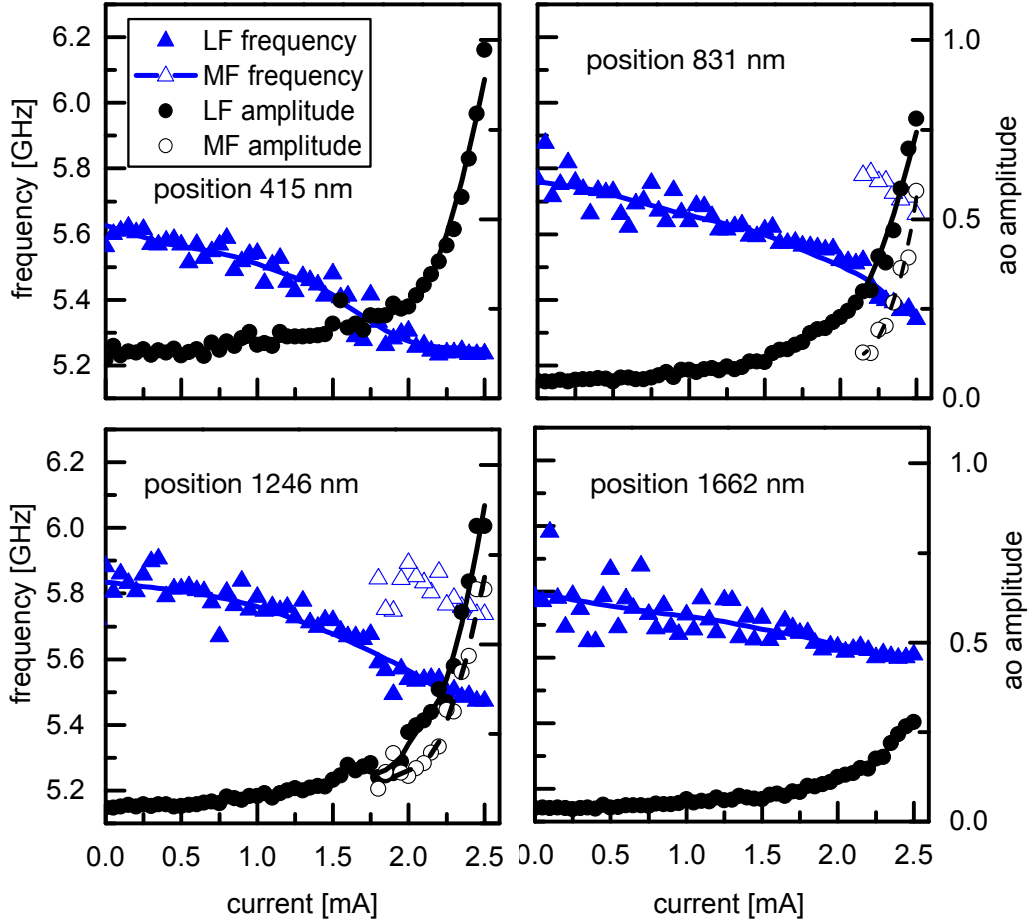


Figure A.7: Intensity and frequency of the auto-oscillation as function of the applied DC currents for different sample positions. A qualitative different amplitude-frequency coupling is observed indicating an additional coupling mechanism in the SHO.

A.7 Fabrication of Ni₈₁Fe₁₉ microstructures for spin waves in domain walls

Fabrication step	Step A	Step B
spin-coated resist mask		
Material	ZEP 520 A, MicroChem	MMA EL 11
resist thickness	150 nm	450 nm
spinning speed	5000 rpm	3000 rpm
heating treatment (prebake)	180 °C for 3 min	150 °C for 1.5 min
Typical electron beam parameters		
aperture	10 - 30 µm	30 - 120 µm
beam current	0.013 nA - 0.22 nA	0.22 nA - 3.2 nA
step size	4 nm	4 nm
dose	30-35 µ C / cm ²	100-120 µ C / cm ²
Developer process (sequential)		
developer	N-amyI acetat (ZED-N50)	
duration of exposure	50 sec	
developer	MIBK:Isopropanol (3:1)	MIBK:Isopropanol (3:1)
duration of exposure	30 sec	40 sec
stopper	Isopropanol	Isopropanol
duration of exposure	30 sec	40 sec
	Dry with nitrogen-gas	Dry with nitrogen-gas
Electron beam deposition		
material / thickness		
first layer	Ti / 3 nm	Ti / 3 nm
2nd layer	Ni ₈₁ Fe ₁₉ / 30 nm	Au / 100 nm
base pressure	1E-8 mBar	1E-8 mBar
Lift-off process		
solvent	Aceton	Aceton
duration	Soak over night	Soak over night
solvent	Isopropanol	Isopropanol
application	ultra-sonic-bath, 30 sec	ultra-sonic-bath, 30 sec
	Dry with nitrogen-gas	Dry with nitrogen-gas

Table A.2: Recipe for the fabrication of the Ni₈₁Fe₁₉ microstructures in the NanoFaro facility of the Helmholtz-Zentrum Dresden - Rossendorf for the study of spin-wave dynamics in domain walls. Two sequential steps denoted A and B have been performed to separately produce the microstructures and Au antennas, respectively.

Versicherung

Hiermit versichere ich, dass ich die vorliegende Arbeit ohne unzulässige Hilfe Dritter und ohne Benutzung anderer als der angegebenen Hilfsmittel angefertigt habe; die aus fremden Quellen direkt oder indirekt übernommenen Gedanken sind als solche kenntlich gemacht. Die Arbeit wurde bisher weder im Inland noch im Ausland in gleicher oder ähnlicher Form einer anderen Prüfungsbehörde vorgelegt.

Die Arbeit wurde unter der wissenschaftlichen Betreuung durch Dr. Helmut Schultheiß und Prof. Dr. Jürgen Faßbender am Helmholtz-Zentrum Dresden - Rossendorf durchgeführt.

Ich erkenne die Promotionsordnung der Fakultät Mathematik und Naturwissenschaften der Technischen Universität Dresden vom 23.02.2011 an.

Es haben keine früheren erfolglosen Promotionsverfahren stattgefunden.

Datum, Ort

Unterschrift

Lebenslauf

Angaben zur Person

Name: Kai Wagner
Geburtstag- und Ort: 9. Oktober 1986, Hilden
Familienstand: ledig

Schulbildung

1993 - 1997 Kempener Grundschule, Erkrath
1997 - 2006 Gymnasium Hochdahl, Erkrath
2006 Allgemeine Hochschulreife (Abitur)

Studium

2007 - 2013 Studium der Physik, Universität Duisburg-Essen
09.2010 Bachelor of Science (B.Sc.) in Physik
Titel der Bachelor-Arbeit:
“In situ frequenzabhängige Ferromagnetische Resonanz an epitaktisch gewachsenen Fe-Schichten”
05.2013 Master of Science (M.Sc.) in Physik
Titel der Master-Arbeit:
“Charakterisierung periodisch strukturierter magnetischer dünner Filme mittels Ferromagnetischer Resonanz”

ab 02.2014 Anstellung am Helmholtz-Zentrum Dresden - Rossendorf
in der Arbeitsgruppe von Dr. H. Schultheiß
ab 03.2015 Beginn des Promotionstudiums an der TU Dresden